Spring 1-1-2016

# Incorporating Uncertainty into Spacecraft Mission and Trajectory Design

Juliana D. Feldhacker
*University of Colorado at Boulder*, jules.feldhacker@gmail.com

# Incorporating Uncertainty into Spacecraft Mission and Trajectory Design

by

**Juliana D. Feldhacker**

B.S., Aerospace Engineering and Mechanics, University of Minnesota, 2011

B.A., Political Science, University of Minnesota, 2011

M.S., Aerospace Engineering Sciences, University of Colorado, 2013

A thesis submitted to the

Faculty of the Graduate School of the

University of Colorado in partial fulfillment

of the requirements for the degree of

Doctor of Philosophy

Department of Aerospace Engineering Sciences

2016

This thesis entitled:
Incorporating Uncertainty into Spacecraft Mission and Trajectory Design
written by Juliana D. Feldhacker
has been approved for the Department of Aerospace Engineering Sciences

Brandon A. Jones

Alireza Doostan

Date

The final copy of this thesis has been examined by the signatories, and we find that both the content and the form meet acceptable presentation standards of scholarly work in the above mentioned discipline.

Feldhacker, Juliana D. (Ph.D., Aerospace Engineering Sciences)

Incorporating Uncertainty into Spacecraft Mission and Trajectory Design

Thesis directed by Prof. Brandon A. Jones

The complex nature of many astrodynamic systems often leads to high computational costs or degraded accuracy in the analysis and design of spacecraft missions, and the incorporation of uncertainty into the trajectory optimization process often becomes intractable. This research applies mathematical modeling techniques to reduce computational cost and improve tractability for design, optimization, uncertainty quantification (UQ) and sensitivity analysis (SA) in astrodynamic systems and develops a method for trajectory optimization under uncertainty (OUU).

This thesis demonstrates the use of surrogate regression models and polynomial chaos expansions for the purpose of design and UQ in the complex three-body system. Results are presented for the application of the models to the design of mid-field rendezvous maneuvers for spacecraft in three-body orbits. The models are shown to provide high accuracy with no *a priori* knowledge on the sample size required for convergence. Additionally, a method is developed for the direct incorporation of system uncertainties into the design process for the purpose of OUU and robust design; these methods are also applied to the rendezvous problem. It is shown that the models can be used for constrained optimization with orders of magnitude fewer samples than is required for a Monte Carlo approach to the same problem.

Finally, this research considers an application for which regression models are not well-suited, namely UQ for the kinetic deflection of potentially hazardous asteroids under the assumptions of real asteroid shape models and uncertainties in the impact trajectory and the surface material properties of the asteroid, which produce a non-smooth system response. An alternate set of models is presented that enables analytic computation of the uncertainties in the imparted momentum from impact. Use of these models for a survey of asteroids allows conclusions to be drawn on the effects of an asteroid's shape on the ability to successfully divert the asteroid via kinetic impactor.

## Dedication

To the memory of Dr. George H. Born − teacher, mentor, supporter and advocate − without whom I would never have made it to this point.

Never give up and never surrender.

## Acknowledgements

I would like to thank my advisor Dr. Brandon Jones for his invaluable guidance and patience throughout the development and execution of my dissertation research. I would also like to thank Dr. George Born and Dr. Jeffrey Parker, who have both served in advising roles during my graduate career in addition to participating as members of my thesis committee. I am very grateful to Dr. Alireza Doostan and Dr. Daniel Scheeres for their extensive technical assistance with my research and for serving on my committee, as well as to the remaining committee member, Dr. Gregory Beylkin. Additionally, I am grateful to Dr. Jerrad Hampton of the University of Colorado for his contributions to this work in the design of experiments, Collin Bezrouk of the University of Colorado for providing state data for the distant retrograde orbit, and Cory Ahrens of the Colorado School of Mines for providing the set of nearly uniform points on a sphere used in the asteroid impact analysis.

To my parents, family, and friends, who have all provided so much support and encouragement throughout this process, I give my love and deepest appreciation. Thank you for putting up with me over these last several years. Thank you to my fellow students in the Colorado Center for Astrodynamics Research for your friendship and teamwork. To Ben Bradley, Jason Leonard, and Eduardo Villalba – your teaching and guidance, particularly in the early years of my graduate career, is much appreciated. Finally, I would like to thank the other members of the faculty and staff of CCAR and the Department of Aerospace Engineering Sciences who provided so much technical, academic, and personal support over the years, including Dr. Penny Axelrad, Joe Tanner, Steve Hart, and Sarah Melssen.

This research was funded in part by the Department of Defense SMART Fellowship; the Jet Propulsion Laboratory, California Institute of Technology under contract 1516188; NASA's Space Technology Research Opportunities – Early Stage Innovations Program under grant NNX14AB08G; and the Zonta International Amelia Earhart Award. The material is based in part on work by Alireza Doostan supported by the U.S. Department of Energy Office of Science, Office of Advanced Scientific Computing Research under Award Number DE-SC0006402 and NSF grant CMMI-1454601.

# Contents

**Chapter**

# Tables

**Table**

# Figures

**Figure**

# Chapter 1

## Introduction and Motivation

The complex nature of astrodynamic systems guarantees the existence of system uncertainties that can lead to stochastic variations in the nominal spacecraft trajectories for any space mission. These uncertainties can be grouped into two categories. Epistemic, or reducible, uncertainties are those that result from incomplete knowledge on the dynamical system under consideration and can consist of measurement errors, incorrect assumptions, and simplifications made in the physical and mathematical models used to define the system. Epistemic uncertainties affecting space missions may include, for example, uncertainties in the spacecraft state estimate, the gravity models of planetary bodies, third body effects, solar radiation pressure (as a function of a spacecraft's coefficient of reflectivity $C_R$), and the drag coefficient $C_D$ of spacecraft in low Earth orbit (LEO). Aleatory, or irreducible, uncertainties, on the other hand, refer to the natural variability that exists in a system. Maneuver execution errors, solar radiation pressure (as a function of the solar flux), and the atmospheric properties of a planet all constitute possible sources of aleatory uncertainties acting on a spacecraft.

The presence of such uncertainties can have implications for many astrodynamic applications. For instance, in spacecraft rendezvous, efforts to better ensure mission success and minimize the probability of collision between the chaser and target spacecraft commonly rely on establishing large keep-out spheres about the target vehicle prior to the commencement of proximity operations. In interplanetary missions, maneuver execution errors and uncertainties in the state estimates early in the transfer can lead to large deviations from the target location upon arrival at a planet. Addi-

tionally, the highly dynamic environments faced by spacecraft whose missions include moon tours at the destination planet make the propagation of uncertainty more difficult during this phase [109]. Both of these factors can affect the ability to achieve low planetary flybys while complying with planetary protection requirements. For conjunction assessment and collision avoidance in Earth orbit, improper characterization and low accuracy propagation of state uncertainties can result in either failure to predict a possible collision or false alarms that result in wasted propellant due to unnecessary avoidance maneuvers. In the general field of mission assurance, current approaches for most missions tend to resort to overly conservative safety factors in the determination of such mission parameters as the amount of excess propellant carried on-board the spacecraft. Ultimately, proper accounting for and modeling of the system stochastics in spacecraft mission design could be the determining factor between the success or failure of a mission.

Each of these applications therefore stands to benefit from the ability to accurately model stochastic systems and to directly incorporate uncertainty into mission and trajectory design in a tractable manner. However, in the modeling of complex astrodynamic systems, a trade-off typically exists between computational expense and high-fidelity analysis capabilities. This problem is common to virtually all engineering disciplines and has implications for design, analysis, optimization, and uncertainty quantification (UQ), among others. The difficulties in modeling spacecraft trajectories arise primarily from the nonlinearity of the dynamical systems under consideration. As a result, the traditional modeling and analysis techniques commonly used in astrodynamics may face either high computational costs or degraded accuracy. These methods include, for example, two-body orbit assumptions [8, 132], massive grid searches for trajectory design and optimization [4, 6, 39, 59, 94], propagation of uncertainty using the linearized state transition matrix (STM) [128], Monte Carlo simulations [110, 111], and local sensitivity analysis via function derivatives [42, 120].

A number of tools have been developed to better address the balance of accuracy and computational cost in each of the areas of design, analysis, optimization, and UQ, and several of these tools have been applied independently to problems in astrodynamics. Surrogate models, for exam-

ple, address the trade-off between accuracy and computational expense by representing a dynamical system as a reduced-order model (ROM), thereby minimizing the need for repeated evaluation of an ordinary differential equation (ODE) solver and other computationally expensive techniques during analysis, yet maintaining high levels of accuracy in the system [119, 104, 61]. Surrogate models have been proven to be an effective means of representing and estimating complex systems involving both large numbers of design variables and inherent uncertainty. Such models have been used in a broad range of aerospace disciplines, including structural design [7], rocket engine component design [28, 93, 131], cavitating flows [45], helicoptor rotor blade vibrations [44], and missile performance [108], and were introduced to trajectory design and optimization in the areas of interplanetary transfers and satellite constellation design [36] as well as low-thrust trajectory optimization [98]. A subset of surrogate models known as generalized polynomial chaos expansions (PCEs) is specifically tailored for the modeling of stochastic systems and is therefore useful for the purpose of uncertainty quantification in nonlinear systems. The application of PCE to the propagation of orbit uncertainties and maneuver execution errors has been studied in [62], [63], and [64]. An alternative approach to the nonlinear propagation of system stochastics is offered by Gaussian mixtures methods (GMM). Rather than generating a global function to provide a direct representation of the system dynamics, GMM propagates only the statistical moments of component distributions used to approximate the uncertainty of the system. GMM has also been used in orbit determination and uncertainty propagation in [43], [21], and [53].

Despite these advancements, little work has been completed to date that addresses a unified approach to mission and trajectory design in stochastic astrodynamic systems. The research presented here develops integrated stochastic design and analysis tools that build upon those methods already in use in astrodynamics and that incorporate additional models and techniques found in other disciplines for the purpose of spacecraft trajectory optimization under uncertainty (OUU). The aim of these tools is to provide tractable, low cost methods for incorporating uncertainty modeling directly into the design and analysis process and for enabling global sensitivity analysis.

Optimization under uncertainty, also referred to as quality design or parameter design, re-

lies on the direct incorporation of system stochastics into the optimization process rather than performing uncertainty quantification only after optimizing a deterministic system. The primary advantage of OUU is the enabling of robust design, which allows for the inclusion of system uncertainties as either optimized parameters or constraints on the optimization cost function. OUU has a rich history in fields such as manufacturing engineering [127, 69], structural design [136, 27], power converters [88], control systems [41], and airfoil design [22].

While numerous approaches to OUU have been developed, this research explores the use of polynomial regression surrogate design models and the related polynomial chaos expansions in the robust optimization of spacecraft trajectories. Regression models and PCEs both rely on the projection of a system response onto an orthogonal polynomial basis, providing a computationally efficient and tractable means of characterizing the effects of system inputs on a given quantity of interest (QOI). The common derivations of these models make them ideally suited for integration into a single model for OUU in which the design parameters and stochastic inputs are differentiated by the choice of the basis functions used. This approach to OUU has previously been demonstrated for applications in tool design [70], airfoil design [22], control systems [55], and structural mechanics [136].

This thesis applies surrogate-based stochastic design models to the robust design of impulsive spacecraft rendezvous maneuvers, taking advantage of the models' ability to represent complex trade spaces for efficient and tractable design, optimization, and analysis. The research specifically explores the capacity of surrogate models to aid in the mission design process in the context of spacecraft rendezvous in the Earth-Moon circular restricted three-body system, including spacecraft in halo orbits about the Earth-Moon $L_2$ libration point (EML-2) and in distant retrograde orbits (DRO) about the Moon. This orbital regime is of particular interest for a number of space missions, including, for example, far-side lunar landers and lunar rovers [16, 3], as well as human exploration missions such as NASA's Asteroid Redirect Mission [52, 10, 77].

The complex nature of the three-body system precludes the use of analytical approximations, necessitating computationally intensive numerical simulations and creating an opportunity for re-

duced computational cost through the application of surrogate models. The use of these models as efficient stochastic design tools can enable significant time savings when performing, for example, robust design, global trajectory optimization, and trade space exploration for exercises in rapid mission design. Additionally, the surrogate models can provide comprehensive information about the system as a whole, including the sensitivity of the QOI to each of the system inputs. The development of rapid trajectory design and optimization tools such as these were identified in [103], in particular, as a priority for enabling future planetary science missions.

Systems also exist that would benefit from the ability to accurately and efficiently account for uncertainties in the mission design process, but which are not well-suited for the use of surrogate models. Global surrogates encounter difficulties in trying to model non-smooth, discontinuous, high order, or multi-modal systems, so other techniques must be developed to conduct UQ in systems with any of these characteristics. One such case is the deflection of potentially hazardous asteroids (PHAs) via kinetic impact. The transfer of momentum from an impactor to an asteroid is heavily dependent on the shape, topology, and surface material properties of the asteroid, yet little information is available regarding these properties for a large number of asteroids in our solar system. As a result, a significant amount of uncertainty is inherent in any mission intending to divert an asteroid by kinetic impact. However, the models typically used to define the asteroid shape are comprised of a collection of triangular facets, and this representation, combined with the dependency of the direction of the imparted momentum on the surface normal at the point of impact, results in discontinuities in the $\Delta \boldsymbol{V}$ acting on the asteroid at the boundaries between facets. While separate surrogate models could potentially be generated for each individual surface, the large number of facets that constitute a single asteroid make this approach impractical. Instead, this research proposes an alternate set of tools to enable an analytic computation of the distribution in the momentum transferred to the asteroid due to uncertain system inputs. The results of this analysis can be used to identify favorable impact locations for improved impactor performance.

Chapter 2 of this thesis defines the astrodynamic systems that are explored in this body of research. Section 2.1 provides an overview of the assumptions central to the circular restricted

three-body problem (CRTBP), lists the resulting equations of motion for the system, and briefly introduces the halo and distant retrograde orbits to be included in the later analysis. Definitions of the design and stochastic spaces considered for rendezvous in each of these orbits are also provided. Section 2.2 then introduces the impact model and asteroid shape models used in the analysis of the kinetic deflection of PHAs. This section also validates the use of the impact model for the purpose of analysis by a comparison to the results of particle-based numerical simulations performed by Lawrence Livermore National Laboratories (LLNL). A discussion of the stochastic considerations for the asteroid impact scenario closes out the chapter.

Chapter 3 details the surrogate models that form the basis for optimization under uncertainty of the spacecraft rendezvous maneuvers, based on the presentation of the methods provided in [31] and [32]. The foundation for the models is first laid out in the context of deterministic design surrogates in Section 3.1, followed by the details specific to PCE in Section 3.2. Section 3.3 outlines the surrogate model development process, which consists of the design of experiments (DOE), model estimation, and validation. Included in this section are descriptions of an alternative sampling measure known as asymptotic sampling and a model solution method for compressive sampling that can both significantly reduce the number of sample data necessary for convergence of the model under appropriate conditions. Finally, Section 3.4 addresses the integration of the deterministic and stochastic models for the purpose of OUU, presents the cost function used in the optimization scheme, and provides an analytic formulation for the final state statistics that is enabled by the surrogate models.

Chapter 4 introduces the concept of sensitivity analysis (SA) and presents methods for both local and global SA that can be used in the spacecraft rendezvous and kinetic deflection problems. These sensitivities provide a measure of the dependence of the system QOI to each of the input parameters, which in turn provides insight into how prescribed changes to the mission design or changes in the level of available knowledge regarding stochastic parameters will influence, for example, the propellant cost of the rendezvous mission or the imparted momentum in the deflection mission. This chapter includes empirical and analytic formulations for the global sensitivity measure

known as the Sobol' sensitivity indices.

Chapter 5 presents results for the application of the surrogate modeling techniques to the problem of spacecraft rendezvous in three-body orbits in the Earth-Moon system, which have previously been published in [31] and [32]. Section 5.1 first demonstrates the use of deterministic regression models for the purpose of non-stochastic design in both the halo orbit and the DRO. A thorough analysis of the accuracy and convergence properties of the models, constructed using two different sampling methods and two different validation techniques, is provided. Additionally, the models are shown to be advantageous for mission design − particularly initial mission design − even without the incorporation of system uncertainties, as they enable rapid exploration of a broad design space, provide insight into the system behavior across that design space, and facilitate analytic calculations of global sensitivities. Section 5.2 then extends the application of the surrogate models to the stochastic rendezvous problem. The ability of compressive sampling techniques to reduce the computational costs associated with the development of the model and to enable modeling of high-dimensional problems is explored, and the models are employed for the constrained optimization of spacecraft rendezvous.

The analytical methods proposed for uncertainty quantification and analysis in the kinetic deflection of PHAs are described in Chapter 6, which draws heavily from [33] and [34]. The first set of tools, presented in Section 6.1, are those which can be used to convert uncertainty in the impact location of the spacecraft into the probability of hitting each of the facets about the asteroid body for a given impact trajectory. This is followed in Section 6.2 by an introduction to the Gaussian mixtures method (GMM), which can be used to map the combined effects of the probability of impacting a facet and the uncertainty in the asteroid material properties to a final distribution on the $\Delta V$ imparted on the asteroid.

The models of Chapter 6 are applied to a survey of asteroid shape models in Chapter 7. Detailed analysis is first presented for impact with the asteroid Golevka in order to validate several simplifying assumptions that are used in the remainder of the study. Three additional asteroids are analyzed to provide comparisons for the Golevka results and to highlight the effects of differences

in local topography on the effectiveness of deflection attempts. The models are then applied to a larger survey of 21 asteroids to identify broader trends based on asteroid shape. These results have also been previously published and can be found in [33] and [34].

Finally, Chapter 8 provides a review of the most significant results and contributions of this body of research. The chapter concludes with a discussion of future work suggested to further improve the models and to expand on the analysis presented in this thesis.

# Chapter 2

# Problem Definition

This chapter introduces two mission scenarios that would benefit from efficient design techniques, a tractable approach to uncertainty quantification, and the ability to perform optimization under uncertainty. Included are a discussion of the advantages afforded to each mission type and a definition of the dynamical system used for each. Section 2.1 discusses the case of spacecraft rendezvous design and optimization in the circular restricted three-body problem (CRTBP), and Section 2.2 covers the case of uncertainty quantification for the kinetic deflection of potentially hazardous asteroids (PHAs).

## 2.1 Rendezvous in the CRTBP

Trajectory design in complex astrodynamic systems typically faces a trade-off between computational expense and model fidelity. In such systems, no explicit solution exists for the acceleration acting on a spacecraft. As a result, trajectory design and optimization, as well as uncertainty propagation, traditionally rely on Monte Carlo analysis and the iterative integration of a system of ordinary differential equations (ODEs). Much recent effort has been focused on developing improved techniques for low thrust trajectory optimization in such systems (see [96, 98, 101, 100], among others), but some missions - particularly crewed missions - require the use of high thrust spacecraft. The current concept of operations for NASA's Asteroid Redirect Mission (ARM), for example, calls for the rendezvous of the crewed Orion spacecraft with the Asteroid Redirect Vehicle (ARV) using impulsive maneuvers [50].

To demonstrate the use of surrogate-based design and optimization under uncertainty (OUU) in astrodynamics, this research applies the methods developed herein to the design of both deterministic and stochastic impulsive rendezvous maneuvers in the Earth-Moon CRTBP. The deterministic design models are first validated for rendezvous in a halo orbit about the Earth-Moon $L_2$ libration point (EML-2) and are then applied to rendezvous in a distant retrograde orbit (DRO) about the moon. The surrogate capabilities are then expanded to include OUU for each of the two orbits. The deterministic and stochastic models are used for the design of the mid-field stage of rendezvous, in which a two-burn sequence carries the chaser vehicle from the point of insertion into the three-body orbit through to the commencement of proximity operations with the target. For rendezvous in the DRO, the test case is defined using the mission parameters proposed for the ARM mission, outlined in [50], and the chaser and target vehicles are taken to be the crewed Orion vehicle and the ARV, respectively.

The ability to provide accurate, efficient characterization and optimization of the stochastic design space for high thrust spacecraft trajectories can produce benefits for a number of considerations in mission design. For example, the models can improve the process of initial mission design by enabling rapid exploration of a broad design space and providing a tractable method for analysis of the sensitivities of the design quantities of interest (QOI), such as the required $\Delta V$ or the time of flight, to the available design parameters. These sensitivities in turn provide insight into how prescribed changes to the mission design by external factors will influence, for example, the propellant or time cost of the mission.

Another design consideration that can benefit from the efficiency and tractability of the surrogate models is mission assurance. Efforts to better ensure mission success commonly rely on conservative safety factors in the determination of such mission parameters as the amount of excess propellant carried on-board the spacecraft and the size of the keep-out sphere established for rendezvous procedures. Better characterization of system uncertainties and the combined effects of stochastic and deterministic mission parameters would likely help to reduce the costs associated with current approaches to mission assurance, and the ability to perform trajectory OUU can provide

advantages in reducing both surplus propellant and the variance in the spacecraft's propagated state.

This section provides a description of the mid-field rendezvous problem for spacecraft in the CRTBP. Section 2.1.1 defines the system dynamics for the CRTBP, and Section 2.1.2 gives an overview of the differential corrector used to generate truth data. Finally, definitions of the design and stochastic spaces to be considered in this study are contained in Sections 2.1.3 and 2.1.4, respectively.

### 2.1.1 System Dynamics

The CRTBP model relies on two main assumptions [132]. First, the model identifies two massive bodies $m_1$ and $m_2$ as the primary and secondary bodies of the system, in this case the Earth and the Moon, and these bodies are assumed to be in coplanar circular orbits about their barycenter. Second, the mass of the third body (i.e. the spacecraft) $m_{sc}$ is taken to be much smaller than the mass of the primary and secondary bodies, $m_{sc} << m_1, m_2$, such that the spacecraft mass can be considered negligible. With these assumptions, the mass ratio of the system is defined as

$$\mu = \frac{m_2}{m_1 + m_2}. \tag{2.1}$$

Further, using the ratio of Equation 2.1, a set of nondimensional parameters may be established for the system in which the mass unit (MU) is defined as the sum of the masses of the primary and secondary bodies, $m_1 + m_2$, and the distance unit (DU) is defined as the total distance between the two bodies. Thus, in dimensionless form, the masses of the bodies are $m_1 = 1 - \mu$ and $m_2 = \mu$, and the geometry of the system follows that which is shown in Fig. 2.1.

The system dynamics of interest for the model are, in dimensionless form,

$$\begin{aligned}
\ddot{x} - 2\dot{y} - x &= -\frac{(1-\mu)(x+\mu)}{r_1^3} - \frac{\mu(x+\mu-1)}{r_2^3} \\
\ddot{y} + 2\dot{x} - y &= -\frac{(1-\mu)y}{r_1^3} - \frac{\mu y}{r_2^3} \\
\ddot{z} &= -\frac{(1-\mu)z}{r_1^3} - \frac{\mu z}{r_2^3}
\end{aligned} \tag{2.2}$$

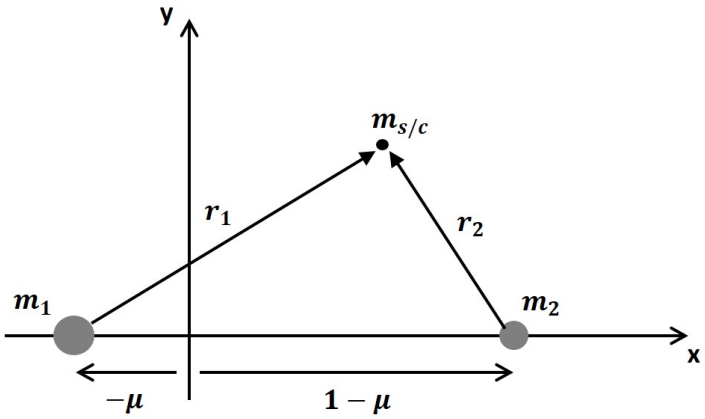


Figure 2.1: System geometry for the non-dimensional three-body problem.

where

$$r_1 = \sqrt{(x+\mu)^2 + y^2 + z^2}, \quad r_2 = \sqrt{(x+\mu-1)^2 + y^2 + z^2}.$$

There exist many different families of orbits in the CRTBP [11], including, for example, planar Lyapunov orbits, halo orbits, and Lissajous orbits, all of which are libration point orbits, in addition to distant retrograde orbits about the Moon. Of particular interest here are halo orbits and distant retrograde orbits, which will be described briefly in the following subsections.

#### 2.1.1.1 Halo Orbits

By setting each of the accelerations in Equation 2.2 to zero and solving for position, a collection of five equilibrium points can be found, known as libration points, which are depicted in Fig. 2.2. The $L_4$ and $L_5$ points are Lyapunov stable, while the three collinear libration points are unstable. A subset of three-body orbit families are located in the vicinity of the libration points and are referred to as libration point orbits (LPOs). LPOs include, for example, halo orbits, Lyapunov orbits, and Lissajous orbits. Halo orbits, such as the example shown in Figure 2.3, are out-of-plane orbits that are periodic in the CRTBP [29, 30]. Halo orbits at EML-2 can be particularly useful for space missions due to their access to the far side of the Moon and the existence of orbits within the family which are not subject to lunar occultation.

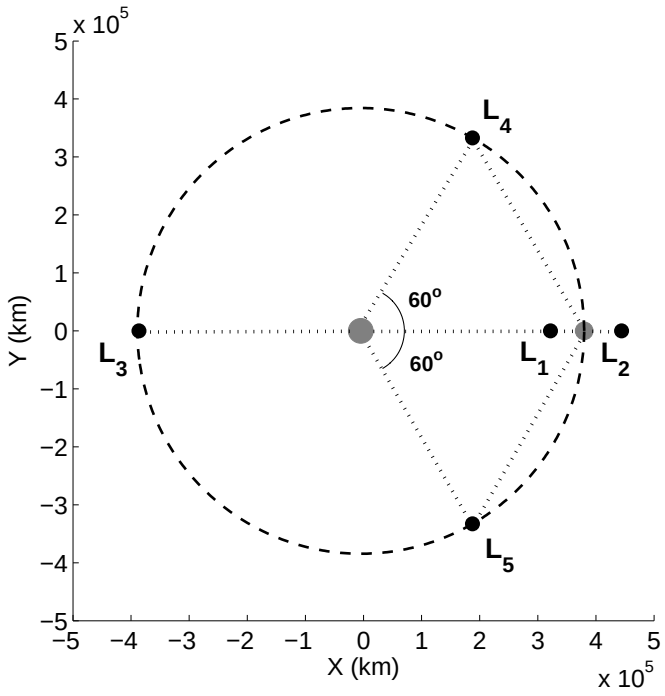


Figure 2.2: Libration points in the Earth-Moon three-body system are located at points of dynamic equilibrium.

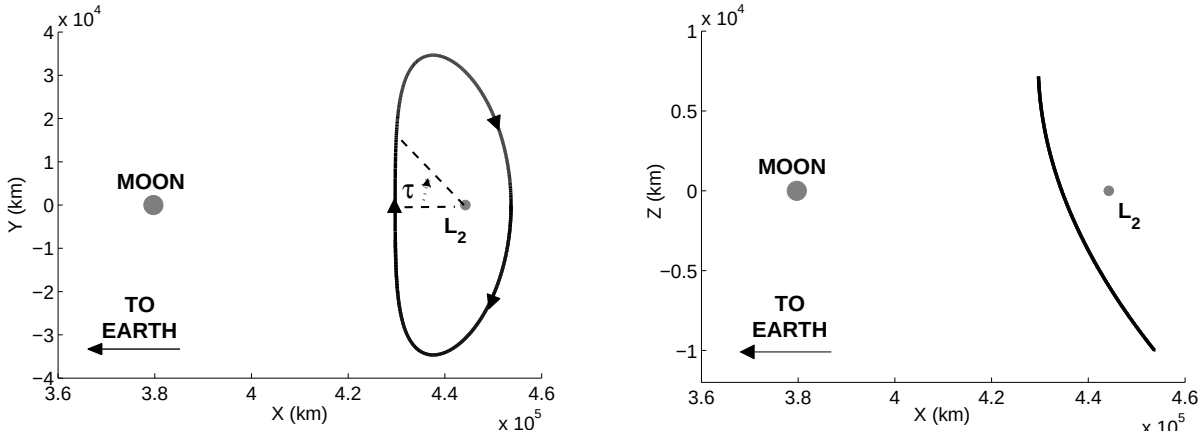


(a) Top view

(b) Side view

Figure 2.3: Example halo orbit at the Earth-Moon $L_2$ libration point. $\tau$ measures spacecraft position within the orbit.

#### 2.1.1.2 Distant Retrograde Orbits

Another family of orbits that exist in the three-body system are known as distant retrograde orbits. These orbits, illustrated in Fig. 2.4, are retrograde orbits about the Moon large enough that Earth's gravitation significantly influences the orbit. Like halo orbits, DROs are periodic in the CRTBP. Unlike orbits about the collinear libration points, however, DROs are Lyapunov stable. This stability, combined with their proximity to the Moon, has made DROs of particular interest for space missions in recent years [84][1] [,2] .

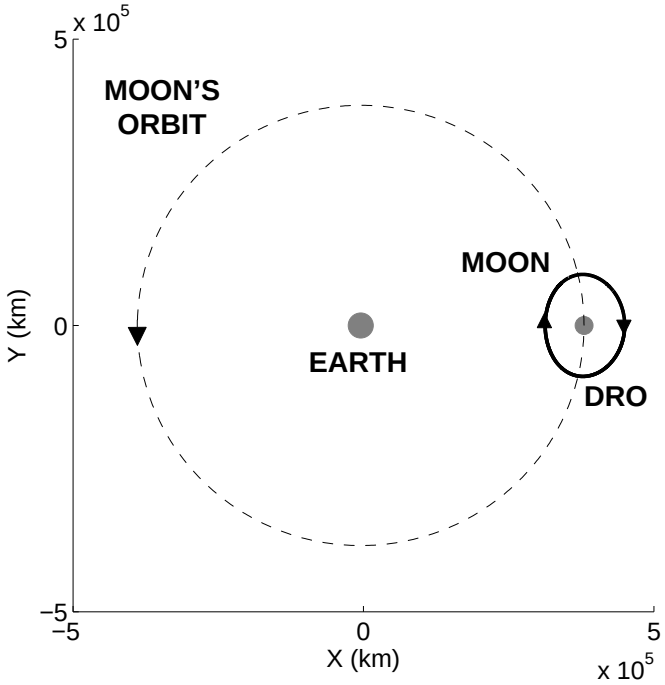


Figure 2.4: Example distant retrograde orbit (DRO) about the Moon.

[1] B. Muirhead, Asteroid Redirect Robotic Mission (ARRM) Reference Mission Concept Study Public Information Package V1, Aug. 2013. NASA, JPL. [Retrieved May 19, 2015] https://www.nasa.gov/sites/default/files/files/Asteroid-Redirect-Robotic-Mission-Muirhead-TAGGED2.pdf.

[2] M. Gates, "Asteroid Redirect Mission Update: Briefing to Small Bodies Assessment Group," Jul. 30, 2014. NASA. [Retrieved May 19, 2015] http://www.lpi.usra.edu/sbag/meetings/jul2014/presentations/0900_Wed_Gates_ARM_activities.pdf.

### 2.1.2 Single-Shooting Differential Corrector

The true $\Delta \boldsymbol{V}$ required for rendezvous between the chaser and target vehicles in the halo orbit and the DRO is determined using the technique of single-shooting differential correction [56]. Differential correctors perform targeting by using the linearized state transition matrix $\Phi(t_f, t_0)$ to adjust an initial state $\boldsymbol{X}_0$ at time $t_0$ such that a desired final state $\boldsymbol{X}_f$ at time $t_f$ can be achieved under the natural system dynamics [95]. In the case of spacecraft targeting, the state vector is composed of the position and velocity of the spacecraft $\boldsymbol{X} = \left[\boldsymbol{R}^T \ \boldsymbol{V}^T\right]^T$, and two constraints are placed on the differential corrector: 1) the initial position of the chaser $\boldsymbol{R}_{c_0}$ is fixed, and 2) the targeted state is taken as the position of the target vehicle at time $t_f$, with the final velocity remaining a free variable. Under these constraints, the initial state of the chaser $\boldsymbol{X}_{c_0}$ is propagated along a nominal trajectory $T(t)$ defined by the system dynamics and the desired time of flight $t$ to the final state $\boldsymbol{X}_{c_f}$, as depicted in Fig. 2.5. The nominal position of the chaser at time $t$ is differenced from the targeted position $\hat{\boldsymbol{R}}_f$ to produce a position deviation,

$$\delta \boldsymbol{R}_{c_f} = \boldsymbol{R}_{c_f} - \hat{\boldsymbol{R}}_{c_f}. \tag{2.3}$$

By decomposing the state transition matrix such that

$$\Phi(t_f, t_0) = \begin{bmatrix} \Phi_{RR}(t_f, t_0) & \Phi_{RV}(t_f, t_0) \\ \Phi_{VR}(t_f, t_0) & \Phi_{VV}(t_f, t_0) \end{bmatrix} = \begin{bmatrix} \frac{\delta \boldsymbol{R}(t_f)}{\delta \boldsymbol{R}(t_0)} & \frac{\delta \boldsymbol{R}(t_f)}{\delta \boldsymbol{V}(t_0)} \\ \frac{\delta \boldsymbol{V}(t_f)}{\delta \boldsymbol{R}(t_0)} & \frac{\delta \boldsymbol{V}(t_f)}{\delta \boldsymbol{V}(t_0)} \end{bmatrix}, \tag{2.4}$$

the deviation of Equation 2.3 can be mapped back to a correction in the initial velocity vector of the chaser using the equation

$$\Delta \boldsymbol{V}_{c_0} = \left[\Phi_{RV}(t_f, t_0)\right]^{-1} \delta \boldsymbol{R}_{c_f}. \tag{2.5}$$

This velocity correction is interpreted as the $\Delta \boldsymbol{V}$ required for targeting. However, because the state transition matrix of Equation 2.4 is linear and the spacecraft are orbiting in a nonlinear dynamical system, the process must be iterated until convergence. The accumulation of the results of Equation 2.5 for all iterations is taken to be the total $\Delta \boldsymbol{V}_0$ required for rendezvous, and the difference between the chaser's velocity and that of the target at time $t$ of rendezvous is taken as $\Delta \boldsymbol{V}_f$.

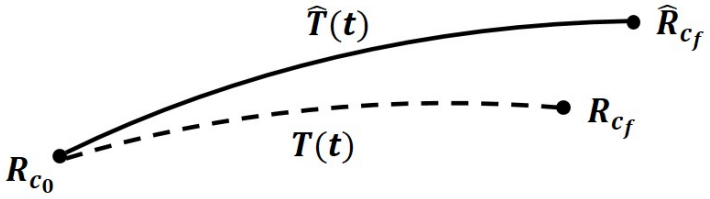


Figure 2.5: Diagram of the single-shooting differential corrector.

### 2.1.3 Design Space

For the spacecraft in the halo orbit and the DRO, modeling and optimization is first performed for the deterministic design problem. The design parameters under consideration for this problem, which are illustrated in Fig. 2.6, are the initial position $\tau(s_1)$ of the chaser about the orbit, the time of flight $t(s_2)$, and the initial separation between the vehicles $\Delta\tau(s_3)$, where $s_1$ is periodic on the interval $[0, 2\pi]$ and $s_2, s_3 \in [-1, 1]$. Thus, the deterministic inputs to the system are $\boldsymbol{s} \in \mathbb{R}^3$ and they can be mapped to the design parameters using the equations

$$\tau = \frac{\tau_{max} - \tau_{min}}{2\pi} s_1 + \tau_{min}$$

for $s_1$ and

$$x_i = \frac{x_{i,max} - x_{i,min}}{2}(s_i + 1) + x_{i,min}, \qquad x_i \in \{t, \Delta\tau\}\,.$$

for $s_2$ and $s_3$. The range of parameter values considered for each type of orbit are provided in Table 2.1. The table also includes the design space used in a 2-dimensional case for rendezvous in the DRO, in which the initial position of the chaser is held constant. This additional study is included to provide a direct comparison of the speed and capability of the surrogate design models to the Monte Carlo analysis presented for the same case in [50].

The quantity of interest for the deterministic problem is the magnitude of the total required change in velocity $\Delta V(\boldsymbol{s}) = |\Delta \boldsymbol{V}(\boldsymbol{s})|$. Figure 2.7 shows the required $\Delta V$ for rendezvous in the halo orbit, as computed using the single shooter, and the $\Delta V$ required for rendezvous in the DRO

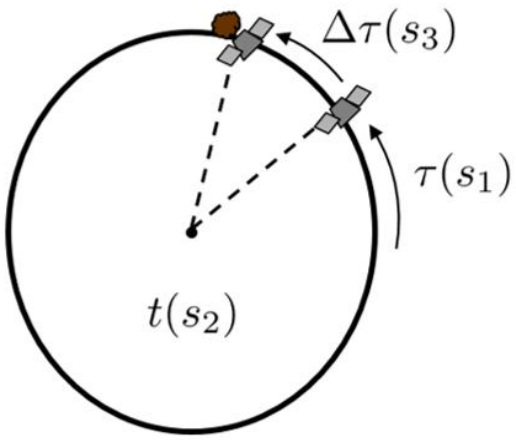


Figure 2.6: Design parameters considered for spacecraft rendezvous in three-body orbits include the initial position $\tau$, time of flight $t$, and initial separation $\Delta\tau$.

is given in Figure 2.8. While the shape of the function in each of the orbits is very similar, the case of the DRO results in lower required $\Delta V$s, primarily due to the smaller values of $\Delta\tau$ under consideration.

Consideration is also given to the optimization of the design parameters in a stochastic system. For this case, the nominal rendezvous trajectory is determined first and is again taken to be a function of the initial configuration of the spacecraft, i.e., the initial position the chaser and the separation between the vehicles, as well as the time of flight. The design space considered

Table 2.1: Design space considered in deterministic maneuver design for rendezvous in three-body orbits.

| | Range | | |
|---|---|---|---|
| | Halo | DRO ($d = 2$) | DRO ($d = 3$) |
| Initial position, $\tau$ (°) | $[0, 360]$ | 0 | $[0, 360]$ |
| Time, $t$ (days) | $[0.25, 1]$ | $[0.25, 1]$ | $[0.25, 1]$ |
| Initial separation, $\Delta\tau$ (°) | $[0.1, 5]$ | $[0.01, 0.25]$ | $[0.01, 0.25]$ |

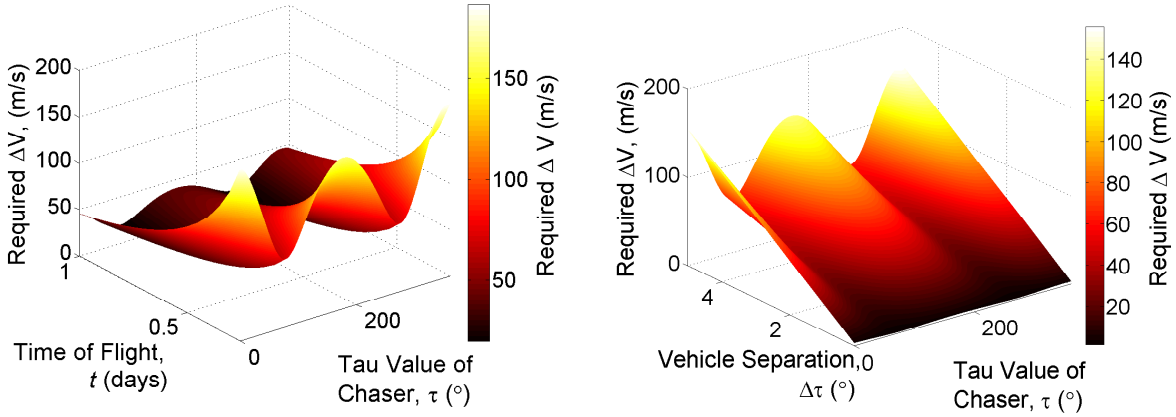


(a) $\Delta\tau = 3^\circ$ (b) $t = 0.5$ days

Figure 2.7: Required $\Delta V$ for spacecraft rendezvous in a 10,000 km z-amplitude halo orbit about EML-2

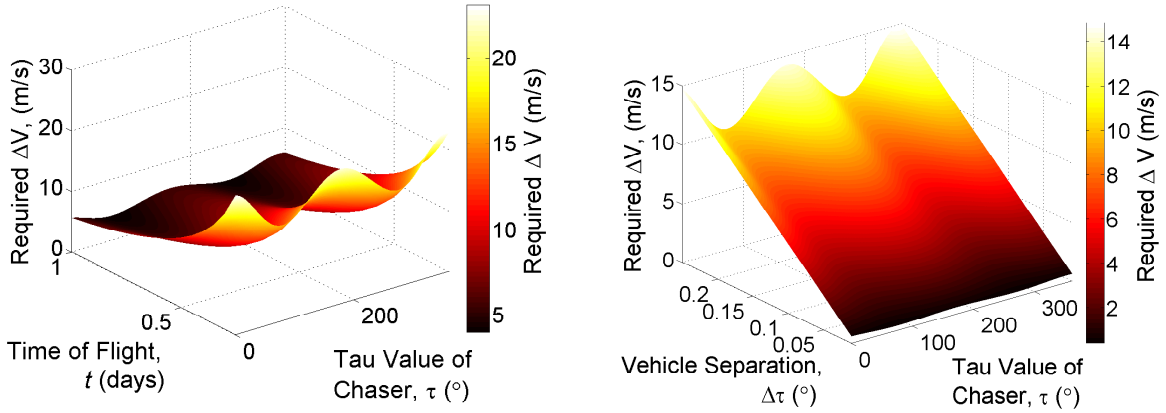


(a) $\Delta\tau = 0.15^\circ$ (b) $t = 0.5$ days

Figure 2.8: Required $\Delta V$ for spacecraft rendezvous in a 70,000 km DRO

for optimization of the stochastic system is smaller than that used for the deterministic system, in an attempt to limit the order of the problem, and is located about the optimum $\tau$ value for the appropriate range of $t$ and $\Delta\tau$ identified by the deterministic models. All three design inputs are therefore defined on the finite interval $[-1, 1]$, and the range of values used for these design parameters are listed in Table 2.2.

Table 2.2: Design input ranges and stochastic distributions for rendezvous in stochastic three-body systems.

| | Range/Distribution | |
|---|---|---|
| Input Parameter | Halo Orbit | DRO |
| $\tau(s_1)$ (°) | [70,85] | [70,85] |
| $t(s_2)$ (days) | [0.5,0.6] | [0.5,0.6] |
| $\Delta\tau(s_3)$ (°) | [0.11,0.15] | [0.01,0.05] |
| $\delta\Delta V(\xi_1)$ (%) | $\mathcal{N} \sim (0,1)$ | $\mathcal{N} \sim (0,1)$ |
| $\theta(\xi_2)$ (°) | $\mathcal{N} \sim (0,1)$ | $\mathcal{N} \sim (0,1)$ |
| $\phi(\xi_3)$ (°) | $\mathcal{U} \sim [0,360]$ | $\mathcal{U} \sim [0,360]$ |
| $\delta\boldsymbol{R}_0(\boldsymbol{\xi}_R)$ (m) | $\mathcal{N} \sim (0,100)$ | $\mathcal{N} \sim (0,100)$ |
| $\delta\boldsymbol{V}_0(\boldsymbol{\xi}_V)$ (mm/s) | $\mathcal{N} \sim (0,0.5)$ | $\mathcal{N} \sim (0,0.5)$ |

### 2.1.4 System Stochastics

The stochastic space included for robust rendezvous optimization in this study consists of uncertainties in the initial state of the chaser spacecraft and deviations in its trajectory caused by errors in the position correction burn $\Delta\boldsymbol{V}_0$. The maneuver execution errors are represented as a deviation in the thrust with respect to the nominal $\Delta\boldsymbol{V}_0(\boldsymbol{s})$. They can be modeled as stochastic deviations in the magnitude of the burn $\delta\Delta V_0(\xi_1)$, as well as its direction, where the direction is characterized by the cone angle $\theta(\xi_2)$ and the rotation about the nominal $\phi(\xi_3)$. An illustration of the maneuver geometry is provided in Fig. 2.9. The burn magnitude and cone angle are taken to be normally distributed, while the rotation angle is uniformly distributed about the circle. The initial state uncertainties are characterized by a Gaussian distribution on deviations in the cartesian components of the initial 3-DOF position $\delta\boldsymbol{R}_0(\boldsymbol{\xi}_R) = [\delta R_{0,x}(\xi_4), \delta R_{0,y}(\xi_5), \delta R_{0,z}(\xi_6)]$ and 3-DOF velocity $\delta\boldsymbol{V}_0(\boldsymbol{\xi}_V) = [\delta V_{0,x}(\xi_7), \delta V_{0,y}(\xi_8), \delta V_{0,z}(\xi_9)]$ of the chaser.

The stochastic space is therefore defined by the independently distributed random variables $\boldsymbol{\xi} \in \mathbb{R}^9$, where $\xi_1, \xi_2, \boldsymbol{\xi}_R, \boldsymbol{\xi}_V \sim \mathcal{N}(0,1)$ and $\xi_3 \sim \mathcal{U}(-1,1)$, and these random variables are mapped

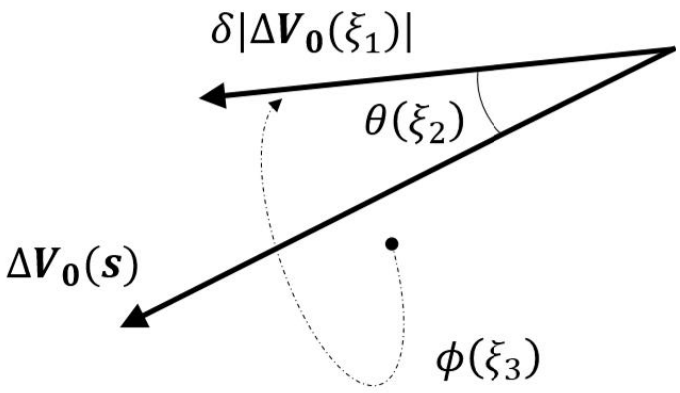


Figure 2.9: Geometry of the maneuver execution errors for $\Delta \boldsymbol{V}_0$

to the values of the burn errors and state uncertainties also contained in Table 2.2. The deviation in the final state of the chaser from the target $\delta \boldsymbol{X}_f(\boldsymbol{s}, \boldsymbol{\xi}) = [\delta \boldsymbol{R}_f^T \ \delta \boldsymbol{V}_f^T]^T$ resulting from these errors is determined by generating a random sample $\boldsymbol{\xi}$ from the joint distribution $\rho(\boldsymbol{\xi})$, applying the perturbed $\Delta \boldsymbol{V}_0(\boldsymbol{s}, \boldsymbol{\xi})$ to the initial state of the chaser, and propagating the perturbed trajectory to time $t$.

The coordinate system used to represent the final state deviations is a form of the NTW satellite coordinate system [132] modified for retrograde orbits in the CRTBP so that the out-of-plane dimension is aligned with the system's angular momentum. Thus, the new coordinate frame TNW is defined such that $T$ is parallel to the spacecraft velocity vector, $N$ is normal to $T$ in the orbital plane, and $W$ is normal to the spacecraft's orbital plane and points in the direction of the angular velocity of the Earth-Moon system. Figure 2.10 illustrates the TNW reference frame.

The QOI for the stochastic design problem are the nominal magnitude of the required change in velocity $\Delta V(\boldsymbol{s}) = |\Delta \boldsymbol{V}(\boldsymbol{s})|$ and the deviation in the final state of the chaser $\delta \boldsymbol{X}_f(\boldsymbol{s}, \boldsymbol{\xi})$. The goal of the optimization problem is to minimize the $\Delta V$ required for rendezvous while limiting the spread of the variance in the final state deviation, as will be stated formally in a later section.

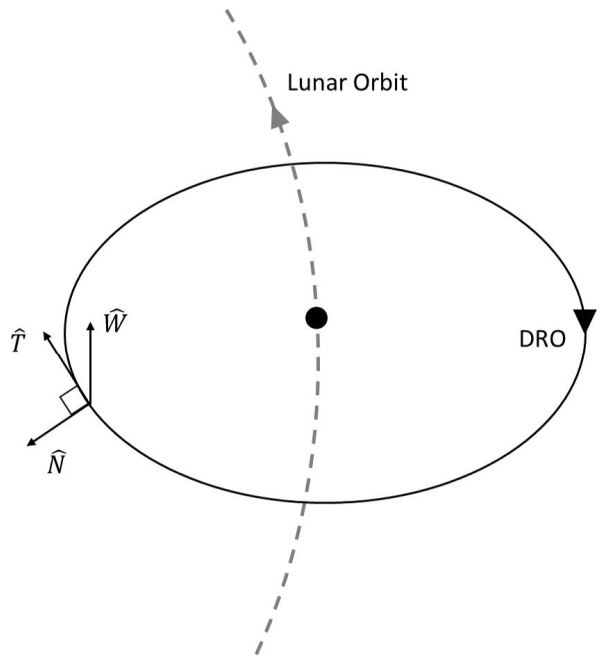


Figure 2.10: Spacecraft TNW reference frame

## 2.2 Kinetic Deflection of Potentially Hazardous Asteroids

The second mission scenario that may benefit from more efficient uncertainty quantification capabilities is the kinetic defletion of potentially hazardous asteroids (PHAs). Kinetic impact provides a technically viable and effective solution for the deflection of PHAs of relatively small size and for which there is sufficient warning time [107]. Kinetic deflection of asteroids relies on a high speed impact between a spacecraft and the PHA, resulting in the transfer of momentum from the impactor to the asteroid body [2]. This technique may provide a high level of delivered momentum and a relatively immediate diversion effect.

Kinetic asteroid deflection has been the subject of much recent study [107, 20, 60, 68, 80, 133]; the majority of the previous work, however, relies on spherical models of asteroids, an assumption which does not provide an accurate representation of the effective momentum transferred during impact. Rather, the local topography described by real asteroid shape models may reduce the effi-

ciency of the transfer by diverting some energy off-axis. Additionally, uncertainty in the transferred momentum is introduced via topography by uncertainties in the asteroid shape model, the impact velocity of the spacecraft, and the surface material properties of the asteroid, as represented by the momentum multiplication factor $\beta$.

Any reduction in the effective momentum transfer to the asteroid can result in undesirable consequences when put into practice. Specifically, a significant enough loss in the delivered $\Delta \boldsymbol{V}$ from intended levels may lead to mission failure. Therefore, a thorough understanding of the effect of asteroid topography on momentum transfer efficiency is necessary in order to fully characterize any kinetic deflection mission.

The work contained in this dissertation studies the effects of real asteroid shapes and stochastic system parameters on the total momentum transferred by the kinetic impactor. Attention is focused on variations caused by the asteroid topography and uncertainties in the impact location. This section provides an overview of the asteroid systems to be considered. Section 2.2.1 presents the analytic momentum transfer model for asteroid impact used in this study, and the asteroid shape models are introduced in Section 2.2.2. Numerical simulations performed for impact with Asteroid 6489 Golevka using particle-based models are provided in Section 2.2.3; these simulations were performed by Lawrence Livermore National Laboratory and are presented here to validate the impact model for use in later analysis. Finally, Section 2.2.4 discusses the system stochastics that may affect the momentum transfer. Later chapters will discuss a number of analytical tools that can be used to improve tractability in the stochastic analysis of kinetic deflection and apply these tools to a collection of asteroid shape models.

### 2.2.1 Asteroid Impact Model

The transfer of momentum to an asteroid from kinetic impact takes place in two phases. The first phase is the direct and immediate transfer of the spacecraft's momentum to the asteroid, while the second phase results from the creation of a surface crater and accompanying ejecta upon impact. This second phase occurs over a finite period of time with the evolution of the ejecta field.

All processes and equations contained in this section are defined relative to an asteroid body-fixed frame, such that the nominal velocity and momentum of the asteroid is zero. In this frame, any rotation of the body can be ignored, although such rotation would affect the $\Delta \boldsymbol{V}$ of the asteroid in an inertial frame.

For a spacecraft of mass $m$ traveling at velocity $\boldsymbol{V}_\infty$ relative to an asteroid of mass $M$, where $\boldsymbol{V}_\infty$ is assumed to be the hyperbolic excess velocity of the spacecraft, the initial momentum of the spacecraft is

$$\boldsymbol{p} = m\boldsymbol{V}_\infty. \tag{2.6}$$

This momentum is transferred directly to the asteroid, resulting in a change in velocity of the asteroid equal to

$$\Delta \boldsymbol{V}_1 = \frac{m}{M+m}\boldsymbol{V}_\infty \approx \gamma \boldsymbol{V}_\infty, \tag{2.7}$$

where it is assumed that $M \gg m$, and $\gamma = m/M$ is the mass ratio of the spacecraft to the asteroid.

Further assuming that the impacting trajectory is within a few tens of degrees of the asteroid's surface normal $\hat{\boldsymbol{n}}$, the spacecraft creates a circular impact crater when it strikes the asteroid's surface. This in turn generates ejecta, some of which will escape the asteroid system. Any escaping ejecta constitutes a net momentum normal to the asteroid's surface, imparting an additional momentum on the asteroid that is also oriented along the normal vector but opposite the direction of motion of the ejecta. The net momentum generated by the ejecta can be quantified using the momentum multiplication factor $\beta$, an empirical parameter for kinetic impact deflections that is dependent on both the impact velocity and the asteroid's material properties, including the equation of state, strength and damage model, and porosity, among others (for a full study of these effects on $\beta$, see [12]) [51, 67, 124]. $\beta$ describes the ratio of the total imparted momentum to the momentum transferred directly by the spacecraft,

$$\beta = \frac{|\Delta \boldsymbol{V}|}{|\Delta \boldsymbol{V}_1|}, \tag{2.8}$$

so that for $\beta = 1$, there is no escaping ejecta and the total imparted momentum is equal to the impacting momentum, and for $\beta > 2$, the momentum resulting from the ejecta is larger than the

impact momentum [54]. Thus, the change in velocity of the asteroid caused by the escaping ejecta is defined as

$$\Delta \boldsymbol{V}_2 = -\gamma \left(\beta - 1\right) \left(\hat{\boldsymbol{n}} \cdot \boldsymbol{V}_\infty\right) \hat{\boldsymbol{n}}. \tag{2.9}$$

Combining Equations 2.7 and 2.9, then, results in a total change in velocity of the asteroid of

$$\Delta \boldsymbol{V} = \gamma \left[\boldsymbol{V}_\infty + \left(\beta - 1\right) \left(\hat{\boldsymbol{n}} \cdot \boldsymbol{V}_\infty\right) \hat{\boldsymbol{n}}\right]. \tag{2.10}$$

The parameter $\beta$, which is known to be a function of both the gravitational force and the physical properties of the asteroid, does not remain constant throughout the body, causing the momentum imparted to the asteroid to vary throughout the temporal evolution of the ejecta field [117]. While this phenomenon is evident in the numerical simulations of Section 2.2.3, a constant value of $\beta$ is used for the analytical results presented in Chapter 7.

### 2.2.2 Asteroid Shape Models

The analysis presented is this body of work is performed using radar-derived shape models for a collection of 21 asteroids, a complete listing of which can be found in Appendix A. The shape model for Asteroid 6489 Golevka [58], selected for its interesting topological features and depicted in Fig. 2.11, is used to first validate the impact model and analytical techniques before these methods are applied to the broader survey of asteroid bodies.

For the analytical techniques, the asteroid shape models are represented as a collection of triangular facets, such as those visible in Fig. 2.11. The model for the asteroid Golevka consists of 4092 facets; facet counts for the remaining asteroids are included in the list contained in Appendix A. The numerical simulations, on the other hand, model the area directly surrounding the impact site as a collection of particles, providing a smoother representation of the body's surface and better enabling the modeling of interactions between individual particles.

In the numerical simulations performed by LLNL, the asteroid Golevka is modeled with a uniform $SiO_2$ composition using the ANEOS semi-analytical equation of state [130, 83, 72]. A

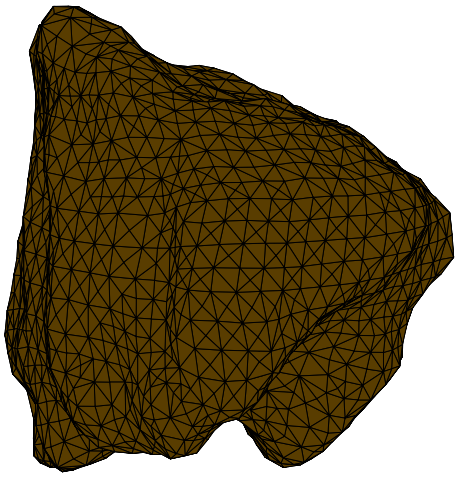

Figure 2.11: Shape model of the asteroid 6489 Golevka. The triangular facets used to define the model are visible.

pressure-dependent strength model, which follows the relation

$$Y_i = Y_0 + \frac{\mu_i P}{1 + \mu_i P/(Y_M - Y_0)}, \tag{2.11}$$

is implemented [78, 19, 66], with cohesion (i.e., shear strength at zero pressure) $Y_0 = 1$ kPA, coefficient of internal friction $\mu_i = 1.2$ [85], and von Mises plastic limit $Y_M = 1.5$ GPa [19]. Finally, a microporosity of 20% is used, while the effects of macroporosity are omitted for this study.

### 2.2.3 Impact Model Validation

This section presents the numerical simulations conducted by LLNL that illustrate the validity of the analytical impact model described in Section 2.2.1. The simulations are performed using an Adaptive Smoothed Particle Hydrodynamics (ASPH) method. This method provides a meshless approach for tracing the mass and velocity of asteroid particles ejected during the cratering process, thus enabling accurate calculation of the total momentum imparted to the asteroid [86]. The model is implemented with the open-source ASPH code Spheral [92, 91]. In each case, the three-dimensional simulation models a total number of particles on the order of $10^6$-$10^7$.

The simulations assume an impactor mass of 10,000 kg, representative of the limits of current launch vehicle technology. The impacts take place along the positive and negative directions of each of the three principal axes of the asteroid, with the impactor traveling at a velocity of 10 km/s relative to the asteroid. In each case, the incoming velocity is directed through the asteroid center of mass (COM). The problem domain is confined to an 80 m radius from the impact site due to the high computational expense of the simulations.

Figure 2.12 depicts the impact simulations after convergence of the model for collision trajectories along each of the principal directions. The images represent the local damage about the impact point resulting from the simulations, as measured by the displacement of individual particles. The ejection of particles from the asteroid due to cratering is evident in the magnified plot of the damage trace in Fig. 2.13.

Although the trajectory of the impactor is directed through the asteroid COM in each of these cases, the orientation of the surface normal at the point of impact, if not aligned with the incoming velocity vector, will cause the ejecta momentum vector to be off-axis, too. Thus, the angle of the resulting deflection, when measured from the impact trajectory, will be greater than zero. Figure 2.14 shows the evolution of the deflection angle over time throughout the duration of the cratering process for impact along Golevka's principal axes. Additionally, Table 2.3 lists the converged values of the angle offset, which vary from 1.53° in the $-y$-direction to 12.80° in the $-x$-direction.

The impact model of Section 2.2.1 relies on the assumption that the angle of the ejecta momentum vector can be adequately modeled by the angle of the surface normal at the point of impact. To validate the model, then, it must be shown that the angle of the ejecta momentum vector determined in the numerical simulations is equivalent to the angle of the corresponding surface normal vector in the triangular facet model. However, as noted previously, the particle representation of the asteroid used in the numerical simulations results in a smooth surface about the point of impact. Additionally, the crater from which the ejecta is generated covers a surface area greater than the size of a single facet in the triangular facet shape model. Therefore, to achieve

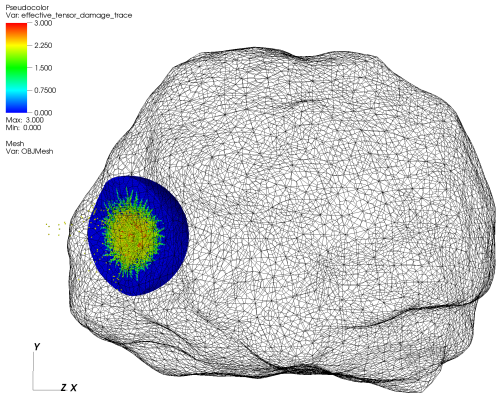


(a) $V_x = 10$ km/s, 0.080 s after impact

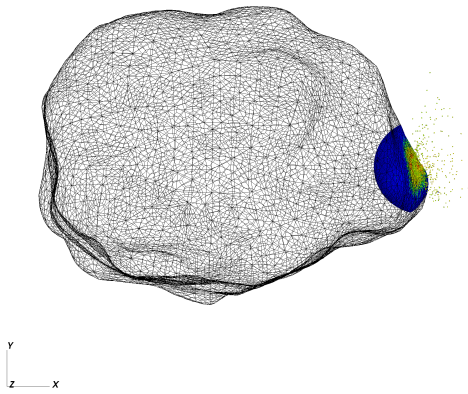


(b) $V_x = -10$ km/s, 0.074 s after impact

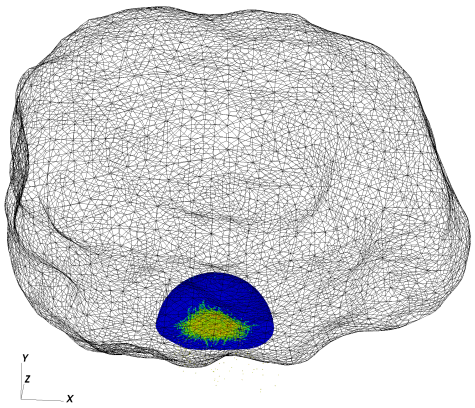


(c) $V_y = 10$ km/s, 0.076 s after impact

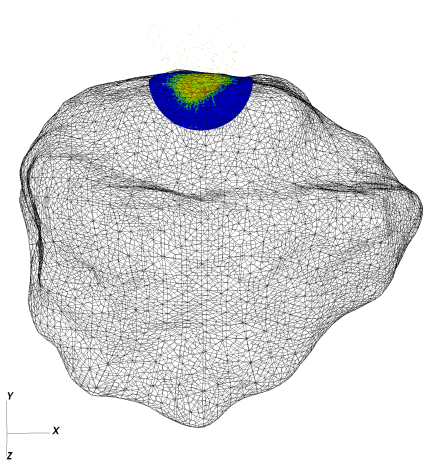


(d) $V_y = -10$ km/s, 0.081 s after impact

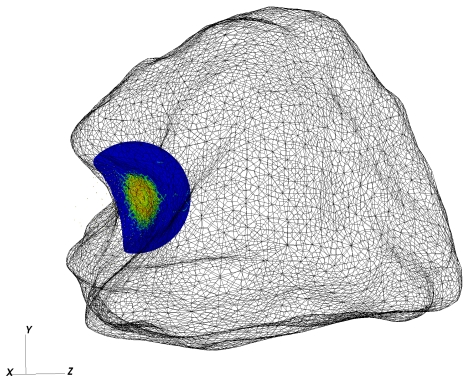


(e) $V_z = 10$ km/s, 0.063 s after impact

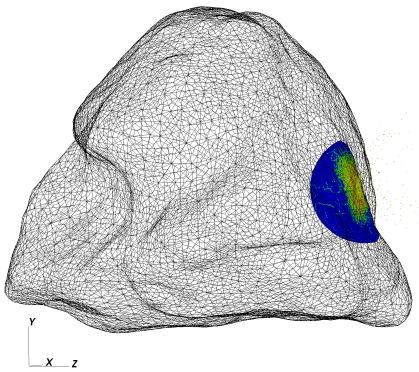


(f) $V_z = -10$ km/s, 0.104 s after impact

Figure 2.12: Damage trace from impact for asteroid 6489 Golevka, confined to an 80 m radius from the point of impact, as produced by numerical simulations in Spheral.

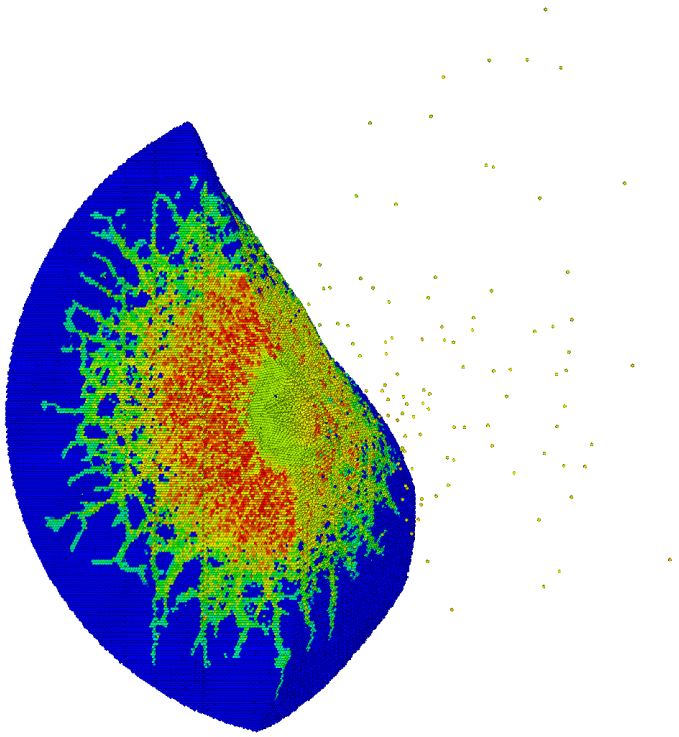

Figure 2.13: Ejecta created by the cratering process as the result of asteroid impact.

an accurate comparison, the surface normal is averaged over 3-5 facets immediately surrounding and including the nominally impacted facet for each impact location, and the surface normal for the analytical model is computed from this average. Table 2.4 shows that, in all but the x-directions, the discrepancies between the converged angles in the numerical simulations and the averaged surface normals is $< 2^{\circ}$. The remaining diparities are likely due to the differences in the surface modeling.

The result of the offset momentum vector is a reduction in the effective value of the $\beta$-parameter at these impact locations. Figure 2.15 shows the evolution of the effective $\beta$ during impact for each site, and the final column of Table 2.3 includes the converged $\beta$ values. The resulting values range from 2.27 to 2.76, a variation of almost 20% due exclusively to the local topography at the impact site. Thus, some of the energy intended to divert the asteroid along

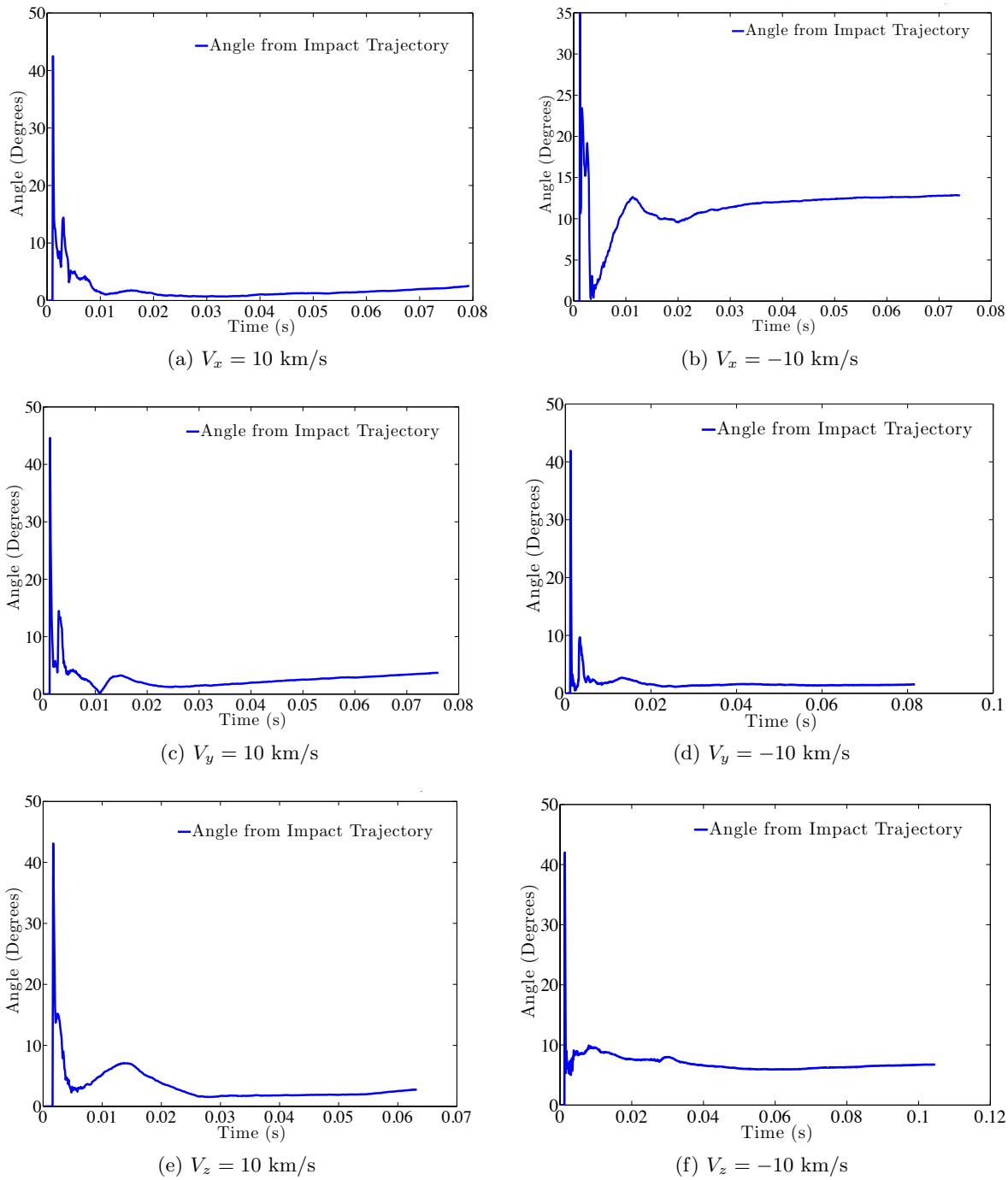


(a) $V_x = 10$ km/s

(b) $V_x = -10$ km/s

(c) $V_y = 10$ km/s

(d) $V_y = -10$ km/s

(e) $V_z = 10$ km/s

(f) $V_z = -10$ km/s

Figure 2.14: Angle of the ejecta momentum vector from the impact trajectory for asteroid 6489 Golevka produced from numerical simulations in Spheral.

Table 2.3: Converged angle offsets and effective $\beta$ values for impact along each of asteroid 6489 Golevka's principal axes produced from numerical simulations in Spheral.

| Impact Direction | Angle Offset (°) | Effective $\beta$ |
|---|---|---|
| x | 2.5220 | 2.5616 |
| -x | 12.8018 | 2.2696 |
| y | 3.6986 | 2.4267 |
| -y | 1.5278 | 2.5052 |
| z | 2.7484 | 2.7565 |
| -z | 6.7536 | 2.3342 |

Table 2.4: Comparison of the angle offsets computed from numerical simulations in Spheral and the angle offsets of the averaged surface normals from the triangular facet shape model for asteroid 6489 Golevka.

| Impact Direction | Angle Offset (°) | Avraged Normal |
|---|---|---|
| x | 5.0440 | 9.24 |
| -x | 25.6037 | 33.09 |
| y | 7.3972 | 8.89 |
| -y | 3.0556 | 4.66 |
| z | 5.4968 | 7.48 |
| -z | 13.5072 | 12.94 |

the impact trajectory is instead used to push the asteroid along the off-axis directions. The total transferred momentum in cartesian coordinates is depicted in Fig. 2.16.

### 2.2.4 System Stochastics

When considering the system described in Equation 2.10, the system inputs $\beta$, $\hat{\boldsymbol{n}}$, and $\boldsymbol{V}_\infty$ are all inherently stochastic, resulting in uncertainties in the $\Delta\boldsymbol{V}$ delivered to the asteroid. An accurate representation of the stochastic nature of this system is essential for a thorough understanding of

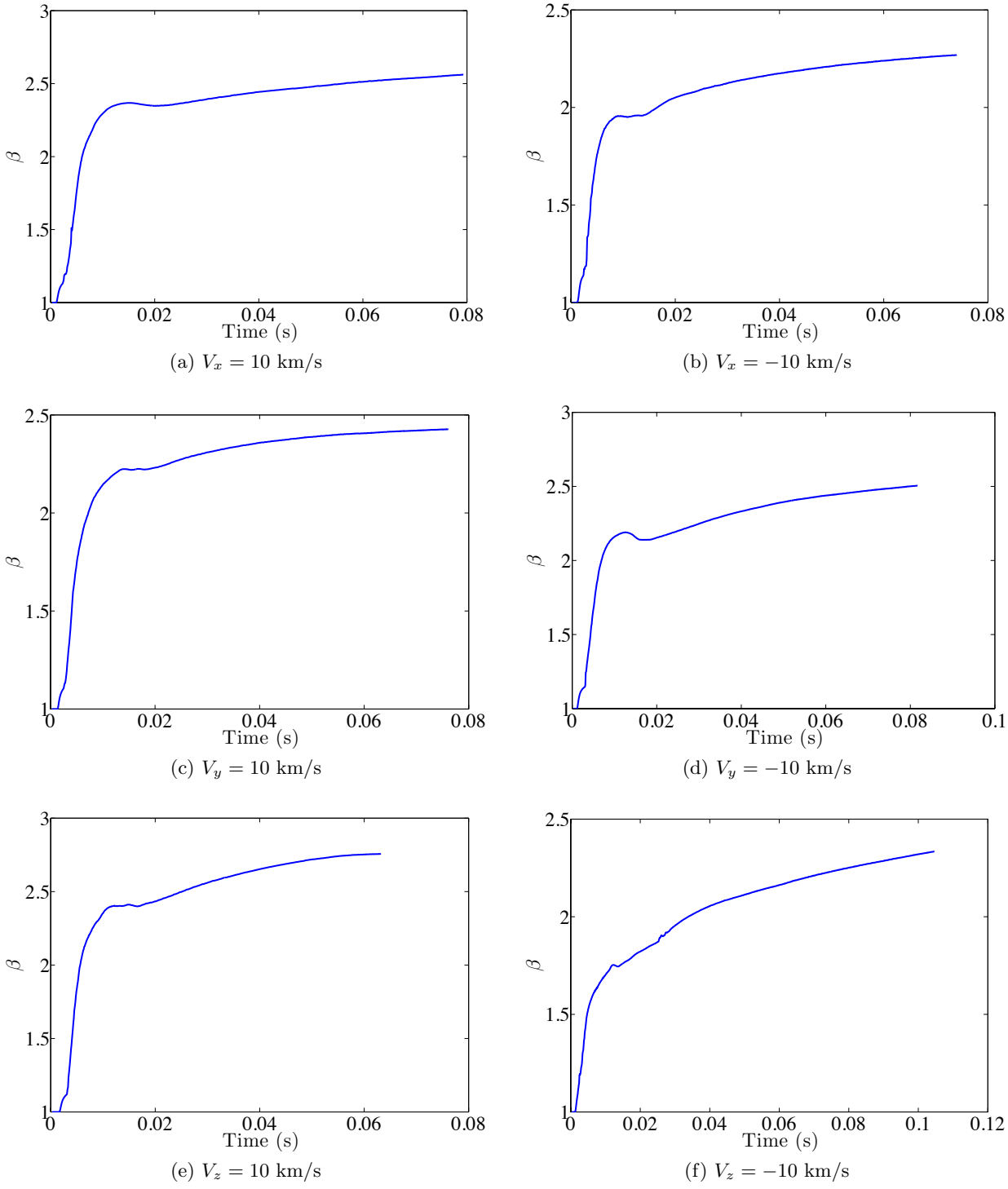


(a) $V_x = 10$ km/s

(b) $V_x = -10$ km/s

(c) $V_y = 10$ km/s

(d) $V_y = -10$ km/s

(e) $V_z = 10$ km/s

(f) $V_z = -10$ km/s

Figure 2.15: Effective value of the $\beta$-parameter for impact with asteroid 6489 Golevka, as produced by numerical simulations in Spheral.

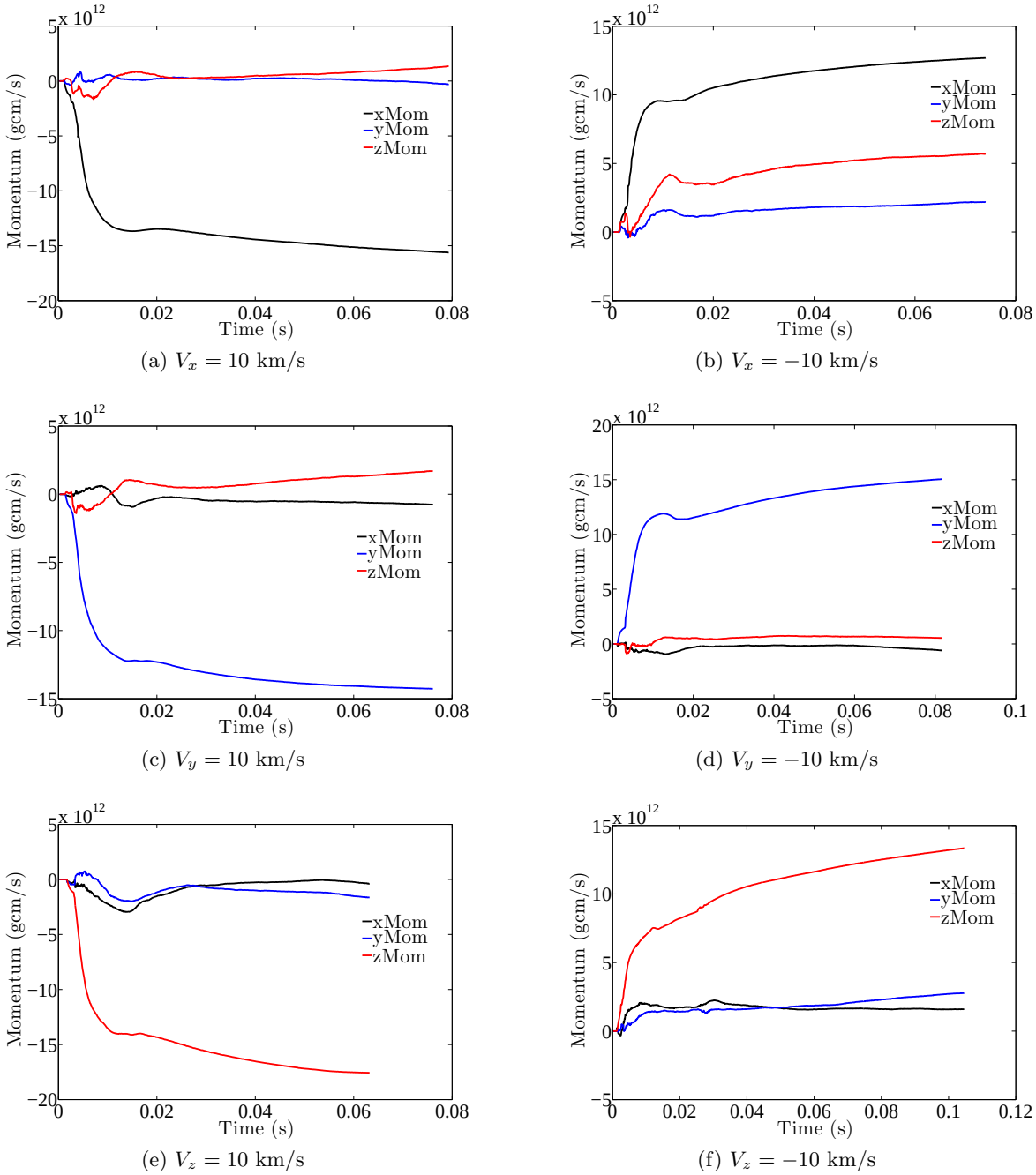


(a) $V_x = 10$ km/s

(b) $V_x = -10$ km/s

(c) $V_y = 10$ km/s

(d) $V_y = -10$ km/s

(e) $V_z = 10$ km/s

(f) $V_z = -10$ km/s

Figure 2.16: Cartesian components of the momentum transferred to asteroid 6489 Golevka upon impact as computed from numerical simulations in Spheral.

the effects of kinetic asteroid deflection. In particular, this research is concerned with characterizing uncertainty attributable to the topography, i.e., $\hat{\boldsymbol{n}}$, and material properties, i.e., $\beta$, of the asteroid.

Because $\beta$ represents the amount of additional momentum imparted on the asteroid beyond the direct impact momentum, uncertainties in $\beta$ can have significant influence on the effective momentum transfer. The uncertainty in $\beta$ arises from the difficulty in characterizing this parameter for a given impact scenario, as demonstrated in [13]. For the remaining analysis, a simplified representation of $\beta$ is assumed, modeled as a Gaussian with mean $\mu_\beta = 2$ and uncertainty of $\sigma_\beta = 1/6$. From Equation 2.10, it is evident that this uncertainty maps linearly into the $\Delta \boldsymbol{V}$.

The topography of the asteroid, as designated by $\hat{\boldsymbol{n}}$, affects the $\Delta \boldsymbol{V}$ resulting from impact by dictating the effective direction of $\beta$. Uncertainties in $\hat{\boldsymbol{n}}$ are the result of uncertainties in the impact location of the kinetic deflector and in the shape model of the asteroid. Uncertainty in the impact location can be easily represented using a bivariate Gaussian distribution in $b_u$ and $b_w$, where the $\hat{\boldsymbol{u}}$-$\hat{\boldsymbol{w}}$ plane is defined perpendicular to the nominal direction of $\boldsymbol{V}_\infty$ (see Fig. 2.17). The uncertainties in each direction are taken to be independent and identically distributed with zero mean and $\sigma = \frac{1}{12}\bar{R}_{ast}$, where $\bar{R}_{ast}$ is the mean radius of the asteroid.

Uncertainties in the asteroid shape generally stem from errors in the radar measurements used to generate shape models. These models characterize the asteroid shape as a collection of triangular facets, defined by the corresponding set of vertices. Uncertainty in the shape model is represented as a correlated Gaussian on the radial distance of the vertices from the asteroid center [81, 82], and the correlated distributions can be used to generate a set of perturbed shape models. The mean displacement of the vertices from the nominal shape model is $\mu_{disp} = 0$, while the covariance is represented as

$$\boldsymbol{\Sigma}_{disp} = \text{chol}\left(s_\sigma \boldsymbol{C}\right), \tag{2.12}$$

where chol() denotes the Cholesky decomposition of the matrix $s_\sigma \boldsymbol{C}$, $\boldsymbol{C}$ is a matrix of the correlations between the vertices, and $s_\sigma$ is a scaling distance. The correlations are given by

$$\boldsymbol{C} = \exp\left(-\frac{\boldsymbol{D}}{2C_l}\right) \tag{2.13}$$

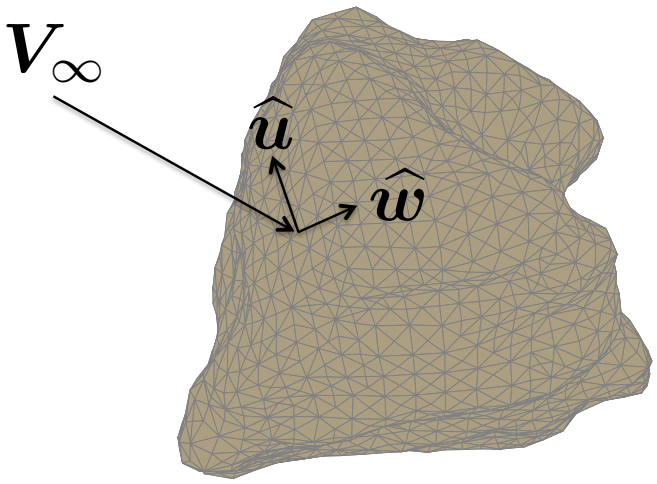


Figure 2.17: Local coordinate system centered at the impact location, in which the $\hat{\boldsymbol{u}}$-$\hat{\boldsymbol{w}}$ plane is oriented perpendicular to $\boldsymbol{V}_\infty$.

for the lower triangular matrix $\boldsymbol{D}$ containing the distance between each pair of vertices in the model and the correlation length $C_l$. A scaling distance of $s_\sigma = 0.01$ m and a correlation distance of $C_l = 0.25$ m are used in this study. The normal vectors corresponding to each facet of the model can then be determined for the perturbed shapes.

# Chapter 3

## Surrogate Models

Many types of surrogate models have been developed for design, optimization, and analysis, including, for example, polynomial regression [24, 9], Kriging [79, 118], and radial basis functions (see [14] for a survey of the the radial basis methods). In each case, the surrogate, or reduced order model (ROM), seeks to use a relatively small number of sample points to generate a global function capable of approximating the system response at any number of other points for a reduced computational cost compared to traditional Monte Carlo methods, as illustrated in Fig. 3.1. In addition to reducing the computational cost, surrogate models provide the ability to perform global analysis, specifically sensitivity analysis, on the system under consideration.

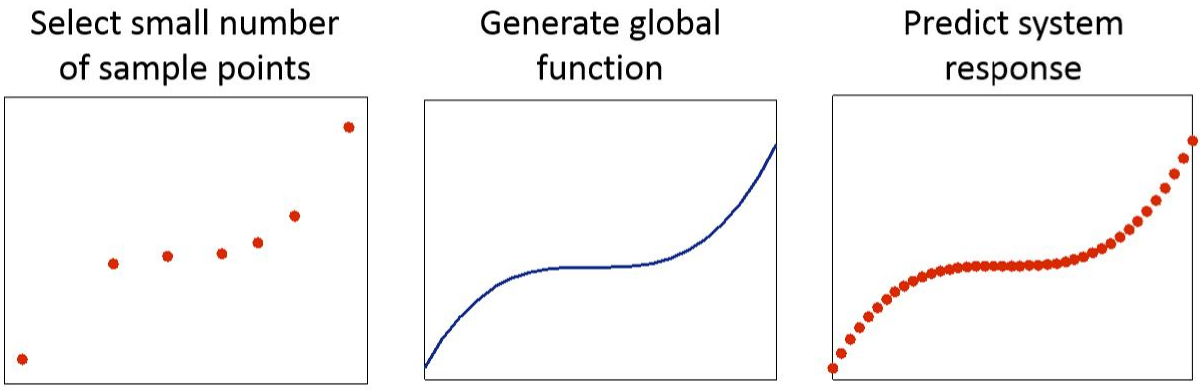


Figure 3.1: Illustration of the use of a surrogate model to predict a system response.

Polynomial regression and radial basis functions both fall under the category of spectral methods, which develop the global surrogate by projecting the system response onto a collection of basis functions. Polynomial basis functions are typically selected to be orthogonal polynomials whose form depends on the structure of the system inputs [9], while the radial basis functions are radially symmetric functions based on Euclidean distance [14]. In the Kriging method, on the other hand, the global function is comprised of a *linear system trend* and fluctuations about that trend [118, 104].

Polynomial regression is selected as the model of choice in this body of work due to the adaptability of the polynomial basis functions. The benefit of this adaptability is twofold: first, in design problems, these functions can be selected based on the physical structure of the design inputs, allowing the basis to be tailored to best represent the system parameters $\boldsymbol{s}$ under consideration. Alternatively, the basis can be chosen according to the probability distribution of stochastic inputs $\boldsymbol{\xi}$ [137, 40]. This method, known as polynomial chaos (PC), is very useful for uncertainty quantification and propagation [139, 74, 121]. The second benefit, then, is that deterministic polynomial regression can be combined with polynomial chaos for the purpose of optimization under uncertainty (OUU), in which the polynomial basis takes the form of the product of the basis functions generated for the deterministic and stochastic dimensions [26, 27].

This chapter provides an introduction to the methods of surrogate modeling. Section 3.1 introduces the mathematical foundations for the models in the context of deterministic design models, and Section 3.2 defines the stochastic version of the models. An overview of the model development process is presented in Section 3.3, including the design of experiments (DOE), model estimation, and model validation. Finally, Section 3.4 describes how the surrogate models can be used for the purpose of OUU.

## 3.1 Polynomial Regression Design Model

Polynomial regression surrogate models represent the dependence of quantities of interest (QOI) on the $d$-dimensional system inputs as the spectral projection of the system response

$\boldsymbol{u}(\boldsymbol{s}) \in S$ onto the subspace $S_P$ defined by an appropriate basis $\psi$, typically selected as orthogonal polynomials (see Fig. 3.2). Thus, the $\Delta \boldsymbol{V}$ required for rendezvous in three body orbits as a function of the design inputs $\boldsymbol{s} = [s_1, s_2, s_3]$ can be expressed using the expansion

$$\Delta \boldsymbol{V}(\boldsymbol{s}) = \sum_{\boldsymbol{\alpha} \in \Lambda_{p,d}} c_{\boldsymbol{\alpha}} \psi_{\boldsymbol{\alpha}}(\boldsymbol{s}), \tag{3.1}$$

where $c_i$ are the polynomial coefficients, $\boldsymbol{\alpha}$ denotes a multi-index

$$\boldsymbol{\alpha} \in \boldsymbol{\Lambda_{p,d}} := \{(\alpha_1, ..., \alpha_d) \in \mathbb{N}_0^d : \parallel \boldsymbol{\alpha} \parallel_1 \leq p\}$$

for $\parallel \boldsymbol{\alpha} \parallel_1 = \sum_i |\alpha_i|$, and $p$ is the total order of the expansion. The resulting number of terms in the expansion is

$$P = \frac{(p+d)!}{p!d!}, \tag{3.2}$$

so that the modeling error $\varepsilon$ associated with a $p$-th order expansion is a truncation error dependent on higher order expansion terms and is defined as

$$\varepsilon = \sum_{i=P+1}^{\infty} c_i(\boldsymbol{s}) \psi_i(\boldsymbol{s}). \tag{3.3}$$

The multivariate basis functions $\psi_{\boldsymbol{\alpha}}(\boldsymbol{s})$ of Equation 3.1 are a tensor product of univariate polynomials

$$\psi_{\boldsymbol{\alpha}}(\boldsymbol{s}) = \psi_{\alpha_1}(s_1) \psi_{\alpha_2}(s_2) \psi_{\alpha_3}(s_3), \tag{3.4}$$

with the choice of basis in each dimension remaining independent. The univariate polynomials $\psi_{\alpha_i}$ of degree $\alpha_i$ form an orthogonal basis, i.e.,

$$\langle \psi_i, \psi_j \rangle = \langle \psi_i^2 \rangle \, \delta_{ij}, \tag{3.5}$$

where $\delta_{ij}$ is the Kronecker delta, $\langle \cdot, \cdot \rangle$ denotes the inner product

$$\langle \psi_{\alpha_i}, \psi_{\alpha_j} \rangle = \int \psi_{\alpha_i}(s) \psi_{\alpha_j}(s) W(s) ds, \tag{3.6}$$

and $W(s)$ is the associated weight.

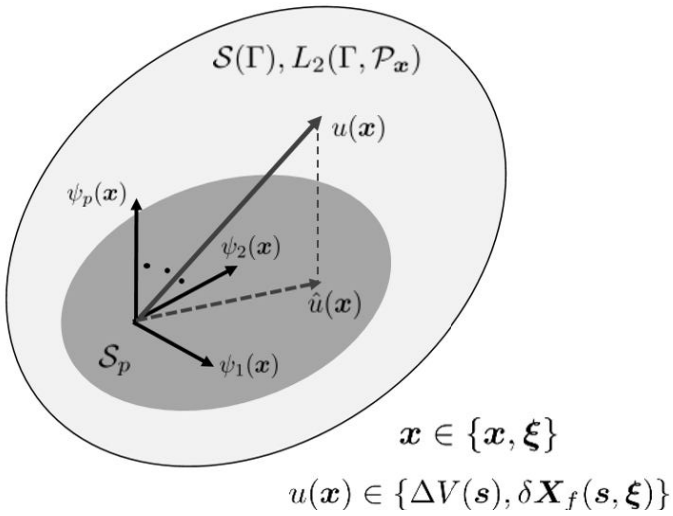


Figure 3.2: Surrogate models project the response $u(\boldsymbol{x}) \in S$ onto the subspace $S_P$ defined by the orthogonal basis $\psi$.

The exact solution for the polynomial coefficients in Equation 3.1 is the projection of the solution $\Delta \boldsymbol{V}$ onto the polynomial basis,

$$c_{\boldsymbol{\alpha}} = \langle \Delta \boldsymbol{V}(\boldsymbol{s}) \psi_{\boldsymbol{\alpha}}(\boldsymbol{s}) \rangle = \int_{\Gamma^d} \Delta \boldsymbol{V}(\boldsymbol{s}) \psi_{\boldsymbol{\alpha}}(\boldsymbol{s}) W(\boldsymbol{s}) d\boldsymbol{s}, \tag{3.7}$$

where

$$\int_{\Gamma^d} \Delta \boldsymbol{V}^2(\boldsymbol{s}) W(\boldsymbol{s}) d\boldsymbol{s} < \infty.$$

By computing the coefficients according to Equation 3.7, the $p$-th order expansion $\Delta \boldsymbol{V}_p(\boldsymbol{s})$ converges in a mean-squares sense to the true response $\Delta \boldsymbol{V}(\boldsymbol{s})$ as the total order $p$ is increased

$$\langle (\Delta \boldsymbol{V}(\boldsymbol{s}) - \Delta \boldsymbol{V}_p(\boldsymbol{s}))^2 \rangle \xrightarrow{m.s.} 0 \qquad \text{as} \qquad p \to \infty. \tag{3.8}$$

However, the solution to Equation 3.7 is typically not straightforward, and a variety of methods have been developed for determining a best estimate of the solution. These solution methods will be discussed in Section 3.3.2.

Many types of functions are available for use as the basis in spectral expansions. In polynomial regression, $\psi$ is generally chosen to be an orthogonal basis dependent on the boundary conditions or

support of the design parameters. These bases are well-documented for a variety of input parameter structures [9]. Of particular interest here are periodic inputs, such as the initial position $\tau(s_1)$ in the purely deterministic rendezvous problem, and inputs defined over a finite interval, including $\tau(s_1)$ in the stochastic design problem and the time of flight $t(s_2)$ and initial separation $\Delta\tau(s_3)$ for both the deterministic and stochastic systems.

Systems dependent on periodic inputs are known to be best modeled using a Fourier basis consisting of the mean system response $a_0$ and the non-constant terms

$$F_i(s) \in \{\cos(i\pi s),\ \ \sin(i\pi s)\}, \tag{3.9}$$

where the sine and cosine terms capture the periodicity of the response [15]. The use of the Fourier basis increases the total number terms $P$ in the expansion due to the presence of both the sine and cosine terms, such that the modified number of expansion terms $P'$ is

$$P' = 2^{d_F} \cdot P - d_F$$

for the number of dimensions $d_F$ along which the solution is approximated using a Fourier basis. Fourier expansions are defined over the interval $s \in [-\pi, \pi]$ or the equivalent $s \in [0, 2\pi]$.

For non-periodic inputs with finite support, $\psi$ can be selected as Legendre polynomials $L(s)$ defined over the interval $s \in [-1, 1]$ [9]. The Legendre polynomials are of the form [105]

$$L(s) = \frac{1}{2^n} \sum_{l=0}^{n/2} (-1)^l \binom{n}{l} \binom{2n-2l}{n} s^{n-2l}, \tag{3.10}$$

or alternatively, using a three-term recurrence relation,

$$L_0 = 1, \qquad L_1(s) = s,$$
$$(n+1)L_{n+1}(s) = (2n+1)sL_n(s) - nL_{n-1}(s). \tag{3.11}$$

## 3.2 Polynomial Chaos Expansions (PCE)

Founded on the work of Wiener, generalized polynomial chaos expansions form a subset of surrogate models that are particularly useful for uncertainty quantification (UQ) [137, 40]. In

PCEs, the basis $\psi$ is used to map the random space $\Omega \equiv L_2(\Gamma, P_\xi)$ through the system dynamics, and the inputs to the model are the stochastic variables $\boldsymbol{\xi} \in \Omega$. For the mapping of the maneuver execution errors and initial state uncertainties $\boldsymbol{\xi} = [\xi_1, ..., \xi_9]$ in the rendezvous problem, the projection of the deviations in the final state of the chaser spacecraft $\delta \boldsymbol{X}_f(\boldsymbol{\xi}) \in S$ onto the subspace $S_p \equiv \{ \psi_0(\boldsymbol{\xi}), \psi_1(\boldsymbol{\xi}), ..., \psi_P(\boldsymbol{\xi}) \} \subset S$, again illustrated in Fig. 3.2, takes the form

$$\delta \boldsymbol{X}_f(\boldsymbol{\xi}) = \sum_{\boldsymbol{\alpha} \in \Lambda_{p,d}} c_{\boldsymbol{\alpha}} \psi_{\boldsymbol{\alpha}}(\boldsymbol{\xi}). \tag{3.12}$$

The fundamental difference between PCEs and the deterministic regression models is that, in polynomial chaos, the basis functions used to define the space $S$ are specifically selected such that they are orthogonal with respect to the *distribution* of the random inputs $\boldsymbol{\xi}$, satisfying the equation

$$\langle \psi_i \psi_j \rangle = \int_\Gamma \psi_i(\boldsymbol{\xi}) \psi_j(\boldsymbol{\xi}) \rho(\boldsymbol{\xi}) d\boldsymbol{\xi} = \delta_{ij} \langle \psi_i^2 \rangle, \tag{3.13}$$

where $\rho(\boldsymbol{\xi})$ is the joint density function of the inputs. The orthogonal basis functions associated with many standard probability distributions, including Gaussian, uniform, and exponential distributions, among others, are contained in the Wiener-Askey scheme [140]. Thus, the probabilists' Hermite polynomials $He(\xi)$ can be used for the normally distributed error in the burn magnitude $\delta V_0(\xi_1)$, cone angle $\theta(\xi_2)$, and initial state deviations $\delta \boldsymbol{R}_0(\boldsymbol{\xi}_R)$, $\delta \boldsymbol{V}_0(\boldsymbol{\xi}_V)$. The Hermite polynomials are defined in [105] as

$$He_n(\xi) = (-1)^n e^{\frac{\xi^2}{2}} \frac{d^n}{d\xi^n} e^{-\frac{\xi^2}{2}} \tag{3.14}$$

and follow the recurrence relation

$$\begin{aligned} He_0 = 1, \qquad He_1(\xi) = \xi, \\ He_{n+1}(\xi) = \xi He_n(\xi) - n He_{n-1}(\xi). \end{aligned} \tag{3.15}$$

Although the circular uniform distribution used to describe the rotation angle $\phi(\xi_3)$ of the maneuver error is not included in the Wiener-Askey scheme, it can readily be shown that the Fourier basis of Equation 3.9 satisfies Equation 3.13 for $\rho(\xi) = 1/2\pi$.

## 3.3 Model Development

Regardless of the the specific model chosen, the model development process includes three steps common to all surrogate models, which are shown in the diagram of Fig. 3.3: design of experiments (DOE), estimation of the surrogate, and model validation [104, 71]. The design of experiments involves the selection of the sample points used to generate the surrogate model, also known as the training data. In model estimation, the true system response is solved for at each of the sample points selected in the DOE, and these solutions are then used to estimate the parameters defining the surrogate. Finally, the resulting model is validated by assessing its predictive capabilities and performing error analysis. Although it is conceptually convenient to describe model development as a sequential process, it should be noted that the process is frequently non-linear and iterative in practice.

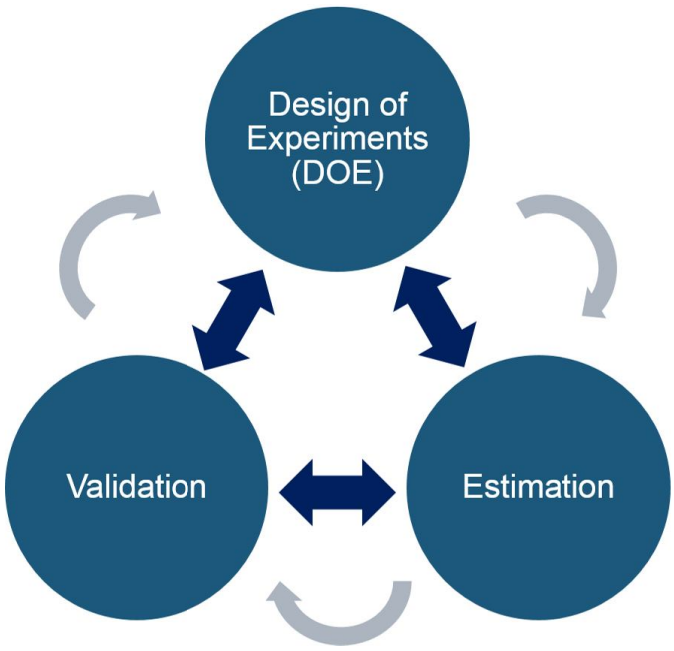


Figure 3.3: Diagram of the model development process.

### 3.3.1 Design of Experiments

The primary concern of the design of experiments is the sampling method used to select training data with which to generate the surrogate model. In some cases, the choice of sampling techniques and model estimation methods are inherently coupled. For example, collocation methods require the use of a deterministic set of quadrature nodes for the training samples. Here, Monte Carlo sampling is chosen for its flexibility and for its compatibility with the solution techniques that will be introduced in Section 3.3.2.

#### 3.3.1.1 Standard Sampling

Monte Carlo sampling provides a basic approach to sample point selection. In standard Monte Carlo sampling, the sample data are randomly generated from a measure orthogonal to the basis functions. Thus, the deterministic sample points $\{\boldsymbol{s}^{(i)}\},\ i = 1, ..., N$ are selected according to a uniform distribution over the defined range of the input parameter, while the random samples $\{\boldsymbol{\xi}^{(i)}\}, i = 1, ..., N$ corresponding to the stochastic inputs are generated from their respective probability distributions.

Modifications on the traditional Monte Carlo sampling approach, such as Latin hypercube sampling (LHS) and orthogonal arrays (OA), have been developed to reduce model bias by attempting to provide a better distribution of samples and prevent clustering of data in the training set [104]. However, one major advantage of traditional Monte Carlo sampling is that it allows for the reuse of data points when the size of the training set must be adjusted to meet accuracy requirements for the model. The structured approach to sampling in LHS and OA can preclude this recycling of data and require that an entirely new set of data be generated each time it is determined that a larger sample size is needed.

#### 3.3.1.2 Asymptotic Sampling

An alternative to the standard orthogonal measures for Monte Carlo sampling is suggested in [48] and [49] for models of high order $p$. This method, termed asymptotic sampling, produces

a weaker dependence of the required number of training samples on $p$, resulting in more rapid convergence of the model for high order expansions. For the uniform distribution associated with the Legendre basis, the corresponding asymptotic sampling measure is the Chebyshev distribution,

$$f_C(s) \equiv \frac{1}{\pi\sqrt{1-s^2}}. \tag{3.16}$$

The use of asymptotic sampling in generating regression models requires that a weighting term be introduced in the polynomial expansion to regain orthogonality between the basis and the sampling measure. The weight function for the Chebyshev distribution is defined as

$$w(s) \equiv (1-s^2)^{1/4}. \tag{3.17}$$

### 3.3.2 Model Estimation

Solution methods to determine the best estimate of the coefficients from the integral of Equation 3.7 can be broadly categorized as either intrusive or non-intrusive [74]. Intrusive methods require modifications to the deterministic system solvers themselves. In the case of the commonly used intrusive method of Galerkin projections, for example, both the design inputs and the solution are projected onto the same subspace $S_p$ spanned by the orthogonal basis functions $\boldsymbol{\psi}$. However, for complex governing equations, the solution of the Galerkin equations may become nontrivial [138]. Additionally, intrusive methods require that new solvers be derived for every dynamical system under consideration.

Conversely, non-intrusive methods are sampling-based methods that rely only on the system inputs and outputs, thus treating the system solver as a black box. The two primary non-intrusive methods for generating a surrogate model are least-squares regression, which aims to minimize the difference between the model prediction and the true value at each of the validation points [37, 87], and pseudospectral collocation, which instead relies on quadrature integration to construct interpolating polynomials using a set of collocation nodes [121]. Non-intrusive methods are particularly attractive for astrodynamics, as they allow for the use of existing propagators and legacy software.

The method of least-squares regression is therefore selected as the primary solution approach used in this body of work.

#### 3.3.2.1 Least-Squares Regression

The method of least squares solves for $c_{\boldsymbol{\alpha}}$ such that the sum of the squares of differences between the system response $\boldsymbol{u}(\boldsymbol{x})\ \forall\ \boldsymbol{u} \in \{\Delta \boldsymbol{V}, \delta \boldsymbol{X}_f\}$, $\boldsymbol{x} \in \{\boldsymbol{s}, \boldsymbol{\xi}\}$ and the model prediction $\boldsymbol{u}_p(\boldsymbol{x})$ is minimized at $N$ random sample points $\{\boldsymbol{x}^{(i)}\},\ i = 1, ..., N$,

$$\hat{c}_{\boldsymbol{\alpha}} = \underset{c_{\boldsymbol{\alpha}}}{\arg\min}\ \frac{1}{N} \sum_{i=1}^{N} \left[ \boldsymbol{u}(\boldsymbol{x}^{(i)}) - \sum_{\boldsymbol{\alpha} \in \boldsymbol{\Lambda}_{\boldsymbol{p},\boldsymbol{d}}} c_{\boldsymbol{\alpha}} \psi_{\boldsymbol{\alpha}}(\boldsymbol{x}^{(i)}) \right]^2 . \tag{3.18}$$

This corresponds to the solution of the normal equation, which is, in matrix form,

$$(\boldsymbol{\Psi}^T \boldsymbol{\Psi}) \hat{\boldsymbol{c}} = \boldsymbol{\Psi}^T \boldsymbol{u}, \tag{3.19}$$

where $\hat{\boldsymbol{c}} \in \mathbb{R}^P$ is the estimated vector of polynomial coefficients, $\boldsymbol{u} \in \mathbb{R}^{N \times M}$ is the vector of realizations of the system response for the M quantities of interest (which can be solved for simultaneously in the regression model), and $\boldsymbol{\Psi}$ is a matrix containing evaluations of the basis functions for each term of the expansion. Using the notation $\{\psi_j\};\ j \in \{1, ..., P\}$, with a one-to-one correlation between $\{\psi_j\}$ and $\{\psi_{\boldsymbol{\alpha}}\}$, the $(i, j)$-th element of $\boldsymbol{\Psi}$ is defined as

$$\boldsymbol{\Psi}\,(i, j) := \psi_j(\boldsymbol{x}^{(i)}), \qquad i = 1, ..., N, \qquad j = 1, ..., P. \tag{3.20}$$

Weighted least-squares regression must be used to accommodate the asymptotic sampling methods of Section 3.3.1.2, resulting in the weighted form of the normal equation

$$\left(\boldsymbol{\Psi}^T \boldsymbol{W}^2 \boldsymbol{\Psi}\right) \boldsymbol{c} = \boldsymbol{\Psi}^T \boldsymbol{W} \boldsymbol{u}. \tag{3.21}$$

#### 3.3.2.2 Orthogonal Matching Pursuit

One particular drawback of surrogate models is that they are subject to the *curse of dimensionality*, which states that the number of terms required in the expansion grows exponentially with respect to both the dimension and the order of the expansion. Thus, for high dimension problems

and problems for which a high order expansion is necessary to achieve a desired accuracy, the number of samples required to generate the model − which is proportional to the number of expansion terms − may become impractically large. However, the issue of the *curse of dimensionality* can be circumvented for problems with a sparse solution, i.e., those for which some large subset of the coefficients are very small and therefore negligible, through the use of compressive sampling (CS).

Compressive sampling is a model estimation technique that leverages problem sparsity by including only those expansion terms with the largest contribution to the QOI, thereby reducing the number of solution realizations needed to generate the model. Greedy pursuit algorithms, for example, aim to satisfy the optimization problem

$$\min_{\boldsymbol{c}} ||\boldsymbol{c}||_0 \quad \text{subject to} \quad ||\boldsymbol{u} - \boldsymbol{\Psi}\hat{\boldsymbol{c}}||_2 \leq \varepsilon. \tag{3.22}$$

To do so, the greedy algorithm iteratively ranks the contributions of each term to the truncation error of the current model and then appends only the most significant term before generating a new model. This process is repeated until the magnitude of the truncation error falls within acceptable bounds.

This research will explore the use of the greedy algorithm known as orthogonal matching pursuit (OMP) to generate a sparse model of the rendezvous problem. In OMP, each of the input dimensions are treated independently [64]. To initialize the model, all coefficients are set to zero and the truncation error is therefore equal to the system response, such that

$$\hat{\boldsymbol{c}}^0 = \boldsymbol{0}, \quad \boldsymbol{\delta}^0 = \boldsymbol{u} - \boldsymbol{\Psi}\hat{\boldsymbol{c}}^0, \quad \Lambda_{p,d} = \emptyset \tag{3.23}$$

On each iteration $k$, the truncation error of the current model is mapped to the expansion terms, and the most significant of the remaining terms is identified by

$$j = \arg\max_{i \notin \Lambda_{p,d}} \frac{\boldsymbol{\Psi}_i^T \boldsymbol{\delta}^k}{||\boldsymbol{\Psi}_i||_2^2}. \tag{3.24}$$

The index set is updated to include the $j$-th term

$$\Lambda_{p,d}^k \leftarrow \Lambda_{p,d}^{k-1} \cup \{j\}, \tag{3.25}$$

and the coefficients of the new model satisfy the minimization problem

$$\hat{\boldsymbol{c}} = \arg\min_{\tilde{\boldsymbol{c}}} ||\boldsymbol{u} - \boldsymbol{\Psi}\hat{\boldsymbol{c}}||_2 \tag{3.26}$$

subject to

$$\text{support}\{\hat{\boldsymbol{c}}\} = \Lambda_{p,d}^{(k)}.$$

The residual associated with the new model is computed as

$$\boldsymbol{\delta}^{(k+1)} = \boldsymbol{u} - \boldsymbol{\Psi}\hat{\boldsymbol{c}}^{(k)}. \tag{3.27}$$

If this residual falls within the required bounds $\varepsilon$, $\hat{\boldsymbol{c}}^{(k)}$ is accepted as the model solution $\hat{\boldsymbol{c}}$. If $|\boldsymbol{\delta}^{(k+1)}| > \varepsilon$, Equations 3.24-3.27 are repeated until either the accuracy requirement is met or a maximum number of iterations is reached. A diagram of this algorithm is provided in Fig. 3.4.

### 3.3.3 Validation

The third step in the model development process involves assessing the ability of the model to accurately predict the true system response. Included in this step is the selection of the validation data set. Model validation is useful in gaining a more complete understanding of any modeling errors and, if multiple surrogates are being considered, in the selection of the surrogate best suited for the system.

To enable more robust analysis during the initial evaluation of the suitability of polynomial regression to the modeling of maneuver design for spacecraft rendezvous, the model predictions can be compared to a very large set of validation points. Using this set of points, the models are evaluated based on the RMS validation errors, calculated as

$$\varepsilon_2 = \sqrt{\frac{1}{M}\sum_{i=1}^{M}\left[\hat{\boldsymbol{u}}^{(i)} - \boldsymbol{u}^{(i)}\right]^2}, \tag{3.28}$$

where $M$ is the size of the validation set, $\hat{\boldsymbol{u}}^{(i)}$ is the model estimate at each of the points in the set, and $\boldsymbol{u}^{(i)}$ is the true value at these points. Table 3.1 provides a description of the validation data sets used to evaluated the deterministic design models for rendezvous in the halo orbit and the DRO.

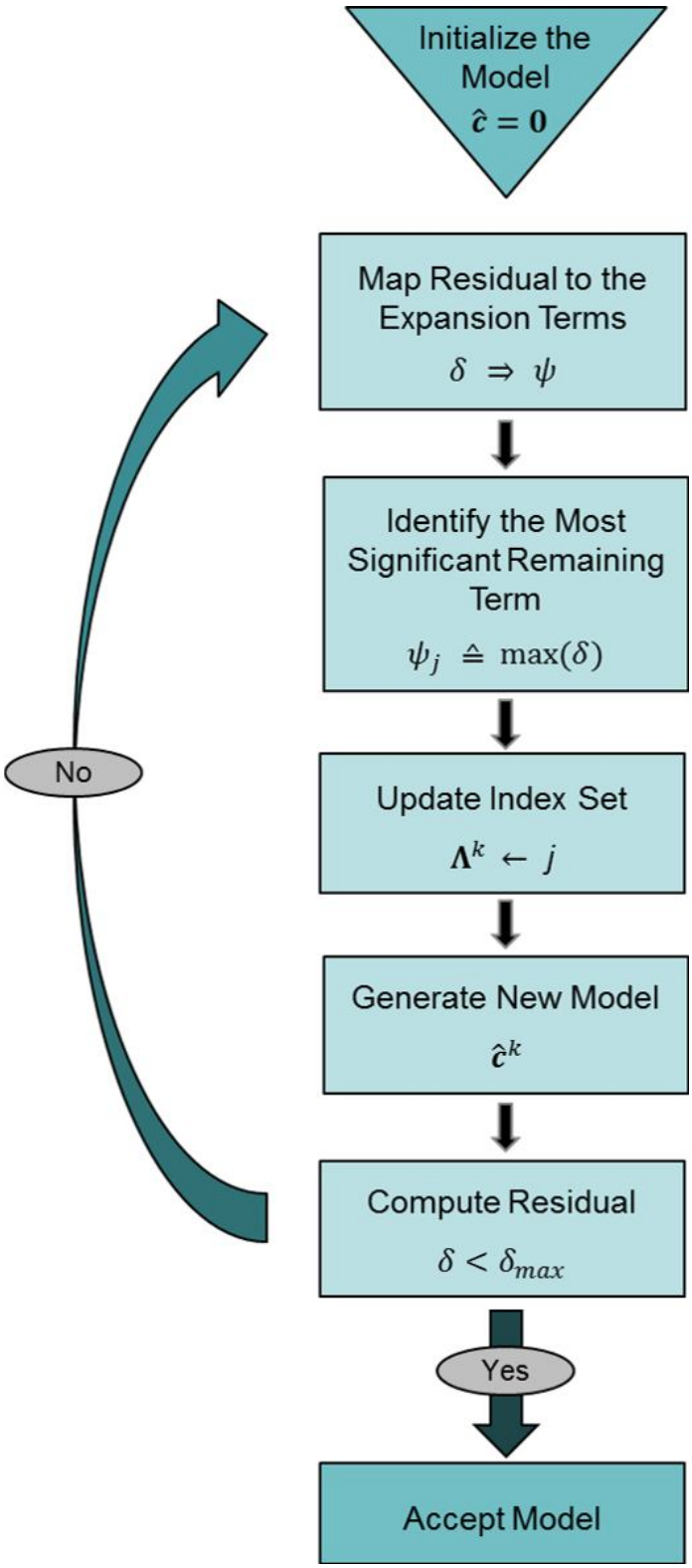


Figure 3.4: Algorithm for compressive sampling via orthogonal matching pursuit.

Table 3.1: Validation data sets

| | Step Size | | | |
|---|---|---|---|---|
| | Initial Position, $\tau$ (°) | Time, $t$ (days) | Initial Separation, $\Delta\tau$ (°) | Total Number of Points |
| Halo Orbit | 2 | 0.05 | 0.1 | 144800 |
| DRO | 2 | 0.05 | 0.01 | 72400 |

However, this approach to model validation is clearly not practical for general applications and rapid model development. Other methods have been developed for validation which impose less computational cost while still providing a thorough and unbiased assessment of the model errors, e.g., $k$-fold cross-validation and bootstrapping, among others [35, 38, 104]. $k$-fold validation has the advantage of allowing all available sample data to be used for both constructing and validating the surrogate model. The process for $k$-fold validation is as follows:

(1) Divide the training data set of size $N$ into $k$ subsets of approximately equal size.

(2) Construct $k$ surrogates, each omitting one subset of data to be used as the validation set.

(3) Compute the model error for each estimated surrogate against its corresponding validation set.

(4) Average the model error from each of the $k$ surrogates to obtain the generalization error estimate.

(5) If the generalization error estimate falls within accuracy requirements, generate a final surrogate using all $N$ data points. If not, increase the size of the data set $N$ and repeat steps 1-4.

The $k$-fold algorithm begins with a first order expansion, and the number of samples is increased incrementally when the RMS error

$$\varepsilon_2 = \sqrt{\frac{1}{N/k}\sum_{i=1}^{N/k}\left[\hat{\boldsymbol{u}}^{(i)} - \boldsymbol{u}^{(i)}\right]^2}, \tag{3.29}$$

is larger than the requirements. When the sample size $N$ reaches the threshold

$$N \geq \gamma \cdot P_{current}, \tag{3.30}$$

where

$$P_{current} = \frac{(p_{current} + d)!}{p_{current}!d!}$$

and $\gamma$ is a design parameter, the expansion order of the model is also increased to

$$p_{new} = p_{current} + 1, \tag{3.31}$$

and the algorithm continues until the generalization error meets the specified accuracy requirements. This adaptive method allows for the generation of models with no *a priori* knowledge on either the required expansion order or the sample size necessary for convergence.

## 3.4 Optimization Under Uncertainty (OUU)

The common derivation of the polynomial regression models and the polynomial chaos expansions can be readily exploited for the purpose of OUU. To accomplish this, Equations 3.1 and 3.12 can be combined to generate a single model that maps both the deterministic and stochastic inputs to the QOI. For spacecraft rendezvous, this takes the form

$$\boldsymbol{u}(\boldsymbol{s}, \boldsymbol{\xi}) = \sum_{\boldsymbol{\alpha} \in \Lambda_{p,d}} c_{\boldsymbol{\alpha}} \psi_{\boldsymbol{\alpha}}(\boldsymbol{s}, \boldsymbol{\xi}), \tag{3.32}$$

where $\boldsymbol{u}(\boldsymbol{s}, \boldsymbol{\xi}) = [\Delta \boldsymbol{V}_f(\boldsymbol{s}) \ \delta \boldsymbol{X}(\boldsymbol{s}, \boldsymbol{\xi})]^T$. It should be noted here that the $\Delta \boldsymbol{V}$ remains a function only of the deterministic inputs $\boldsymbol{s}$, while the state uncertainties $\delta \boldsymbol{X}_f$ are a function of both the deterministic and stochastic parameters. Following Equation 3.4, the basis functions are generated by taking the tensor product of the basis functions in each of the deterministic and stochastic dimensions, i.e.,

$$\psi_{\boldsymbol{\alpha}}(\boldsymbol{s}, \boldsymbol{\xi}) = \psi_{\boldsymbol{\alpha},1_s}(s_1) \times \cdots \times \psi_{\boldsymbol{\alpha},d_s}(s_{d_s}) \times \psi_{\boldsymbol{\alpha},1_\xi}(\xi_1) \times \cdots \times \psi_{\boldsymbol{\alpha},d_\xi}(\xi_{d_\xi}). \tag{3.33}$$

### 3.4.1 Optimization Cost Function

The polynomial form of the system response in Equation 3.32, which is an explicit function of the system inputs and is easily differentiable, is well-suited for use in the cost function of an optimization scheme. The optimization problem seeks to minimize the objective function $J(\boldsymbol{s}, \boldsymbol{\xi})$ subject to inequality constraints $\boldsymbol{F}(\boldsymbol{s}, \boldsymbol{\xi})$ on the final state variance:

$$\min_{\boldsymbol{s}} J(\boldsymbol{s}, \boldsymbol{\xi}) = |\Delta \boldsymbol{V}(\boldsymbol{s})| \tag{3.34}$$

$$\text{s.t.} \quad \boldsymbol{\sigma}^2_{\delta \boldsymbol{X}_f}(\boldsymbol{s}, \boldsymbol{\xi}) \leq \boldsymbol{\sigma}^2_{max}$$

$$\boldsymbol{s}_l \leq \boldsymbol{s} \leq \boldsymbol{s}_u.$$

There also exists an explicit analytic solution for the first order derivatives with respect to each of the design and stochastic inputs. The Jacobian, which is comprised of these derivatives and is used in gradient-based optimization schemes, is defined as

$$DJ = \frac{\partial \boldsymbol{u}(\boldsymbol{s}, \boldsymbol{\xi})}{\partial \boldsymbol{s} \partial \boldsymbol{\xi}}. \tag{3.35}$$

The optimization method used in this body of work is based on an interior point algorithm, which relies on determining a sequence of solutions to approximate minimization problems (see, for example, [17]). The interior point algorithm is implemented using Matlab's $fmincon$ optimizer.

### 3.4.2 Final State Statistics

Another major advantage of the polynomial expansion model is that it provides analytic representations for the propagated system stochastics [27]. This is a particularly useful property for robust optimization, as it eliminates the need to perform a Monte Carlo analysis at each candidate in the optimization process to determine whether the solution meets the given constraints in Equation 3.34. The derivations of these formulas are as follows.

For a PCE generated only in $\boldsymbol{\xi}$ at a single design point, the mean of the final state deviation

is obtained by integrating over the domain $\Gamma^{d_\xi}$,

$$\boldsymbol{\mu} = E[\delta \boldsymbol{X}_f(\boldsymbol{\xi})] = \int_{\Gamma^{d_\xi}} \delta \boldsymbol{X}_f(\boldsymbol{\xi}) \rho(\boldsymbol{\xi}) d\boldsymbol{\xi} = \int_{\Gamma^{d_\xi}} \left( \sum_{\boldsymbol{\alpha} \in \Lambda_{p,d}} \boldsymbol{c}_{\boldsymbol{\alpha}}(\boldsymbol{\xi}) \psi_{\boldsymbol{\alpha}}(\boldsymbol{\xi}) \right) \rho(\boldsymbol{\xi}) d\boldsymbol{\xi}. \tag{3.36}$$

Because $\psi_0 = 1$ and $E[\psi_{\boldsymbol{\alpha}}] = 0 \; \forall \; \boldsymbol{\alpha} \neq \mathbf{0}$, Equation 3.36 can be simplified to

$$\boldsymbol{\mu} = c_0(\boldsymbol{\xi}). \tag{3.37}$$

Similarly, the variance is defined as the inner product $\langle \cdot, \cdot \rangle$ of $\delta \boldsymbol{X}_f(\boldsymbol{s})$ minus the square of the mean response,

$$\begin{aligned} \boldsymbol{\sigma}^2 &= E[(\delta \boldsymbol{X}_f(\boldsymbol{\xi}) - E[\delta \boldsymbol{X}_f(\boldsymbol{\xi})])(\delta \boldsymbol{X}_f(\boldsymbol{\xi}) - E[\delta \boldsymbol{X}_f(\boldsymbol{\xi})])^T] = \langle \delta \boldsymbol{X}_f(\boldsymbol{\xi}), \delta \boldsymbol{X}_f(\boldsymbol{\xi}) \rangle - \boldsymbol{\mu}^2 \\ &= \int_{\Gamma^{d_\xi}} \left( \sum_{\boldsymbol{\alpha} \in \Lambda_{p,d}} \boldsymbol{c}_{\boldsymbol{\alpha}}(\boldsymbol{\xi}) \psi_{\boldsymbol{\alpha}}(\boldsymbol{\xi}) \right) \left( \sum_{\boldsymbol{\alpha} \in \Lambda_{p,d}} \boldsymbol{c}_{\boldsymbol{\alpha}}(\boldsymbol{\xi}) \psi_{\boldsymbol{\alpha}}(\boldsymbol{\xi}) \right)^T \rho(\boldsymbol{\xi}) d\boldsymbol{\xi} - \boldsymbol{\mu}^2, \end{aligned} \tag{3.38}$$

and, from Equation 3.13, the right-hand side can be reduced to

$$\boldsymbol{\sigma}^2 = \sum_{\substack{\boldsymbol{\alpha} \in \Lambda_{p,d} \\ \boldsymbol{\alpha} \neq \mathbf{0}}} \boldsymbol{c}_{\boldsymbol{\alpha}}(\boldsymbol{\xi}) \boldsymbol{c}_{\boldsymbol{\alpha}}(\boldsymbol{\xi})^T \left\langle \psi_{\boldsymbol{\alpha}}^2(\boldsymbol{\xi}) \right\rangle. \tag{3.39}$$

With the proper normalization of the basis functions, both the mean and variance of the deviations in the propagated state are functions only of the expansion coefficients.

Extending these integrals to Equation 3.32, the expectation of the basis functions in the deterministic dimensions at design point $\boldsymbol{s}$ is equivalent to the evaluation of the basis at that point, such that the mean of $\delta \boldsymbol{X}_f$ is equal to

$$\begin{aligned} \boldsymbol{\mu} = E\left[\delta \boldsymbol{X}_f(\boldsymbol{s}, \boldsymbol{\xi})\right] &= E\left[ \sum_{\boldsymbol{\alpha} \in \Lambda_{p,d}} \boldsymbol{c}_{\boldsymbol{\alpha}}(\boldsymbol{s}) \psi_{\boldsymbol{\alpha}}(\boldsymbol{s}) \psi_{\boldsymbol{\alpha}}(\boldsymbol{\xi}) \right] \\ &= \int_{\Gamma^d} \left( \sum_{\boldsymbol{\alpha} \in \Lambda_{p,d}} \boldsymbol{c}_{\boldsymbol{\alpha}}(\boldsymbol{s}) \psi_{\boldsymbol{\alpha}}(\boldsymbol{s}) \psi_{\boldsymbol{\alpha}}(\boldsymbol{\xi}) \right) \rho(\boldsymbol{\xi}) d\boldsymbol{\xi} = \sum_{\substack{\boldsymbol{\alpha}_{\boldsymbol{s}} \in \Lambda_{p,d} \\ \boldsymbol{\alpha}_{\boldsymbol{\xi}} = \mathbf{0}}} \boldsymbol{c}_{(\boldsymbol{\alpha}_{\boldsymbol{s}}, \boldsymbol{\alpha}_{\boldsymbol{\xi}})}(\boldsymbol{s}) \psi_{\boldsymbol{\alpha}_{\boldsymbol{s}}}(\boldsymbol{s}), \end{aligned} \tag{3.40}$$

where $\boldsymbol{\alpha}_{\boldsymbol{s}}$ and $\boldsymbol{\alpha}_{\boldsymbol{\xi}}$ are the columns of the multi-index corresponding to the deterministic and stochas-

tic dimensions, respectively, and $\Lambda_{p,c} = \Lambda_{\boldsymbol{s}} \otimes \Lambda_{\boldsymbol{\xi}}$. Likewise, the variance is

$$\begin{aligned}\boldsymbol{\sigma}^2 &= E[(\delta \boldsymbol{X}_f(\boldsymbol{s},\boldsymbol{\xi}) - E[\delta \boldsymbol{X}_f(\boldsymbol{s},\boldsymbol{\xi})])(\delta \boldsymbol{X}_f(\boldsymbol{s},\boldsymbol{\xi}) - E[\delta \boldsymbol{X}_f(\boldsymbol{s},\boldsymbol{\xi})])^T] \\ &= \int_{\Gamma^d} \left( \sum_{\boldsymbol{\alpha} \in \Lambda_{p,d}} \boldsymbol{c}_{\boldsymbol{\alpha}}(\boldsymbol{s}) \psi_{\boldsymbol{\alpha}}(\boldsymbol{s}) \psi_{\boldsymbol{\alpha}}(\boldsymbol{\xi}) \right) \left( \sum_{\boldsymbol{\alpha} \in \Lambda_{p,d}} \boldsymbol{c}_{\boldsymbol{\alpha}}(\boldsymbol{s}) \psi_{\boldsymbol{\alpha}}(\boldsymbol{s}) \psi_{\boldsymbol{\alpha}}(\boldsymbol{\xi}) \right) \rho(\boldsymbol{\xi}) d\boldsymbol{\xi} - \boldsymbol{\mu}^2 \\ &= \sum_{\substack{(\boldsymbol{\alpha}_{\boldsymbol{s}}, \boldsymbol{\alpha}_{\boldsymbol{\xi}}) \in \Lambda_{p,d} \\ \boldsymbol{\alpha}_{\boldsymbol{\xi}} \neq \boldsymbol{0}}} \boldsymbol{c}_{(\boldsymbol{\alpha}_{\boldsymbol{s}}, \boldsymbol{\alpha}_{\boldsymbol{\xi}})}(\boldsymbol{s}) \psi_{\boldsymbol{\alpha}_{\boldsymbol{s}}}(\boldsymbol{s}) \sum_{\boldsymbol{\alpha}'_{\boldsymbol{s}} \in \Lambda_{\boldsymbol{s}}} \boldsymbol{c}_{(\boldsymbol{\alpha}'_{\boldsymbol{s}}, \boldsymbol{\alpha}_{\boldsymbol{\xi}})}(\boldsymbol{s}) \psi_{\boldsymbol{\alpha}'_{\boldsymbol{s}}}(\boldsymbol{s}). \end{aligned} \quad (3.41)$$

Again, both $\boldsymbol{\mu}$ and $\boldsymbol{\sigma}^2$ are functions only of deterministic variables.

# Chapter 4

## Sensitivity Analysis (SA)

The goal of sensitivity analysis (SA) is to determine how individual model outputs depend on each of the system inputs and to quantify these dependencies using a set of sensitivity indices. Analysis of the sensitivities can be split into two types: local SA and global SA. Local SA provides insight into how the quantity of interest (QOI) is impacted by perturbations directly about a particular nominal design solution and is valid only over a finite interval about the nominal. Global SA, on the other hand, generates an overall picture of how each system input, considered across its entire design or stochastic space, will influence the results of the QOI. In particular, analysis of variance (ANOVA) is a method which seeks to perform global SA by estimating the contributions of variations in each input dimension to the total variance of the QOI [125].

Knowledge regarding the influence of each of the various system parameters on the QOI can be particularly useful for mission design and optimization. In the context of deterministic design, SA measures the impact each of the design parameters has on, for example, $\Delta V$ costs, and highlights those parameters that can be most effective in controlling mission costs. In the case of uncertainty quantification (UQ) and optimization under uncertainty, SA provides information regarding how both the design and stochastic inputs are reflected in the final state statistics; such analysis can be used to measure the robustness of the design, among other applications.

The models presented in Chapter 3 enable efficient means for both local and global SA that are typically not available when employing probabilistic approaches to optimization and UQ. This chapter discusses how each type of sensitivity analysis can be applied to the design problem and

provides an overview of the techniques used to conduct such an analysis. Section 4.1 introduces local sensitivity analysis via local derivatives, while Section 4.2 presents a set of parameters known as the Sobol' sensitivity indices, derived from a stochastic decomposition of the expansion model, which are recommended for use as a measure of sensitivity in global sensitivity analysis of stochastic design problems. Finally, Section 4.3 proposes a set of "pseudo-Sobol' indices" for use in global SA in deterministic design problems, as the stochastic derivation of the Sobol' indices is not applicable to the deterministic systems.

## 4.1 Local Sensitivity Analysis

Local sensitivity analysis entails determining a set of system derivatives that are valid only over a finite region about a given nominal solution to the system. Thus, the local sensitivity index $\mathcal{L}_i$ is a measure of the slope of the model output with respect to each of the system inputs $x_i$ at a single point in the parameter space. The index can consist of all first-order local sensitivities, second-order local sensitivities, etc., corresponding to the function derivatives of the same order. Local SA does not provide any insight into the effects of large-scale changes in the input parameters.

Approaches to local sensitivity analysis can be categorized as either direct methods or indirect methods [113]. Indirect methods rely on empirical calculations of the local sensitivity indices and can be slower and less accurate than direct methods. A commonly used indirect method is the finite-difference approximation, in which the system solution $\boldsymbol{y}$ is computed for both the nominal inputs $x_i$ and a collection of perturbations in the inputs $\Delta x_i$ about the nominal, and the derivative of the response is approximated as

$$\mathcal{L}_i = \frac{\delta \boldsymbol{y}}{\delta x_i} \approx \frac{\boldsymbol{y}\left(x_i + \Delta x_i\right) - \boldsymbol{y}\left(x_i\right)}{\Delta x_i}, \qquad i = 1, ..., d. \tag{4.1}$$

The accuracy of this approximation can be significantly influenced by the size of the perturbation $\Delta x_i$ used. For too large a step size, the assumption of the local linearity of the solution may be violated, while too small a step size may result in a failure to capture any measurable change in the system response.

Direct methods, on the other hand, consist of analytical solutions to the response derivatives, resulting in a system of sensitivity differential equations. For an ordinary differential equation

$$\frac{d\boldsymbol{y}}{dt} = f\left(\boldsymbol{y}, \boldsymbol{x}\right)$$

with state variables $\boldsymbol{y}$ and parameters $\boldsymbol{x}$ (e.g., the equations of motion for the CRTBP in Equation 2.2, where $\boldsymbol{y} = [x, y, z, \dot{x}, \dot{y}, \dot{z}]$ and $x = \mu$), the system of sensitivity differential equations is defined as

$$\frac{d}{dt}\frac{\partial \boldsymbol{y}}{\partial x_j} = \frac{\partial \boldsymbol{f}}{\partial \boldsymbol{y}}\frac{\partial \boldsymbol{y}}{\partial x_j} + \frac{\partial \boldsymbol{f}}{\partial x_i}. \tag{4.2}$$

Once again, the explicit form of the expansion models for the rendezvous problem proves advantageous, as the analytical derivatives are equivalent to the Jacobian of Equation 3.35. Thus, the set of local sensitivities is

$$\boldsymbol{\mathcal{L}} = DJ = \frac{\partial \boldsymbol{u}\left(\boldsymbol{s}, \boldsymbol{\xi}\right)}{\partial \boldsymbol{s} \partial \boldsymbol{\xi}}. \tag{4.3}$$

In this study, the local sensitivity indices are used primarily in the context of the derivative-based optimization problem, but they could also be used to assess the robustness of a design solution by determining the effects of small errors or perturbations in the rendezvous maneuvers on the final position variance.

## 4.2 Sobol' Sensitivity Indices

One measure of the global sensitivity of the QOI to the system inputs is the Sobol' sensitivity indices, which are a relative measure of the variance in the QOI attributable to the individual inputs to the total variance of the system. These indices can be computed empirically from a Monte Carlo simulation of the system. Alternatively, some surrogates, such as the PCEs presented in the previous chapter, yield an analytic solution to the Sobol' indices as a function of the expansion coefficients.

The derivation of the Sobol' indices is based on the decomposition of the model $y = f(\boldsymbol{x})$ for $y \in \{\Delta \boldsymbol{V}, \delta \boldsymbol{X}_f\}$ and $\boldsymbol{x} \in \{\boldsymbol{s}, \boldsymbol{\xi}\}$ into summands of its input dimensions, such that

$$f(x_1, ..., x_k) = f_0 + \sum_{i=1}^{k} f_i(x_i) + \sum_{1 \le i < j \le k} f_{ij}(x_i, x_j) + \cdots + f_{1,2,...,k}(x_1, ..., x_k). \tag{4.4}$$

In [122], it is shown that the total variance $D$ of the function $f(x)$ can be decomposed into the contributions of each system input in the same way, i.e.,

$$D = \sum_{i=1}^{k} D_i + \sum_{1 \le i < j \le k} D_{ij} + \cdots + D_{1,2,\ldots,k}, \tag{4.5}$$

where

$$D_i = \mathcal{V}(E(y|x_i)),$$

$$D_{ij} = \mathcal{V}(E(y|x_i, x_j)) - D_i - D_j \quad \forall\ x_i \in \{\boldsymbol{s}, \boldsymbol{\xi}\}, \quad y \in \{\Delta \boldsymbol{V}, \delta \boldsymbol{X}_f\},$$

etc., for all correlated terms. The Sobol' indices are defined as the ratio of the variance in $y$ due to dimension $j$ to the total variance $D$, so that the first order indices are given by

$$S_j^1 = \frac{D_j}{D}. \tag{4.6}$$

Defining

$$U_j = \int E^2(y|x_j = \tilde{x}_j) p_j(\tilde{x}_j) \mathrm{d}\tilde{x}_j, \tag{4.7}$$

the variance due to each input dimension can be expressed as

$$\mathcal{V}(\mathcal{E}(y|x_j)) = U_j - E^2(y), \tag{4.8}$$

and Equation 4.6 becomes

$$S_j^1 = \frac{U_j - E^2(y)}{\mathcal{V}(y)}. \tag{4.9}$$

Similarly, the total effect $S_j^T$ of dimension $j$, which includes the effects of the first order terms and all correlated terms, is given by

$$S_j^T = 1 - \frac{D_{-j}}{D} = 1 - \frac{U_{-j} - E^2(j)}{\mathcal{V}(y)}, \tag{4.10}$$

where the notation $D_{-j}$ refers to the variance due to the set of all dimensions except the $j$-th dimension.

### 4.2.1 Sampling-Based Indices

One approach to the computation of the Sobol' indices requires a Monte Carlo simulation of $n$ independent samples, as laid out in [112]. This technique is useful when a surrogate representation of the system is not available, as in the case of kinetic deflection of asteroids (reasons for this will be discussed in Chapter 6). In the empirical calculation of the Sobol' indices, two sample matrices $\boldsymbol{M}_1$ and $\boldsymbol{M}_2$ of size $n \times k$ are generated,

$$\boldsymbol{M}_1 = \begin{pmatrix} x_{11} & x_{12} & \cdots & x_{1k} \\ x_{21} & x_{22} & \cdots & x_{2k} \\ \cdots & & & \\ x_{n1} & x_{n2} & \cdots & x_{nk} \end{pmatrix}, \quad \boldsymbol{M}_2 = \begin{pmatrix} x'_{11} & x'_{12} & \cdots & x'_{1k} \\ x'_{21} & x'_{22} & \cdots & x'_{2k} \\ \cdots & & & \\ x'_{n1} & x'_{n2} & \cdots & x'_{nk} \end{pmatrix}, \tag{4.11}$$

where $k$ is the number of random inputs to the system. The matrices of Equation 4.11 are referred to as the "sample" and "re-sample" matrices. Another set of $k$ matrices $N_j$ is also generated, in which all elements except $x_j$ are "re-sampled", i.e., $x_j$ is taken from $\boldsymbol{M}_1$, while the remaining elements are extracted from $\boldsymbol{M}_2$, resulting in

$$\boldsymbol{N}_j = \begin{pmatrix} x'_{11} & x'_{12} & \cdots & x_{1j} & \cdots & x'_{1k} \\ x'_{21} & x'_{22} & \cdots & x_{2j} & \cdots & x'_{2k} \\ \cdots & \cdots & \cdots & \cdots & \cdots & \cdots \\ x'_{n1} & x'_{n2} & \cdots & x_{nj} & \cdots & x'_{nk} \end{pmatrix}. \tag{4.12}$$

Function evaluations for each row of the matrices in Equations 4.11 and 4.12 are used to calculate estimates of the parameters in Equation 4.9, which are defined in [112] for the first order indices as

$$\hat{U}_j = \frac{1}{n-1} \sum_{r=1}^{n} f(x_{r1}, x_{r2}, ..., x_{rk}) f(x'_{r1}, x'_{r2}, ..., x'_{r(j-1)}, x_{rj}, x'_{r(j+1)}, ..., x'_{rk}) \tag{4.13}$$

and

$$\hat{E}^2 = \frac{1}{n} \sum_{r=1}^{n} f(x_{r1}, x_{r2}, ..., x_{rk}) f(x'_{r1}, x'_{r2}, ..., x'_{rk}). \tag{4.14}$$

For the total indices, it follows that

$$\hat{U}_j = \frac{1}{n-1}\sum_{r=1}^{n} f(x_{r1}, x_{r2}, ..., x_{rk}) f(x_{r1}, x_{r2}, ..., x_{r(j-1)}, x'_{rj}, x_{r(j+1)}, ..., x_{rk}), \tag{4.15}$$

and it is shown in [112] that $\hat{E}^2$ is better estimated by

$$\hat{E}^2 = \left[\frac{1}{n}\sum_{r=1}^{n} f(x_{r1}, x_{r2}, ..., x_{rk})\right]^2. \tag{4.16}$$

The empirical method for solving the Sobol' indices is convenient in that it may be used with any model, including the full dynamics for the system. However, from Equations 4.13 and 4.14, this approach requires $n(k+2)$ realizations of the model, which can be computationally expensive for some models. Additionally, convergence with $n$ may be slow.

### 4.2.2 Analytic Indices

Alternatively, if a polynomial chaos expansion (PCE) representation has been developed for a system, the Sobol' indices for any subset of the input dimensions may be computed analytically at no additional computational cost. The algorithm, developed in [125], relies on two principles. First, the orthogonality of the bases used in the expansion allow the mean and variance of the system response to be expressed as

$$E[\boldsymbol{u}(\boldsymbol{\xi})] = c_0 \tag{4.17}$$

and

$$D_{PC} = \mathcal{V}\left[\sum_{i=1}^{P-1} c_i \Psi_i(\boldsymbol{\xi})\right] = \sum_{i=1}^{P-1} c_i^2 E[\Psi_i^2(\boldsymbol{\xi})], \tag{4.18}$$

respectively. Second, the polynomial expansion can be decomposed following Equation 4.4. The Sobol' decomposition of the expansion takes the form

$$\begin{aligned}\boldsymbol{u}(\boldsymbol{\xi}) = c_0 + \sum_{i=1}^{d}\sum_{\boldsymbol{\alpha}\in\mathcal{I}_i} c_{\boldsymbol{\alpha}}\Psi_{\boldsymbol{\alpha}}(\xi_i) + \sum_{\substack{1\le i_1\\ <i_2\le d}}^{d}\sum_{\boldsymbol{\alpha}\in\mathcal{I}_{i_1,i_2}} c_{\boldsymbol{\alpha}}\Psi_{\boldsymbol{\alpha}}(\xi_{i_1},\xi_{i_2}) + \cdots \\ + \sum_{\substack{1\le i_1<\cdots\\ <i_s\le d}}^{d}\sum_{\boldsymbol{\alpha}\in\mathcal{I}_{i_1,\ldots,i_s}} c_{\boldsymbol{\alpha}}\Psi_{\boldsymbol{\alpha}}(\xi_{i_1},\ldots,\xi_{i_s}) + \cdots + \sum_{\boldsymbol{\alpha}\in\mathcal{I}_{1,2,\ldots,d}} c_{\boldsymbol{\alpha}}\Psi_{\boldsymbol{\alpha}}(\xi_1,\ldots,\xi_d),\end{aligned} \tag{4.19}$$

where $\mathcal{I}_{i_1,\dots,i_s} \subset \mathbf{\Lambda}_{p,d}$ is the set of $\boldsymbol{\alpha}$ tuples such that only the indices $(i_1, \dots, i_s)$ are non-zero. The first order PC-based Sobol' indices are then derived as

$$S^1_{i_1,\dots,i_s} = \sum_{\boldsymbol{\alpha} \in \mathcal{I}_{i_1,\dots,i_s}} \frac{c^2_{\boldsymbol{\alpha}} E[\mathbf{\Psi}^2_{\boldsymbol{\alpha}}]}{D_{PC}}, \tag{4.20}$$

and the total indices are merely the summation over all lower order indices containing dimensions $j_1, \dots, j_t$,

$$S^T_{j_1,\dots,j_t} = \sum_{(i_1,\dots,i_s) \in \mathcal{I}_{j_1,\dots,j_t}} S_{i_1,\dots,i_s}. \tag{4.21}$$

## 4.3 Pseudo-Sobol' Indices

For deterministic design parameters, the bases used are not stochastic in nature, and therefore the analytical derivation of the Sobol' indices in Section 4.2 no longer holds. Instead, a similar set of indices are proposed, which are an extrapolation of Equation 4.20 and still provide a relative measure of the dependence of the system response on a given input. The proposed indices are defined as

$$S^1_i = \frac{D_i}{D}, \tag{4.22}$$

where

$$D_i = \sum_{\boldsymbol{\alpha}^i \in \mathbf{\Lambda}_{p,i}} c_{\boldsymbol{\alpha}^i} \tag{4.23}$$

and

$$D = \sum_{i=1}^{d} D_i. \tag{4.24}$$

Again, these indices enable global SA for deterministic systems at no additional cost beyond that required to build the design surrogate.

# Chapter 5

# Rendezvous Design in the CRTBP

Maneuver design and optimization for spacecraft in three-body orbits is well-suited for application of the surrogate modeling techniques described in Chapter 3, as the nonlinearity of the circular restricted three-body problem provides opportunity for reductions in computational costs, while the smoothness of the system dynamics enables the system to be accurately modeled with a combination of Legendre and Fourier polynomials. By generating the surrogate models for the purpose of design, the need for repeated integration of the full system dynamics for trade space exploration and optimization can be limited to the number of samples necessary for convergence of the model. Additionally, the use of surrogates in the robust design problem precludes the need for expensive Monte Carlo simulations to propagate system uncertainties during the optimization process.

This chapter presents the results of models generated for the rendezvous problems defined in Section 2.1 for halo orbits about the Earth-Moon $L_2$ (EML-2) point and for distant retrograde orbits (DRO) about the moon. Deterministic models are presented first in Section 5.1, followed by stochastic models for robust design in Section 5.2.

## 5.1 Deterministic Maneuver Design

This section considers rendezvous design for purely deterministic systems. Surrogates are used to model the $\Delta V$ cost of rendezvous over the design space described in Table 2.1, which considers design points about the entire orbits and over a broad range of values for time of flight and initial

spacecraft separation. Generation of these models allows for rapid trade space exploration during the initial mission design phase.

### 5.1.1 Rendezvous in a Halo Orbit

A design surrogate is first built for the case of rendezvous in the 10,000 km halo orbit using a Fourier basis in the periodic $\tau$ dimension and a Legendre basis in the finite, non-periodic $t$ and $\Delta\tau$ dimensions. This section presents the results of models generated using both standard and asymptotic sampling and compares the performance of each. The standard sampling method associated with the Legendre basis is uniform random sampling, while the corresponding asymptotic method samples from a Chebyshev distribution. For the Fourier basis, on the other hand, uniform sampling serves as both the standard and asymptotic sampling methods.

#### 5.1.1.1 Standard Sampling

Figure 5.1 shows the RMS validation error calculated using the full validation set of Table 3.1 for the model of the total $\Delta V$ generated using uniform random sampling in all three input dimensions, as a function of the expansion order and sample size. For each sample size, the RMS error is averaged over 100 independent data sets. It is readily evident that the approximation error decreases with increasing expansion order until it reaches an error floor with a $9^{\text{th}}$ order expansion. The larger errors associated with the lower order expansions correspond to the truncation error defined in Equation 3.3. As the order of the expansion approaches infinity, or, in the case of lower order dynamic systems, as the expansion order approaches the true system order, the truncation error should approach zero.

The error floor, which levels off at about 0.18 m/s for large sample sizes, has two potential sources. First, as the truth data used to initialize the model is generated by numerical simulations, any round-off errors in the simulation will translate into errors in the surrogate. The accuracy levels of the differential corrector being used, though, would suggest that numerical errors contribute very little, if any, to the error floor seen here. The more likely source of the error stems from the rapid

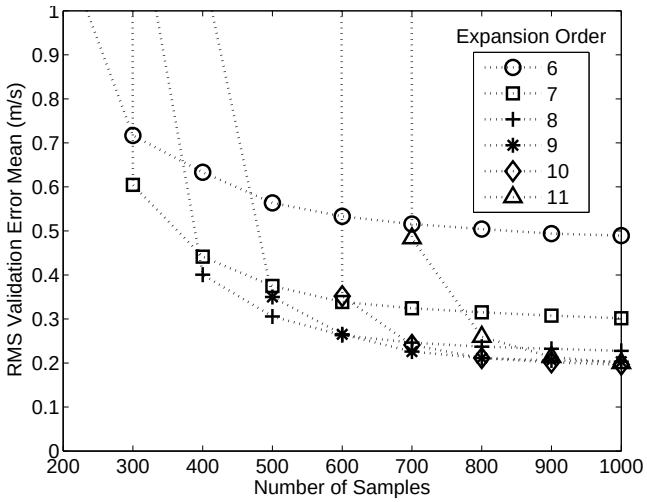


Figure 5.1: RMS validation errors averaged over 100 independent data sets for surrogates constructed using Monte Carlo sampling from a uniform distribution for rendezvous in a halo orbit.

decay in the true $\Delta V$ along the time dimension $t$ as evidenced in Fig. 2.7. Generalized spectral expansions based on global smooth polynomials such as Legendre polynomials are recognized in [73] to face difficulties in accurately modeling a steep dependence of the QOI on an input parameter. Because of this behavior in the time dimension, there simply may not exist a more accurate, low order representation of the system; rather, a very high order expansion may be required to completely capture the system response.

Despite this floor, the modeling errors drop below 0.25 m/s using on the order of only 100 training points. For example, a $9^{\text{th}}$ order expansion generated with 700 samples produces a validation error of 0.226 m/s. This expansion order results in $P = 385$ terms, and the corresponding coefficients can be found in Fig. 5.2. The drop in the coefficients of almost four orders of magnitude indicates a relatively fast convergence in the expansion. Figure 5.3(a) shows the model's predictions for the required $\Delta V$ as a function of the initial position and time of flight for $\Delta\tau = 3°$, and Fig. 5.3(b) shows the associated model errors. These errors are primarily concentrated at low values of $t$. Additionally, the errors appear to have a dominating periodic structure in the $\tau$ dimension. While the magnitude of this periodic error can be decreased by increasing the expansion order, the ability comes at the cost of significantly increasing the sample size.

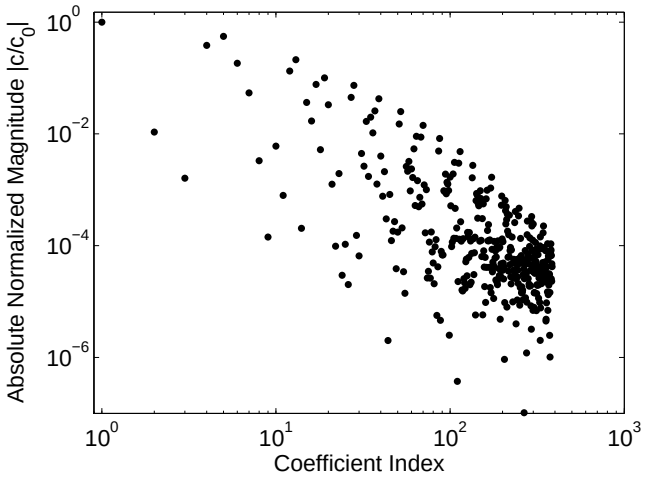


Figure 5.2: Coefficients for a 9$^{\text{th}}$ order Fourier polynomial expansion, normalized to the first term coefficient, as constructed from 700 uniform Monte Carlo samples for rendezvous in a halo orbit.

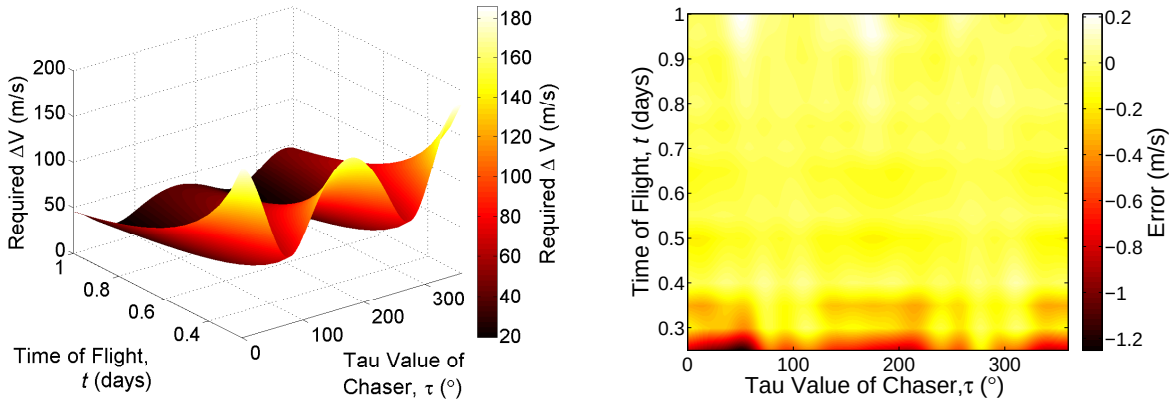


(a) Predicted $\Delta V$

(b) Model errors

Figure 5.3: Model results of a 9$^{\text{th}}$ order Fourier polynomial expansion generated using 700 Monte Carlo realizations of a uniform distribution for rendezvous in a halo orbit at $\Delta\tau = 3°$.

#### 5.1.1.2 Asymptotic Sampling

A comparison of the RMS errors for a model generated using asymptotic sampling, presented in Fig. 5.4, to the errors resulting from standard sampling techniques in Fig. 5.1 reveals that the use of Chebyshev, rather than uniform, random sampling in the $t$ and $\Delta\tau$ dimensions leads to more

rapid convergence of the model errors, particularly for higher order expansions. Specifically, in the $9^{\text{th}}$ order expansion required to reach the error floor, the substitution of Chebyshev sampling results in a slightly smaller RMS validation error (0.207 m/s) using only 500 samples, almost 30% fewer than the number of samples necessary for convergence when uniform sampling is used in all three dimensions. Even more significant than the convergence rate of the validation errors is the difference in the variance of the RMS error over the 100 data sets. Figure 5.5 shows that the variance in the RMS is reduced by almost an order of magnitude when asymptotic sampling is used.

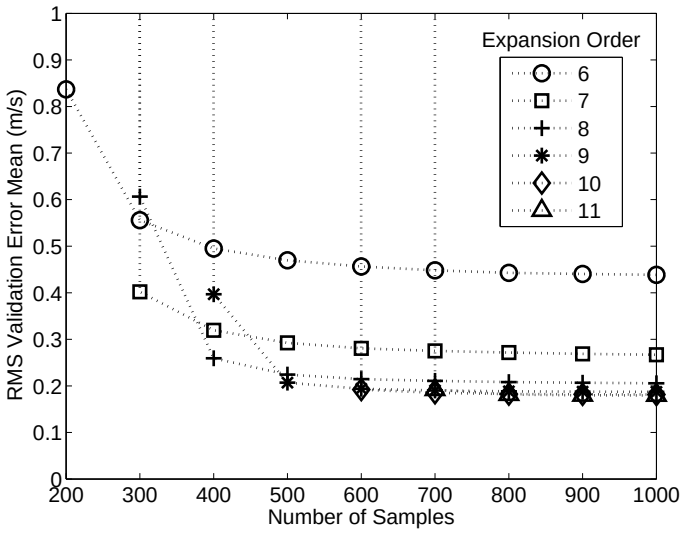


Figure 5.4: RMS validation errors averaged over 100 independent data sets for surrogates constructed using Monte Carlo sampling from a uniform distribution in $\tau$ and from a Chebyshev distribution in $t$ and $\Delta\tau$ for rendezvous in a halo orbit.

Chebyshev sampling is therefore taken to be the superior sampling method associated with the Legendre basis for the rendezvous application considered here. The coefficients for a $9^{\text{th}}$ order expansion constructed from 500 training samples, shown in Fig. 5.6, are very similar to those in Fig. 5.2 and reach the same level of convergence. The resulting model predictions can be found in Fig. 5.7. Figure 5.7(b) shows the model errors at $\Delta\tau = 3°$, which are indeed smaller than those associated with uniform sampling in Fig. 5.3(b) above.

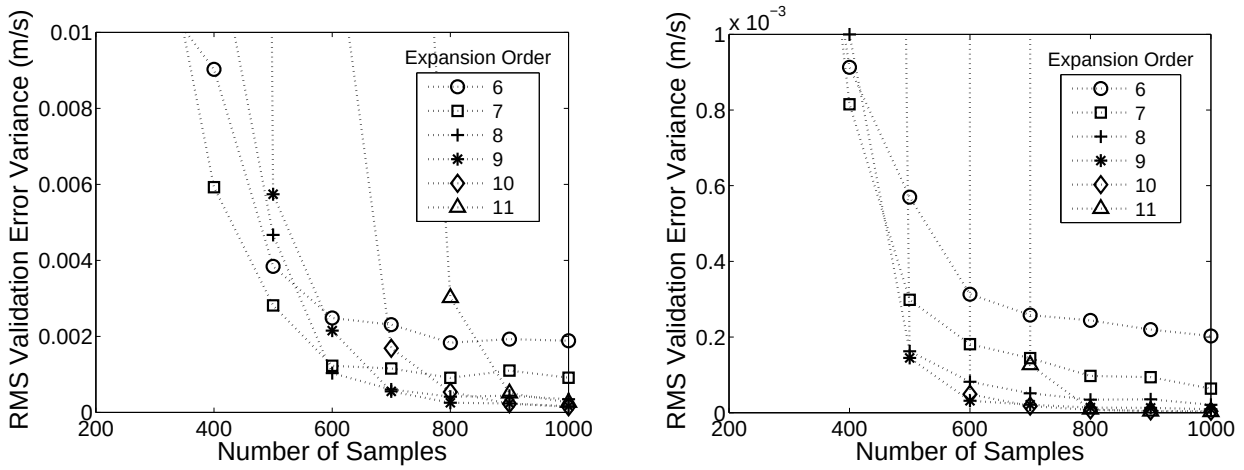


(a) Uniform sampling in $\tau$, $t$, and $\Delta\tau$

(b) Uniform sampling in $\tau$, Chebyshev in $t$ and $\Delta\tau$

Figure 5.5: Variance of the RMS validation errors for surrogates constructed from 100 independent data sets for rendezvous in a halo orbit.

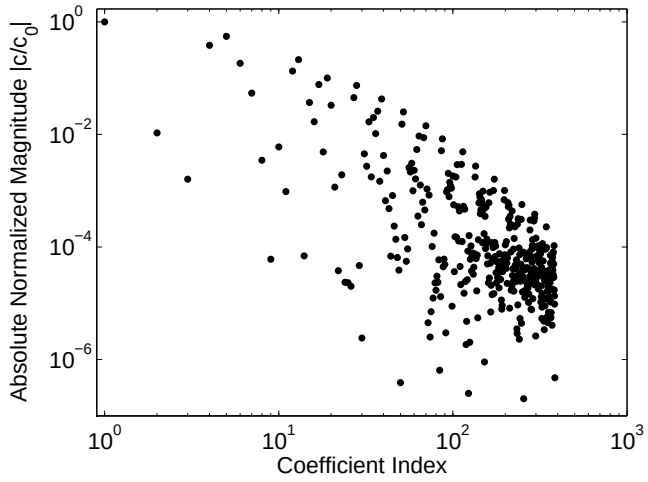


Figure 5.6: Coefficients for a $9^{\text{th}}$ order Fourier polynomial expansion, normalized to the first term coefficient, as constructed from 500 Monte Carlo samples from a uniform distribution in $\tau$ and from a Chebyshev distribution in $t$ and $\Delta\tau$ for rendezvous in a halo orbit.

In computing the $\Delta V$ required for rendezvous, a single function evaluation using the surrogate model is up to two orders of magnitude faster than when using the full fidelity propagators. Further, the matrix form of Equation 3.21 allows for simultaneous evaluation of the surrogate for multiple design inputs, such that the marginal cost of computing the solution at multiple design points

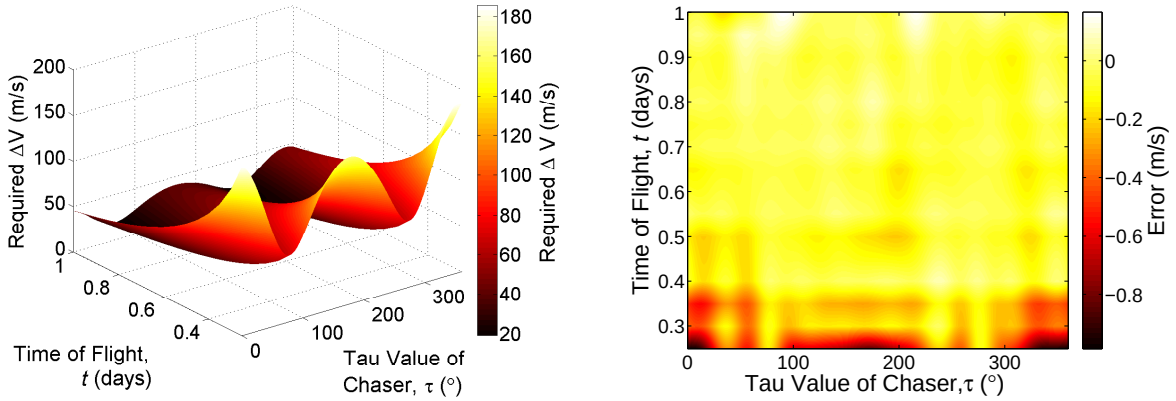


(a) Predicted $\Delta V$

(b) Model errors

Figure 5.7: Model results of a $9^{\text{th}}$ order Fourier polynomial expansion generated using 500 Monte Carlo realizations of a uniform distribution in $\tau$ and a Chebyshev distribution in $t$ and $\Delta\tau$ for rendezvous in a halo orbit at $\Delta\tau = 3°$.

is negligible. Thus, significant cost savings over traditional propagators are accumulated when modeling the variation of the $\Delta V$ over the complete design space.

One limitation still present in the model is its difficulty in accurately predicting system behavior at the boundaries of the design space. In Fig. 5.7(b), for example, the largest errors are concentrated near $t = 0.25$ days. Similarly, comparing Fig. 5.7 to Fig. 5.8, the model is clearly better able to capture the system response at a separation of $\Delta\tau = 3°$ than at the boundary value of $\Delta\tau = 0.1°$. This behavior indicates that a higher order solution is required to fully capture the system response at these boundaries, as evidenced by the periodic nature of the errors, with an associated increase in computational cost. Alternatively, consideration of a smaller design space may result in a lower order system and thereby reduce the errors at the boundaries. Although the magnitude of the errors at $\Delta\tau = 0.1°$ is generally small (see Fig. 5.8(b)), they may affect performance in applications such as optimization and are therefore worth noting. Finally, Fig. 5.9 shows the component-wise errors for the initial and final burns. The errors, which are smaller than those corresponding to the magnitude of the total $\Delta V$, are predominantly concentrated in the $y$-direction and are largest for short transfer times.

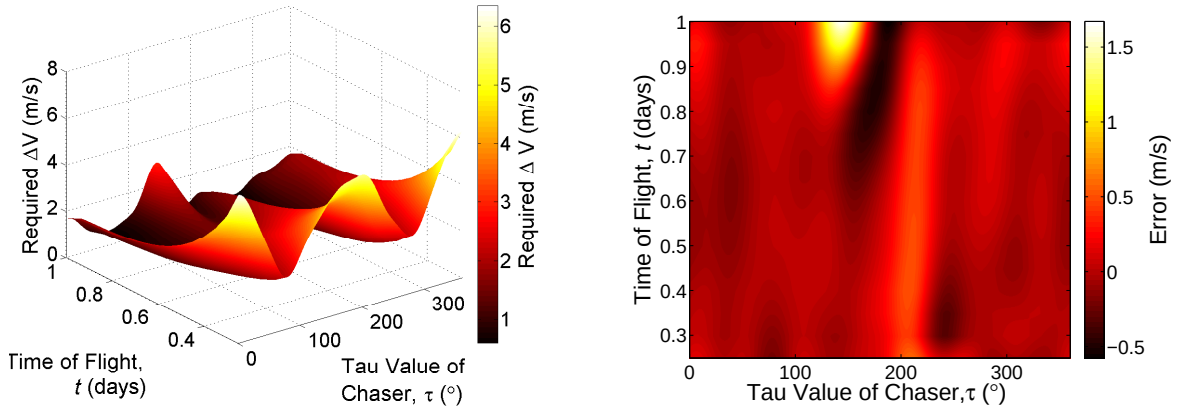


(a) Predicted $\Delta V$

(b) Model errors

Figure 5.8: Model results of a 9$^{\text{th}}$ order Fourier polynomial expansion generated using 500 Monte Carlo realizations of a uniform distribution in $\tau$ and a Chebyshev distribution in $t$ and $\Delta\tau$ for rendezvous in a halo orbit at $\Delta\tau = 0.1°$.

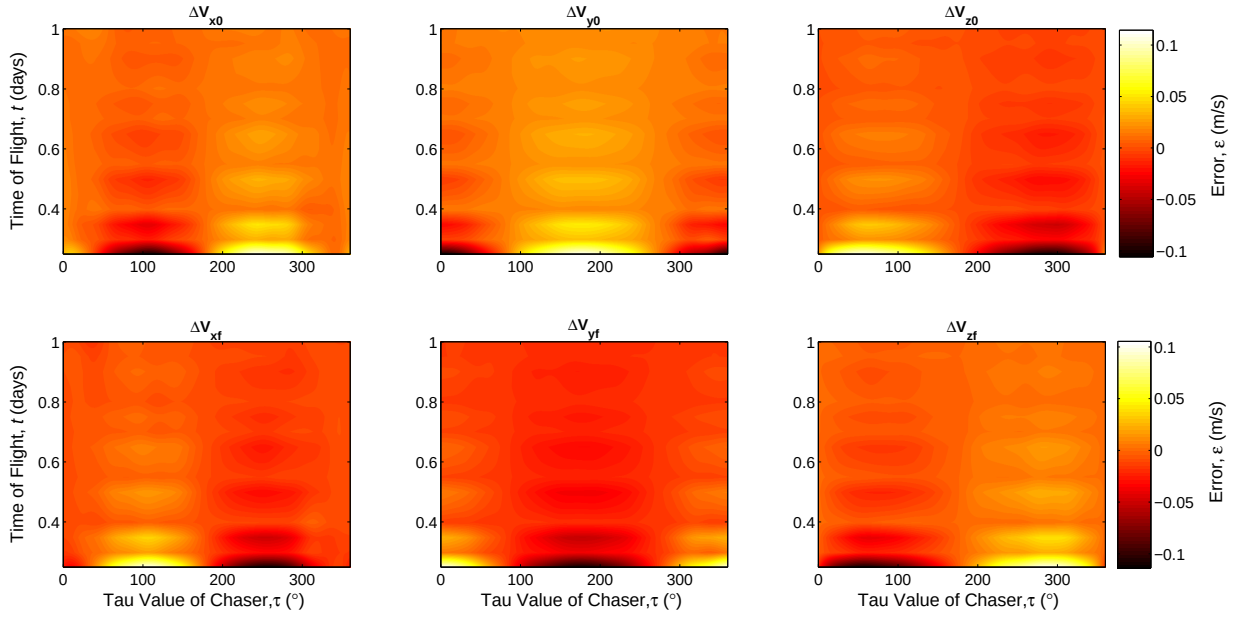


Figure 5.9: Component-wise model errors of a 9$^{\text{th}}$ order Fourier polynomial expansion generated using 500 Monte Carlo realizations of a uniform distribution the $\tau$ and a Chebyshev distribution in $t$ and $\Delta\tau$ for rendezvous in a halo orbit at $\Delta\tau = 3°$.

The full data set used for the validation of the previous two models is not generally available when developing a surrogate. Therefore, with the asymptotic sampling method in place for the DOE, a new model is generated for rendezvous in the halo orbit using the autonomous model generator and $k$-fold validation scheme outlined in Chapter 3, with $k = 10$ candidate surrogates. Figure 5.10 shows the convergence of the $k$-fold RMS error as a function of sample size. Increases in the expansion order are clearly evident in the step decreases in the RMS error, while increases in the sample size within a given order generally do not improve the model accuracy. Additionally, the $k$-fold errors appear to reach smaller values than the errors calculated from the full validation set, likely due to the spatial concentration of the larger modeling errors, which are therefore less likely to be represented in the smaller $k$-fold set a compared to the full set. The $k$-fold RMS accuracy requirement, then, is set to 0.05 m/s, and the model generator converges on a solution using a $9^{\text{th}}$ order expansion with $N = 620$ training samples; when compared to the full validation set, the model results in an RMS error of 0.1957 m/s. Figure 5.11 contains the model and its errors at $\Delta\tau = 3°$, which are very similar to the results obtained from the fixed order model.

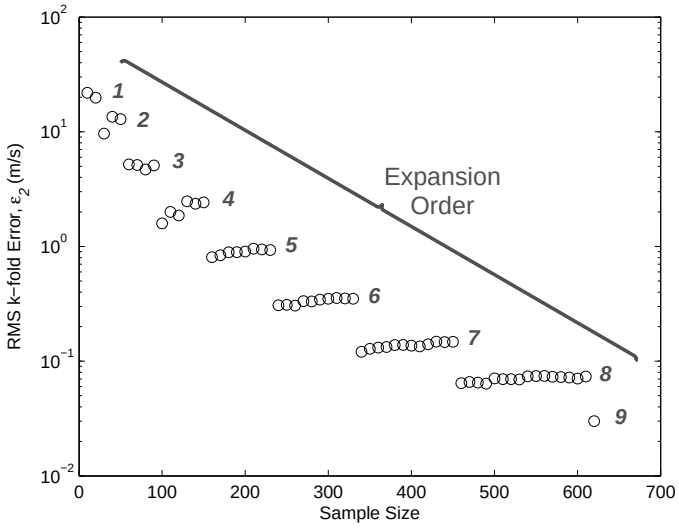


Figure 5.10: $k$-fold RMS errors with $k = 10$ for a surrogate constructed using Monte Carlo sampling from a uniform distribution in $\tau$ and from a Chebyshev distribution in $t$ and $\Delta\tau$ for rendezvous in a halo orbit.

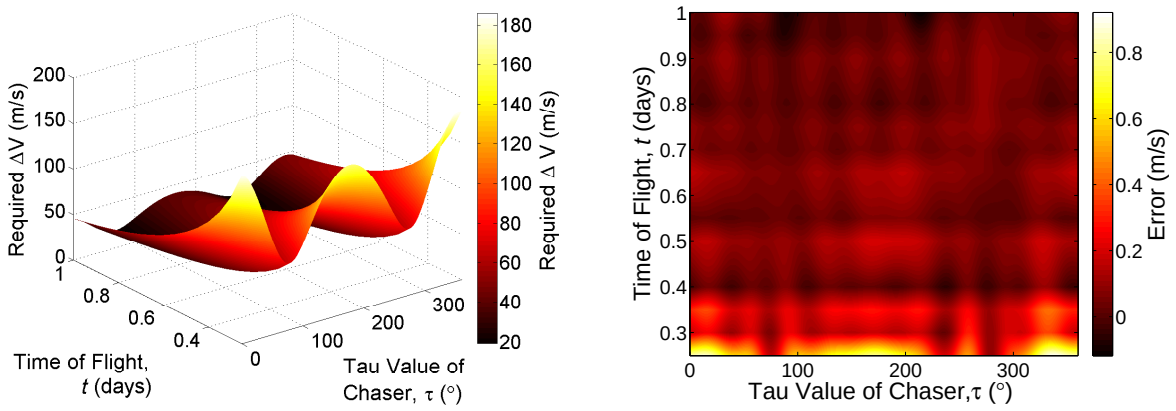


(a) Predicted $\Delta V$

(b) Model errors

Figure 5.11: Model results after $k$-fold convergence with $k = 10$ for a Fourier polynomial expansion generated using Monte Carlo realizations of a uniform distribution in $\tau$ and a Chebyshev distribution in $t$ and $\Delta\tau$ for rendezvous in a halo orbit at $\Delta\tau = 3°$.

The global sensitivity of the required $\Delta V$ to each of the design parameters can be represented by the analytically computed Sobol' sensitivity indices. The total indices for rendezvous about the halo orbit are included in Table 5.1. The values of the indices indicate that $\tau$, $t$, and $\Delta\tau$ all provide measurable contributions to the $\Delta V$, which is consistent with behavior of the model response seen in Figs. 5.7 and 5.8, although the influence of the spacecraft separation $\Delta\tau$ is most significant.

#### 5.1.1.3 Optimization

While the primary purpose of the surrogate models developed in this section is to provide design data across the entire trade space, the representation of the required $\Delta V$ in the form of an

Table 5.1: Total sensitivity indices for the $\Delta V$ required for rendezvous in a halo orbit as a function of the three-dimensional design parameters.

| | $\tau$ | $t$ | $\Delta\tau$ |
|---|---|---|---|
| Sensitivity Index, $S^T$ | 0.155 | 0.311 | 0.507 |

explicit function of the design inputs also makes these surrogates ideally suited for cheap evaluation of the cost function in optimization problems seeking to minimize the $\Delta V$ for spacecraft rendezvous, such as the cost function of Equation 3.34. For optimization of the deterministic system considered in this section, an unconstrained form of the cost function is used.

Figure 5.12 shows the results of the optimizer applied to the problem of minimizing the total $\Delta V$ for rendezvous in the halo orbit over all three design inputs, $\tau$, $t$, and $\Delta\tau$. Because a local optimizer is used for this problem, two different optimal design points, corresponding to the two local minima seen in Fig. 5.12, can be reached depending on the initial guess; both are depicted in the figure.

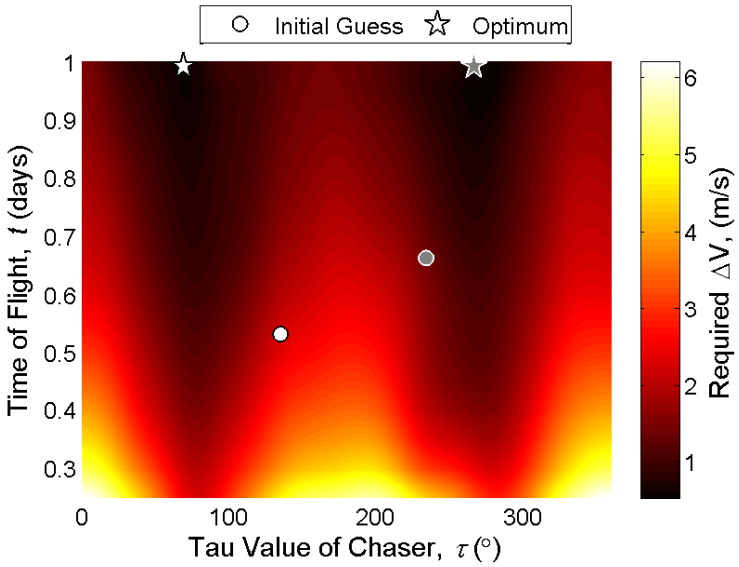


Figure 5.12: Optimized input parameters for minimum $\Delta V$ rendezvous in a halo orbit. The optimal solutions are both located at $\Delta\tau = 0.01°$.

### 5.1.2 Rendezvous in a DRO

In order to demonstrate the black box functionality of the surrogate model framework for general applications in the three-body system, the framework developed above in the context of the halo orbit is next applied to the 70,000 km DRO considered in [50]. The results presented here

are produced by simply changing the input conditions for the target and chaser vehicles, i.e., no additional development cost is necessary for modifications to the tool. The only computational cost involved is that associated with the generation of new samples to build a model specific to this application. A surrogate is first generated for a 2-dimensional system in which the initial position of the chaser is fixed, in order to accommodate a direct comparison to the NASA study. The model is then expanded to include $\tau$ as a third input dimension.

#### 5.1.2.1 2-Dimensional Model

In the NASA study of [50], a Monte Carlo simulation is used to conduct an analysis of the total $\Delta V$ cost of mid-field rendezvous for the Asteroid Redirect Mission (ARM), in which the Orion vehicle uses a two-burn sequence to rendezvous with the Asteroid Redirect Vehicle (ARV). The study considers spacecraft separated by approximately $0.01-0.22^\circ$ from a single initial position, with discrete rendezvous times of 6, 12, and 24 hours. Solutions are presented for approximately 100 isolated points for which the Orion vehicle is initially trailing the ARV and about the same number of points for which the Orion is ahead of the target.

Figure 5.13 shows that using the models developed here for the case considering only the $t$ and $\Delta\tau$ design dimensions with Legendre bases in each, very accurate surrogates can be built with fewer training samples than the $\sim 100$ points examined in the previous study for the case of the chaser trailing the target. In fact, an 8th order model achieves an RMS validation accuracy of $< 10^{-2}$ using only 60 samples, resulting in a full dynamical model for only about half the cost of the limited Monte Carlo analysis.

#### 5.1.2.2 3-Dimensional Model

Figure 5.14 presents the validation errors with $\tau$ included as a third design dimension for the DRO, again using a Fourier basis in the $\tau$ dimension. While the model is still able to achieve accuracies comparable to the two-dimensional case, it requires on the order of 100 training samples to do so. The associated errors are much smaller than those seen in the case of the halo orbit, and

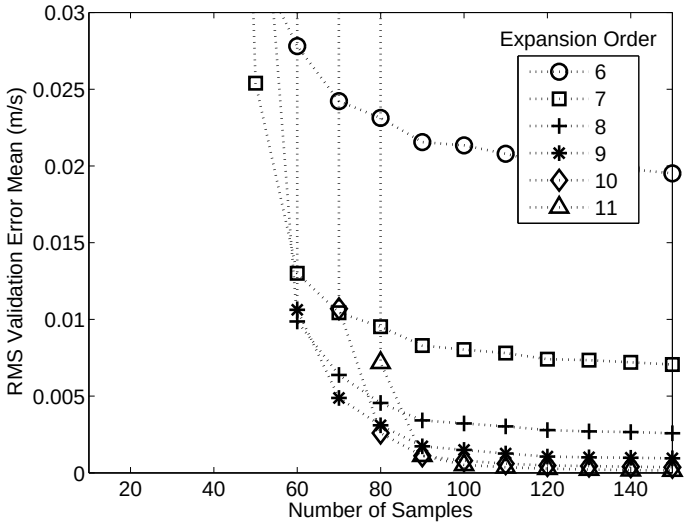


Figure 5.13: RMS validation errors averaged over 100 independent data sets for a surrogate constructed using Monte Carlo sampling from a Chebyshev distribution in $t$ and $\Delta\tau$ for rendezvous in a DRO with $d = 2$.

the error floor that existed for the halo orbit is not present. Instead, the RMS error continually approaches 0 with increasing expansion order and sample size. This is likely a direct result of the smaller range of $\Delta\tau$ values under consideration, which restricts the problem to a lower order system.

From Fig. 5.14, a $9^{\text{th}}$ order expansion generated from 500 training samples with an associated RMS error of $2.369 \times 10^{-3}$ m/s is selected for further analysis. Figure 5.15 contains the model coefficients for this expansion, and Figs. 5.16 and 5.17 show the resulting model and its errors for two different values of $\Delta\tau$. Again, the smaller range of vehicle separation angles greatly improves the performance of the model, particularly at the boundaries of the design space, as seen in the shape of the predicted $\Delta V$ for the smallest separation.

Finally, with an accuracy requirement of $10^{-3}$ m/s, the $k$-fold generator once again converges on a $9^{\text{th}}$ order expansion using 620 training samples, as seen in Fig. 5.18. The model results for $\Delta\tau = 0.15°$ can be found in Fig. 5.19. This last model is used to calculate the total Sobol' sensitivity indices for the design parameters in the DRO, and the results are provided in Table 5.2. From these

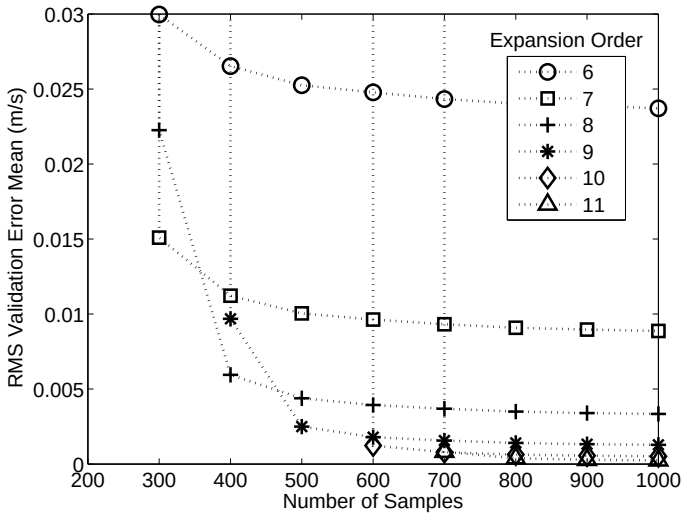


Figure 5.14: RMS validation errors averaged over 100 independent data sets for a surrogate constructed using Monte Carlo sampling from a uniform distribution in $\tau$ and from a Chebyshev distribution in $t$ and $\Delta\tau$ for rendezvous in a DRO with $d = 3$.

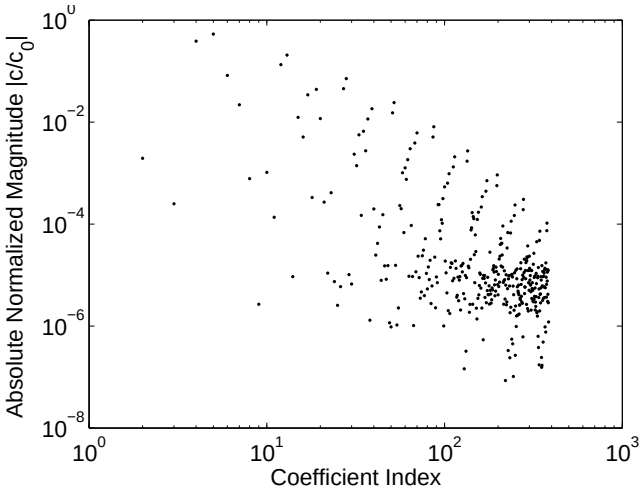


Figure 5.15: Coefficients for a $9^{\text{th}}$ order Fourier polynomial expansion, normalized to the first term coefficient, as constructed from 500 Monte Carlo samples from a uniform distribution in $\tau$ and from a Chebyshev distribution in $t$ and $\Delta\tau$ for rendezvous in a DRO.

indices, the separation between the spacecraft is seen to again have the largest impact on the $\Delta V$ cost, and the time of flight also shows a significant contribution. However, the relative effect of the initial position is much smaller for rendezvous in the DRO than for the halo.

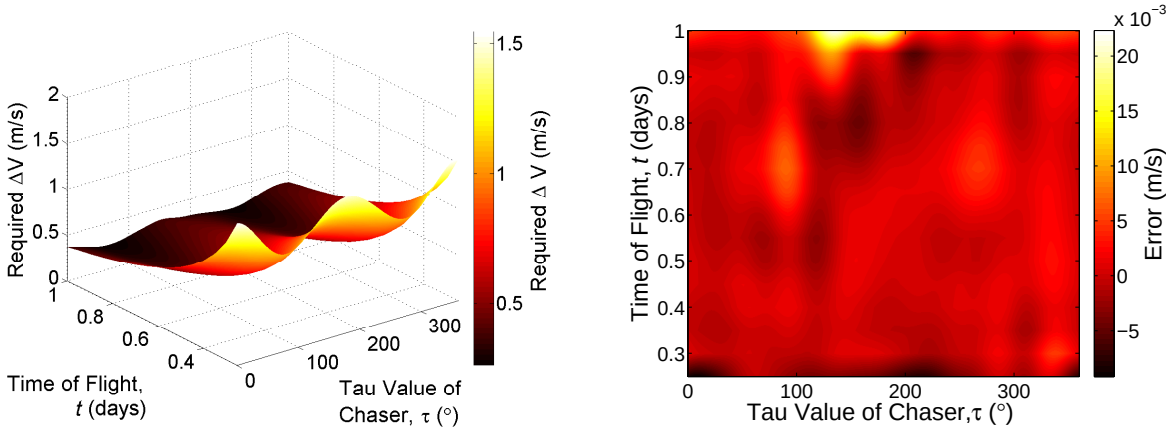


(a) Predicted $\Delta V$ (b) Model errors

Figure 5.16: Model results of a 9$^{\text{th}}$ order Fourier polynomial expansion generated using 500 Monte Carlo realizations of a uniform distribution in $\tau$ and a Chebyshev distribution in $t$ and $\Delta\tau$ for rendezvous in a DRO at $\Delta\tau = 0.01°$.

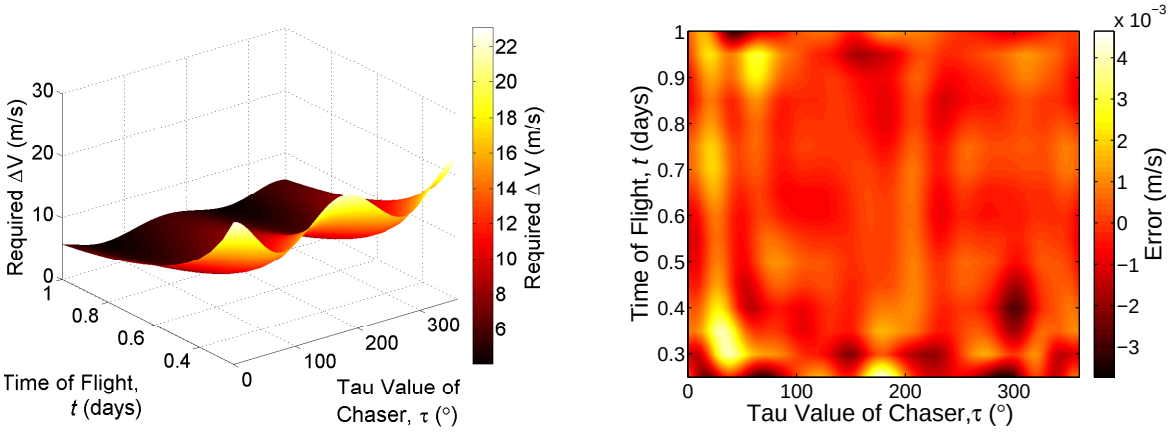


(a) Predicted $\Delta V$ (b) Model errors

Figure 5.17: Model results of a 9$^{\text{th}}$ order Fourier polynomial expansion generated using 500 Monte Carlo realizations of a uniform distribution in $\tau$ and a Chebyshev distribution in $t$ and $\Delta\tau$ for rendezvous in a DRO at $\Delta\tau = 0.15°$.

#### 5.1.2.3 Optimization

Figure 5.20 shows the optimal design solutions to minimize the required $\Delta V$ for rendezvous in the DRO. Again, two different local optima exist. Assuming good *a priori* knowledge on both the

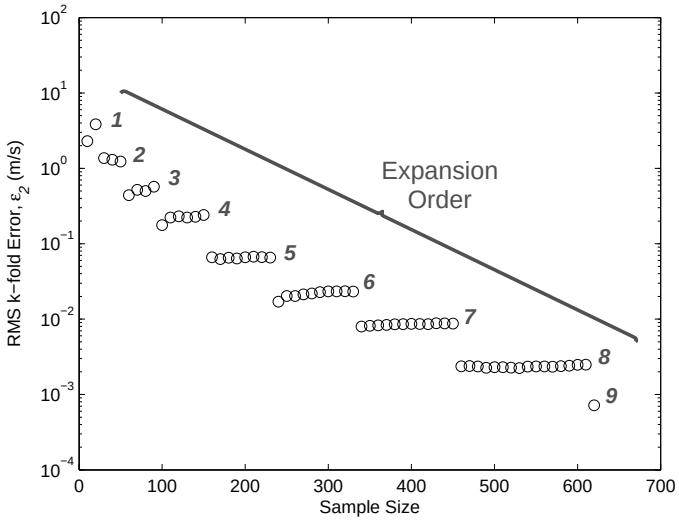


Figure 5.18: $k$-fold RMS errors with $k = 10$ for a Fourier polynomial expansion generated using Monte Carlo realizations of a uniform distribution in $\tau$ and a Chebyshev distribution in $t$ and $\Delta\tau$ for rendezvous in a DRO.

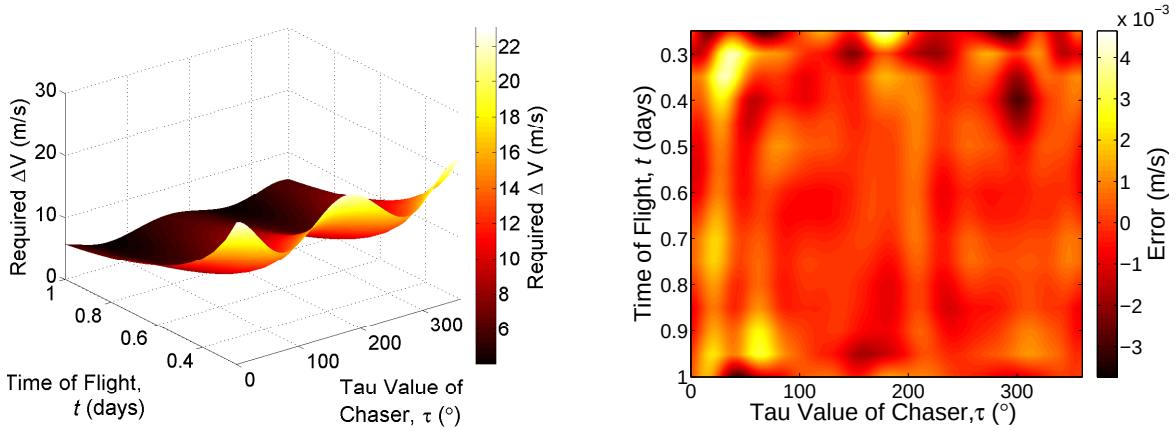


(a) Predicted $\Delta V$

(b) Model errors

Figure 5.19: Model results after $k$-fold convergence with $k = 10$ for a Fourier polynomial expansion generated using Monte Carlo realizations of a uniform distribution in $\tau$ and a Chebyshev distribution in $t$ and $\Delta\tau$ for rendezvous in a DRO at $\Delta\tau = 0.15°$.

Table 5.2: Total sensitivity indices for the $\Delta V$ required for rendezvous in a DRO as a function of the three-dimensional design parameters.

| | $\tau$ | $t$ | $\Delta\tau$ |
|---|---|---|---|
| Sensitivity Index, $S_i^T$ | 0.041 | 0.404 | 0.617 |

number and general location of local minima, the identification of both optima using a high fidelity differential corrector with the *fmincon* optimizer requires on the order of hundreds of function calls, although the actual number of calls varies significantly with the initial guess. Thus the surrogate model, which provides much more information across the full design space than simply the isolated location of the minimum $\Delta V$, can be built and verified for approximately the same computational cost as the optimization of the $\Delta V$ using the full-fidelity solutions with *a priori* knowledge on the structure of the system response.

Conversely, in cases with an unknown solution structure, identification of all local minima would require many more function calls to the full-fidelity models, increasing the cost of global optimization. Instead, the low computational cost associated with a polynomial cost function can facilitate the identification of the global minimum by conducting a survey of many initial guesses to identify all local minima. Additionally, once the model is generated, it can be re-used for optimization under changing constraints throughout the mission design process, providing further cost savings. Finally, having identified the minimum total $\Delta V$ using surrogate-based optimization, the $x$-, $y$-, and $z$-components for each of the two burns can be extracted from the model, and these solutions can be used as the initial guess for high-fidelity optimization tools, such as the robust optimization methods presented in the next section.

## 5.2 Robust Maneuver Design

Having shown that the regression models can be successfully used for maneuver design in spacecraft rendezvous, they are now modified to incorporate system stochastics as a means of

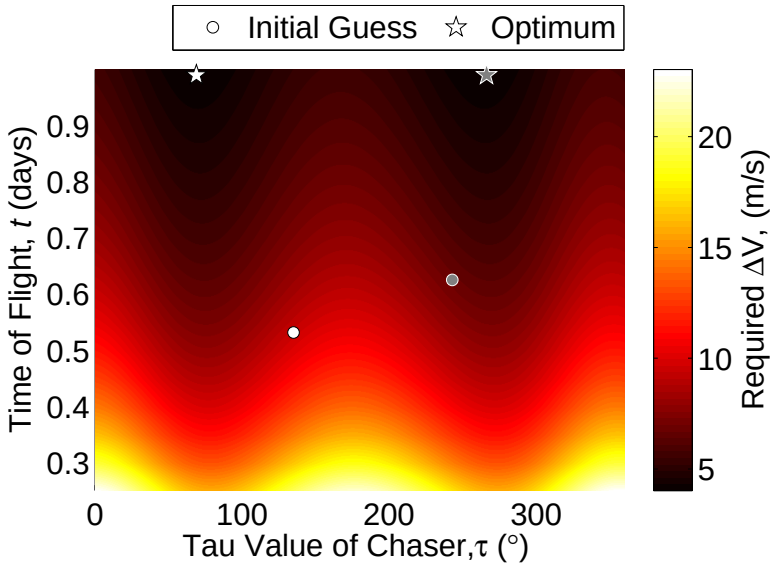


Figure 5.20: Optimized input parameters for minimum $\Delta V$ rendezvous in a DRO. The optimal solutions are both located at $\Delta\tau = 0.01°$.

enabling optimization under uncertainty and robust design. This section presents the results of the robust models as applied to both the halo orbit and the DRO.

### 5.2.1 Robust Rendezvous Design in a Halo Orbit

Models are first built for the required $\Delta V$ and resulting final state deviation $\delta \boldsymbol{X} f$ for the halo orbit test case described in Table 2.2. The analysis presented here includes a comparison of dense models generated using the traditional least-squares solution method and sparse models generated via orthogonal matching pursuit (OMP). The models are then used to perform optimization on the design problem and to compute the variance in $\delta \boldsymbol{X}_f$ of the chaser spacecraft at the point of rendezvous.

#### 5.2.1.1 Dense Model

The dense model is generated using the $k$-fold cross-validation technique and incorporating only the design parameters and maneuver execution errors; due to the relative magnitudes of the

QOI, the model errors are weighted as

$$\boldsymbol{\delta}^{(i)} = \left[\delta\Delta V^{(i)} \;\; 10 \times \delta\boldsymbol{R}_f^{(i)} \;\; 100 \times \delta\boldsymbol{V}_f^{(i)}\right]^T,$$

where $\boldsymbol{\delta}^{(i)}$ denotes the difference between the model prediction and the true value for validation sample $[\boldsymbol{s}^{(i)} \;\; \boldsymbol{\xi}^{(i)}]^T$. With a convergence requirement of $1 \times 10^{-3}$, this equates to an accuracy of 1 mm/s in $\Delta V$, 0.1 mm in final position, 0.01 mm/s in final velocity.

For this case, the $k$-fold algorithm converges on a $5^{\text{th}}$ order expansion generated with 1290 training samples, resulting in an RMS error of $2.85 \times 10^{-4}$. Figure 5.21 shows the evolution of the RMS errors as a function of the sample size and expansion order. From this plot, it can be seen that the model converges relatively quickly as the expansion order is increased. However, the dimensionality of the problem results in a fairly large sample size, particularly in relation to the number of samples needed for a $5^{\text{th}}$ order expansion in the 3-dimensional deterministic design problem considered in the previous section.

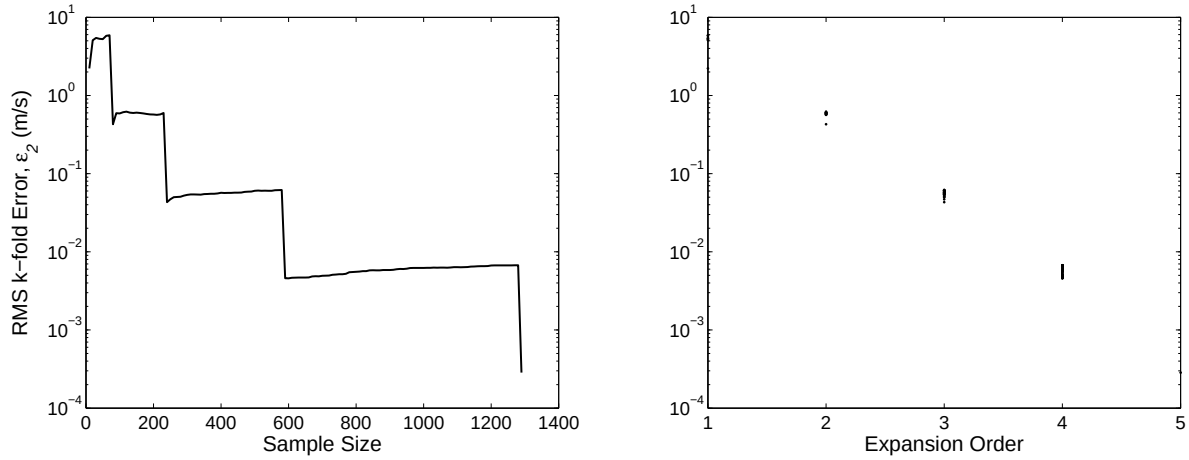


Figure 5.21: Weighted $k$-fold RMS error as a function of sample size and expansion order for a dense model of rendezvous in a halo orbit.

Figures 5.22 and 5.23 contain the coefficients corresponding to the $5^{\text{th}}$ order expansion for the required $\Delta V = |\Delta\boldsymbol{V}|$ and the final state deviation $\delta\boldsymbol{X}_f$, respectively. The coefficients have been normalized with respect to the first coefficient $c_0$ for each output dimension. These coefficients again

indicate good convergence of the model, dropping by about 7 orders of magnitude for $\Delta V$ and 4-5 orders of magnitude for $\delta \boldsymbol{X}_f$. Additionally, it is evident from the coefficients that rendezvous in the halo orbit over the design space considered here yields a sparse expansion very well-suited for the use of compressive sampling techniques. The boxed-in coefficients in Fig. 5.22 represent those terms with the largest effect on the $\Delta V$ that would therefore likely be recovered by compressive sampling. This same sparsity is seen for $\delta \boldsymbol{X}_f$.

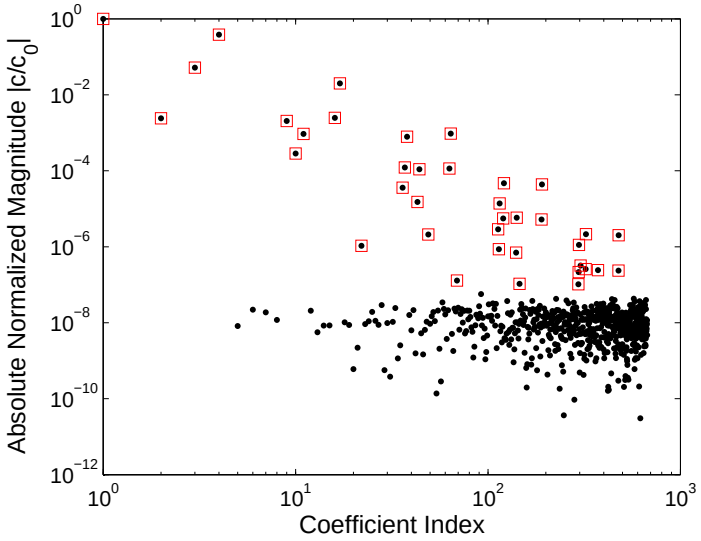


Figure 5.22: Normalized expansion coefficients for a dense 6-dimensional, $5^{\text{th}}$ order model of the required $\Delta V$ as a function of the design parameters $\tau$, $t$, and $\Delta\tau$ for rendezvous in a halo orbit. Boxed-in points represent those terms that would likely be recovered with compressive sampling.

#### 5.2.1.2 Sparse Model

Another model is built for this test case using OMP to leverage the sparsity of the problem. This procedure does not follow the $k$-fold algorithm; instead, a user-defined sample size is used to generate the $5^{\text{th}}$ order expansion identified from the dense model, and the result is validated using an additional 1500 randomly generated validation samples. The implementation of $k$-fold cross-validation with OMP is reserved for future work.

The sparse model was found to obtain 3-4 digits of accuracy using only 200 samples, about

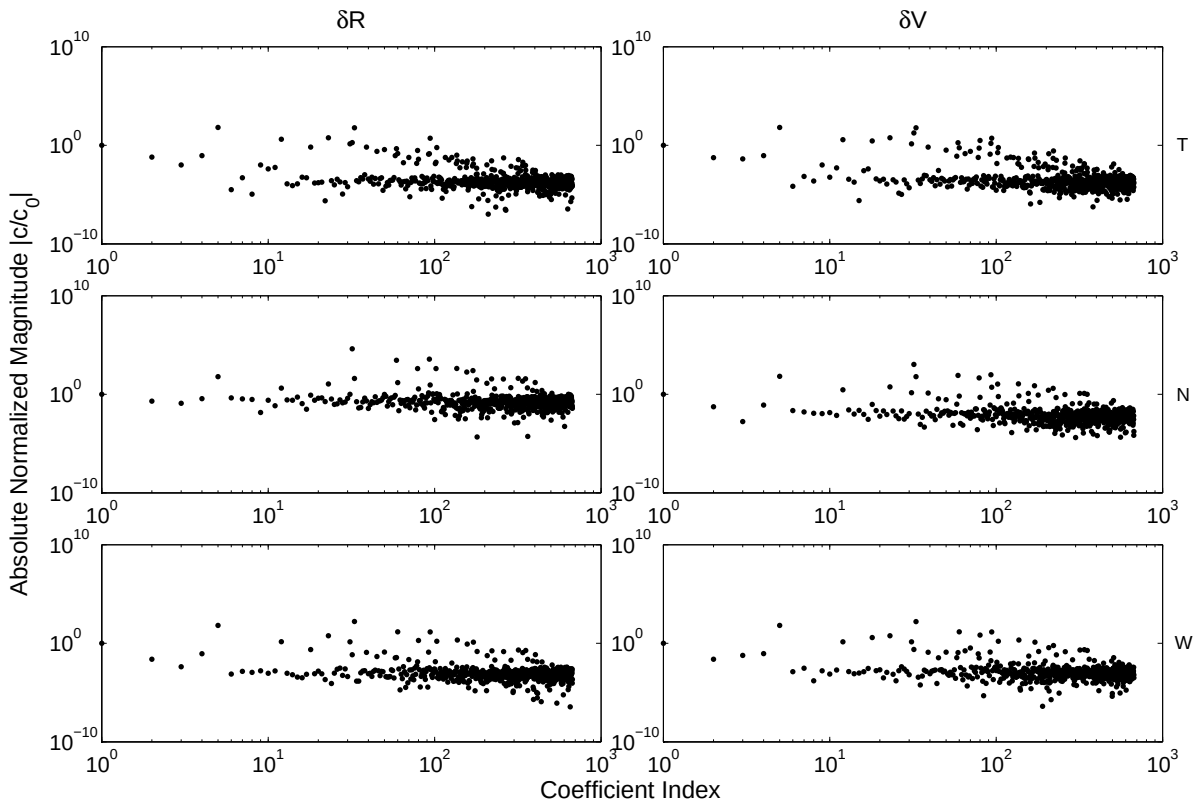


Figure 5.23: Normalized expansion coefficients for a dense 6-dimensional, $5^{\text{th}}$ order model of the final state deviations $\delta \boldsymbol{X}_f$ as a function of design parameters and maneuver execution errors for rendezvous in a halo orbit.

15% of the sample size required for the dense model. The expansion coefficients for the sparse model are provided in Figs. 5.24 and 5.25. A comparison of these to Figs. 5.22 and 5.23 shows good agreement in the computed coefficients, with the sparse coefficients consistent with their respective dense coefficients to at least $10^{-5}$. The number of recovered terms in the expansion ranged from 35-145, depending on the output dimension, as opposed to 672 expansion terms for each output in the dense model.

#### 5.2.1.3 Optimization Under Uncertainty

Once generated, the surrogate can be used to optimize the rendezvous problem over the design space to find the minimum $\Delta V$ meeting given constraints on the variance of the final state

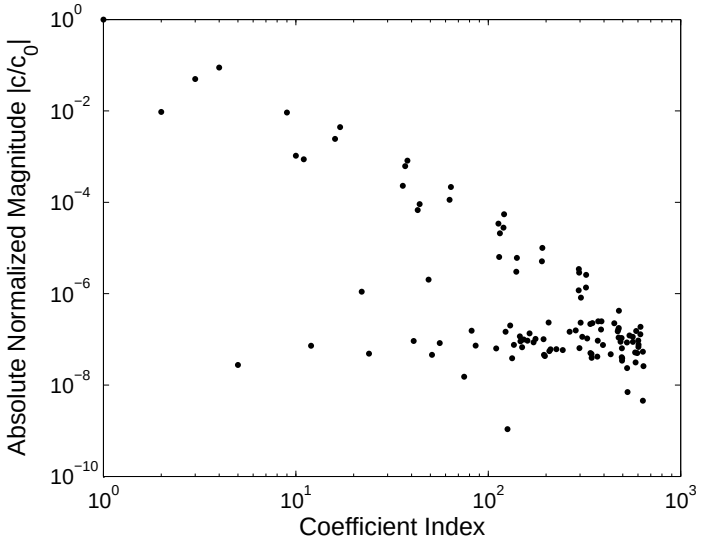


Figure 5.24: Normalized expansion coefficients for a sparse 6-dimensional, $5^{\text{th}}$ order model of the required $\Delta V$ as a function of the design parameters $\tau$, $t$, and $\Delta\tau$ for rendezvous in a halo orbit.

deviation. Here, the cost function of Equation 3.34 is minimized using the interior point algorithm, with a maximum position variance of 100 m in each of the $T$-, $N$-, and $W$-directions. The optimized solutions identified from the dense and sparse models are listed in Table 5.3, which shows that the relative accuracy of the sparse model to the dense model results in the identification of the same optimal design point by each.

Table 5.3: Optimum design point identified using the surrogate models for rendezvous in a halo orbit with a constraint on each direction of the position variance of 100 $\text{m}^2$.

| | $\Delta V$ (m/s) | $\tau$ (°) | $t$ (days) | $\Delta\tau$ (°) |
|---|---|---|---|---|
| Dense Model | 1.10 | 75.11 | 0.60 | 0.11 |
| Sparse Model | 1.10 | 75.10 | 0.60 | 0.11 |

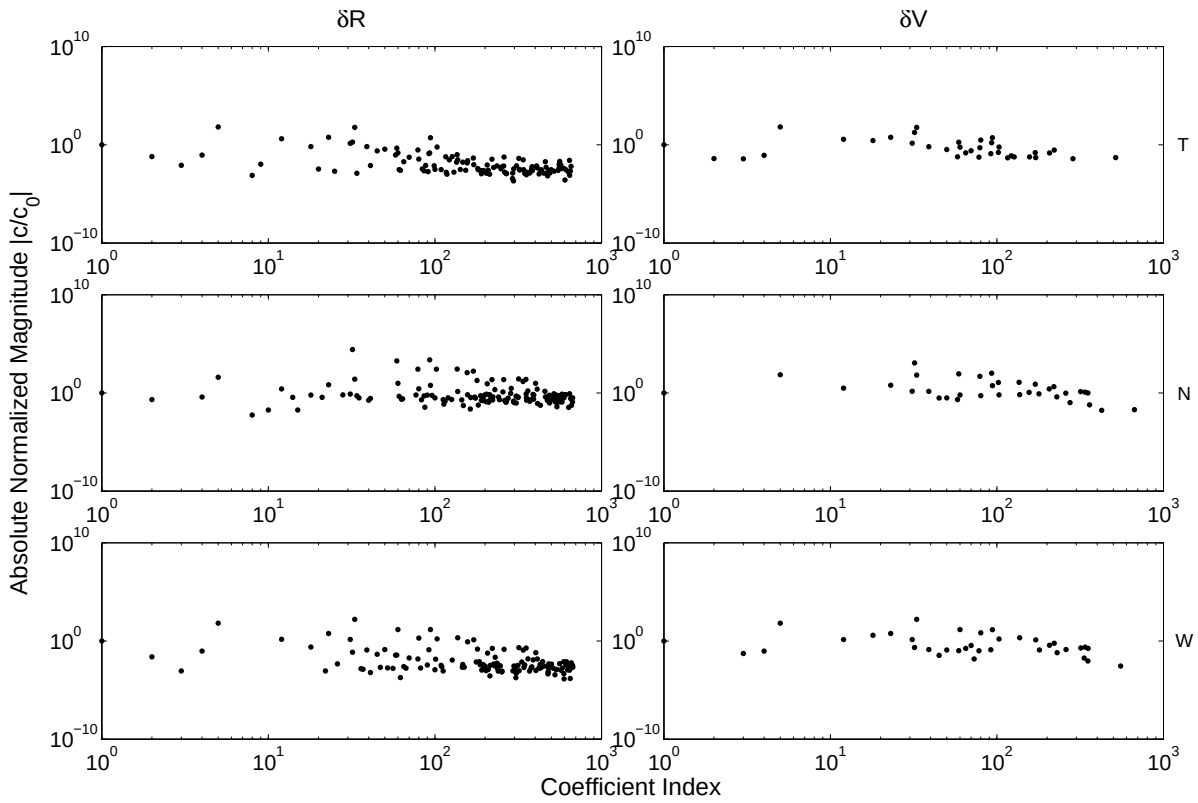


Figure 5.25: Normalized expansion coefficients for a sparse 6-dimensional, $5^{\text{th}}$ order model of the final state deviations $\delta \boldsymbol{X}_f$ as a function of design parameters and maneuver execution errors for rendezvous in a halo orbit.

From the sparse model, the optimizer converged on a solution of $\Delta V = 1.10$ m/s at the design point $\tau = 75.10°$, $t = 0.60$ days, and $\Delta\tau = 0.11°$. The variance at this point as computed via the analytic formula of Equation 3.38, from both the dense and sparse models, is compared to that resulting from a Monte Carlo sampling of the full dynamical model in Table 5.4, where it can be seen that the analytic computations achieve $\text{m}^2$-level accuracy in the position variance and $< 1$ $\text{mm}^2/\text{s}^2$-level accuracy in the velocity variance. However, the Monte Carlo simulation requires more than $10^5$ samples to converge to the same level of accuracy in position variance achieved by the analytic computation; a plot of the convergence in variance for the Monte Carlo can be found in Fig. 5.26. Additionally, to perform constrained optimization on the system, the Monte Carlo simulation would have to be repeated at every candidate design point. Taking into consideration

the 45 function calls made by the optimizer, robust optimization using traditional Monte Carlo methods with the full dynamical model quickly becomes very computationally expensive. The analytic approach, on the other hand, requires only the initial 200 points used to generate the model, independent of the number of function calls in the optimization process.

Table 5.4: Comparison of the final state variance at the constrained optimal solution for rendezvous in a halo orbit, as computed via both Monte Carlo sampling and the analytical functions enabled by polynomial surrogates.

| | Variance | | | | | |
|---|---|---|---|---|---|---|
| | $R_T$ (m) | $R_N$ (m) | $R_W$ (m) | $V_T$ ($mm^2/s^2$) | $V_N$ ($mm^2/s^2$) | $V_W$ ($mm^2/s^2$) |
| Monte Carlo | 91.01 | 93.56 | 89.92 | 36.43 | 34.91 | 32.23 |
| Analytic (dense) | 90.79 | 93.67 | 90.13 | 36.35 | 34.96 | 32.31 |
| Analytic (sparse) | 90.92 | 93.72 | 90.21 | 36.59 | 35.01 | 32.45 |

The plots in Fig. 5.27 show the change in the final position variance of the chaser as a function of each of the design parameters for the rendezvous problem. In each case, two of the design inputs are held constant at their optimized values, while the remaining dimension is varied across the design space. The figure highlights the importance of adequate knowledge regarding the effects of system parameters on the propagated uncertainties. For both the initial position and the initial separation, the variance grows by approximately 75% across the input range. Using this information on the behavior of the variance, the acceptable range for each of the mission parameters can be limited such that any requirements on targeting precision at the point of rendezvous can be met.

In the optimization of this particular rendezvous problem, the optimal design in terms of minimizing $\Delta V$ nearly coincides with the design solution that results in the smallest final state variance, such that the difference between position variance for the constrained and unconstrained optima is a matter of only a few $m^2$. However, the effect of optimization constraints on the propagated variance can be more significant when considering weighted cost functions. If it is of

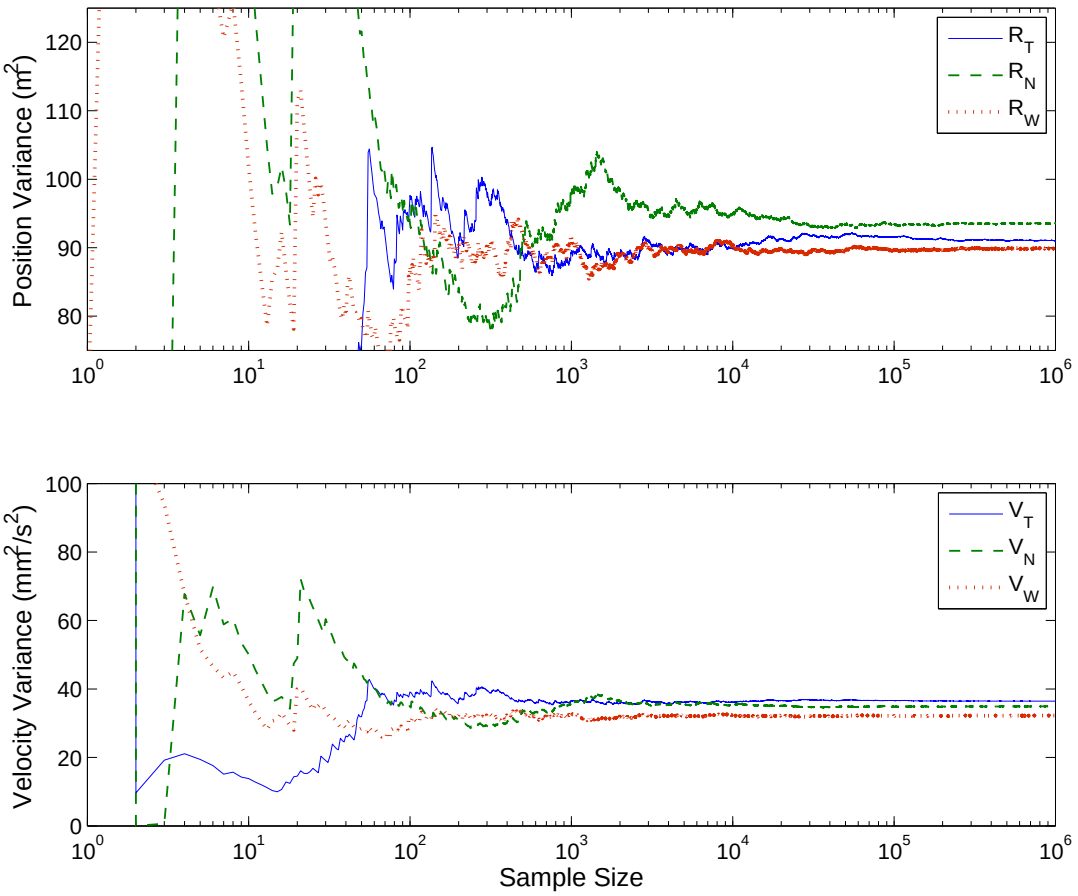


Figure 5.26: Convergence of the position and velocity variance for the optimized rendezvous maneuver in a halo orbit using Monte Carlo sampling of the full system dynamics.

interest, for example, to maintain a larger separation between the vehicles at the point of orbit insertion by the chaser, the cost function can be taken as a weighted sum of the required $\Delta V$ and the initial separation, such as

$$\min_{\boldsymbol{s}} J(\boldsymbol{s}, \boldsymbol{\xi}) = |\Delta \boldsymbol{V}(\boldsymbol{s})| - s_3$$

$$\text{s.t.} \quad \boldsymbol{\sigma}^2(\delta \boldsymbol{X}_f) \leq \boldsymbol{\sigma}^2_{max}$$

$$\boldsymbol{s}_l \leq \boldsymbol{s} \leq \boldsymbol{s}_u.$$

where $s_3 \in [-1, 1]$ is used so that both terms in the cost function are of approximately the same order

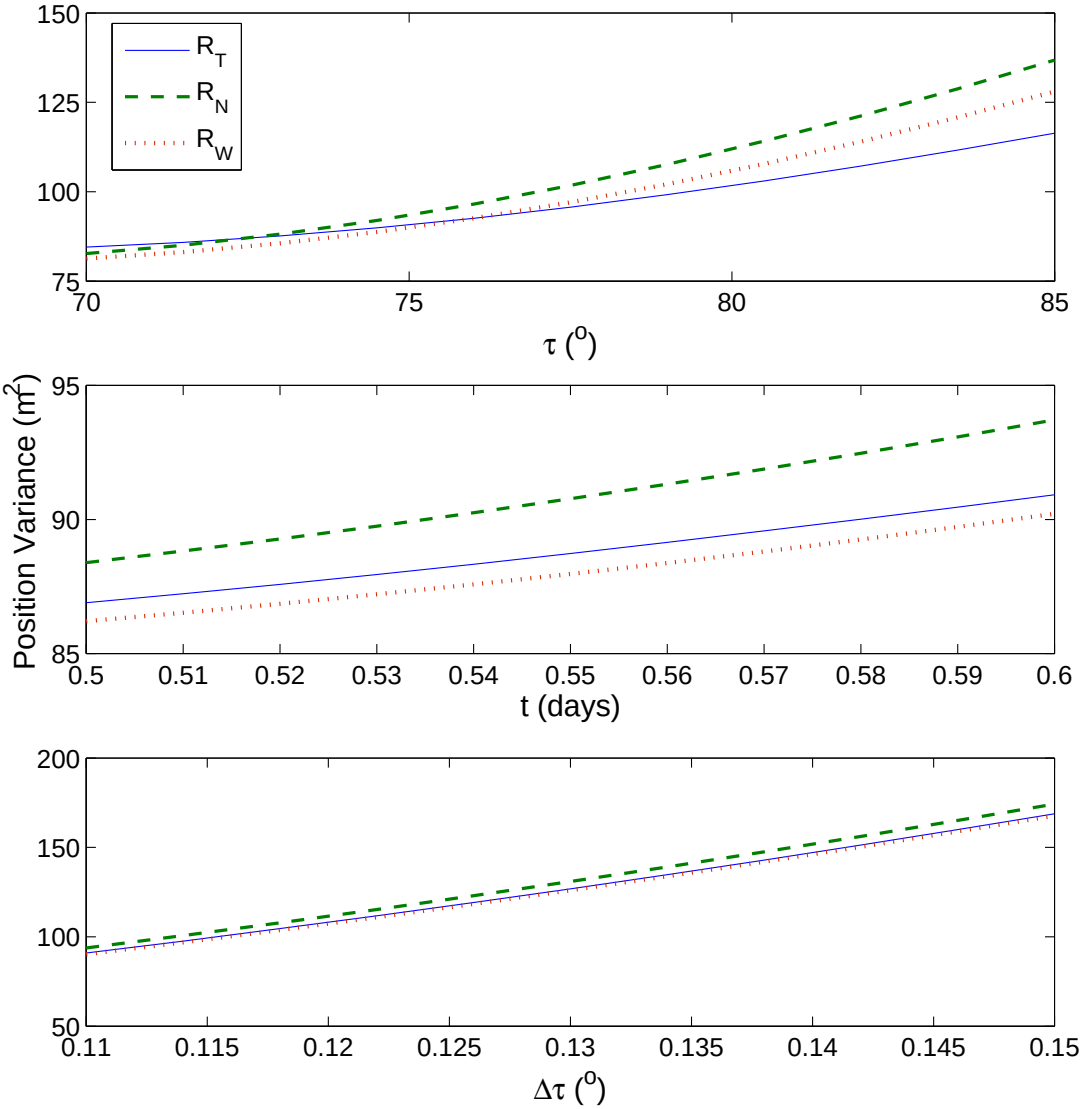


Figure 5.27: Final position variance as a function of the design paramters about the optimal design solution for rendezvous in a halo orbit.

of magnitude. In this case, unconstrained optimization pushes the solution to the largest possible separation angle, and the resulting position variance is $\sim$ 170 m$^2$ in each direction. Therefore, setting a constraint on the position variance of $<$ 170 m$^2$ will drive the optimal solution to a new design point. Table 5.5 compares the optimal design with a variance constraint of 100 m$^2$ in

Table 5.5: Constrained and unconstrained solutions to the weighted optimization problem for rendezvous in a halo orbit.

| | $\Delta V$ (m/s) | $\tau$ (°) | $t$ (days) | $\Delta\tau$ (°) | $\sigma^2_{R_T}$ (m$^2$) | $\sigma^2_{R_N}$ (m$^2$) | $\sigma^2_{R_W}$ (m$^2$) |
|---|---|---|---|---|---|---|---|
| Unconstrained | 1.55 | 75.03 | 0.60 | 0.150 | 168.6 | 173.8 | 167.4 |
| Constrained in $R$ | 1.23 | 70.00 | 0.60 | 0.120 | 100.0 | 97.8 | 96.1 |

position to that resulting from the unconstrained weighted optimization problem. While the time of flight remains the same for both solutions, the optimal design points for the initial position and separation of the spacecraft are different for each of the optimization problems, leading to different values for the required $\Delta V$ and the propagated position variance.

#### 5.2.1.4 ANOVA

Table 5.6 contains the total Sobol' indices for the rendezvous model, which provide insight regarding the importance of each of the deterministic and stochastic system parameters to the model outputs. It should be reiterated that these indices provide a relative, rather than absolute, contribution for each of the system inputs. Several things can be noticed from Table 5.6. First, the values of the indices representing the dependence of $\Delta V$ on the maneuver execution errors are in the noise of the surrogate's accuracy and are therefore effectively zero. This reflects that the $\Delta V$ is effectively a function only of the design inputs, as expected from the original problem definition. The vehicle separation has the largest influence on the $\Delta V$, although the time of flight also has relatively strong effect. On the other hand, the maneuver execution errors represent the most significant influence on the final state statistics. Further examination of the indices corresponding to $\delta \boldsymbol{X}_f$ reveals that the burn magnitude and the combined effect of the burn angles are almost equally important in determining the in-track component of both the position and velocity deviation, while deviations in the $R$- and $W$-components are caused primarily by errors in the burn angles. This is

consistent with expectations as, for example, out-of-plane deviations cannot result from an in-plane maneuver simply from errors in the burn magnitude; rather, errors must be present in the direction of the burn in order for magnitude errors to produce out-of-plane effects.

Table 5.6: Total Sobol' indices for the 6-dimensional halo problem.

| | Output | | | | | | |
|---|---|---|---|---|---|---|---|
| Parameter | $\Delta V$ | $\delta R_T$ | $\delta R_N$ | $\delta R_W$ | $\delta V_T$ | $\delta V_N$ | $\delta V_W$ |
| $\tau(s_1)$ | 0.0169 | 2.23e-3 | 2.46e-3 | 3.62e-3 | 1.92-3 | 2.85-3 | 3.62e-3 |
| $t(s_2)$ | 0.237 | 6.79e-5 | 5.92e-5 | 7.53e-5 | 1.51e-3 | 8.74e-4 | 1.23e-3 |
| $\Delta\tau(s_3)$ | 0.748 | 6.07e-3 | 3.92e-3 | 4.47e-3 | 6.00e-3 | 3.93e-3 | 4.47e-3 |
| $\delta\Delta V(\xi_1)$ | 2.40e-11 | 0.551 | 5.22e-5 | 0.142 | 0.529 | 3.67e-3 | 0.143 |
| $\theta(\xi_2)$ | 2.26e-11 | 0.225 | 0.500 | 0.429 | 0.236 | 0.498 | 0.429 |
| $\phi(\xi_3)$ | 3.00e-11 | 0.225 | 0.500 | 0.429 | 0.236 | 0.498 | 0.428 |

#### 5.2.1.5 Initial State Uncertainties

The final model generated for rendezvous in the halo orbit incorporates initial state uncertainties defined in Table 2.2 in addition to the maneuver execution errors. With 12 dimensions and a $5^{\text{th}}$ order expansion, the dense model for this problem would require 8008 expansion terms, necessitating a very large number of training samples and presenting computational issues when attempting to solve for the coefficients. As a result, this is a case in which the use of compressive sampling is essential to the ability to produce a surrogate for the system.

With the use of compressive sampling, a model is generated that results in an RMS error of $1.5 \times 10^{-3}$ using only 450 samples and recovering between 175 to 250 terms for each output. The coefficients corresponding to these terms can be found in Figs. 5.28 and 5.29. Because the $\Delta V$ is a function only of the design parameters and is therefore independent of the number of stochastic parameters included in the model, the coefficients in Fig. 5.28 match those seen for

the 6-dimensional problem in Fig. 5.24. Figure 5.29, on the other hand, shows that many more terms are needed to capture the effects of the 12-dimensional problem on the final state deviations, particularly in the velocity components.

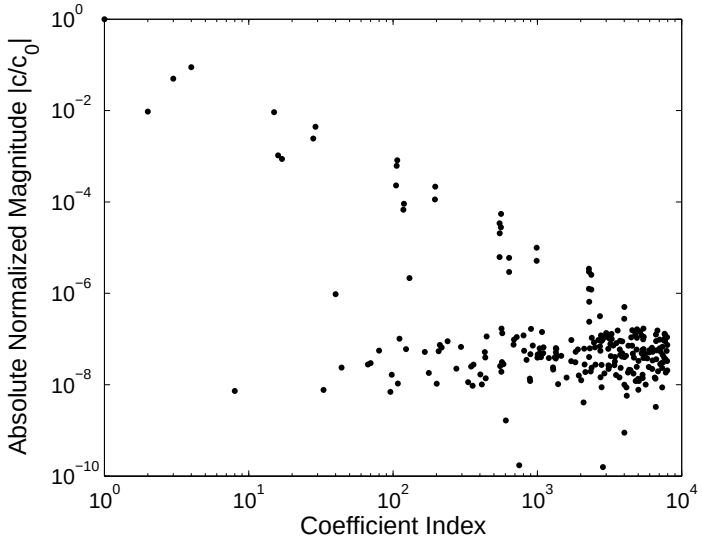


Figure 5.28: Normalized expansion coefficients for a sparse 12-dimensional, $5^{\text{th}}$ order model of the required $\Delta V$ as a function of the design parameters $\tau$, $t$, and $\Delta\tau$ for rendezvous in a halo orbit.

As expected, increasing the number of stochastic input parameters causes a corresponding increase in the variance of the propagated state of the chaser. Table 5.7 compares the variance resulting from the combined effects of the maneuver execution errors and the initial state uncertainties to that caused by the burn errors alone. The table shows a growth of about 10 $\text{m}^2$ in each of the position variances, but the growth in the velocity variance is much smaller, being on the order of only $10^{-1}$ $\text{mm}^2/\text{s}^2$.

Although the variance changes at a given optimal solution with the inclusion of the initial state uncertainties, the optimal design that minimizes $\Delta V$ does not change. The optimum is constant regardless of the stochastic inputs under consideration, as non-deterministic parameters have no effect on the nominal $\Delta V$. Rather, the additional stochastic dimensions impact only constrained optimization problems, for which the constraints may no longer be achievable, and, potentially,

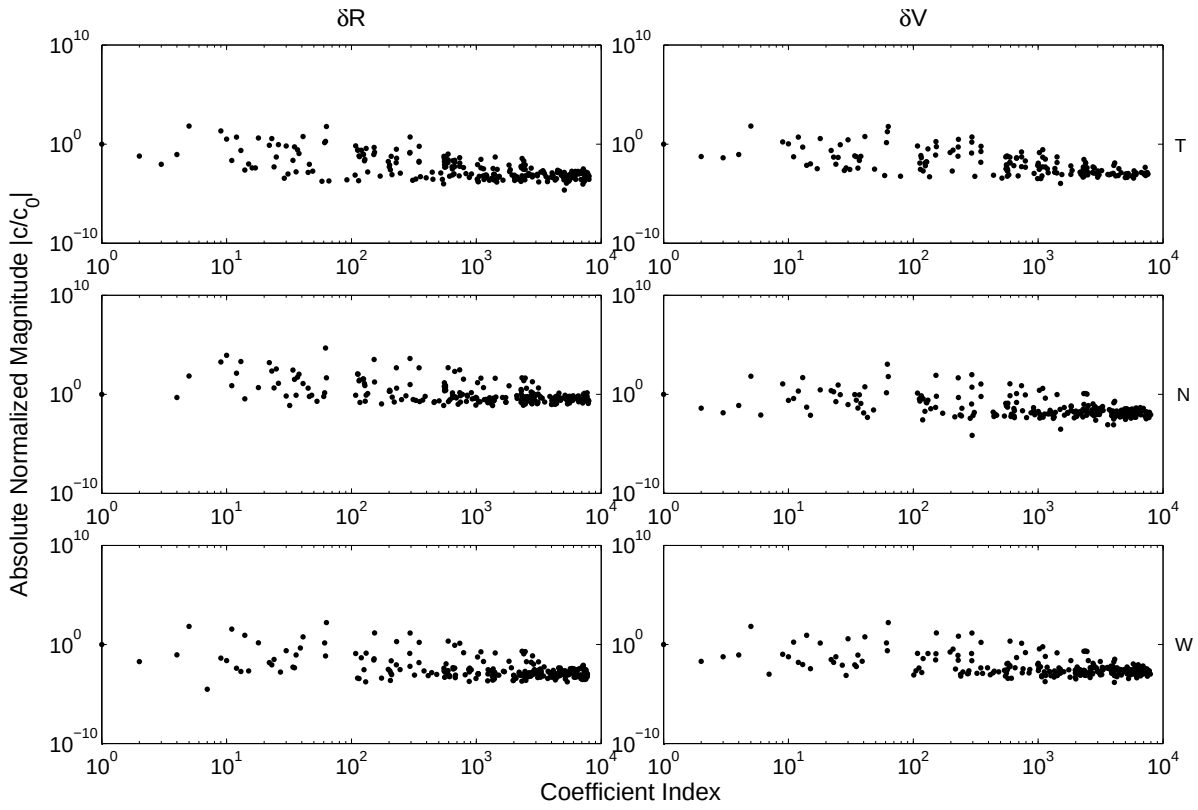


Figure 5.29: Normalized expansion coefficients for a sparse 12-dimensional, $5^{\text{th}}$ order model of the final state deviations $\delta \boldsymbol{X}_f$ as a function of design parameters, maneuver execution errors, and initial state uncertainties for rendezvous in a halo orbit.

Table 5.7: Comparison of the final state variance caused by maneuver execution errors only to the variance resulting from maneuver execution errors and initial state uncertainties for rendezvous in a halo orbit.

| | Variance | | | | | |
|---|---|---|---|---|---|---|
| | $R_T$ ($m^2$) | $R_N$ ($m^2$) | $R_W$ ($m^2$) | $V_T$ ($mm^2/s^2$) | $V_N$ ($mm^2/s^2$) | $V_W$ ($mm^2/s^2$) |
| Meneuver Only | 90.92 | 93.72 | 90.21 | 36.59 | 35.01 | 32.45 |
| Maneuver + State | 102.38 | 104.48 | 100.26 | 36.67 | 35.19 | 32.56 |

weighted optimization problems.

Table 5.8 contains the Sobol' indices for the 12-dimensional rendezvous problem. In particular, the indices show that the effect of the initial state uncertainties is very small compared to that of the maneuver execution errors, which still drive the final state deviations. The only noticeable contribution made by the initial state uncertainties is in the influence of the initial position variance on the final position variance. This reflects the relative consistency in the velocity variance despite the incorporation of the initial state uncertainties that was evident in Table 5.7. The values of the Sobol' indices in Table 5.8 hold true only for the level of uncertainty considered in this study, though, and any change in the relative knowledge on the performance of the spacecraft thruster or on the accuracy of the initial state estimate for the chaser would cause their relative influence on the QOI to change as well.

### 5.2.2 Robust Rendezvous Design in a DRO

Finally, the robust design methods are used to optimize maneuvers for rendezvous in the distant retrograde orbit about the Moon. The results presented below provide not only an analysis of the models themselves and of the system dynamics in the DRO, but also a comparison of the models and system dynamics to their counterparts for the halo orbit.

#### 5.2.2.1 Dense Model

For rendezvous in the DRO, the $k$-fold algorithm once again converges on a $5^{\text{th}}$ order dense model with 672 expansion terms and requiring 1290 training samples. This reflects the similarity in the system order of the halo orbit and the DRO that was previously seen in the broader design space when generating the deterministic design surrogates. The relative accuracy of the two models is also consistent with the design models; the accuracy of the stochastic surrogate for the DRO is an order of magnitude better than that of the halo, with an RMS error of $7.02 \times 10^{-5}$. The convergence of the RMS error for the dense model of the DRO is shown in Fig. 5.30.

The expansion coefficients of the model for $\Delta V$ and $\delta \boldsymbol{X}_f$ are provided in Figs. 5.31 and 5.32,

Table 5.8: Total Sobol' indices for a sparse model incorporating maneuver execution errors and initial state uncertainties for rendezvous in a halo orbit.

| | Output | | | | | | |
|---|---|---|---|---|---|---|---|
| Parameter | $\Delta V$ | $\delta R_T$ | $\delta R_N$ | $\delta R_W$ | $\delta V_T$ | $\delta V_N$ | $\delta V_W$ |
| $\tau(s_1)$ | 0.0169 | 3.89e-3 | 3.51e-3 | 3.47e-3 | 2.01e-3 | 2.92e-3 | 3.61e-3 |
| $t(s_2)$ | 0.237 | 1.10e-4 | 9.88e-5 | 7.83e-5 | 1.52e-3 | 8.73e-4 | 1.23e-3 |
| $\Delta\tau(s_3)$ | 0.748 | 5.71e-3 | 3.78e-3 | 4.30e-3 | 5.97e-3 | 3.93e-3 | 4.47e-3 |
| $\delta\Delta V(\xi_1)$ | 1.09e-11 | 0.517 | 5.04e-5 | 0.136 | 0.527 | 3.66e-3 | 0.143 |
| $\theta(\xi_2)$ | 1.02e-11 | 0.211 | 0.482 | 0.412 | 0.235 | 0.497 | 0.427 |
| $\phi(\xi_3)$ | 3.49e-11 | 0.211 | 0.482 | 0.412 | 0.235 | 0.497 | 0.427 |
| $\sigma^2_{0,R_T}(\xi_4)$ | 1.41e-11 | 0.0554 | 2.54e-3 | 6.75e-8 | 3.38e-4 | 1.12e-4 | 3.75e-7 |
| $\sigma^2_{0,R_N}(\xi_5)$ | 1.31e-11 | 2.89e-3 | 0.0320 | 2.32e-8 | 1.41e-4 | 2.80e-6 | 1.22e-7 |
| $\sigma^2_{0,R_W}(\xi_6)$ | 1.13e-11 | 6.31e-8 | 3.49e-8 | 0.0384 | 3.57e-7 | 1.58e-7 | 9.45e-5 |
| $\sigma^2_{0,V_T}(\xi_7)$ | 1.47e-11 | 3.05e-3 | 6.75e-5 | 4.51e-9 | 3.14e-3 | 6.62e-5 | 1.72e-8 |
| $\sigma^2_{0,V_N}(\xi_8)$ | 1.12e-11 | 1.00e-4 | 1.86e-3 | 3.97e-9 | 1.22e-4 | 1.91e-3 | 9.52e-9 |
| $\sigma^2_{0,V_W}(\xi_9)$ | 1.13e-11 | 3.04e-9 | 4.61e-9 | 2.24e-3 | 8.25e-9 | 7.57e-9 | 2.31e-3 |

which show that the $\Delta V$ coefficients decrease by 8 orders of magnitude while the $\delta \boldsymbol{X}_f$ coefficients see a reduction of about 4-6 orders of magnitude. The figures also reveal the sparsity in the solution for rendezvous the DRO. Further, the coefficients for the $N$- and $W$-components of the position variance, as well as the $W$-component of the velocity variance, exhibit an interesting structure in that all of the largest coefficients correspond to higher expansion terms, while the low order coefficients are very small. This type of behavior is indicative of a case in which compressive sampling techniques will succeed in generating an accurate model where many traditional sampling techniques would likely fail.

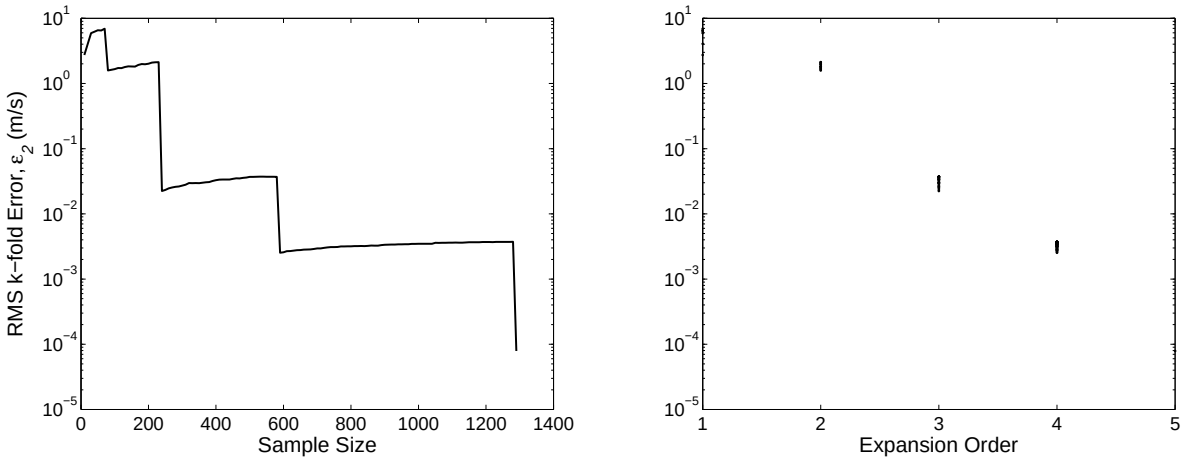


Figure 5.30: Weighted $k$-fold RMS error as a function of sample size and expansion order for a dense model of rendezvous in a DRO.

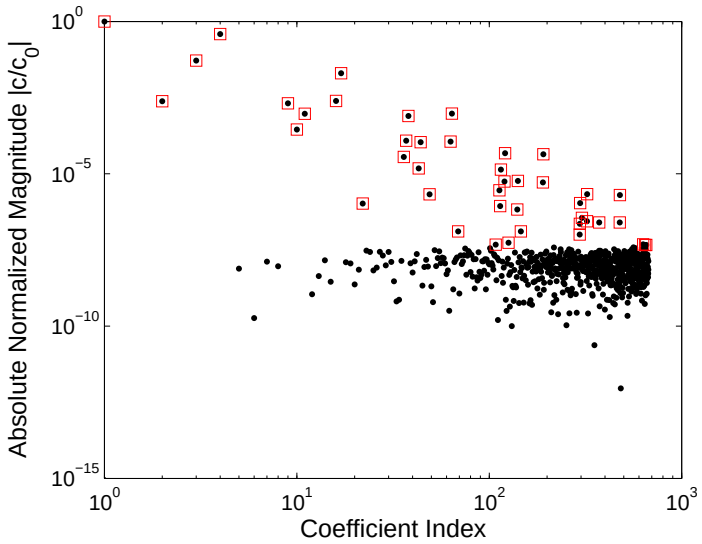


Figure 5.31: Normalized expansion coefficients for a dense 6-dimensional, $5^{\text{th}}$ order model of the required $\Delta V$ as a function of the design parameters $\tau$, $t$, and $\Delta\tau$ for rendezvous in a DRO. Boxed-in points represent those terms that would likely be recovered with compressive sampling.

#### 5.2.2.2 Sparse Model

Employing the compressive sampling techniques to a $5^{\text{th}}$ order model of rendezvous in the DRO produces an RMS error of $5.06 \times 10^{-4}$ from 250 training samples, less than 20% of the

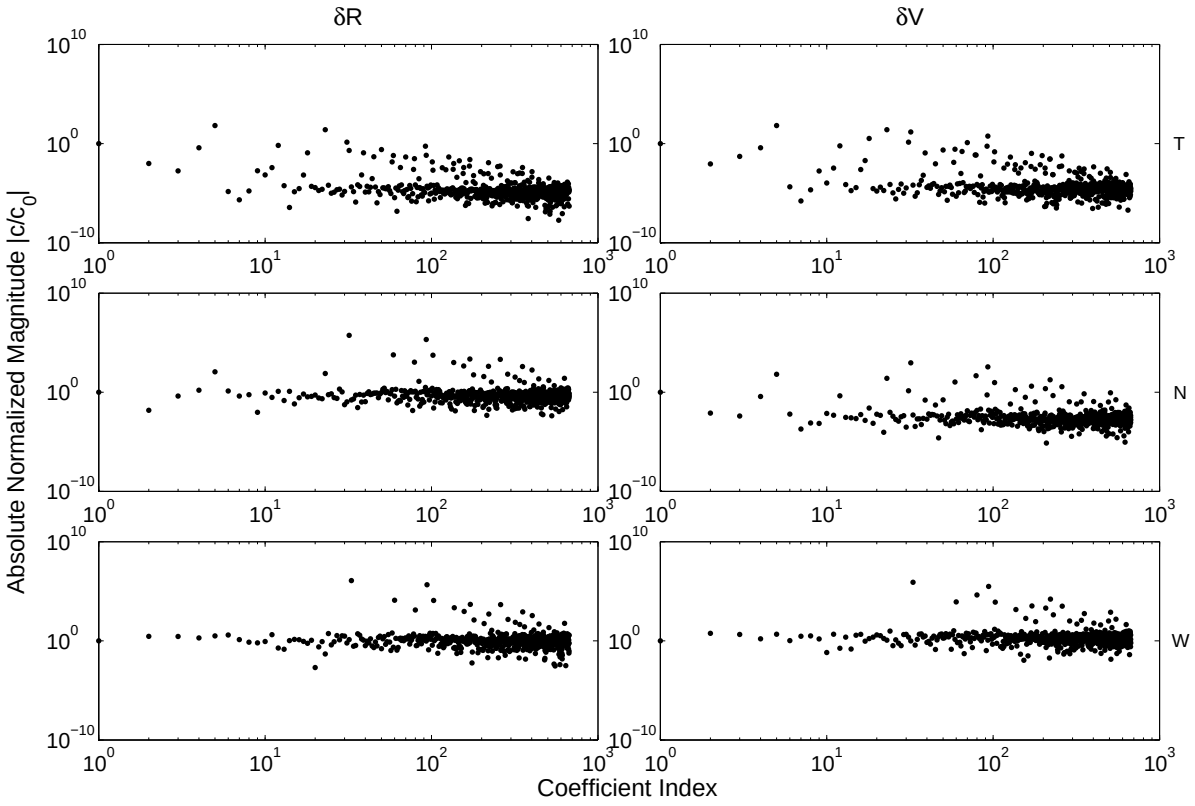


Figure 5.32: Normalized expansion coefficients for a dense 6-dimensional, $5^{\text{th}}$ order model of the final state deviations $\delta \boldsymbol{X}_f$ as a function of design parameters and maneuver execution errors for rendezvous in a DRO.

number of samples used for the dense surrogate. The models for each output are comprised of 25-190 expansion terms, coefficients for which are included in Figs. 5.33 and 5.34. These coefficients show good agreement with the corresponding coefficients in the dense model. As in the halo orbit (see Fig. 5.25), fewer expansion terms are recovered for the models representing the response of the final velocity deviations in the DRO than are recovered for the position deviations and the $\Delta V$.

#### 5.2.2.3 Optimization Under Uncertainty

Upon examination, the effects of the maneuver execution errors are found to grow less quickly in the DRO than they do in the halo orbit, resulting in smaller values on the final state variance. The constraint on the optimization problem for rendezvous in the DRO is therefore set to a maximum

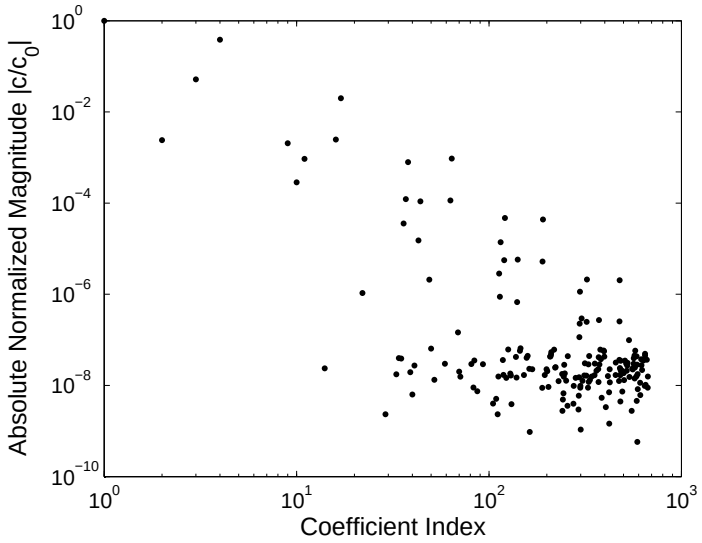


Figure 5.33: Normalized expansion coefficients for a sparse 6-dimensional, $5^{\text{th}}$ order model of the required $\Delta V$ as a function of the design parameters $\tau$, $t$, and $\Delta\tau$ for rendezvous in a DRO.

position variance of 20 m in each of the $T$-, $N$-, and $W$-directions. The optimizer, which makes a total of 70 function calls, converges on a solution of $\Delta V = 35.2$ cm/s at $\tau = 71.30°$, $t = 0.6$ days, and $\Delta\tau = 0.01°$ with 70 function calls, only $0.02°$ different in the initial position than the optimal design as determined from the dense model, as evidenced in Table 5.9. In both the halo and the DRO, then, minimizing the $\Delta V$ drives the solution to the smallest possible initial separation and the longest time of flight, consistent with the system dynamics. Table 5.10 compares the analytic computations of the variance at the optimal solution of the sparse model to a Monte Carlo analysis and reveals that the analytic formulas for the position variance agree to $10^{-1}$ m$^2$.

Figure 5.35 shows the evolution of the final state statistics as a function of sample size for the Monte Carlo simulation. Approximately $9 \times 10^5$ samples are required for the Monte Carlo to converge to the 3 digits of accuracy in $\delta\boldsymbol{R}_f$ provided by the analytic formulas. Between this larger simulation size and the greater number of function calls made by the optimizer, rendezvous optimization in the DRO using a Monte Carlo approach is even more computationally expensive than optimization in the halo orbit, providing opportunity for equivalently higher cost savings through the use of a surrogate model for robust design.

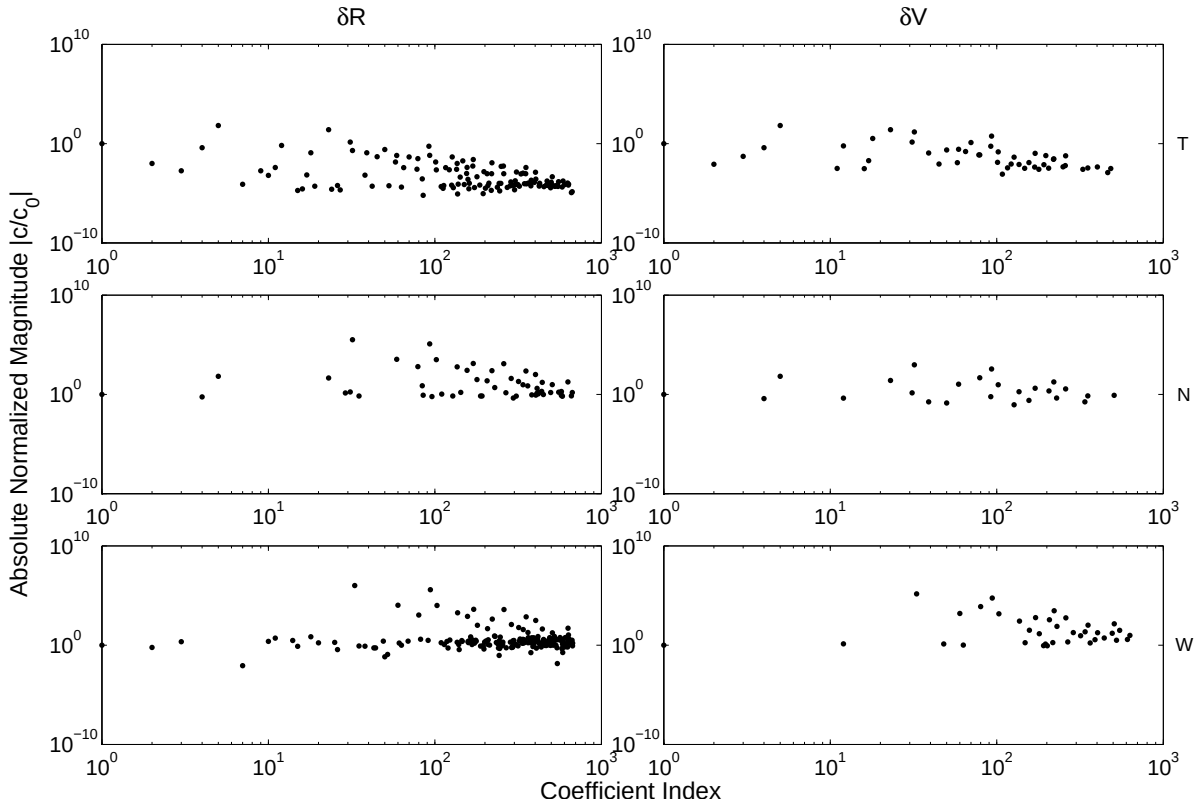


Figure 5.34: Normalized expansion coefficients for a sparse 6-dimensional, $5^{\text{th}}$ order model of the final state deviations $\delta \boldsymbol{X}_f$ as a function of design parameters and maneuver execution errors for rendezvous in a DRO.

Table 5.9: Optimum design point identified using the surrogate models for rendezvous in a DRO with a constraint on each direction of the position variance of 20 $\text{m}^2$.

| | $\Delta V$ (cm/s) | $\tau$ (°) | $t$ (days) | $\Delta\tau$ (°) |
|---|---|---|---|---|
| Dense Model | 35.2 | 71.58 | 0.60 | 0.01 |
| Sparse Model | 35.2 | 71.60 | 0.60 | 0.01 |

Table 5.10: Comparison of the final state variance at the constrained optimal solution for rendezvous in a DRO, as computed via both Monte Carlo sampling and the analytical functions enabled by polynomial surrogates.

| | Variance | | | | | |
|---|---|---|---|---|---|---|
| | $R_T$ ($m^2$) | $R_N$ ($m^2$) | $R_W$ ($m^2$) | $V_T$ ($mm^2/s^2$) | $V_N$ ($mm^2/s^2$) | $V_W$ ($mm^2/s^2$) |
| Monte Carlo | 13.18 | 19.93 | 19.65 | 5.11 | 7.60 | 7.13 |
| Analytic (dense) | 13.13 | 20.00 | 19.62 | 5.09 | 7.61 | 7.10 |
| Analytic (sparse) | 13.13 | 20.00 | 19.62 | 5.09 | 7.60 | 7.11 |

The variability in the computed variance of the final position deviation as a function of the design parameters about the optimal design point in the DRO also differs significantly from the behavior seen in the halo orbit. First, the initial position of the chaser has little effect on the final variance in this region the state space, and the time of flight has virtually no effect at all. At the same time, the growth of the position variance with increasing separation between the spacecraft is much more pronounced − a difference of only 0.04° in the angular separation produces a 25 times increase in the magnitude of variance.

Another trend noticeable in Fig. 5.36 is that the $N$- and $W$-components of the final position variance are nearly equal in magnitude throughout the design space, while the in-track component is consistently smaller. Because of this difference in magnitude, constraints on the position variance can be set independently in each dimension. Here, the weighted cost function introduced in Section 5.2.1.3 is used to demonstrate how different forms of the constraints can drive the optimal design. Table 5.11 compares the optimal design and associated position variance for weighted optimization problems with constraints $\sigma^2_{\boldsymbol{R}} = 100\text{m}^2$ and $\sigma^2_{R_T} = 50\text{m}^2$ to the unconstrained weighted optimization problem. Although the required $\Delta V$ remains consistent to within 5 cm/s in all three cases, the final position variance ranges from 50 to 330 $m^2$ in $T$ and from about 75 to 500 $m^2$ in $N$ and $W$ with the changing constraints. This shows that informed planning can control the level of

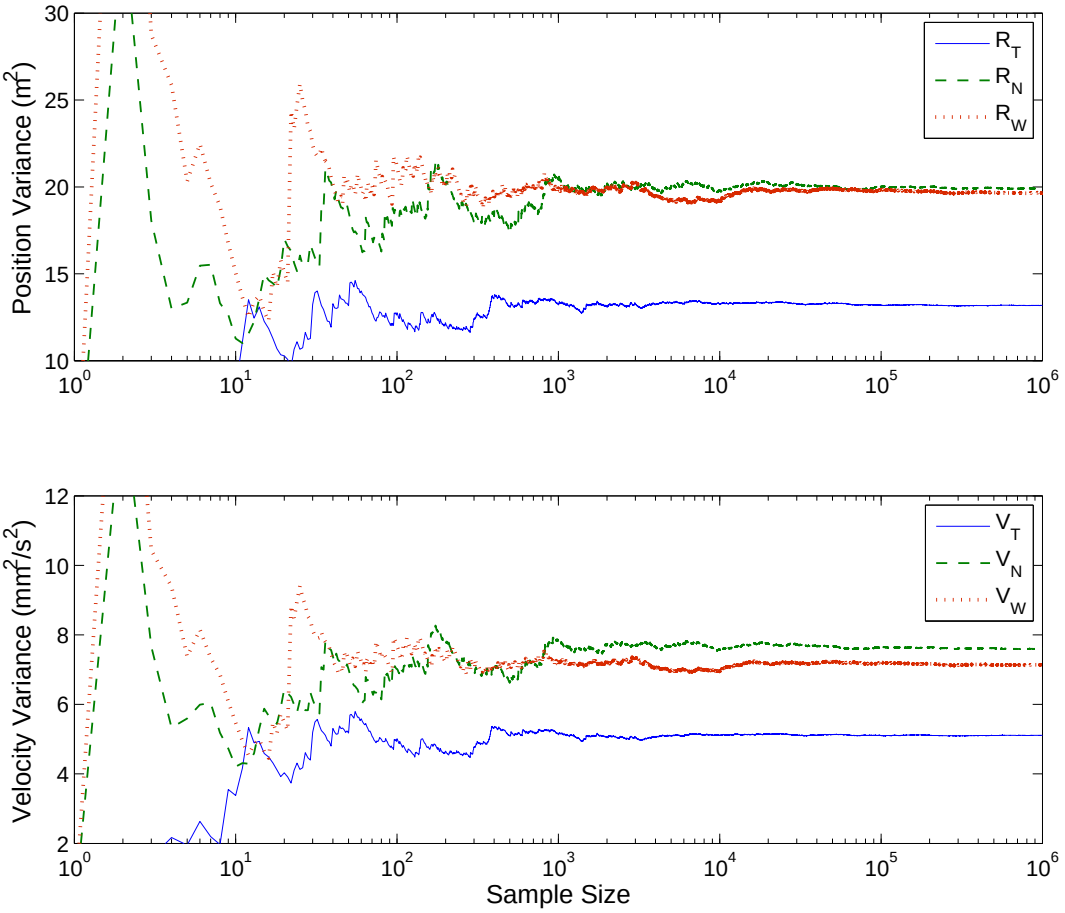


Figure 5.35: Convergence of the position and velocity variance for the optimized rendezvous maneuver in a DRO using Monte Carlo sampling of the full system dynamics.

propagated state uncertainty, in some cases without even generating any additional $\Delta V$ costs.

#### 5.2.2.4 ANOVA

The differences between the dynamical systems of the two orbit types are further reflected in the Sobol' indices, which are provided in Table 5.12 for the DRO. First, the relative impacts of $\tau$ and $t$ on the required $\Delta V$ are much smaller, so that the $\Delta V$ is a function almost solely of $\Delta\tau$. The relative influence of $\Delta\tau$ has grown for each of the final state deviations, too; in the halo orbit,

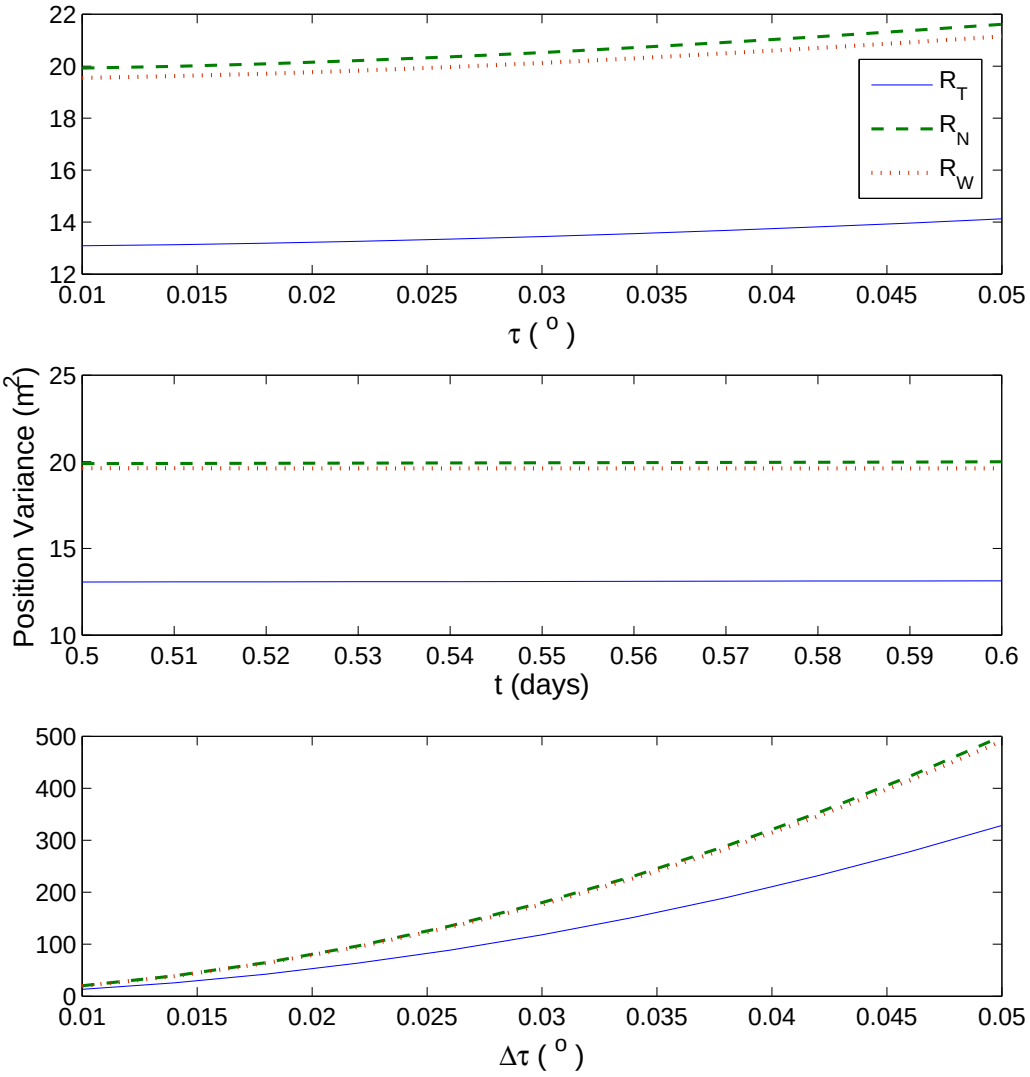


Figure 5.36: Final position variance as a function of the design paramters about the optimal design solution for rendezvous in a DRO.

the influence of $\Delta\tau$ on the final state deviations was negligible, while in the DRO, it can be seen to have a coupled effect with the maneuver execution errors, particularly for the in-track deviations. Finally, the influence of the pointing errors on the in-track deviations and of the burn magnitude on the out-of-plane deviations have effectively disappeared.

Table 5.11: Constrained and unconstrained solutions to the weighted optimization problem for rendezvous in a DRO.

| | $\Delta V$ (m/s) | $\tau$ (°) | $t$ (days) | $\delta\tau$ (°) | $\sigma^2_{R_T}$ (m$^2$) | $\sigma^2_{R_N}$ (m$^2$) | $\sigma^2_{R_W}$ (m$^2$) |
|---|---|---|---|---|---|---|---|
| Unconstrained | 1.29 | 74.57 | 0.6 | 0.050 | 331.6 | 505.6 | 495.9 |
| Constrained in $R$ | 1.33 | 74.62 | 0.6 | 0.022 | 65.6 | 100.0 | 98.1 |
| Constrained in $R_T$ | 1.34 | 74.68 | 0.6 | 0.019 | 50.0 | 76.2 | 74.8 |

Table 5.12: Total Sobol' indices for the 6-dimensional DRO problem.

| | Output | | | | | | |
|---|---|---|---|---|---|---|---|
| Parameter | $\Delta V$ | $\delta R_T$ | $\delta R_N$ | $\delta R_W$ | $\delta V_T$ | $\delta V_N$ | $\delta V_W$ |
| $\tau(s_1)$ | 7.67e-5 | 1.03e-4 | 5.97e-5 | 5.71e-5 | 8.73e-5 | 6.67e-5 | 5.79e-5 |
| $t(s_2)$ | 0.0205 | 3.85e-6 | 2.32e-6 | 9.06e-7 | 2.43e-3 | 1.23e-3 | 1.38e-3 |
| $\Delta\tau(s_3)$ | 0.982 | 0.129 | 0.0645 | 0.0645 | 0.126 | 0.0648 | 0.0645 |
| $\delta\Delta V(\xi_1)$ | 2.58e-13 | 1.00 | 5.01e-5 | 5.00e-5 | 0.950 | 4.93e-3 | 4.99e-5 |
| $\theta(\xi_2)$ | 1.49e-13 | 4.69e-4 | 0.500 | 0.500 | 0.0250 | 0.498 | 0.500 |
| $\phi(\xi_3)$ | 2.68e-13 | 5.20e-6 | 0.500 | 0.500 | 0.0246 | 0.498 | 0.500 |

#### 5.2.2.5 Initial State Uncertainties

Once more, a sample size of 450 training points is sufficient to generate a 12-dimensional model that includes the design parameters, maneuver execution errors, and initial state uncertainties; the coefficients for $\Delta V$ and $\delta \boldsymbol{X}_f$ can be found in Figs. 5.37 and 5.38, respectively. A noticeable difference in the model for the DRO is the number of recovered expansion terms necessary to capture the behavior of the velocity deviations, which ranges from only 55 to 95 terms compared to the 175-250 terms for the halo orbit. The number of recovered terms for the $\Delta V$ and final position variance in

the DRO are more comparable to the halo, sitting at 210-250.

Table 5.13 lists the components of the final state variance produced by the maneuver execution errors and initial state uncertainties at the constrained optimal design point. The addition of the state uncertainties causes the propagated uncertainty in $T$ to almost double in size, while the variance in both $N$ and $W$ is increased by about 50%. Thus, the initial state uncertainties have a significant relative impact on the knowledge of the spacecraft state at the time of rendezvous for this optimal design solution.

The influence of the initial uncertainties seems to be countered by the Sobol' indices provided in Table 5.14, which indicate that the these initial uncertainties have very little relative effect overall on the system outputs. This is due to the fact that the absolute increase in the propagated variance due to the initial state uncertainties remains fairly constant across the design space. Therefore, while an increase on the order of 10 $m^2$ is noticeable compared to the variance of 10-20 $m^2$ induced by the maneuver execution errors at the optimal design, it is dwarfed by the growth in variance caused by increasing $\Delta\tau$ (which in turn magnifies the effect of $\delta\Delta V$ because of the proportional

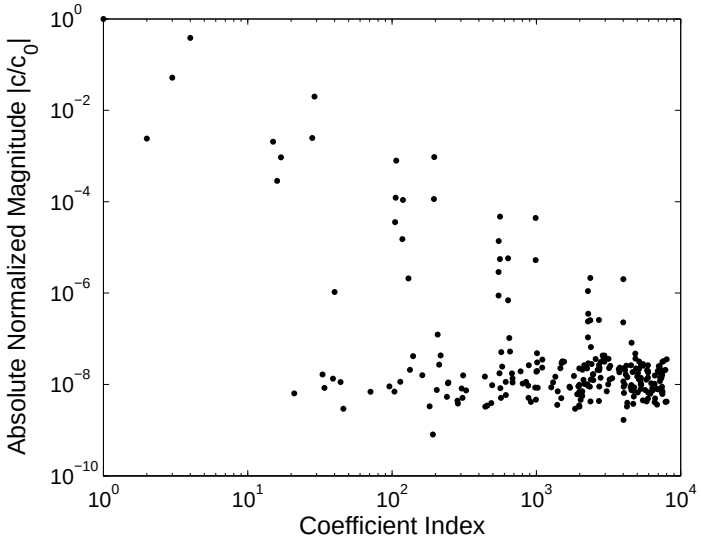


Figure 5.37: Normalized expansion coefficients for a sparse 12-dimensional, $5^{\text{th}}$ order model of the required $\Delta V$ as a function of the design parameters $\tau$, $t$, and $\Delta\tau$ for rendezvous in a DRO.

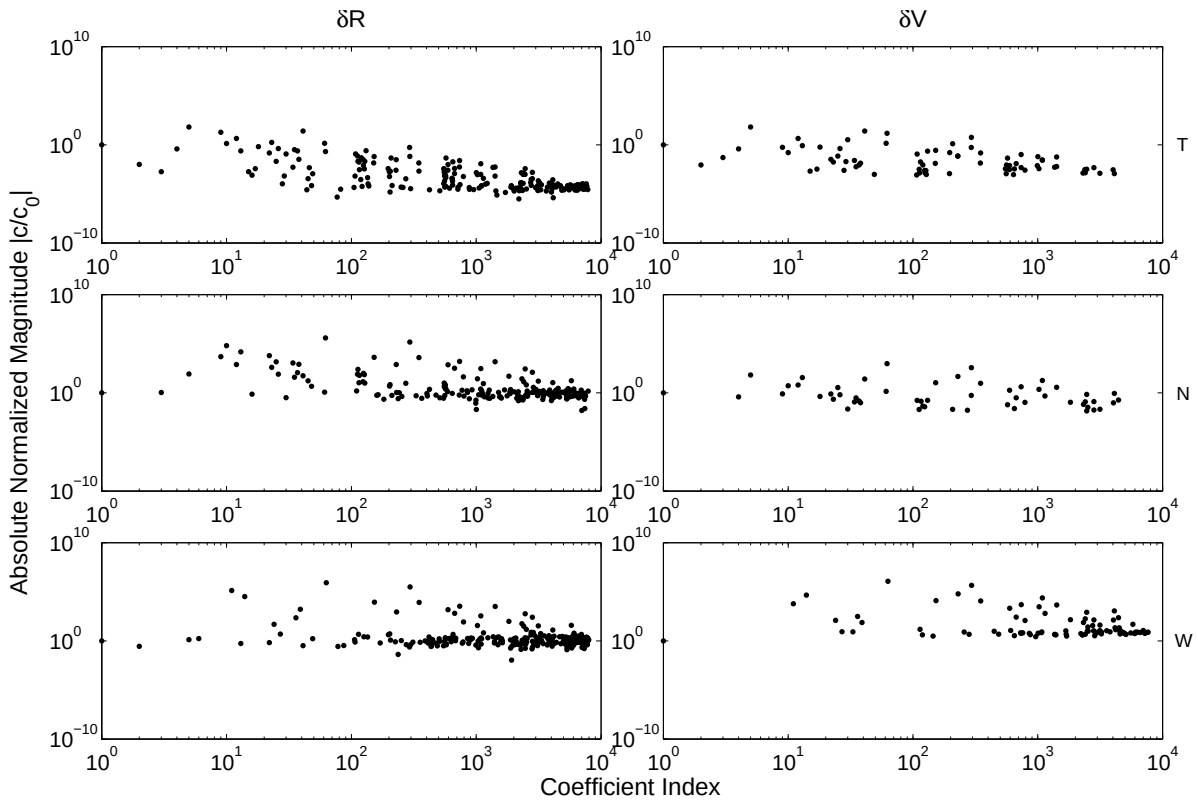


Figure 5.38: Normalized expansion coefficients for a sparse 12-dimensional, $5^{\text{th}}$ order model of the final state deviations $\delta \boldsymbol{X}_f$ as a function of design parameters, maneuver execution errors, and initial state uncertainties for rendezvous in a DRO.

Table 5.13: Comparison of the final state variance caused by maneuver execution errors only to the variance resulting from maneuver execution errors and initial state uncertainties for rendezvous in a DRO.

| | Variance | | | | | |
|---|---|---|---|---|---|---|
| | $R_T$ (m) | $R_N$ (m) | $R_W$ (m) | $V_T$ ($\text{mm}^2/\text{s}^2$) | $V_N$ ($\text{mm}^2/\text{s}^2$) | $V_W$ ($\text{mm}^2/\text{s}^2$) |
| Maneuver Only | 13.13 | 20.00 | 19.62 | 5.09 | 7.60 | 7.11 |
| Maneuver + State | 24.20 | 31.06 | 29.90 | 5.36 | 7.88 | 7.36 |

relation of $\delta\Delta V$ to the nominal $\Delta V$). This is demonstrated in a comparison of Figs. 5.36 and 5.39, in which the increased variance resulting from the initial state uncertainties is easily visible for the $\tau$ and $t$ dimensions, but much less so for $\Delta\tau$. It can be concluded, then, that both local and global effects are important in mission design. In this rendezvous problem, the global sensitivity measures for the final state variance mask the importance of the initial state uncertainties to the propagated variance directly about the optimal design point, while the increase in the final state variance due to the initial state uncertainties at the optimal design overstate their contributions for other solutions in the design space.

Table 5.14: Total Sobol' indices for a sparse model of rendezvous in a DRO with maneuver execution errors and initial state uncertainties.

| | Output | | | | | | |
|---|---|---|---|---|---|---|---|
| Parameter | $\Delta V$ | $\delta R_T$ | $\delta R_N$ | $\delta R_W$ | $\delta V_T$ | $\delta V_N$ | $\delta V_W$ |
| $\tau(s_1)$ | 7.67e-5 | 7.17e-4 | 2.80e-4 | 5.57e-5 | 1.21e-4 | 7.90e-5 | 5.78e-5 |
| $t(s_2)$ | 0.0205 | 3.32e-5 | 1.31e-5 | 4.47e-6 | 2.42e-3 | 1.23e-3 | 1.38e-3 |
| $\Delta\tau(s_3)$ | 0.9821 | 0.120 | 0.0629 | 0.0630 | 0.125 | 0.0647 | 0.0644 |
| $\delta\Delta V(\xi_1)$ | 2.92e-14 | 0.927 | 4.88e-5 | 4.88e-5 | 0.9467 | 4.92e-3 | 4.98e-5 |
| $\theta(\xi_2)$ | 6.43e-14 | 4.35e-4 | 0.487 | 0.488 | 0.0249 | 0.497 | 0.499 |
| $\phi(\xi_3)$ | 1.70e-13 | 4.81e-6 | 0.487 | 0.488 | 0.0245 | 0.497 | 0.499 |
| $\sigma^2_{0,R_T}(\xi_4)$ | 2.59e-14 | 0.0679 | 3.51e-4 | 9.65e-11 | 5.75e-5 | 1.20e-6 | 5.15e-10 |
| $\sigma^2_{0,R_N}(\xi_5)$ | 3.72e-14 | 9.37e-4 | 0.0235 | 7.37e-11 | 4.92e-6 | 2.67e-5 | 5.06e-10 |
| $\sigma^2_{0,R_W}(\xi_6)$ | 5.71e-14 | 1.05e-11 | 1.37e-10 | 0.0227 | 0 | 0 | 2.35e-5 |
| $\sigma^2_{0,V_T}(\xi_7)$ | 6.63e-14 | 3.76e-3 | 1.48e-5 | 8.09e-11 | 3.75e-3 | 5.13e-5 | 4.08e-10 |
| $\sigma^2_{0,V_N}(\xi_8)$ | 7.54e-14 | 4.35e-5 | 1.30e-3 | 1.00e-10 | 1.59e-4 | 1.29e-3 | 2.08e-10 |
| $\sigma^2_{0,V_W}(\xi_9)$ | 1.25e-13 | 8.58e-12 | 1.45e-10 | 1.31e-3 | 0 | 0 | 1.33e-3 |

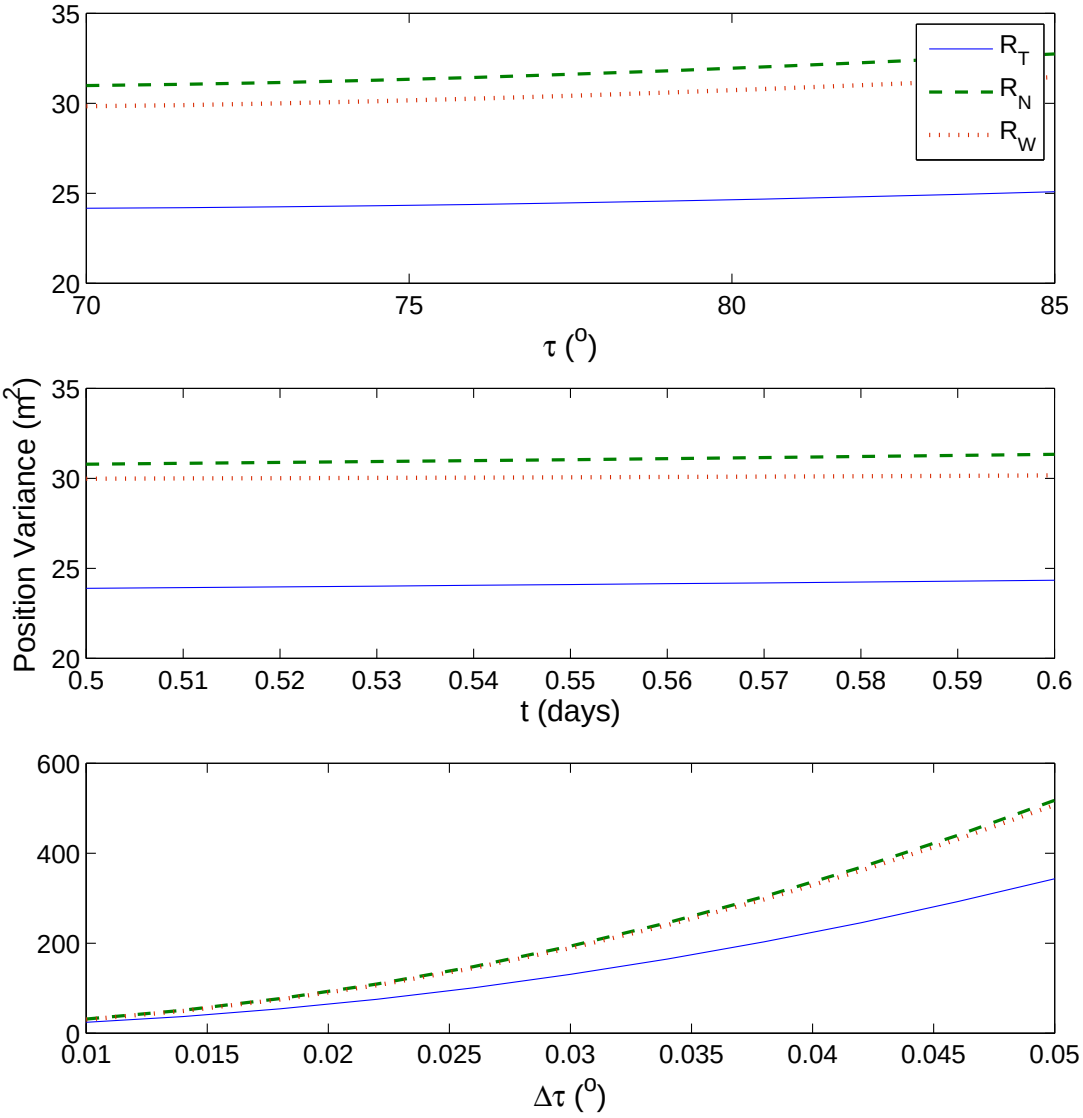


Figure 5.39: Final position variance as a function of the design paramters about the optimal design solution for rendezvous in a DRO with initial state uncertainties.

# Chapter 6

## Analytic Impact Models

Some systems cannot be well-represented using the methods of polynomial regression and polynomial chaos. These two techniques are most successful in modeling smooth continuous functions, but may fail when applied to non-smooth, discontinuous, very high order, or multi-modal systems. Modeling the uncertainties that result from kinetic impact with non-spherical asteroids represented using triangular facet shape models is one such case. As a consequence of the triangular facet representation, the momentum imparted on the asteroid can be subject to sharp, discontinuous jumps in its vector direction at the juncture between two faces. While some mitigation techniques exist that enable surrogate models to accommodate non-smooth and multi-modal characteristics, e.g., multi-element generalized polynomial chaos (ME-gPC) [134], the large number of facets that comprise the asteroid shape models make these techniques impractical for modeling kinetic impact. Instead, alternative methods for uncertainty quantification must be implemented.

One option is to conduct a Monte Carlo analysis that incorporates random realizations of deviations in the impact trajectory and the surface properties of the asteroid and employs computationally expensive ray-tracing methods to determine the impacted facet of the asteroid and the corresponding surface normal. However, in some cases, analytical tools can provide a more tractable means of analyzing the effects of the uncertainties in $\beta$ and $\hat{\boldsymbol{n}}$ on the resulting $\Delta \boldsymbol{V}$. This chapter presents several analytical tools that can together be applied to the problem of kinetic deflection of potentially hazardous asteroids (PHAs) under stochastic system parameters for the purpose of recovering the posterior distribution of the momentum imparted to the asteroid, as a

function of uncertainties in the impact location, the $\beta$-parameter, and the asteroid shape model, at reduced computational costs compared to the traditional Monte Carlo approach. These tools can be divided into two steps. The first step, laid out in Section 6.1, uses analytical formulas to determine the probability of impact with each facet about the asteroid body given the non-spherical shape model and uncertainties in the impact location of the kinetic impactor. The second step, which enlists a Gaussian mixtures method, considers the computed probabilities of impact, along with uncertainties in $\beta$, to produce a quantitative measure of the associated uncertainties in the effective momentum transferred to the asteroid; this process is outlined in Section 6.2.

## 6.1 Probability of Impact

The first set of anlaytical tools introduced in this chapter are used to determine the probability of impacting each facet about the asteroid for a given nominal trajectory of the kinetic impactor and the bivariate Gaussian distribution describing stochastic deviations in the realizations of this nominal trajectory. The approach relies on the representation of the asteroid shapes using the triangular facet shape model of Fig. 2.11. With this model, the probability of hitting any given facet can be determined analytically as a function of the incoming velocity vector, precluding the need for the inefficient ray-tracing methods mentioned above. Converting the uncertainties in the impact location to probabilities of impact with a facet in this way takes advantage of the dependence of the surface normal $\hat{\boldsymbol{n}}$ on the impacted facet to simplify the process of computing the $\Delta V$ on the asteroid [33, 34].

To determine the impact probabilities, the bivariate distribution in the impact location is integrated over each of the facets comprising the asteroid model, a process which relies on the projection of the facets onto the plane perpendicular to the incoming velocity vector. Since only those facets for which a component of the normal vector is anti-parallel to $\boldsymbol{V}_\infty$ are accessible by a spacecraft traveling along that path, a projection of the normal vectors onto $\boldsymbol{V}_\infty$ is used to filter out all facets not meeting this criteria. The vertices of the remaining facets are projected onto the $\hat{\boldsymbol{u}}$-$\hat{\boldsymbol{w}}$ plane, and the bivariate impact deviation probability density function (pdf) is integrated over

the resulting domain, as in Fig. 6.1, to determine the probability of impact. The analytic solution to the integral of a bivariate Gaussian distribution over a triangular domain is readily available in literature; the procedure laid out below is based on Example 9 of [1].

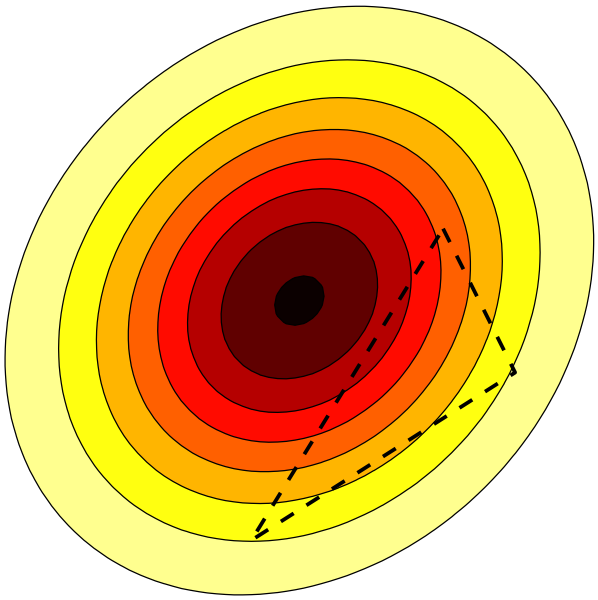

Figure 6.1: Integration of the bivariate Gaussian distribution on the impact location over the projection of the facet to determine the probability of impact.

To integrate the bivariate Gaussian over a triangle, the coordinates over which the integral is to be taken are first transformed such that one variable is defined by a circular normal distribution, using the transformations

$$s = \frac{1}{\sqrt{2+2\rho}}\left(\frac{u-\mu_u}{\sigma_u} + \frac{w-\mu_w}{\sigma_w}\right)$$
$$t = \frac{-1}{\sqrt{2-2\rho}}\left(\frac{u-\mu_u}{\sigma_u} - \frac{w-\mu_w}{\sigma_w}\right). \tag{6.1}$$

The integral over the triangle therefore becomes

$$\int\int_{A(u,w)} (\sigma_u\sigma_w)^{-1} g\left(\frac{u-\mu_u}{\sigma_u}, \frac{w-\mu_w}{\sigma_w}, \rho\right) dudw = \int\int_{A^*(s,t)} g(s,t,0)dsdt, \tag{6.2}$$

where $A^*(s,t)$ is the transformed region obtained from Equation 6.1.

In the transformed coordinates, the integral over each type of triangle depicted in (a)-(c) of Fig. 6.2 can be computed according the their respective formulas, as follows:

$$\begin{aligned} &\text{(a)} \quad \int_0^h \int_0^{\frac{k}{h}s} g(s,t,0)\ dsdt = V(h,k) \\ &\text{(b)} \quad \int\int_{A^*(s,t)} g(s,t,0)\ dsdt = V(h,k_2) + V(h,k_1) \\ &\text{(c)} \quad \int\int_{A^*(s,t)} g(s,t,0)\ dsdt = V(h,k_2) - V(h,k_1), \end{aligned} \tag{6.3}$$

where

$$h = \frac{|t_2 s_1 - t_1 s_2|}{\sqrt{(s_2-s_1)^2+(t_2-t_1)^2}}$$

$$k_1 = \frac{|s_1(s_2-s_1)+t_1(t_2-t_1)|}{\sqrt{(s_2-s_1)^2+(t_2-t_1)^2}}$$

$$k_2 = \frac{|s_2(s_2-s_1)+t_2(t_2-t_1)|}{\sqrt{(s_2-s_1)^2+(t_2-t_1)^2}}.$$

The terms $V(h,k_i)$ of Equation 6.3 are defined as

$$V(h,ah) = \frac{1}{2\pi}\int_0^h \int_0^{as} \exp^{-\frac{1}{2}(s^2+t^2)}\, dsdt = \frac{1}{4} + L(h,0,\rho) - L(0,0,\rho) - \frac{1}{2}Q(h) \tag{6.4}$$

where $L$ is the multivariate normal cumulative distribution function (cdf), $Q$ is the univariate normal cdf, and

$$\rho = -\frac{a}{\sqrt{1+a^2}}.$$

If necessary, the area under consideration can be deconstructed into component triangles, and the integrals summed to determine the probability over the reconstructed triangle.

In some cases, facets are partially obscured due to self-shadowing of the asteroid, and this obscuration must be taken into consideration when computing probabilities of impact. The method of identifying and accounting for partially obscured facets involves determining the visibility between all facets contained in the shape model, a process which can be completed in advance to further reduce computation time. If a facet is visible to any others, the possibility exists for a reduced probability of hitting that facet. The facet under consideration and all other visible facets

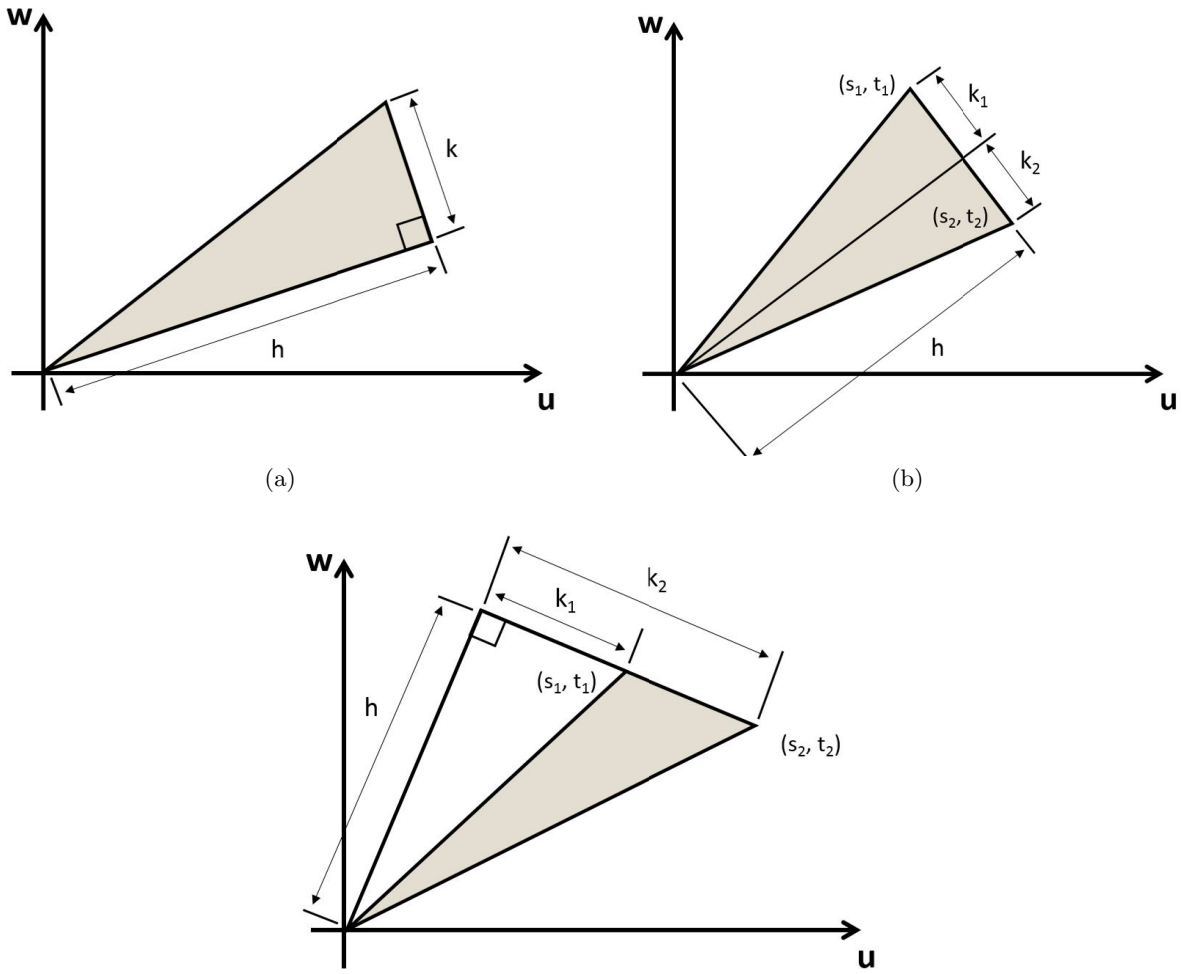


Figure 6.2: Triangular geometries corresponding to the standard bivariate integral formulations of Equation (6.3).

are projected onto the $\hat{\boldsymbol{u}}$-$\hat{\boldsymbol{w}}$ plane, and the separating axis theorem [47] is used to identify any overlapping or touching triangles in this plane. The separating axis theorem tests for overlap by projecting two facets onto some arbitrary axis such that each forms an interval on that axis, as in Fig. 6.3. If the intervals do not overlap, i.e.,

$$R_A + R_B < D \cdot L$$

for projection lengths $R_A$, $R_B$, and $D \cdot L$, then the axis onto which the facets are projected is

a *separating axis*, and the two facets are disjoint. Because two disjoint triangles can always be separated by a line parallel to an edge from each triangle, a finite number of axes may be tested to determine whether the faces are disjoint [46].

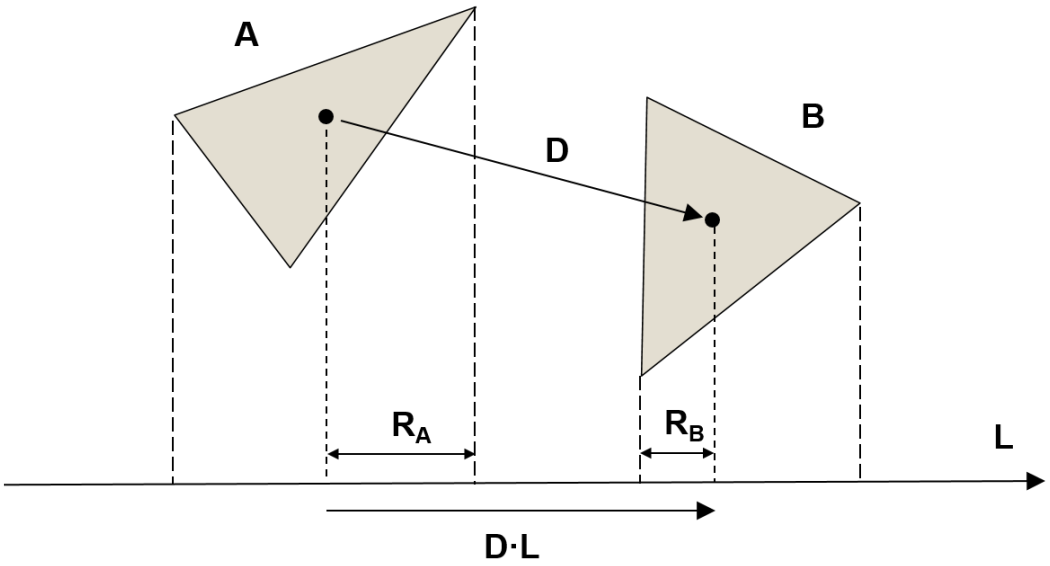


Figure 6.3: Projection of two triangles onto the axis $L$ to determine overlap using the separating axis theorem.

For any overlapping triangles, the Sutherland-Hodgman algorithm is used to solve for the polygon describing the region of overlap [126]. The algorithm, originally developed for use in computer graphics, employs a method of reentrant polygon clipping, which "clips off" those parts of a polygon extending beyond the boundary of a defined viewing window, i.e., the overlapping triangle in the asteroid problem. To accomplish this clipping, the triangular face to be clipped is represented as an ordered sequence of vertices $[P_1, P_2, P_3]$, such as those illustrated in Fig. 6.4. The new polygon describing the overlapping region is also saved as a sequence of vertices as it is generated.

To initiate the process, the first point $P_1$ is flagged as the start of the original triangular facet and renamed $S$. Beginning with a single edge of the overlapping triangle (termed the clipping

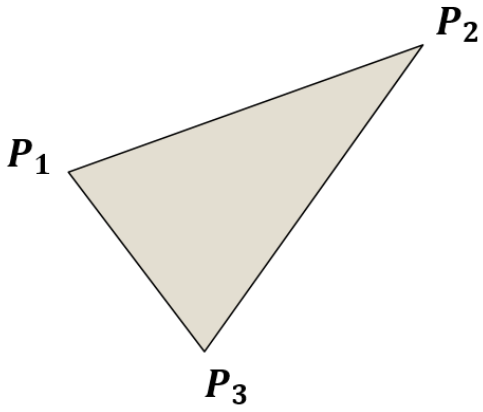


Figure 6.4: Triangular facets are defined by their vertices for polygon clipping using the Sutherland-Hodgman algorithm.

boundary), it is determined whether this initial point lies on the "visible" side of this boundary. If so, the point $S$ is saved to the sequence of vertices defining the new polygon. Continuing through the remaining vertices of the original triangle, each point $P_i$ is sequentially tested to determine whether the segment $\overline{SP_i}$ crosses the clipping boundary. If not, either 1) $P_i$ lies on the visible side of the clipping boundary and is saved to the new polygon, or 2) $P_i$ does not lie on the visible side and is omitted from the new sequence. In either case, $P_i$ becomes the new $S$, and the process continues for point $P_{i+1}$.

If $\overline{SP_i}$ does cross the clipping boundary, the point of intersect $I$ must be determined. From the ratio of similar triangles, as depicted in Fig. 6.5 and for which the relation

$$\frac{|P_1R_1|}{|P_2R_2|} = \frac{|P_1I|}{|P_2I|} \tag{6.5}$$

holds, the point of intersect can be computed as

$$I = \alpha\vec{P}_2 + (1-\alpha)\vec{P}_1 - \overrightarrow{P}_1 + \alpha\left(\vec{P}_2 - \vec{P}_1\right), \tag{6.6}$$

where

$$\alpha = \frac{|P_1I|}{P_1P_1} = \frac{|P_1R_1|}{|P_1R_1|} + |P_2R_2|. \tag{6.7}$$

Again, one of two scenarios may exist. If the line $\overline{SP_i}$ crosses from the visible side to the non-visible side, only the point $I$ is saved to the new polygon ($S$ having already been saved in the previous step). If $\overline{SP_i}$ instead crosses into the visible side of the clipping boundary, both $I$ and $P_i$ are saved. $P_i$ is then renamed $S$, and the process is repeated for all $P_i$, culminating with $\overline{SP_1}$. Once the procedure has been completed for the the first clipping edge, the resulting polygon is clipped against each of the remaining edges of the overlapping triangle in turn. A diagram of this process is provided in Fig. 6.6.

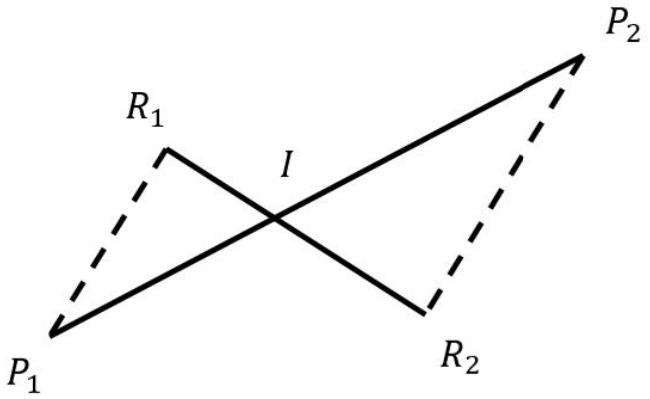


Figure 6.5: The ratio of similar triangles can be used to calculate the point of intersect for two arbitrary line segments.

The overlapping polygon produced by the Sutherland-Hodgman algorithm is then redefined as a collection of triangles using Delaunay triangulation [76], and the sum of the integrals over these smaller triangles, again computed from Equation 6.3, defines the total probability over the obscured region. Figure 6.7 illustrates the process of solving for the overlap and the subsequent triangulation for two example triangles. The computed probability corresponding to the overlapping region is subtracted from the original probability of impacting the current facet under consideration, and the procedure continues for all overlapping triangles. The corrected probability of impact for a given facet, then, is the integral over that facet less the integrals over all obscured regions.

As will be shown in the results, variations in the asteroid shape model lead to variations in the

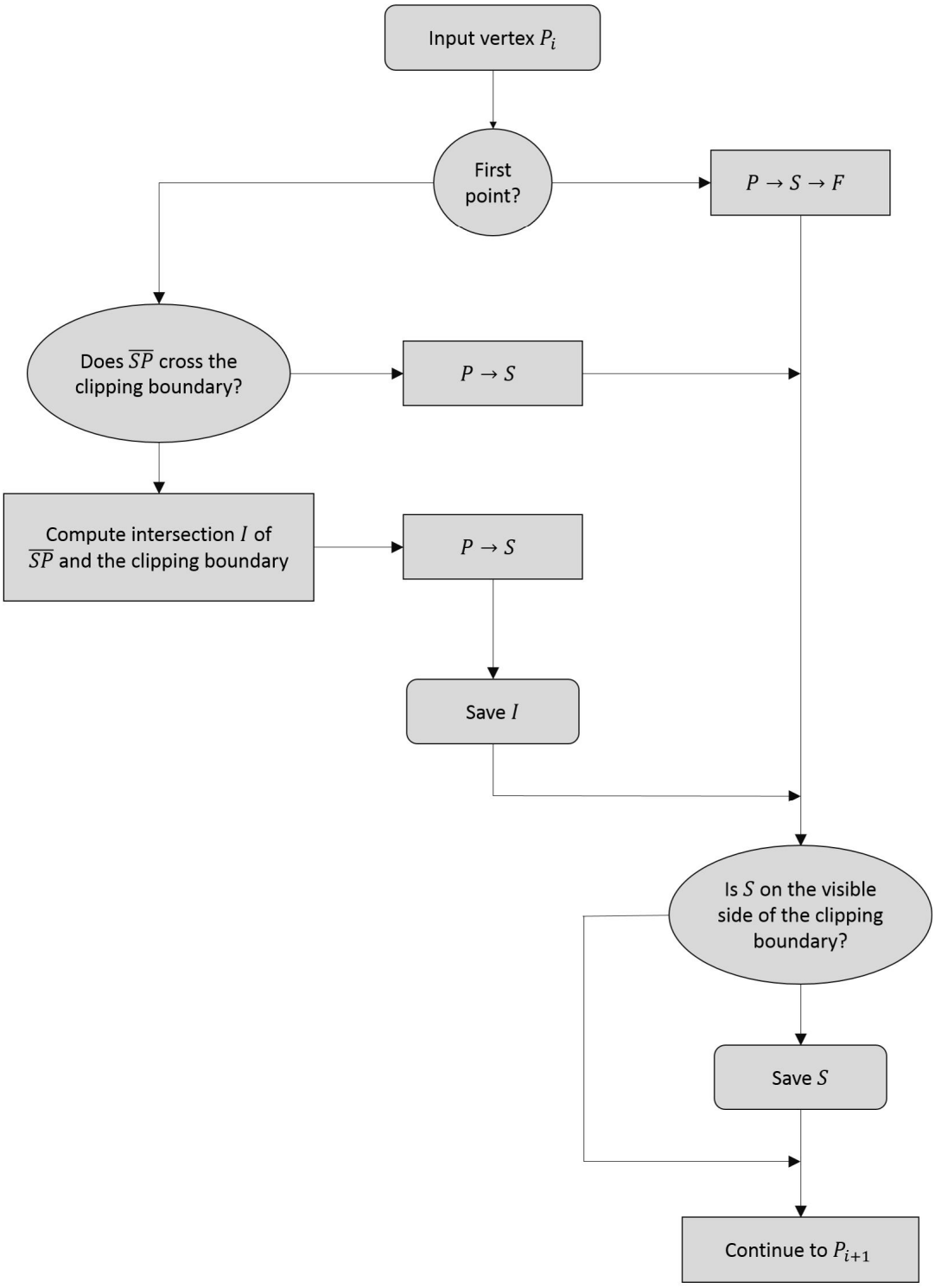


Figure 6.6: Sutherland-Hodgman algorithm of polygon clipping used to determine the region of overlap between two facets in the asteroid shape model.

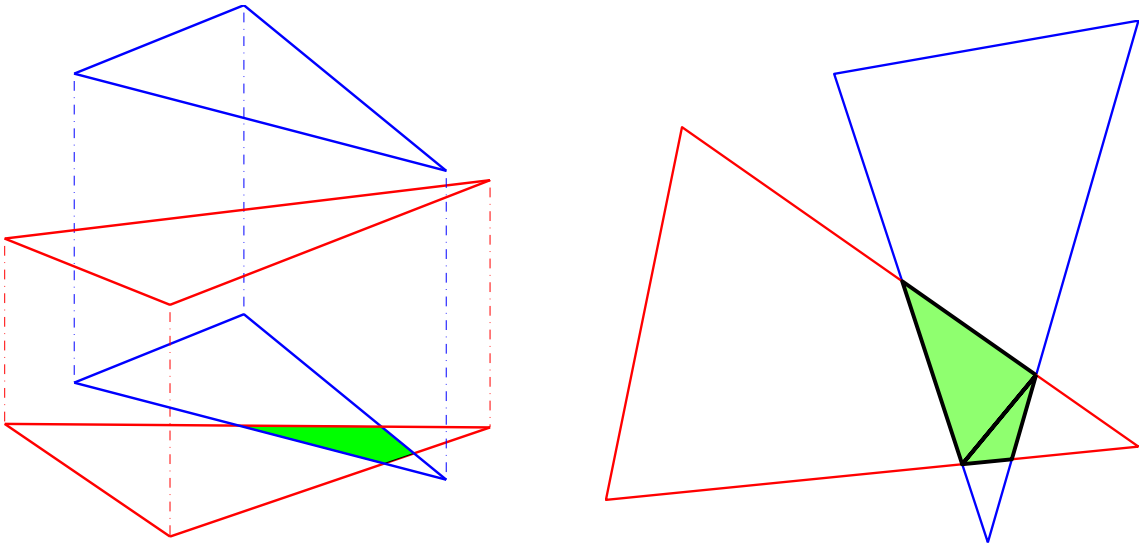

(a) Overlapping regions after projection onto two-dimensional plane

(b) Delaunay triangulation of the overlapping region

Figure 6.7: Illustration of the method of determining overlapping regions for two triangular facets.

direction of $\hat{\boldsymbol{n}}$ but do not have a significant effect on the probability of hitting a facet. Therefore, the probability of hitting each facet is assumed constant for the sake of analysis, with the probabilities associated with the nominal shape model derived using the above techniques; the corresponding normal vectors are selected according to randomly generated realizations of perturbed shapes.

## 6.2 Gaussian Mixtures Method

The Gaussian mixtures method (GMM) is frequently used in uncertainty quantification to propagate a known, non-Gaussian *a priori* distribution through nonlinear system dynamics. To do so, the *a priori* pdf is represented using a summation of $N$ component Gaussian distributions, such that

$$p(x) = \sum_{i=1}^{N} w_i g(x|\mu_i, \Sigma_i), \tag{6.8}$$

where $\mu_i$ and $\Sigma_i$ are the mean and covariance matrix of the component distributions, respectively. The first and second moments of the component distributions are then propagated through the system dynamics, and the summation is repeated to determine the posterior distribution.

Conversely, Equation 6.8 can instead be used to approximate an unknown *a priori* distribution when some definition of the component distributions is readily available. This technique is well-suited for the approximation of the asteroid $\Delta \boldsymbol{V}$ in cases where the asteroid shape is assumed to be well-known, e.g., when its shape model is derived from reconnaissance or characterization missions. In these cases, the uncertainty in the $\Delta \boldsymbol{V}$ is a function only of uncertainties in the impact location, represented as the probability of impacting a facet, and in $\beta$; any uncertainty in the shape model is omitted.

Within a facet, the normal vector $\hat{\boldsymbol{n}}$ remains fixed, and the $\Delta \boldsymbol{V}$ imparted on the asteroid is a linear function of the asteroid's $\beta$-parameter. It follows that any uncertainties in the $\Delta \boldsymbol{V}$ are linearly related to the uncertainties in $\beta$. For a Gaussian distribution in $\beta$, then, the distribution in $\Delta \boldsymbol{V}$ for impact within a given facet is also Gaussian. Thus, the distributions in $\Delta V$ for each facet can be taken as the component Gaussians of the GMM, weighted by the corresponding hit probabilities for the facets as computed using the techniques described above. The mean $\Delta \boldsymbol{V}$ from impact along $\boldsymbol{V}_\infty$ is then defined as

$$E\left[\Delta \boldsymbol{V}\right]_{mix} = \sum_{i=1}^{N} w_i \cdot E\left[\Delta \boldsymbol{V}\right]_i, \tag{6.9}$$

in which the mean $\Delta \boldsymbol{V}$ for each facet $i$ is, from Equation 2.10,

$$E\left[\Delta \boldsymbol{V}\right]_i = \gamma[\boldsymbol{V}_\infty + (E\left[\beta\right] - 1)(\hat{\boldsymbol{n}} \cdot \boldsymbol{V}_\infty)\hat{\boldsymbol{n}}]. \tag{6.10}$$

Similarly, the variance is defined as

$$\mathcal{V}\left[\Delta \boldsymbol{V}\right]_{mix} = \left[\sum_{i=1}^{N} w_i \cdot \mathcal{V}\left[\Delta \boldsymbol{V}\right]_i + E\left[\Delta \boldsymbol{V}\right]_i E\left[\Delta \boldsymbol{V}\right]_i^T\right] - E\left[\Delta \boldsymbol{V}\right]_{mix} E\left[\Delta \boldsymbol{V}\right]_{mix}^T, \tag{6.11}$$

where

$$\mathcal{V}\left[\Delta \boldsymbol{V}\right]_i = \gamma^2[(\hat{\boldsymbol{n}} \cdot \boldsymbol{V}_\infty)^2 \hat{\boldsymbol{n}}\hat{\boldsymbol{n}}^T]\mathcal{V}\left[\beta\right], \tag{6.12}$$

again from Equation 2.10.

To account for the non-zero probability of the impactor missing the asteroid altogether – a result of the Gaussian definition of the uncertainties in $b_u$ and $b_w$ – the weights in the summations

of Equations 6.9 and 6.11 can be normalized as

$$w_i' = \frac{w_i}{\sum_{i=1}^{N} w_i} \tag{6.13}$$

such that the hit probabilities sum to 1, and Equations 6.9 and 6.11 are interpreted as the mean and covariance given that the spacecraft does, in fact, hit the asteroid [34].

# Chapter 7

## Characterizing Uncertainty in the Kinetic Deflection of PHAs

The methods and techniques contained in Chapter 6 are useful for improving tractability in the analysis of both highly accurate asteroid shape models and those which contain a level of uncertainty, but the application of the methods differs in each case. For the well-defined shape model, the expected change in velocity $E[\Delta \boldsymbol{V}]$, as well as its variance $\mathcal{V}[\Delta \boldsymbol{V}]$, can be computed purely analytically by first determining the probability of impacting each facet for a given $\boldsymbol{V}_\infty$ and then using the Gaussian mixtures method to define the distribution in the effective $\Delta \boldsymbol{V}$. In the case of the stochastic shape models, on the other hand, the Gaussian mixtures method is no longer applicable. Instead, a Monte Carlo analysis must be used to determine the mean and variance of the $\Delta \boldsymbol{V}$. However, the tools for determining the hit probabilities are still relevant, and, as a result, each realization of the Monte Carlo simply requires the evaluation of the low-cost algebraic function given in Equation 2.10.

Section 7.1 of this chapter presents detailed analysis and results for the validation of these techniques as applied to the asteroid Golevka, both with and without uncertainty in the shape model. The analysis considers a set of 1992 nominal impact locations uniformly distributed about the asteroid body and directed through its center of mass (COM)[1] , and results are given for the mean and standard deviation of the imparted $\Delta \boldsymbol{V}$. Additionally, the sensitivities of the effective $\Delta \boldsymbol{V}$ to uncertainties in the impact location and $\beta$ are provided by the Sobol' sensitivity indices, computed using the sampling-based method laid out in Chapter 4. The analysis is then extended

[1] The set of nearly uniform points on the sphere were provided by Cory Ahrens of the Colorado School of Mines.

to three additional asteroids − 1950DA, Yorp, and Nereus − in Sections 7.2-7.4 for comparison to the Golevka results. Well-defined shape models are assumed for each of these additional asteroids. Finally, a broader-level analysis is presented on the distributions in the expected $\Delta \boldsymbol{V}$ for a larger survey of 21 asteroids in Section 7.5, again assuming well-defined shape models for each.

The values of the $\Delta \boldsymbol{V}$ presented here are normalized by the mass fraction and $\boldsymbol{V}_\infty$ and are therefore non-dimensional; this allows for comparison across asteroids, independent of the mass of the bodies, and provides results relative to the impacting velocity. Further, all results are given as the effective $\Delta V$, i.e., the projection of the total $\Delta \boldsymbol{V}$ onto the direction of $\boldsymbol{V}_\infty$, with the assumption that any off-axis $\Delta V$ is undesirable. For $\mu_\beta = 2$, the maximum achievable value of the effective $\Delta V$ is 2.

## 7.1 Golevka

Figure 7.1 shows the spatial distribution of the mean and standard deviation of the expected $\Delta V$ on the asteroid Golevka resulting from kinetic impact for the case of a high accuracy shape model. The results are presented as a function of the nominal impact location about the body. In Fig. 7.1a, there clearly exists a strong dependence of $E[\Delta V]$ on the local topography. Flatter regions of the asteroid, i.e., those regions where the surface is mostly perpendicular to a radial vector from the asteroid's center, experience a high $\Delta V$ in the direction of the impact, while steep regions, in which the surface is oriented more nearly parallel to the radial vector, experience significant losses in $\Delta V$, indicating an inefficient transfer of momentum to the asteroid. The standard deviation, depicted in Fig. 7.1b, is similarly dependent on the shape, although slightly less so than the mean.

Figure 7.2 presents a histogram of the expected $\Delta V$ for the nominal impact locations about the asteroid. From this distribution, which shows significant variation in the magnitudes of the effective $\Delta V$, the mean expected $\Delta V$ is found to be 1.75 with a standard deviation of 0.15. The minimum and maximum values of 1.24 and 1.98, respectively, represent a 34% total variation in $E[\Delta V]$. Because the variance of the component distributions in $\beta$ on each facet do not affect the mean of the Gaussian mixture (see Equation 6.10), the distribution of the expected $\Delta V$ in Fig. 7.2

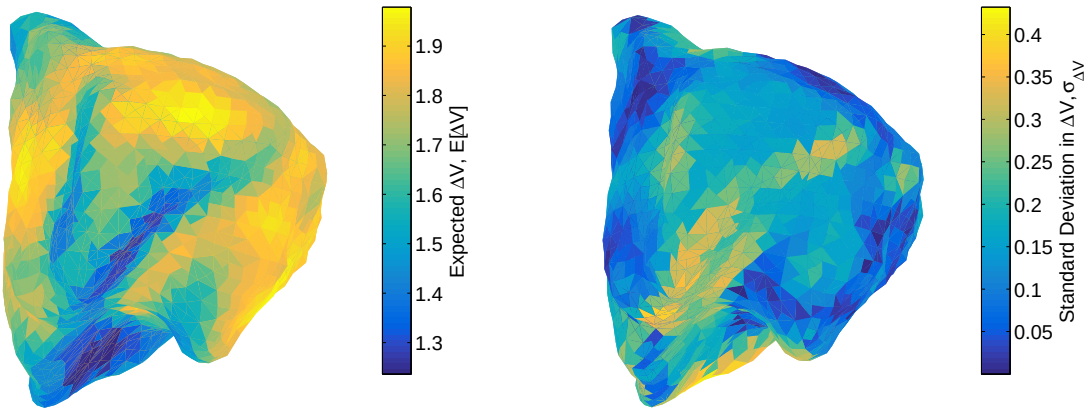


(a) Mean expected $\Delta V$ (b) Standard deviation in the expected $\Delta V$

Figure 7.1: Spatial distribution of the mean and standard deviation in the expected $\Delta V$ for the asteroid Golevka under constant shape model assumptions.

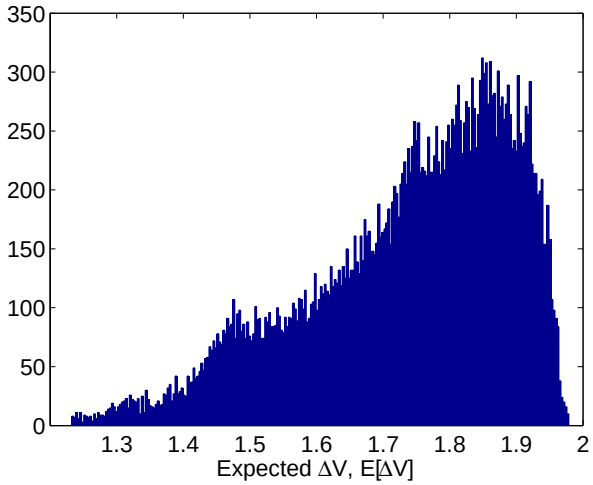


Figure 7.2: Frequency distribution of the mean expected $\Delta V$ for the asteroid Golevka under constant shape model assumptions.

can be attributed entirely to the impact location and the asteroid topography. The 34% variation, then, suggests that the shape of the body can have a substantial influence on the effectiveness of a kinetic impactor.

A relative measure of the dependence of the variance in the $\Delta V$ to the uncertain system

inputs is provided by the Sobol' sensitivity indices. Here, the uncertainties in $V_{\infty,u}$ and $V_{\infty,w}$ are collected into a single term representing the uncertainty in the impact location, and the Monte Carlo samples are generated using realizations of the impacted facet. Figure 7.3 shows the convergence of the first order and total Sobol' indices with increasing sample size for the effective and off-axis components of the $\Delta \boldsymbol{V}$, as well as its total magnitude, for a single impact trajectory $\boldsymbol{V}_\infty$. For each sample size, 100 independent sample sets were used to generate the mean and variance of the indices. While the mean values of the indices are apparently independent of sample size, the variance experiences statistical convergence with increasing $n$. The convergence characteristics for 1950DA, Yorp, and Nereus were all found to be similar to those illustrated in Fig. 7.3 for Golevka, so a sample size of $10^6$ is selected for subsequent analysis for all asteroids under consideration, and the convergence plots have been omitted for the remaining bodies.

The mean values given in the left-hand plots of Fig. 7.3 show that the sum of the relative effects of $\beta$ and the impact location is very close to one, i.e., $S_\beta + S_{uw} \approx 1$, implying that there is little to no correlated effect of the random inputs on the imparted velocity and indicating that the $S_\beta$ indices are complements to the $S_{uw}$ indices. Consequently, nearly complete information on the relative importance of the system inputs can be achieved by examining only one set of indices, allowing the number of function evaluations required to generate the indices for this application to be cut from $n(k+2)$ to $n(k+1)$, if so desired and if the slight reduction in accuracy is deemed acceptable.

Figure 7.4 shows the first order Sobol' indices for the effective $\Delta V$ as a function of the nominal impact location about Golevka for a sample size of $n = 10^6$. It is readily evident from the plots that the relative effects of the uncertainty in $\beta$ portrayed in Fig. 7.4b are complementary to the effects of the position uncertainty given in Fig. 7.4a about the entirety of the body, consistent with the conclusions drawn from Fig. 7.3. Additionally, in both the impact location indices $S^1_{uw}$ and the $\beta$ indices $S^1_\beta$, there again exists significant variation with respect to topography. The flat regions of the asteroid noted previously to have higher values of the expected $\Delta V$ are also more sensitive to uncertainties in $\beta$, while the steep regions are more sensitive to uncertainties in the impact location.

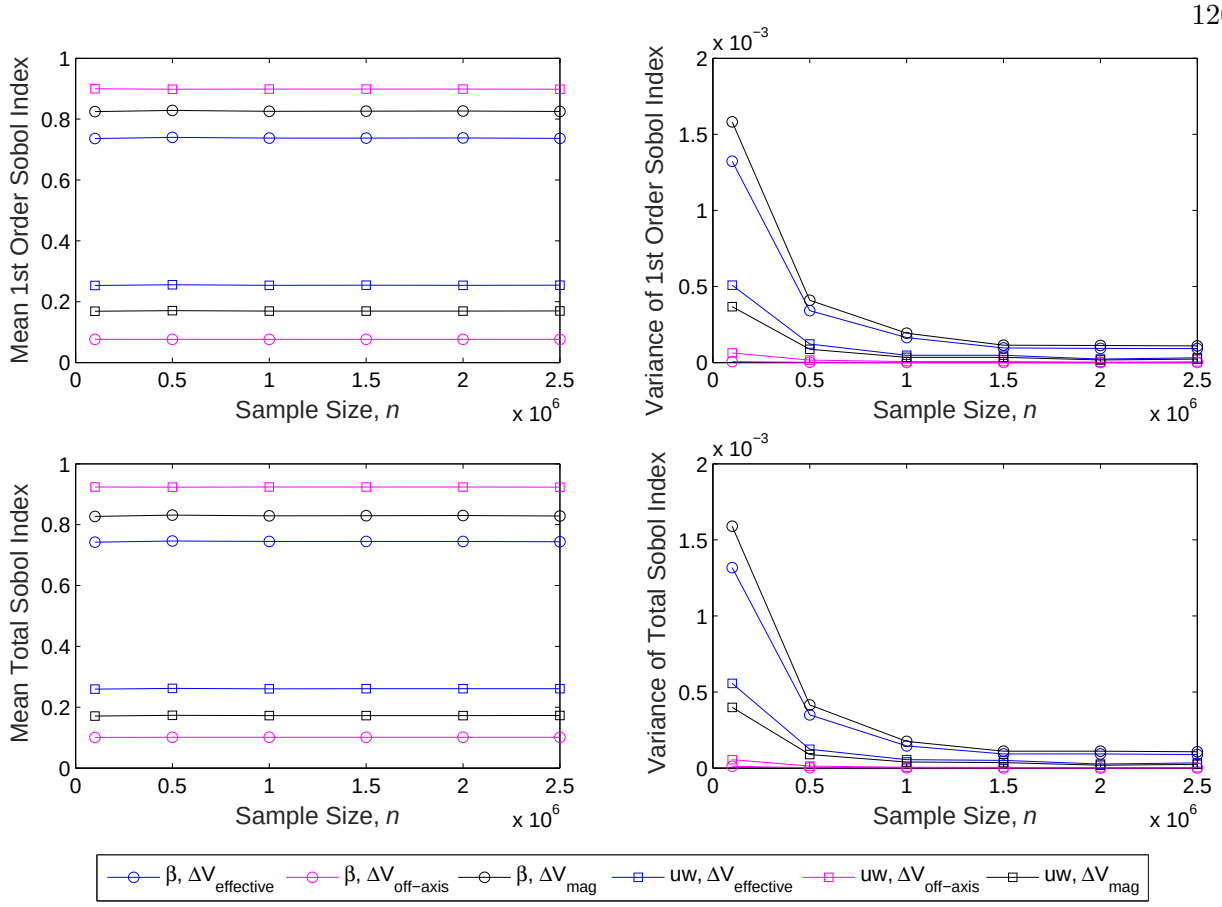


Figure 7.3: Mean and variance of realizations of the Sobol' indices $S_\beta$ and $S_{uw}$ for 100 independent sample sets over a range of sample sizes $n$.

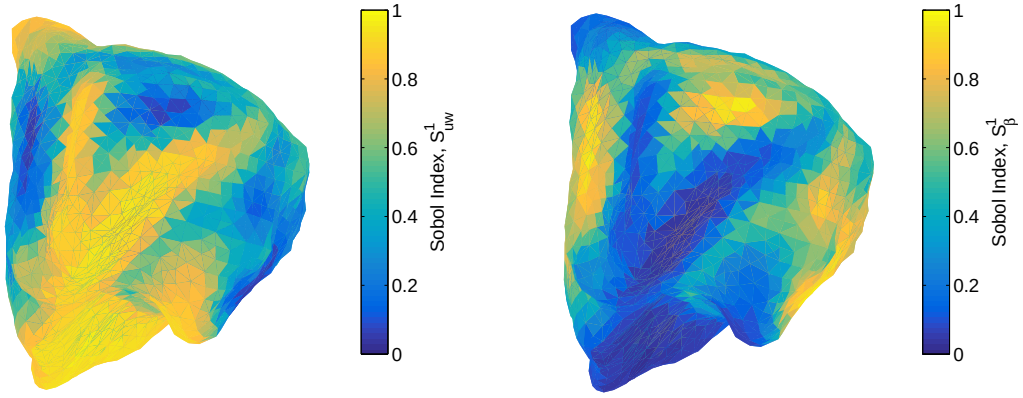


(a) Sensitivity to impact location

(b) Sensitivity to $\beta$

Figure 7.4: First order Sobol' indices of the variance in the expected $\Delta V$ for the asteroid Golevka.

While the Sobol' indices provide a good method for quantifying the dependence of the variance in $\Delta V$ for a given solution to the system, the solution itself is contingent on the values defining the distribution of the stochastic inputs. To examine this effect, the mean and standard deviation of the expected $\Delta V$ are evaluated for three values of uncertainty in the impact location $\sigma_{uw}$, with the mean $\mu_{uw}$ equal to the nominal targeting trajectory in each case, and for three values of the mean in the $\beta$-parameter $\mu_\beta$ (because $\Delta V$ is linearly related to $\beta$, the expected $\Delta V$ is independent of $\sigma_\beta$). The results are provided in Tables 7.1 and 7.2. In each case, the $\sigma$-value for the alternate stochastic input is set to zero.

Table 7.1: Mean and standard deviation of the expected $\Delta V$ for three values of uncertainty in the impact location $\sigma_{uw}$. $\bar{R}_{ast}$ is the average radius of the asteroid.

| $\frac{1}{6}\bar{R}_{ast}$ | $\frac{1}{12}\bar{R}_{ast}$ | $\frac{1}{24}\bar{R}_{ast}$ |
|---|---|---|
| $1.73 \pm 0.12$ | $1.75 \pm 0.15$ | $1.75 \pm 0.18$ |

Table 7.2: Mean and standard deviation of the expected $\Delta V$ for three values of the mean $\beta$-parameter $\mu_\beta$.

| 1.5 | 2.0 | 2.5 |
|---|---|---|
| $1.38 \pm 0.10$ | $1.75 \pm 0.21$ | $2.13 \pm 0.46$ |

These results suggest that, in order to achieve an accurate estimate of the distribution in the expected $\Delta V$ that may result from a kinetic deflection attempt, an accurate understanding and definition of the asteroid material properties is important. Improperly defined values of $\beta$ may affect the resulting $E[\Delta V]$ by the same order as the topography of the body. On the other hand, while the previous results made clear the dependence of $\Delta V$ on the nominal impact location, changes in the level of uncertainty in spacecraft targeting for a given $\boldsymbol{V}_\infty$ does not appear to have a significant effect on the expected deflection.

Next, a Monte Carlo analysis is conducted to compute the mean and standard deviation of $E[\Delta V]$ when Golevka's shape model is included as a third stochastic dimension. To simplify the evaluation of each realization of the Monte Carlo, the probability of hitting a given facet is assumed constant for all shape realizations, such that the perturbations in the shape model affect only the normal vector of each facet. To illustrate that this is a valid assumption, the $\Delta V$ values calculated from a Monte Carlo analysis using ray tracing techniques are compared to those generated using the constant probability assumption for four different $\boldsymbol{V}_\infty$ vectors. Each of the impact trajectories targets a different characteristic type of terrain, e.g., ridge, flat surface, or valley, as depicted by the markers in Fig. 7.5. The distributions on the expected $\Delta V$ are provided in Fig. 7.6. In each case, the distribution generated using the constant probabilities provides a good match to the results of the ray tracing algorithm.

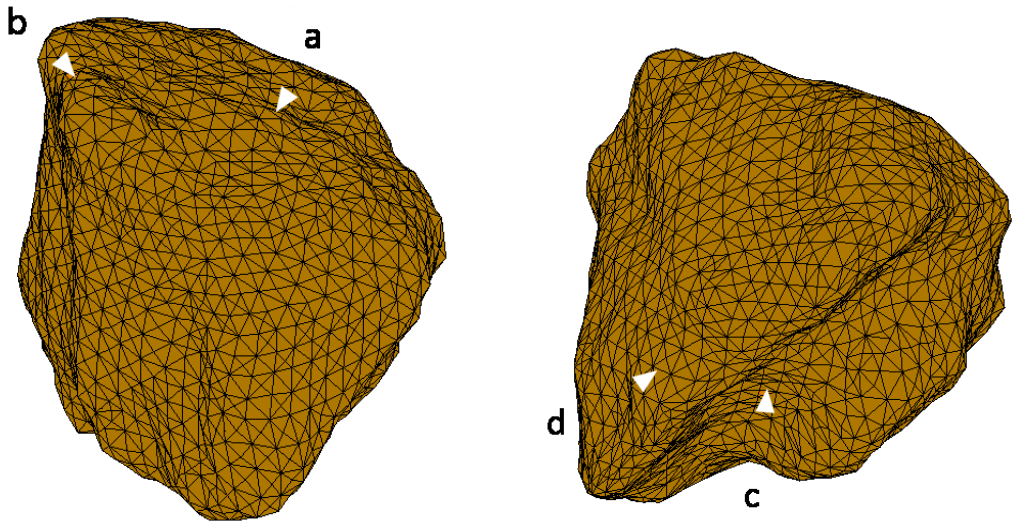


(a) (b)

Figure 7.5: Impact locations about the asteroid Golevka used to validate the constant shape model assumption.

Using this assumption of constant hit probabilities for uncertain shape models, the Monte Carlo analysis is conducted for nominal impact trajectories about the body, and the resulting changes in velocity can be found in Fig. 7.7. The expected values of $\Delta V$, shown in Fig. 7.7a, are

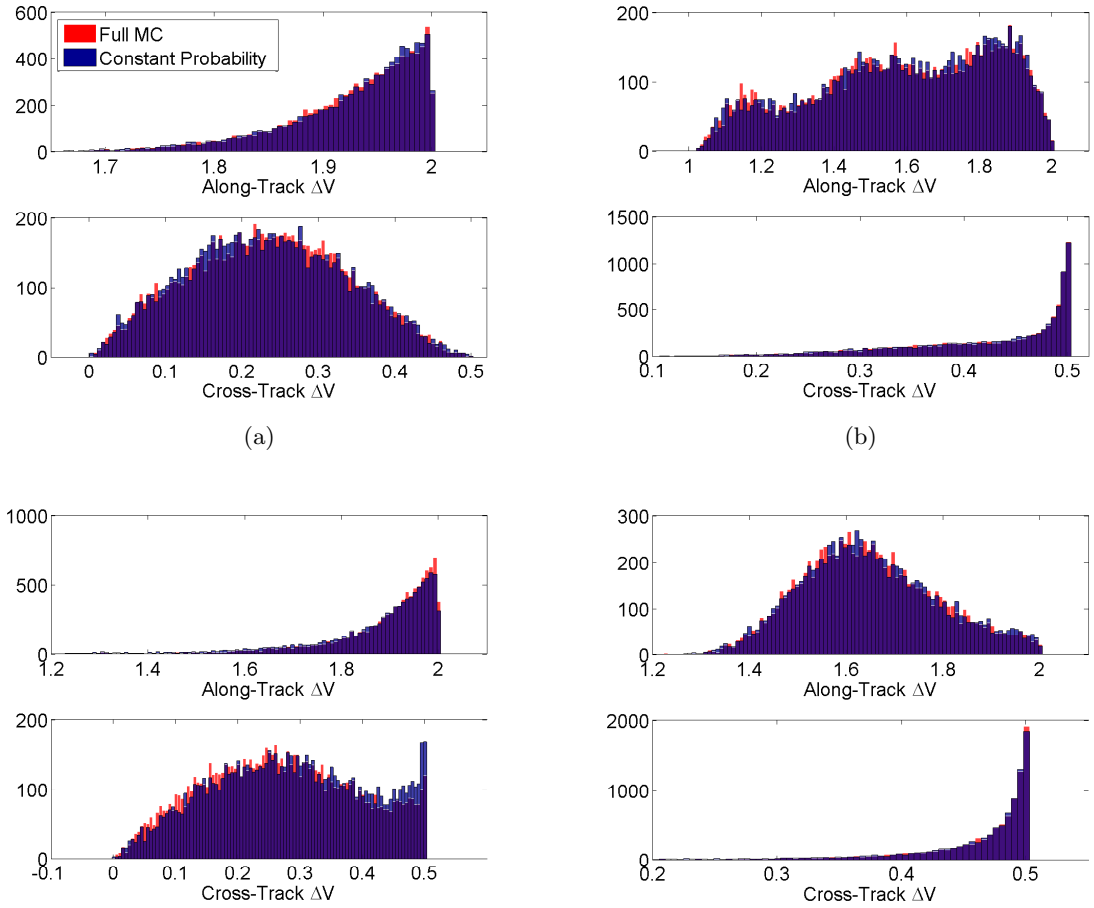


Figure 7.6: Distributions in $\Delta V$ using ray tracing methods compared to the distributions obtained assuming constant hit probabilities for the asteroid Golevka. Each plot (a)-(d) corresponds to the impact locations indicated in Fig. 7.5.

reminiscent of the results seen in Fig. 7.1a for the constant geometric model. The distribution of the expected $\Delta V$ in Fig. 7.7b is also very similar to the results seen previously. In fact, with a mean expected $\Delta V$ of 1.75 and minimum and maximum values of 1.24 and 1.95, respectively, the assumption of a well-known shape model provide roughly two to three digits of precision in the results. Overall, uncertainties in the shape model, at least on the scale used in this study, do not appear to have much of an effect on the imparted $\Delta V$. When the computation time for conducting the Monte Carlo analysis is compared to that of evaluating an analytical model, a well-known shape model is likely a reasonable assumption in an effort to reduce computational costs.

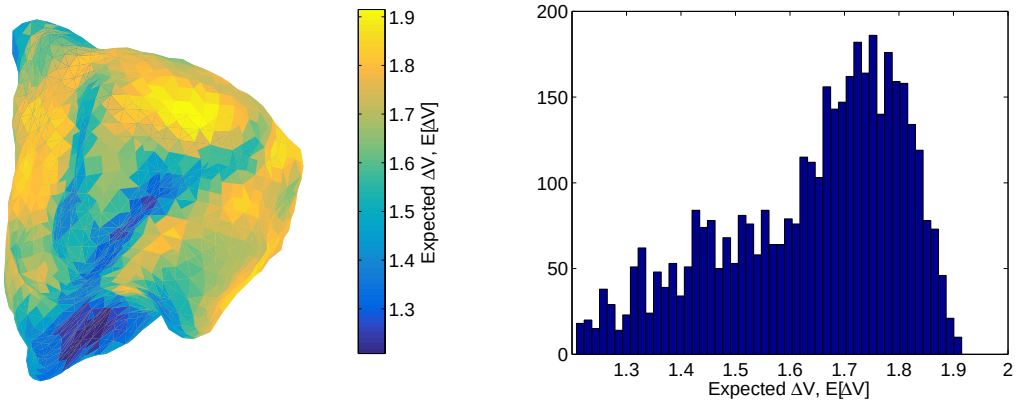


(a) Mean expected $\Delta V$

(b) Expected $\Delta V$

Figure 7.7: Spatial and frequency distributions of the mean expected $\Delta V$ with uncertain shape models for the asteroid Golevka.

## 7.2 1950DA

Figure 7.8 provides the shape model for the asteroid 1950DA, which by examination is more nearly spherical than Golevka, and the spatial distributions of the analytically computed $\Delta V$ statistics are shown in Fig. 7.9. The relative lack of irregularities in the shape of 1950DA produces two major differences when compared to Golevka. First, Fig. 7.10 shows that the distribution of $\Delta V$ ranges only from 1.54 to 1.99, smaller than the range covered by the distribution in $\Delta V$ for Golevka. Further, a larger majority of the results are concentrated at higher values than were seen in the previous case, resulting in a slightly higher mean $\Delta V$ of 1.87 over the body. Despite these differences, the magnitude varies by about 23% over the body, suggesting that the $\Delta V$ is still sensitive to impact location and asteroid topography for 1950DA, with the greatest losses occurring about the asteroid's equator.

The second effect of the differences in topography is evident in Fig. 7.11, which indicates that the variation in the effective $\Delta V$ is much more predominantly dependent on uncertainties in $\beta$ than is the case for Golevka. Almost all regions outside the equator have indices of $S_\beta^1 > 0.5$, indicating that these areas are more sensitive to uncertainties in $\beta$ than they are to uncertainties

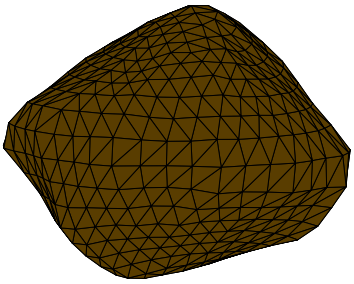

Figure 7.8: Triangular facet shape model for the asteroid 1950DA.

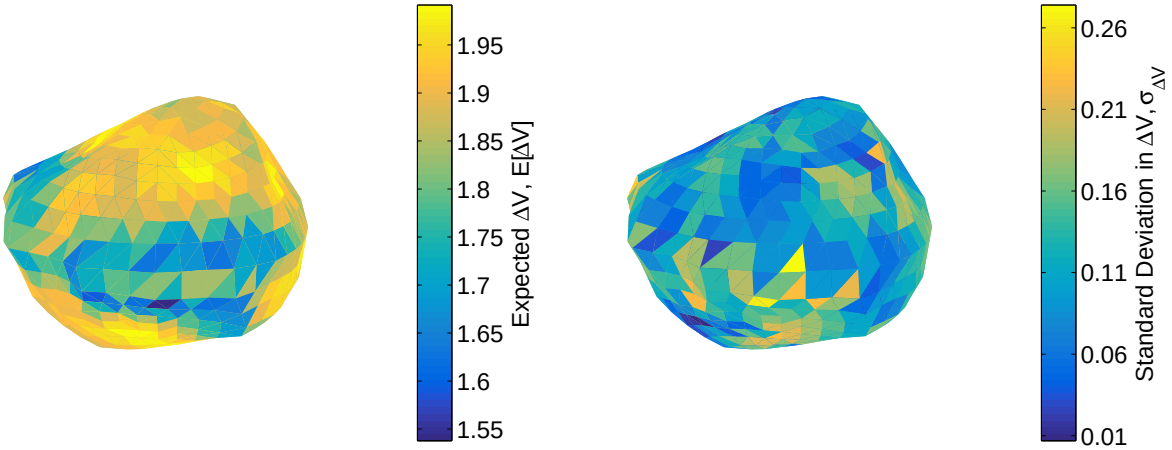


(a) Mean expected $\Delta V$

(b) Standard deviation in the expected $\Delta V$

Figure 7.9: Spatial distribution of the mean and standard deviation in the expected $\Delta V$ for the asteroid 1950DA under constant shape model assumptions.

in the impact location. The high dependence on $\beta$ is a result of the more gradual curvature of the body in these regions.

## 7.3 Yorp

Figure 7.12 shows that the shape of the asteroid Yorp is fairly similar to that of 1950DA. This similarity is reflected in the distribution of $E[\Delta V]$, as in Fig. 7.13. In fact, the range of expected values seen for Yorp, at 1.54-1.99, is nearly identical to the range seen for 1950DA. The

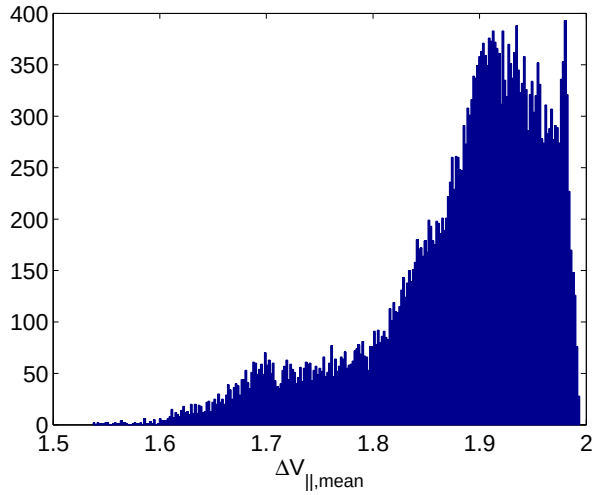


Figure 7.10: Frequency distribution of the mean expected $\Delta V$ for the asteroid 1950DA under constant shape model assumptions.

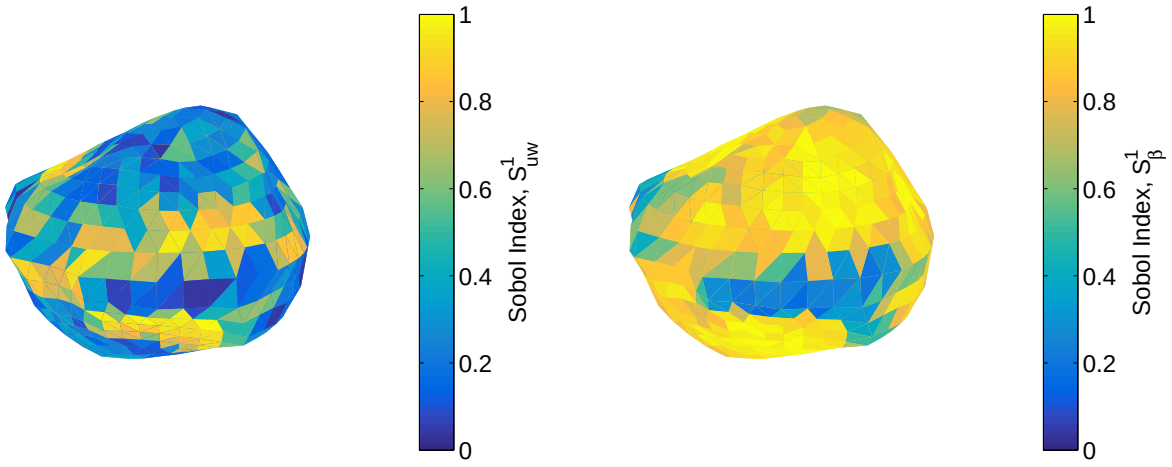


(a) Sensitivity to the impact location

(b) Sensitivity to $\beta$

Figure 7.11: First order Sobol' indices of the variance in the expected $\Delta V$ for the asteroid 1950DA.

frequency distribution for Yorp (Fig. 7.14) is less skewed toward the larger magnitudes, however, and produces a mean of 1.85.

As for the previous two asteroids, the projection of the $S^1_\beta$ indices for Yorp depicted in Fig. 7.15 is qualitatively similar to that of its variation in $\Delta V$. Three protrusions at higher latitudes, as well

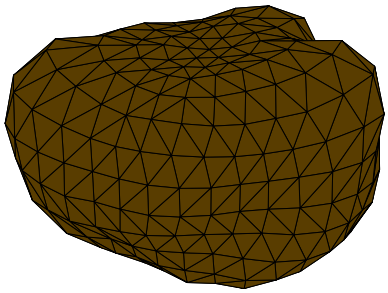

Figure 7.12: Triangular facet shape model for the asteroid Yorp.

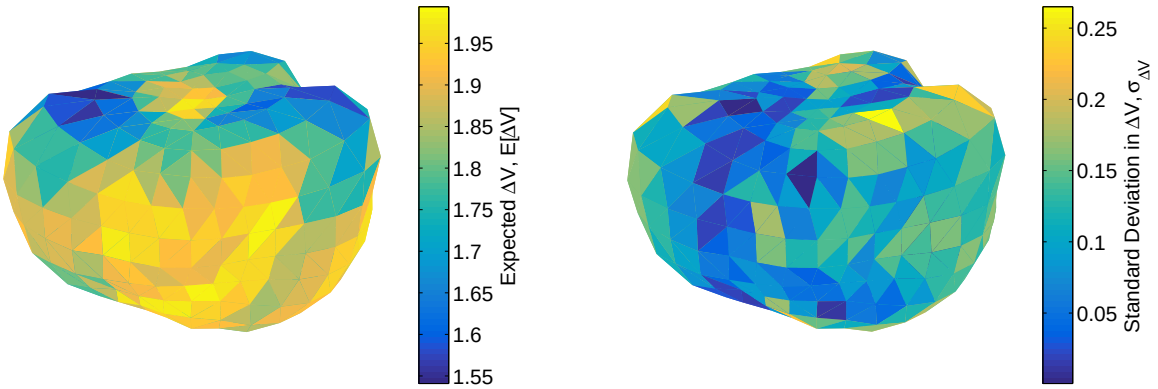


(a) Mean expected $\Delta V$

(b) Variance in expected $\Delta V$

Figure 7.13: Spatial distribution of the mean and standard deviation in the expected $\Delta V$ for the asteroid Yorp under constant shape model assumptions.

as a single protrusion in the lower latitudes, are dominated by uncertainty in the impact position, while the remainder of the asteroid is primarily affected by uncertainties in $\beta$.

## 7.4 Nereus

The last asteroid considered independently in this study is Nereus, which is depicted in Fig. 7.16. Although Nereus is more oblong in shape than either 1950DA or Yorp, the range of the expected changes in velocity seen in Fig. 7.18 is equivalent to the ranges seen for the other two. The distribution is even less skewed than that of Yorp, with a mean over the body of 1.82.

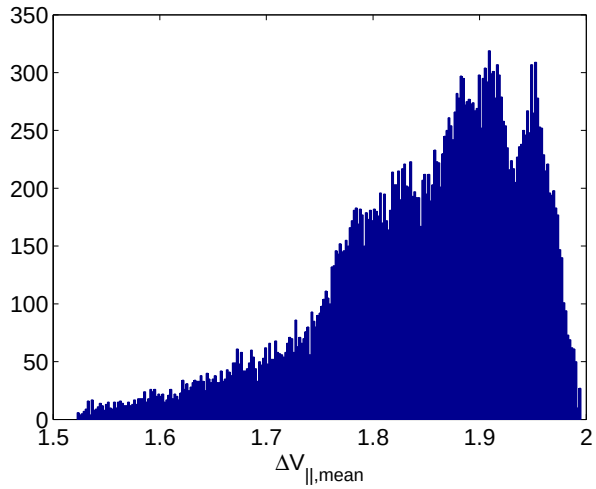


Figure 7.14: Frequency distribution of the mean expected $\Delta V$ for the asteroid Yorp under constant shape model assumptions.

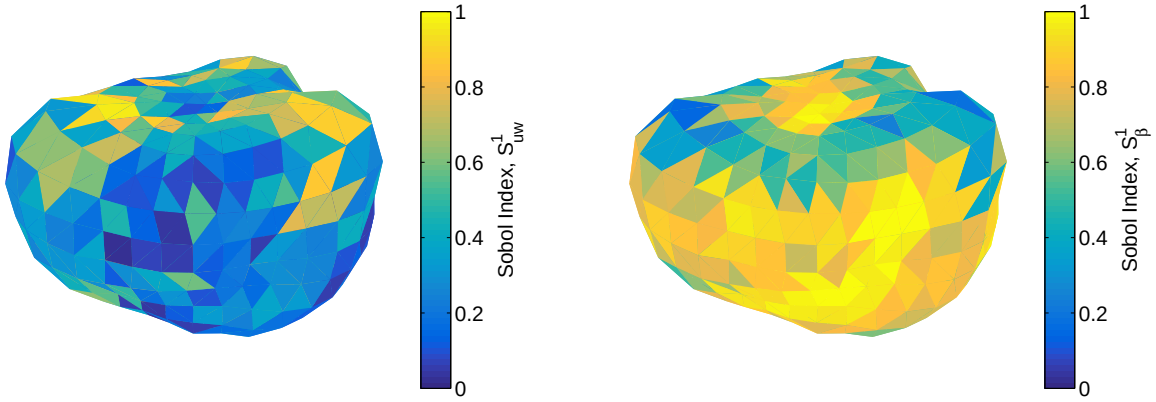


(a) Sensitivity to the impact location

(b) Sensitivity to $\beta$

Figure 7.15: First order Sobol' indices of the variance in the expected $\Delta V$ for the asteroid Yorp.

In the spatial distribution of the $\Delta V$ provided in Fig. 7.17, the long smooth sides of this asteroid correspond to regions of higher $\Delta V$, while the narrow ends correspond to drops in magnitude. The orientation of each of these regions is consistent with previous conclusions regarding the correlation between the effective $\Delta V$ and the angle of the local surface with respect to the center of the body.

Figure 7.19 shows that the uncertainty in the distribution of the $\Delta V$ for Nereus is again more

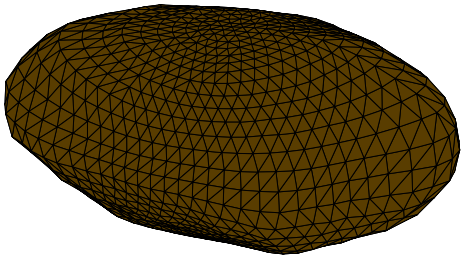

Figure 7.16: Triangular facet shape model for the asteroid Nereus.

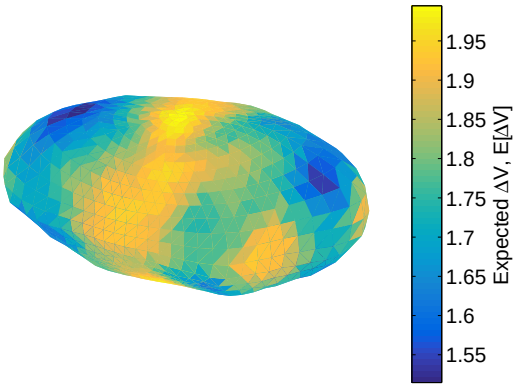


(a) Mean expected $\Delta V$

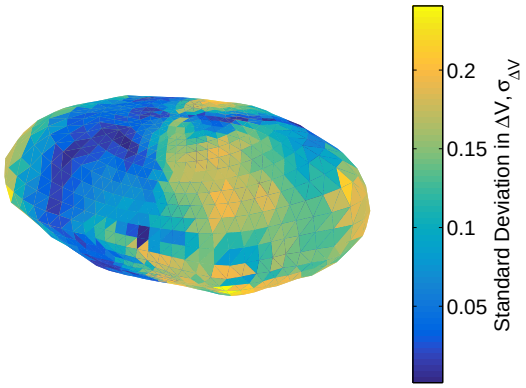


(b) Variance in expected $\Delta V$

Figure 7.17: Spatial distribution of the mean and standard deviation in the expected $\Delta V$ for the asteroid Nereus under constant shape model assumptions.

sensitive to variations in the $\beta$ parameter about most of the body, leaving Golevka as the only one of the four asteroids considered in this study to be primarily impacted by uncertainty in the impact location over a sizable portion of its surface. Thus it can be concluded that the relative influence of the uncertain input parameters is dependent not on the general shape of the asteroid, but more specifically on the presence of localized irregularities and steep surfaces about the body, such as the ridges found on Golevka.

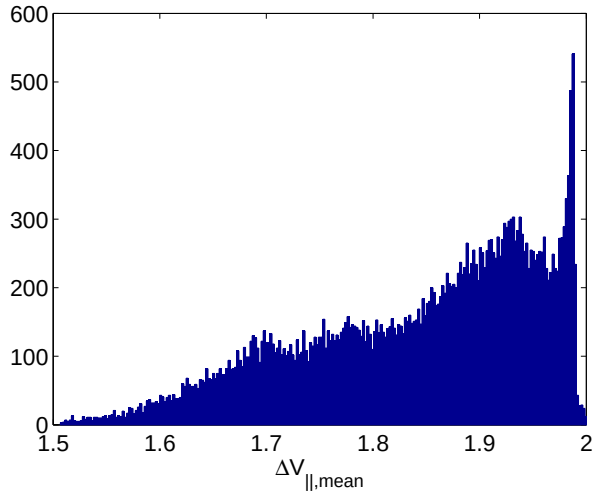


Figure 7.18: Frequency distribution of the mean expected $\Delta V$ for the asteroid Nereus under constant shape model assumptions.

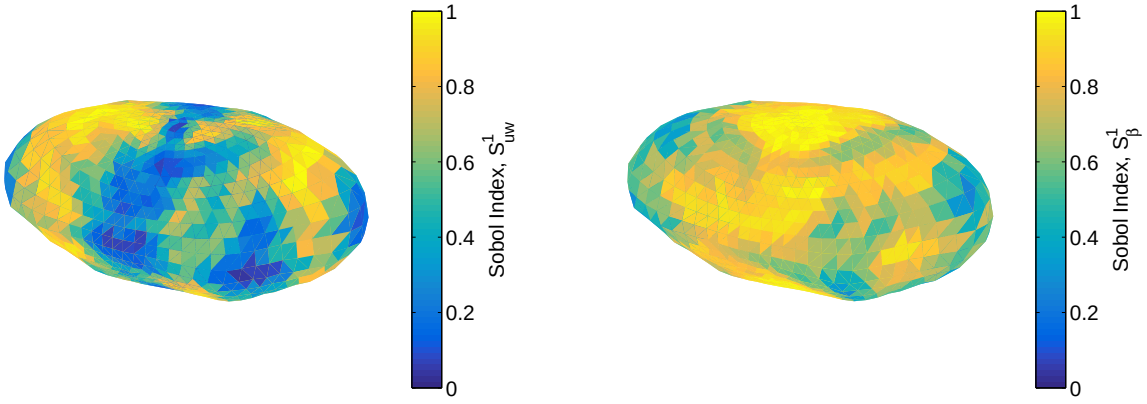


(a) Sensitivity to the impact location

(b) Sensitivity to $\beta$

Figure 7.19: First order Sobol' indices of the variance in the expected $\Delta V$ for the asteroid Nereus.

## 7.5 Asteroid Survey

Finally, the Gaussian mixtures method is applied to the collection of asteroids listed in Appendix A. Figure 7.20 presents the distributions on the resulting $E[\Delta V]$ for impact locations about each body. These distributions, which differ significantly depending on the asteroid, reiterate

the sensitivity of the imparted $\Delta V$ to the asteroid topography. Both the range and the skewness of the $\Delta V$ varies greatly across the set of asteroid models. Asteroids such as 1994CC experience less than a 10% spread in the expected $\Delta V$, whereas Mithra shows losses of almost 50% between its maximum and minimum values.

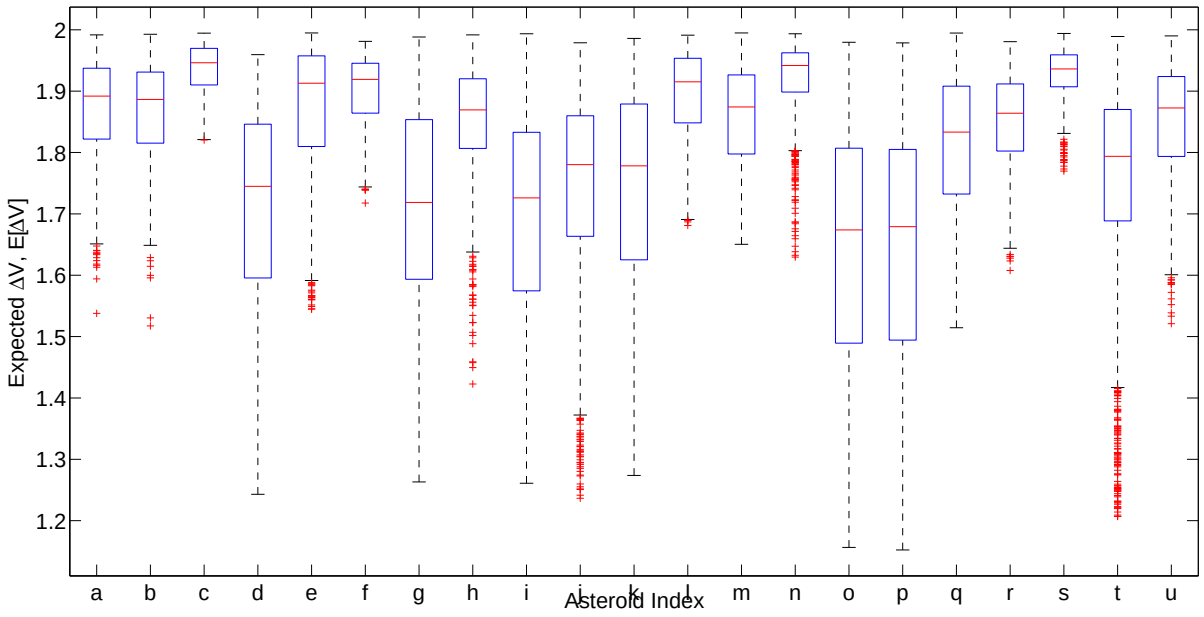


Figure 7.20: Distribution of $\Delta V$ for the asteroid models listed in Appendix A. Center lines indicate the median values, box edges indicate the $25^{th}$ and $75^{th}$ percentiles, end lines indicate the extrema, and hash marks indicate outliers.

The results for these two extremes, as projected onto their respective shape models, are provided in Fig. 7.21 (from Fig. 7.21b, it is evident that some faces are not accessible to an impactor directed through the asteroid's COM; these faces are omitted from the analysis but have been colored based on interpolation of the surrounding faces for simplicity in presentation of the figure). Not surprisingly, 1994CC is fairly spherical in shape, such that many of its surfaces are nearly perpendicular in relation to the body's center. As discussed previously, these regions experience higher realizations of the imparted $\Delta V$, resulting in a distribution in the expected $\Delta V$ that is concentrated at the higher end of the scale. Mithra, on the other hand, is very irregular in shape.

The many faces for which the surface normal is oriented at a steep angle with respect to the body's center lead to more disperse distributions, as these areas experience significant inefficiencies in the effective $\Delta V$. Individual results for the expected $\Delta V$ for each of the asteroid bodies included in the survey are contained in Appendix B, and the corresponding sensitivity indices can be found in Appendices C and D.

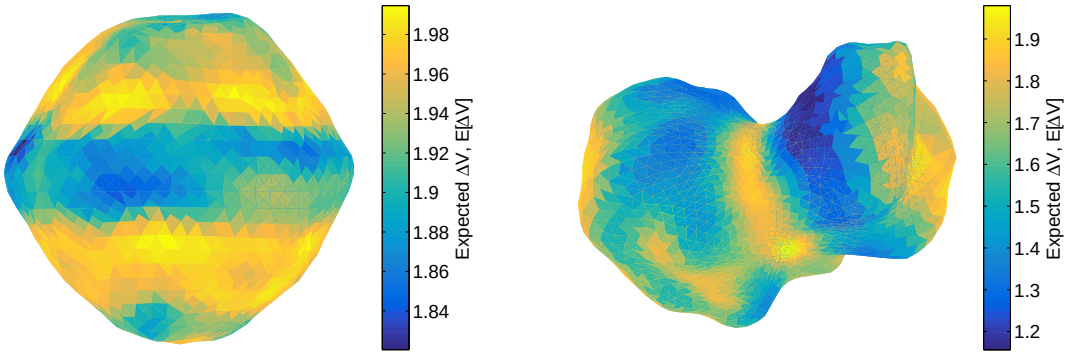


(a) 1994CC

(b) Mithra (prograde)

Figure 7.21: Spatial distributions of the mean expected $\Delta V$ for the asteroids 1994CC and Mithra.

# Chapter 8

# Conclusions and Future Work

This dissertation has explored the ability to efficiently and tractably characterize uncertainties inherent in astrodynamic systems and to incorporate these uncertainties into the design and optimization of spacecraft missions. This chapter reviews the main contributions and results produced by this research and suggests areas for future work to further improve the methods and analysis that were presented here.

## 8.1 Summary of Results

A model was first generated to represent the $\Delta V$ required for rendezvous in a halo orbit as a function of the initial position $\tau$ of the chaser, the time of flight $t$, and the initial separation $\Delta\tau$ between the spacecraft. For this case, an RMS error of $< 0.25$ m/s was achieved by a $9^{\text{th}}$ order expansion generated from 700 training samples. Because of the relatively high expansion order of the model, the use of asymptotic sampling was then shown to enable a reduction in the number of training data to 500 samples. Further, the ability to generate the model autonomously was demonstrated using the method of $k$-fold cross validation, which produced a $9^{\text{th}}$ order expansion for the system with no *a priori* knowledge on the expansion order or sample size necessary for convergence. This model was subsequently used both to minimize the $\Delta V$ required for rendezvous and to conduct global sensitivity analysis on the system. The sensitivity indices revealed that the initial separation of the spacecraft has the most significant influence on the required $\Delta V$, while the initial position of the chaser had the weakest effect.

Once the surrogate framework was developed for spacecraft rendezvous, it was used to construct a model for the problem of rendezvous in a distant retrograde orbit (DRO) by simply changing the training data used to solve for the expansion coefficients. For this case, both 2- and 3-dimensional design problems were considered. In the 2-dimensional problem, which included only the time of flight and initial separation of the spacecraft, 60 training samples were sufficient to produce an RMS error of $< 10^{-3}$, while the 3-dimensional design model resulted in the same level of accuracy with a sample size of 620. Again, the sensitivity indices revealed that the $\Delta V$ required for rendezvous is most sensitive to the initial $\Delta\tau$.

Next, the design surrogates were integrated with polynomial chaos expansions (PCEs) to produce stochastic design models for the purpose of optimization under uncertainty (OUU). When applied to the problem of rendezvous in three-body orbits with the three design parameters and a 3-dimensional maneuver execution error, the $k$-fold validation algorithm converged on a $5^{\text{th}}$ order expansion using 1290 sample points for both the halo orbit and the DRO. However, a $5^{\text{th}}$ order sparse model generated using orthogonal matching pursuit (OMP) was able to obtain comparable accuracy to the dense model for only 200 samples in the halo orbit and 250 samples in the DRO, a cost reduction of 80-85%. The surrogate models enabled the use of analytic formulas for the final state statistics of the chaser, which agreed with the results on the final position variance computed from a Monte Carlo simulation to $< 0.5$ m$^2$ in the halo orbit and $< 10^{-1}$ m$^2$ in the DRO. The final surrogate constructed for the rendezvous problem added the initial state uncertainties of the chaser to the stochastic space, resulting in a 12-dimensional problem. $5^{\text{th}}$ order sparse models of the system were built for each type of orbit using only 450 realizations.

The stochastic design models were then used to perform robust design for spacecraft rendezvous by taking advantage of the analytic formulation of the final state variance to constrain the final position variance of the chaser in one or all dimensions. Although the constraints did not affect the solution when the cost function consisted only of the nominal $\Delta V$, differences in the position variance on the order of 100 m$^2$ were seen between the constrained and unconstrained optima for a weighted cost function consisting of the nominal $\Delta V$ and the initial separation between the

spacecraft. For the case of the DRO, an improvement of $\sim 400$ m$^2$ in the $N$ and $W$ components of position variance resulting from a constraint of 50 m$^2$ on the in-track position variance came at an additional $\Delta V$ cost of only 5 cm/s, highlighting the potential of informed mission planning in improving the mission design process.

Finally, alternative methods were developed for uncertainty quantification in the analysis of the kinetic deflection of potentially hazardous asteroids due to the inability of surrogate models to accurately capture non-smooth behavior such as the sharp changes in the imparted $\Delta \boldsymbol{V}$ at the boundary between two facets in the asteroid shape models. These alternative methods allowed for the analytic computation of the expected $\Delta V$ imparted to an asteroid as a function of the impact location of the spacecraft and the $\beta$-parameter of the asteroid, both of which are stochastic parameters, and consideration was also given to uncertainty in the shape model of the asteroid body. The techniques used to model the system included converting uncertainty in the impact trajectory into the probability of impacting each of the facets in the shape model and then using a Gaussian mixtures method to map the impact probabilities and the uncertainty in $\beta$ to the effective momentum transfer.

## 8.2 Conclusions

This research demonstrated that surrogate models can provide a low cost, tractable means of characterizing the design space for spacecraft missions and enabling trajectory optimization under uncertainty. Further, while standard regression models generated using realizations from a traditional Monte Carlo sampling measure were shown to be capable of providing good accuracy in the solution to the system response, careful selection of the techniques used for the design of experiments (DOE), model estimation, and model validation can improve the models by reducing the number of training data required for convergence and enabling autonomous generation of the surrogates. For example, in the case of deterministic maneuver design for rendezvous in three-body orbits, which requires a high order expansion to accurately characterize the system, the use of an asymptotic sampling measure in the DOE cut the required sample size by almost 30%. The

stochastic design models, on the other hand, yielded sparse solutions to the system, allowing for the use of sparse estimation methods. By leveraging the sparsity in the solution, the number of training samples was reduced by 80-85% compared to the dense model.

In addition to reducing the number of training samples necessary for convergence, the use of OMP enabled the initial state uncertainties of the chaser to be modeled in addition to the maneuver execution errors and the three design parameters. A $5^{\text{th}}$ order dense model of this 12-dimensional problem would result in 8008 expansion terms, requiring a very large sample size and causing computational issues in the solution of the coefficients. Thus, the use of dense surrogates to model such high-dimensional systems would likely be unfeasible.

Both the deterministic and stochastic design models demonstrated significant cost reductions in comparison to Monte Carlo simulations. When the surrogate model constructed for the 2-dimensional design problem in the DRO was compared to a Monte Carlo analysis of the same problem previously conducted by NASA, the surrogates were shown to be capable of providing more complete information on the dynamical system for just over half computational cost of the Monte Carlo. Further, extending the model to the 3-dimensional design problem revealed important trends in the system response that were not evident from the Monte Carlo simulation.

The application of the regression models to the problem of robust design yielded even more significant reductions in computational cost. While the use of Monte Carlo simulations for OUU requires on the order of $10^5 - 10^6$ realizations to converge in the propagated variance at each candidate solution to the cost function, the analytic formulation of the final state variance enabled by the surrogate allowed for the propagation of uncertainty at no additional cost beyond that required to initially generate the model. Therefore, when the number of function calls made by the optimizer is taken into account, the stochastic design surrogates require 4-5 orders of magnitude fewer realizations of the full system dynamics for the purpose of robust design.

Finally, alternative methods were shown to be useful for uncertainty quantification and design analysis in systems ill-suited to the use of polynomial surrogates. By applying analytic models to a survey of real asteroid shapes, the effective transfer of momentum to an asteroid during a kinetic

deflection attempt was shown to have a strong dependence on both the local topography and the surface material properties of the asteroid. Analysis of impact with the asteroid Golevka revealed a variation of 34% in the magnitude of the expected effective $\Delta V$ about the body that is attributable solely to the asteroid topography, with the greatest losses in the effective momentum occurring in regions with steep surface angles. The variance of the $\Delta V$ in these same regions was found to be most sensitive to uncertainties in the impact location of the spacecraft, while the variance of the imparted $\Delta V$ from impact with flatter areas of the asteroid was most sensitive to uncertainty in the $\beta$-parameter. Changes in the mean value of $\beta$ also produced losses in the expected $\Delta V$ of approximately the same order of magnitude as the losses caused by the topography of the body, suggesting that proper characterization of the asteroid's material properties is equally important in gaining a complete understanding of the effects of kinetic impact. Conversely, the incorporation of uncertainty in the shape model itself was not found to contribute to the uncertainty in the momentum transfer. Finally, the amount of variability in the expected $\Delta V$ of the asteroid differed greatly for each of the asteroid shapes included in a survey of 21 asteroid models. Those asteroids that were most nearly spherical in shape experienced variations of only 10% in the expected $\Delta V$ about the body, while the most irregularly shaped asteroids were subject to variations of more than 50%.

## 8.3 Future Work

A number of opportunities exist for continuing the work presented in this thesis in order to further expand the capabilities of the methods that were developed and to increase the scope of the analysis for each of the systems. This section presents recommended improvements for the stochastic surrogate design models and suggests an extension to the analysis of the kinetic deflection of asteroids.

One area open for further development in the robust design methods is the optimization of the design of experiments (DOE) for the stochastic sparse design models. Hampton and Doostan have shown in [49] that the DOE for dense models generated via least-squares regression can be

optimized through the use of coherence-optimal sampling, which bounds the probabilistic coherence parameter of the system and in turn bounds the number of samples necessary for convergence of the model. The same approach, which is based on Markov Chain Monte Carlo (MCMC) sampling, is advanced in [48] for use in the $l_1$-minimization of sparse models. To optimize the sampling method for models generated via OMP, the equivalent parameter that must be bounded is the *mutual coherence parameter*. Work therefore needs to be done showing that the coherence-optimal MCMC sampling does, in fact, yield a bound on the mutual coherence. The coherence-optimal sampling method can then be applied to the problem of robust design of rendezvous maneuvers to further reduce the number of samples necessary to generate the stochastic design models.

Additional work lies in further automating the robust design process, an effort that will involve several steps. First, the $k$-fold cross-validation algorithm used to generate the deterministic models in Section 5.1 and the dense stochastic models in Section 5.2 can be adapted for the construction of sparse models using OMP. As currently implemented for the rendezvous problem, the OMP algorithm requires a user-defined expansion order and sample size. It is of interest to be able to instead generate the sparse models with no *a priori* knowledge on either of these model parameters. The ability to construct a sparse model via OMP using the $k$-fold algorithm was developed in [135], and this approach can be directly applied to the models presented here.

Another necessary step in automating the process of robust design is to bridge the gap between the broad design space considered for the optimization of the deterministic design models and the more localized design space considered for optimization under uncertainty. In the current models, the high expansion order required to accurately model the broader design space for initial mission design combined with the high dimensionality of the stochastic models used in robust design would result in an extremely large number of expansion terms and a correspondingly large sample size to generate the models. Further, the ability to use compressive sampling techniques to limit the number of terms included in the model is impeded by the lack of sparsity in the deterministic models that represent the full design space. Therefore, a modified approach is necessary to enable robust design over the full design space considered in Section 5.1.

One option for bridging the gap is to use multi-element models to reduce the dimensionality of the problem. In multi-element methods, the input parameter space is divided into collection of elements, and the full system is represented by a weighted set of models generated for each element of the parameter space. The weight corresponding to each of the elements is proportional to the probability of a sample realization falling within that element. Decomposition of the state space continues until either the model error is sufficiently small in each of the elements or until the weights associated with any elements producing large modeling errors are small enough that those elements do not contribute significantly to the total error of the model. Using multi-element methods in the deterministic dimensions of the full design space may reduce the expansion order required in each element enough to accommodate the high dimensionality of the stochastic space.

Another opportunity for enabling robust design over the broader design space lies in the application of multi-fidelity models [5]. Multi-fidelity methods use coarse models to provide an initial estimate of the optimal solution to the problem. Once the general location of the optimal solution has been identified, high fidelity models are generated for the area immediately about the nominal design point. The transition from the coarse to the fine models in multi-fidelity models is fully automated. If each of these modifications are made to the stochastic surrogate models, the capabilities of the robust design tools for the purpose of mission and trajectory design would be greatly enhanced.

Finally, in the characterization of uncertainties in the kinectic deflection of asteroids, the primary area for future work is to extend the analysis presented in this dissertation by propagating the variability in the imparted $\Delta V$ to the time at which the asteroid intersects the Earth's orbit. By propagating to the time of intersect, the distribution in the $\Delta V$ acting on the asteroid is converted into the more concrete concept of probability of impact.

## Bibliography


[1] Milton Abramowitz and Irene A. Stegun. Handbook of Mathematical Functions: with Formulas, Graphs, and Mathematical Tables. Dover Publications, New York, 1965.

[2] Thomas J. Ahrens and Alan W. Harris. Deflection and fragmentation of near-earth asteroids. Nature, 360(6403):429–433, 1992.

[3] Leon Alkalai, Benjamin Solish, John Elliott, Tim McElrath, Joergen Mueller, and Jeffrey Parker. Orion / moonrise : A proposed human & robotic sample return mission from the lunar south pole-aitken basin. In Proceedings of the IEEE Aerospace Conference, Big Sky, MT, 2013.

[4] Dale Arney and Alan Wilhite. Visualization of the multidimensional human interplanetary mission design space. Journal of Spacecraft and Rockets, 46(6):1325–1328, 2009.

[5] J. W. Bandler, Q. S. Cheng, S. A. Dakroury, A. S. Mohamed, M. H. Bakr, K. Madsen, and J. Sondergaard. Space mapping: the state of the art. Microwave Theory and Techniques, IEEE Transactions on, 52(1):337–361, 2004.

[6] Brent W. Barbee, Ronald G. Mink, and Daniel R. Adamo. Methodology and results of the near-earth object ( neo ) human space flight ( hsf ) accessible targets study ( nhats ). In AAS/AIAA Astrodynamics Specialist Conference, Girdwood, AK, 2011.

[7] J. F. M. Barthelemy and R. T. Haftka. Approximation concepts for optimum structural design - a review. Structural Optimization, 5:129–144, 1993.

[8] Roger R. Bate, Donald D. Mueller, and Jerry E. White. Fundamentals of Astrodynamics. Dover Publications, New York, NY, 1971.

[9] John P. Boyd. Chebyshev and Fourier Spectral Methods: Second Revised Edition. Courier Corporation, 2001.

[10] John R. Brophy and Brian Muirhead. Near-earth asteroid retrieval mission (arm) study. In 33rd International Electric Propulsion Conference, Washington, DC, 2013.

[11] R. A. Broucke. Periodic orbits in the restricted three-body problem with earth-moon masses, nasa technical report 32-1168. Technical report, Jet Propulsion Laboratory, Pasadena, CA, 1968.

[12] Megan Bruck Syal, J. Michael Owen, and Paul M. Miller. Deflection by kinetic impact: Sensitivity to asteroid properties. Icarus, 2016.

[13] Megan Bruck Syal, J. Michael Owen, and Cody Raskin. Disruption limits of kinetic-impactor mitigation scenarios. In William Ailor and Richard J. Tremayne-Smith, editors, Proceedings of the 4th IAA Planetary Defense Conference, Frascati, Roma, Italy, 2015.

[14] M. D. Buhmann. Radial basis functions. Acta Numerica, 9(January 2000):1–38, 2000.

[15] H. Burkill. Sums of trigonometric series. Proceedings of the London Mathematical Society, 12(1):690–706, 1962.

[16] Jack O. Burns, David A. Kring, Joshua B. Hopkins, Scott Norris, T. Joseph W. Lazio, and Justin Kasper. A lunar l2-farside exploration and science mission concept with the orion multi-purpose crew vehicle and a teleoperated lander/rover. Advances in Space Research, 52:306–320, 2013.

[17] Richard H. Byrd, Mary E. Hribar, and Jorge Nocedal. An interior point algorithm for large-scale nonlinear programming. SIAM Journal on Optimization, 9(4):877–900, 1999.

[18] Albert Cohen, Mark A. Davenport, and Dany Leviatan. On the stability and accuracy of least squares approximations. Foundations of Computational Mathematics, 13:819–834, 2013.

[19] Gareth S. Collins, H. Jay Melosh, and Boris A. Ivanov. Modeling damage and deformation in impact simulations. Meteoritics and Planetary Science, 39(2):217–231, 2004.

[20] Bruce A. Conway. Near-optimal deflection of earth-approaching asteroids. Journal of Guidance, Control, and Dynamics, 24(5):1035–1037, 2001.

[21] Kyle Jordan DeMars. Nonlinear Orbit Uncertainty Prediction and Rectification for Space Situational Awareness. Ph.d., University of Texas at Austin, 2010.

[22] Michael Dodson and Geoffrey T. Parks. Robust aerodynamic design optimization using polynomial chaos. Journal of Aircraft, 46(2):635–646, mar 2009.

[23] Alireza Doostan and Houman Owhadi. A non-adapted sparse approximation of pdes with stochastic inputs. Journal of Computational Physics, 230(8):3015–3034, 2011.

[24] Norman R. Draper and Harry Smith. Applied Regression Analysis. John Wiley & Sons, Inc, New York, third edition, 1998.

[25] Bradley Efron and Robert J. Tibshirani. An Introduction to the Bootstrap. Chapman & Hall/CRC, New York, 1993.

[26] Michael Eldred. Recent advances in non-intrusive polynomial chaos and stochastic collocation methods for uncertainty analysis and design. In 50th AIAA/ASME/ASCE/AHS/ASC Structures, Structural Dynamics, and Materials Conference, number \, AIAA Paper 2009-2274, Reston, Virigina, may 2009. American Institute of Aeronautics and Astronautics.

[27] Michael S. Eldred. Design under uncertainty employing stochastic expansion methods. International Journal for Uncertainty Quantification, 1(2):119–146, 2011.

[28] R. Farmer, G. Cheng, H. Trinh, and K. Tucker. A design tool for liquid rocket engine injectors. In 36th AIAA/ASME/SAE/ASEE Joint Propulsion Conference & Exhibit, AIAA Paper 2000-3499, Huntsville, AL, 2000.

[29] Robert W. Farquhar. Station-keeping in the vicinity of collinear libration points with an application to a lunar communications problem. In Spaceflight Mechanics Specialist Symposium, pages 519–535, 1966.

[30] Robert W. Farquhar. Future missions for libration-point satellites. Astronautics and Aeronautics, 7:52–56, 1969.

[31] Juliana D. Feldhacker, Brandon A. Jones, and Alireza Doostan. Trajectory optimization under uncertainty for rendezvous in the crtbp. In 26th AAS/AIAA Space Flight Mechanics Conference, AAS Paper 16-471, Napa, CA, 2016.

[32] Juliana D. Feldhacker, Brandon A. Jones, Alireza Doostan, and Jerrad Hampton. Reduced cost mission design using surrogate models. Advances in Space Research, 57(2):588–603, 2016.

[33] Juliana D. Feldhacker, Brandon A. Jones, Alireza Doostan, Daniel J. Scheeres, and Jay W. McMahon. Kinetic deflection uncertainties for real asteroid shapes. In William Ailor and Richard J. Tremayne-Smith, editors, Proceedings of the 4th IAA Planetary Defense Conference, Paper IAA-PDC-15-P-67, Frascati, Roma, Italy, 2015.

[34] Juliana D. Feldhacker, Brandon A. Jones, Alireza Doostan, Daniel J. Scheeres, and Jay W. McMahon. Shape dependence of kinetic deflection for a survey of real asteroids. In AIAA/AAS Astrodynmics Specialist Conference, AAS Paper 15-642, Vail, CO, 2015.

[35] Alexander I.J. Forrester and Andy J. Keane. Recent advances in surrogate-based optimization. Progress in Aerospace Sciences, 45(1-3):50–79, jan 2009.

[36] Shawn E. Gano, Harold Kim, and Don E. Brown II. Comparison of three surrogate modeling techniques : Datascape, kriging, and second order regression. In 11th AIAA/ISSMO Multidisciplinary Analysis and Optimization Conference, number September, AIAA Paper 2006-7048, Portsmouth, Virginia, 2006.

[37] W. Gautschi. Orthogonal Polynomials: Computation and Approximation. Oxford University Press, New York, NY, 2004.

[38] Seymour Geisser. The predictive sample reuse method with applications. Journal of the American Statistical Association, 70(350):320–328, 1975.

[39] L. E. George and L. D. Kos. Interplanetary mission design handbook : Earth-to-mars mission opportunities and mars-to-earth return opportunities 2009-2024. Technical Report NASA / TM-1998-208533, NASA Scientific and Technical Information Program Office, Newport News, VA, 1998.

[40] Roger G. Ghanem and Pol D. Spanos. Stochastic Finite Elements: A Spectral Approach. Springer-Verlag, New York, NY, 1991.

[41] Pradipto Ghosh and Bruce A. Conway. Near-optimal feedback strategies synthesized using a spatial statistical approach. Journal of Guidance, Control, and Dynamics, 36(4):905–919, jul 2013.

[42] Philip E. Gill, Walter Murray, and Michael A. Saunders. Large-scale sqp methods and their application in trajectory optimization. International Series of Numerical Mathematics, 115:29–42, 1994.

[43] Daniel Giza, Puneet Singla, and Moriba Jah. An approach for nonlinear uncertainty propagation: Application to orbital mechanics. In AIAA Guidance, Navigation, and Control Conference, number August, AIAA Paper 2009-6082, Chicago, IL, 2009.

[44] Bryan Glaz, Tushar Goel, Li Liu, Peretz P. Friedmann, and Raphael T. Haftka. Multiple-surrogate approach to helicopter rotor blade vibration reduction. AIAA Journal, 47(1):271–282, 2009.

[45] Tushar Goel, Siddharth Thakur, Raphael T. Haftka, Wei Shyy, and Jinhui Zhao. Surrogate model-based strategy for cryogenic cavitation model validation and sesitivity evaluation. International Journal for Numerical Methods in Fluids, 58(March):969–1007, 2008.

[46] S. Gottschalk. Separating axis theorem. technical report tr96-02. Technical report, Department of Computer Science, UNC, Chapel Hill, 1996.

[47] S. Gottschalk, M. C. Lin, and D. Manocha. Obbtree: A hierarchical structure for rapid interference detection. In John Fujii, editor, Proceedings of the 23rd Annual Conference on Computer Graphics and Interactive Techniques SIGGRAPH '96, pages 171–180, Paper ACM-0-89791-746-4/96/008, New Orleans, LA, 1996. ACM Press.

[48] Jerrad Hampton and Alireza Doostan. Compressive sampling of polynomial chaos expansions: Convergence analysis and sampling strategies. Journal of Computational Physics, 280:363–386, jan 2014.

[49] Jerrad Hampton and Alireza Doostan. Coherence motivated sampling and convergence analysis of least squares polynomial chaos regression. Computer Methods in Applied Mechanics and Engineering, 290:73–97, 2015.

[50] Heather D. Hinkel, Scott P. Cryan, Christopher D'Souza, David P. Dannemiller, Jack P. Brazzel, Gerald L. Condon, William L. Othon, and Jacob Williams. Rendezvous and docking strategy for crewed segment of the asteroid redirect mission. In SpaceOps Conference, AIAA Paper 2014-1796, Pasadena, CA, 2014.

[51] Keith A. Holsapple and Kevin R. Housen. Momentum transfer in asteroid impacts. i. theory and scaling. Icarus, 221(2):875–887, 2012.

[52] Joshua Hopkins, William Pratt, Caley Buxton, Selena Hall, Andrew Scott, Robert Farquhar, and David Dunha. Proposed orbits and trajectories for human missions to the earth-moon l2 region. In 64th International Astronautical Congress, pages 1682–1703, Beijing, China, 2013.

[53] Joshua T. Horwood, Nathan D. Aragon, and Aubrey B. Poore. Adaptive gaussian sum filters for space surveillance tracking. IEEE Transactions on Automatic Control, 139(8):1777 – 1790, 2011.

[54] K.R. Housen and K.A. Holsapple. Deflecting asteroids by impacts: What is beta. In Steve Mackwell, Eileen Stansbery, and David Draper, editors, Lunar and Planetary Institute Science Conference, Vol. 43, Paper 2539, Woodlands, TX, 2012.

[55] Franz S. Hover and Michael S. Triantafyllou. Application of polynomial chaos in stability and control. Automatica, 42(5):789–795, may 2006.

[56] K. C. Howell and H. J. Pernicka. Numerical determination of lissajous trajectories in the restricted three-body problem. Celestial Mechanics, 41(1-4):107–124, 1987.

[57] Chao Hu and Byeng D. Youn. Adaptive-sparse polynomial chaos expansion for reliability analysis and design of complex engineering systems. Structural and Multidisciplinary Optimization, 43(3):419–442, sep 2010.

[58] R. Hudson. Radar observations and physical model of asteroid 6489 golevka. Icarus, 148:37–51, 2000.

[59] D. Izzo, V. M. Becerra, D. R. Myatt, S. J. Nasuto, and J. M. Bishop. Search space pruning and global optimisation of multiple gravity assist spacecraft trajectories. Journal of Global Optimization, 38(2):283–296, 2007.

[60] Dario Izzo. Optimization of interplanetary trajectories for impulsive and continuous asteroid deflection. Journal of Guidance, Control, and Dynamics, 30(2):401–408, 2007.

[61] R. Jin, W. Chen, and T. W. Simpson. Comparative studies of metamodelling techniques under multiple modelling criteria. Structural and Multidisciplinary Optimization, 23(1998):1–13, 2001.

[62] Brandon A. Jones and Alireza Doostan. Satellite collision probability estimation using polynomial chaos. Advances in Space Research, 52:1860–1875, 2013.

[63] Brandon A. Jones, Alireza Doostan, and George H. Born. Nonlinear propagation of orbit uncertainty using non-intrusive polynomial chaos. Journal of Guidance, Control, and Dynamics, 36(2):430–444, mar 2013.

[64] Brandon A. Jones, Nathan Parrish, and Alireza Doostan. Postmaneuver collision probability estimation using sparse polynomial chaos expansions. Journal of Guidance, Control, and Dynamics, 38(8):1425–1437, 2015.

[65] John L. Junkins, Maruthi R. Akella, and Kyle T. Alfrined. Non-gaussian error propagation in orbital mechanics. Journal of Astronautical Sciences, 44(4):541–563, 1996.

[66] Martin Jutzi. Sph calculations of asteroid disruptions : The role of pressure dependent failure models. Planetary and Space Science, 107:3–9, 2015.

[67] Martin Jutzi and Patrick Michel. Hypervelocity impacts on asteroids and momentum transfer i. numerical simulations using porous targets. Icarus, 229:247–253, 2014.

[68] Ralph Kahle, Gerhard Hahn, and Ekkehard Kührt. Optimal deflection of neos en route of collision with the earth. Icarus, 182:482–488, 2006.

[69] Andre I. Khuri and John A. Cornell. Response Surfaces: Designs and Analyses. Marcel Dekker, Inc, New York, NY, second edition, 1996.

[70] Nam H. Kim, Haoyu Wang, and Nestor V. Queipo. Efficient shape optimization under uncertainty using polynomial chaos expansions and local sensitivities. AIAA Journal, 44(5):1112–1115, 2006.

[71] Slawomir Koziel, David Echeverría-Ciaurri, and Leifur Leifsson. Surrogate-based methods. In Slawomir Koziel and Xin-She Yang, editors, Computational Optimization, Methods and Algorithms series: Studies in Computational Intelligence, chapter 3, pages 33–60. Springer-Verlag, 2011.

[72] R. G. Kraus, S. T. Stewart, D. C. Swift, C. A. Bolme, R. F. Smith, S. Hamel, B. D. Hammel, D. K. Spaulding, D. G. Hicks, J. H. Eggert, and G. W. Collins. Shock vaporization of silica and the thermodynamics of planetary impact events. Journal of Geophysical Research, 117, 2012.

[73] O. P. Le Maître, O. M. Knio, H. N. Najm, and R. G. Ghanem. Uncertainty propagation using wiener-haar expansions. Journal of Computational Physics, 197:28–57, 2004.

[74] O. P. Le Maître and Omar M. Knio. Spectral Methods for Uncertainty Quantification: With Applications to Computational Fluid Dynamics. Springer Science & Business Media, New York, NY, 2010.

[75] O. P. Le Maître, H. N. Najm, R. G. Ghanem, and O. M. Knio. Multi-resolution analysis of wiener-type uncertainty propagation schemes. Journal of Computational Physics, 197:502–531, 2004.

[76] D. T. Lee and B. J. Schachter. Two algorithms for constructing a delaunay triangulation. International Journal of Computer & Information Sciences, 9(3):219–242, 1980.

[77] Pedro Lopez, Mark A Mcdonald, Jose M Caram, Heather D Hinkel, Jonathan T Bowie, Paul A Abell, Bret G Drake, and Roland M Martinez. Extensibility of human asteroid mission to mars and other destinations. In SpaceOps Conference, AIAA Paper 2014-1699, Pasadena, CA, 2014.

[78] N. Lundborg. Strength of rock-like materials. International Journal of Rock Mechanics and Mining Sciences & Geomechanics Abstracts, 5(5):427–454, 1968.

[79] G. Matheron. Principles of geostatistics. Economic Geology, 58:1246–1266, 1963.

[80] Colin R. McInnes. Deflection of near-earth asteroids by kinetic energy impacts from retrograde orbits. Planetary and Space Science, 52:587–590, 2004.

[81] Jay W. McMahon and Daniel J. Scheeres. A statistical analysis of yorp coefficients. In John Spencer and Andrew Steffl, editors, American Astronomical Society, Division for Planetary Sciences Meeting #45 Abstracts, Paper 112.17, Denver, CO, 2013.

[82] Jay W. McMahon and Daniel J. Scheeres. The effect of shape model uncertainty on the geophysical predictions of binary asteroids. In Faith Vilas, editor, American Astronomical Society, Division for Planetary Sciences Meeting #46, Paper 503.05, Tucson, AZ, 2014.

[83] H. J. Melosh. A hydrocode equation of state for sio2. Meteoritics and Planetary Science, 42(12):2079–2098, 2007.

[84] Xu Ming and Xu Shijie. Exploration of distant retrograde orbits around moon. Acta Astronautica, 65:853–860, 2009.

[85] J.K. Mitchell, W.N. Houston, R.F. Scott, N.C. Costes, W.D. Carrier, and L.G. Bromwell. Mechanical properties of lunar soil: Density, porosity, cohesion, and angle of internal friction. In Proceedings of the Third Lunar Science Conference, Vol. 3, pages 3235–3253, Paper 1200, Houston, TX, 1972. The MIT Press.

[86] J.J. Monaghan. Smoothed particle hydrodynamics. Annual Review of Astronomy and Astrophysics, 30:543–574, 1992.

[87] D.C. Montgomery and E.a. Peck. Introduction to Linear Regression Analysis. John Wiley & Sons, Inc, New York, NY, 1992.

[88] A. Monti, F. Ponci, and T. Lovett. A polynomial chaos theory approach to the control design of a power converter. In 35th Annual IEEE Power Electronics Specialists Conference, volume 6, pages 4809–4813, Aachen, Germany, 2004. Ieee.

[89] Habib N. Najm. Uncertainty quantification and polynomial chaos techniques in computational fluid dynamics. Annual Review of Fluid Mechanics, 41(1):35–52, jan 2009.

[90] Yew S. Ong, Prasanth B. Nair, and Andrew J. Keane. Evolutionary optimization of computationally expensive problems via surrogate modeling. AIAA Journal, 41(4):687–696, apr 2003.

[91] J. M. Owen. Asph modeling of material damage and failure. In B. D. Rogers, editor, Proceedings of the 5th International SPHERIC SPH Workshop, Paper LLNL-PROC-430616, Manchester, United Kingdom, 2010.

[92] J. Michael Owen, Jens V. Villumsen, Paul R. Shapiro, and Hugo Martel. Adaptive smoothed particle hydrodynamics : Methodology ii. The Astrophysical Supplement Series, 116:155–209, 1998.

[93] Nilay Papila, Wei Shyy, Lisa Griffin, and Daniel J. Dorney. Shape optimization of supersonic turbines using global approximation methods. Journal of Propulsion and Power, 18(3):509–518, 2002.

[94] Jeffrey S. Parker. Families of low-energy lunar halo transfers. In AAS/AIAA Spaceflight Dynamics Conference, AAS Paper 06-132, Tampa, FL, 2006.

[95] Jeffrey S. Parker and Rodney L. Anderson. Low-Energy Lunar Trajectory Design. John Wiley & Sons, Inc, Hoboken, NJ, 2014.

[96] H. J. Peng, Q. Gao, Z. G. Wu, and W. X. Zhong. Symplectic adaptive algorithm for solving nonlinear two-point boundary value problems in astrodynamics. Celestial Mechanics and Dynamical Astronomy, 110:319–342, 2011.

[97] Haijun Peng, Xin Jiang, and Biaosong Chen. Optimal nonlinear feedback control of spacecraft rendezvous with finite low thrust between libration orbits. Nonlinear Dynamics, 76:1611–1632, 2014.

[98] Haijun Peng, Chunfeng Yang, Yunpeng Li, Sheng Zhang, and Biaosong Chen. Surrogate-based parameter optimization and optimal control for optimal trajectory of halo orbit rendezvous. Aerospace Science and Technology, 26(1):176–184, apr 2013.

[99] Ji Peng, Jerrad Hampton, and Alireza Doostan. A weighted 1-minimization approach for sparse polynomial chaos expansions. Journal of Computational Physics, 267:92–111, 2014.

[100] Mauro Pontani and Bruce A. Conway. Optimal finite-thrust rendezvous trajectories found via particle swarm algorithm. Advances in the Astronautical Sciences, 142(6):3781–3800, 2012.

[101] Mauro Pontani, Pradipto Ghosh, and Bruce a. Conway. Particle swarm optimization of multiple-burn rendezvous trajectories. Journal of Guidance, Control, and Dynamics, 35(4):1192–1207, 2012.

[102] Friedrich Pukelsheim. Optimal Design of Experiments. John Wiley & Sons, Inc, New York, NY, 1993.

[103] Marco Quadrelli, Lincoln Wood, Joseph E. Riedel, Michael C. McHenry, MiMi Aung, Laureano Cangahuala, Richard Volpe, Patricia M. Beauchamp, and James A. Cutts. Guidance navigation and control technology assessment for future planetary science missions. Journal of Guidance, Control, and Dynamics, 38(7), 2015.

[104] Nestor V. Queipo, Raphael T. Haftka, Wei Shyy, Tushar Goel, Rajkumar Vaidyanathan, and P. Kevin Tucker. Surrogate-based analysis and optimization. Progress in Aerospace Sciences, 41:1–28, 2005.

[105] Earl D. Rainville. Special Functions. The Macmillan Company, New York, NY, first edition, 1960.

[106] Holger Rauhut and Rachel Ward. Sparse legendre expansions via 1 -minimization. Journal of Approximation Theory, 164(5):517–533, 2012.

[107] Jason C. Reinhardt, Matthew Daniels, and M. Elisabeth Paté-cornell. Probabilistic analysis of asteroid impact risk mitigation programs. In Todd Paulos, Stephen Hora, and Curtis Smith, editors, Proceedings of the 12th Probabilistic Safety Assessment and Management Conference, Paper 151, Honolulu, HI, 2014.

[108] David B. Riddle, Roy J. Hartfield, John E. Burkhalter, and Rhonald M. Jenkins. Genetic-algorithm optimization of liquid-propellant missile systems. Journal of Spacecraft and Rockets, 46(1):151–159, 2009.

[109] Ryan Russell. Survey of spacecraft trajectory design in strongly perturbed environments. Journal of Guidance, Control, and Dynamics, 35(3):705–720, 2012.

[110] Chris Sabol, Christopher Binz, Alan Segerman, Kevin Roe, and W. Paul. Probability of collision with special perturbations dynamics using the monte carlo method. In AAS/AIAA Astrodynamics Specialist Conference, AAS Paper 2010-134, Girdwood, AK, 2011.

[111] Chris Sabol, Thomas Sukut, Keric Hill, Kyle T. Alfriend, Brendan Wright, You Li, and Paul Schumacher. Linearized orbit covariance generation and propagation analysis via simple monte carlo simulations. In 20th Annual AAS/AIAA Spaceflight Mechanics Meeting, AAS Paper 2010-134, San Diego, CA, 2010.

[112] A. Saltelli, T.H. Andres, and T. Homma. Sensitivity analysis of model output. Computational Statistics & Data Analysis, 15:211–238, 1993.

[113] A. Saltelli, K. Chan, and E. M. Scott, editors. Sensitivity Analysis. John Wiley & Sons, Ltd, New York, NY, 2000.

[114] Andrea Saltelli. Making best use of model valuations to compute sensitivity indices. Computer Physics Communications, 145:280–297, 2002.

[115] Thomas J. Santner, Brian J. Williams, and William Notz. The Design and Analysis of Computer Experiments. Springer Science & Business Media, New York, NY, 2003.

[116] Daniel J. Scheeres, Megan Bruck Syal, Jay W. McMahon, Juliana D. Feldhacker, Brandon A. Jones, Alireza Doostan, J. Michael Owen, Paul Miller, E. Herbold, and E. Asphaug. Characterizing the effect of asteroid topography on hazardous asteroid kinetic impact deflection. In William Ailor and Richard J. Tremayne-Smith, editors, Proceedings of the 4th IAA Planetary Defense Conference, Frascati, Roma, Italy, 2015.

[117] Daniel J. Scheeres, Jay W. Mcmahon, Brandon A. Jones, and Alireza Doostan. Variation of delivered impulse as a function of asteroid shape. In Proceedings of the 2015 IEEE Aerospace Conference, Big Sky, MT, 2015.

[118] T. W. Simpson, T. M. Mauery, J. Korte, and F. Mistree. Kriging models for global approximation in simulation-based multidisciplinary design optimization. AIAA Journal, 39(12):2233–2241, 2001.

[119] Timothy W. Simpson, Dennis K. J. Lin, and Wei Chen. Sampling strategies for computer experiments: Design and analysis, 2001.

[120] Jon A. Sims, Paul A. Finlayson, Edward A. Rinderle, Matthew A. Vavrina, and Theresa D. Kowalkowski. Implementation of a low-thrust trajectory optimization algorithm for preliminary design. In AIAA/AAS Astrodynmics Specialist Conference, AIAA Paper 2006-6746, Keystone, CO, 2006.

[121] Ralph C. Smith. Uncertainty Quantification: Theory, Implementation, and Applications. Society for Industrial and Applied Mathematics, Philadelphia, PA, 2014.

[122] I. M. Sobol'. Sensitivity estimates for nonlinear mathematical models. Mathematical Modeling and Computational Experiments, 1:407–414, 1993.

[123] Christian Soize and Roger Ghanem. Physical systems with random uncertainties: Chaos representations with arbitrary probability measure. SIAM Journal on Scientific Computing, 26(2):395–410, jan 2004.

[124] A. M. Stickle, J. A. Atchison, O. S. Barnouin, A. F. Cheng, D. A. Crawford, and C. M. Ernst. Modeling momentum transfer from kinetic impacts : Implications for redirecting asteroids. Procedia Engineering, 103:577–584, 2015.

[125] Bruno Sudret. Global sensitivity analysis using polynomial chaos expansions. Reliability Engineering & System Safety, 93(7):964–979, jul 2008.

[126] Ivan E. Sutherland and Gary W. Hodgman. Reentrant polygon clipping. Communications of the ACM, 17(1):32–42, 1974.

[127] Genichi Taguchi and Don Clausing. Robust quality. Harvard Business Review, 68(February):65–75, 1990.

[128] Byron D. Tapley, Bob E. Schutz, and George H. Born. Statistical Orbit Determination. Elsevier Inc, San Diego, CA, 1st edition, 2004.

[129] Gabriel Terejanu, Puneet Singla, Tarunraj Singh, and Peter D. Scott. Uncertainty propagation for nonlinear dynamic systems using gaussian mixture models. Journal of Guidance, Control, and Dynamics, 31(6):1623–1633, 2008.

[130] S.L. Thompson and H.S. Lauson. Improvements in the chart d radiation-hydrodynamic code iii: Revised analytic equations of state. sc-rr–71-0714. Technical report, Sandia National Laboratory, Albuquerque, NM, 1972.

[131] Rajkumar Vaidyanathan, Nilay Papila, Wei Shyy, P. Kevin Tucker, Lisa W. Griffin, Raphael T. Haftka, and Norman Fitz-Coy. Neural network and response surface methodology for rocket engine component optimization. In 8th AIAA/USAF/NASA/ISSMO Symposium on Multidisciplinary Analysis and Optimization, AIAA Paper 2000-4880, Long Beach, CA, 2000.

[132] David A. Vallado. Fundamentals of Astrodynamics and Applications. Springer, New York, third edition, 2007.

[133] Massimiliano Vasile and Camilla Colombo. Optimal impact strategies for asteroid deflection. Journal of Guidance, Control, and Dynamics, 31(4):858–872, 2008.

[134] Xiaoliang Wan and George Em Karniadakis. An adaptive multi-element generalized polynomial chaos method for stochastic differential equations. Journal of Computational Physics, 209(2):617–642, nov 2005.

[135] R. Ward. Compressed sensing with cross validation. IEEE Transactions on Information Theory, 55(12):5773–5782, 2009.

[136] Gary Gimeno Weickum. Reduced Order Models for Design Optimization Under Uncertainty. Ph.d., University of Colorado, 2009.

[137] Norbert Wiener. The homogeneous chaos. American Journal of Mathematics, 60(4):897–936, 1938.

[138] Dongbin Xiu. Fast numerical methods for stochastic computations : A review. 5(2):242–272, 2009.

[139] Dongbin Xiu. Numerical Methods for Stochastic Computations: A Spectral Method Approach. Princeton University Press, Princeton, NJ, 2010.

[140] Dongbin Xiu and George E. M. Karniadakis. The wiener-askey polynomial chaos for stochastic differential equations. SIAM Journal on Scientific Computing, 24(2):619–644, 2002.

# Appendix A

## List of Asteroid Shape Models

Table A.1: List of asteroids included in the asteroid survey of Chapter 7, with the number of facets comprising their respective shape models.

| Label | Asteroid Shape Model | # of Facets |
|---|---|---|
| (a) | 1950DA (retrograde) | 1016 |
| (b) | 1992SK | 1016 |
| (c) | 1994CC | 3996 |
| (d) | 1996HW1 (low res) | 2780 |
| (e) | 1998WT24 | 7996 |
| (f) | 2008EV5 | 3996 |
| (g) | Bacchus | 4092 |
| (h) | Betulia | 2292 |
| (i) | Castalia | 4092 |
| (j) | Golevka | 4092 |
| (k) | Itokawa (low res) | 768 |
| (l) | KW4 (alpha) | 9168 |
| (m) | KW4 (beta) | 2292 |
| (n) | KY26 | 4092 |
| (o) | Mithra (prograde) | 5996 |
| (p) | Mithra (retrograde) | 5996 |
| (q) | Nereus | 2292 |
| (r) | Rashalom | 2292 |
| (s) | RQ36 | 2292 |
| (t) | Toutatis (low res) | 12796 |
| (u) | Yorp | 572 |

# Appendix B

## Mean Expected $\Delta V$ for a Survey of Asteroid Shape Models

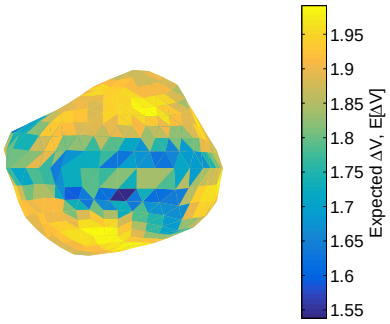


(a) 1950DA (retrograde)

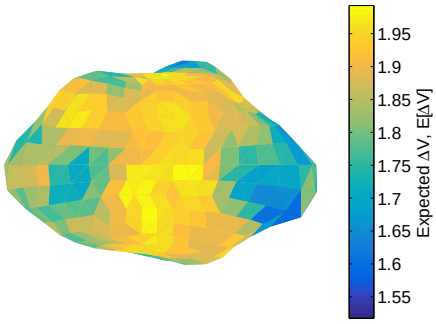


(b) 1992SK

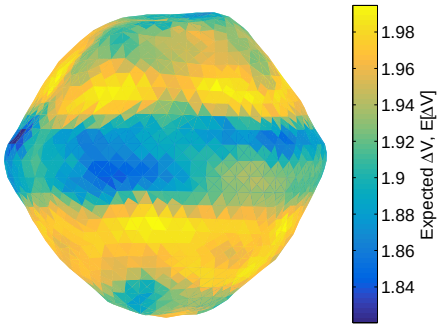


(c) 1994CC

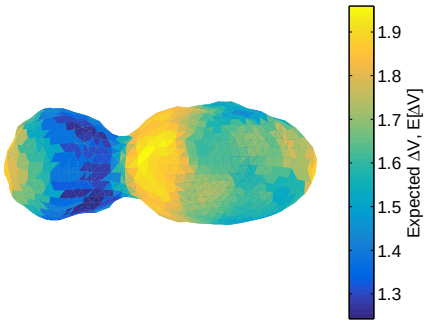


(d) 1996HW1 (low res)

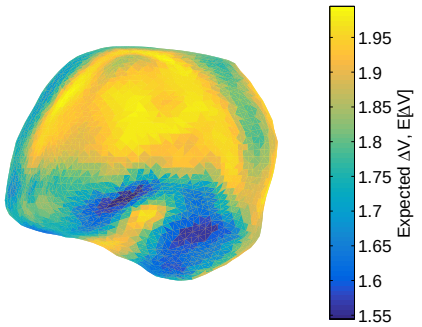


(a) 1998WT24

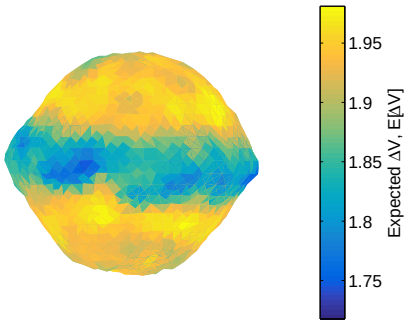


(b) 2008EV5

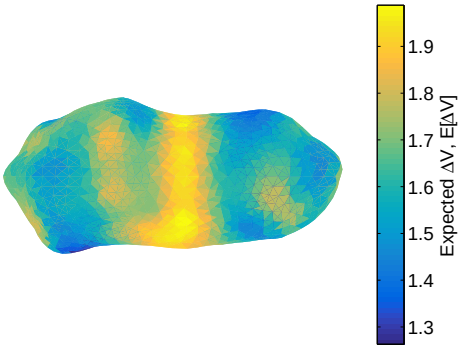


(c) Bacchus

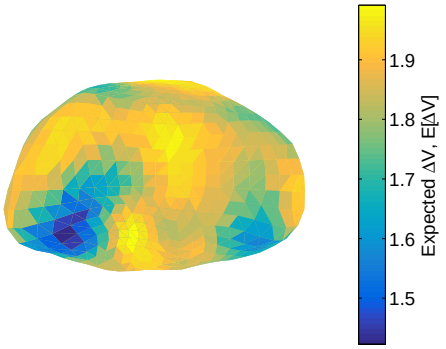


(d) Betulia

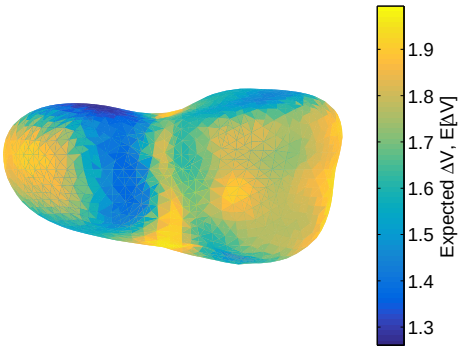


(e) Castalia

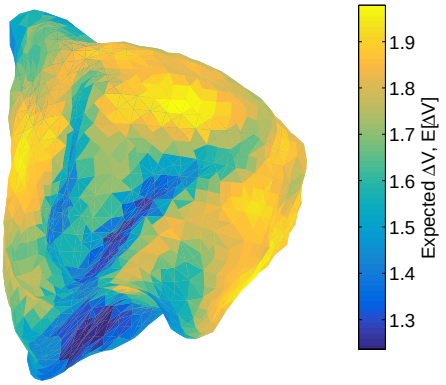


(f) Golevka

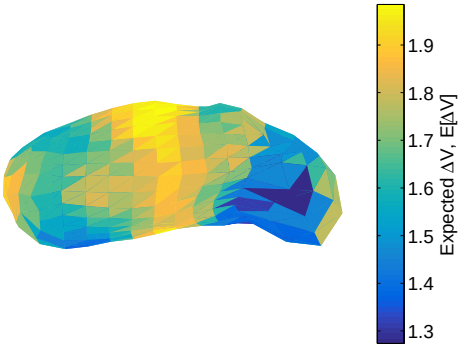


(a) Itokawa (low res)

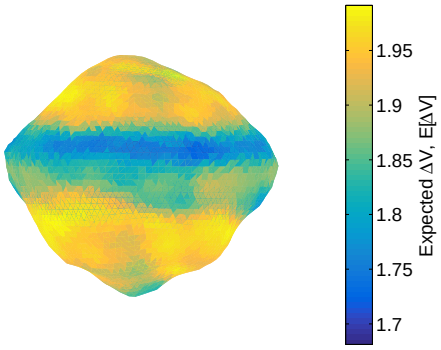


(b) KW4 (alpha)

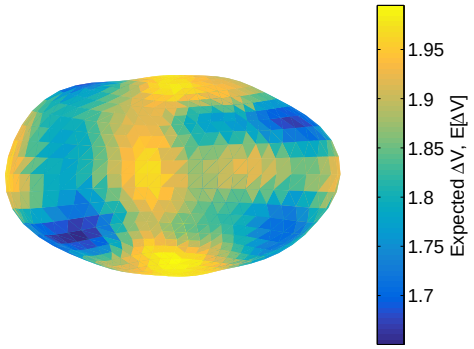


(c) KW4 (beta)

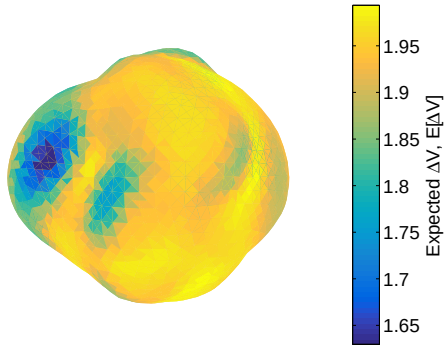


(d) KY26

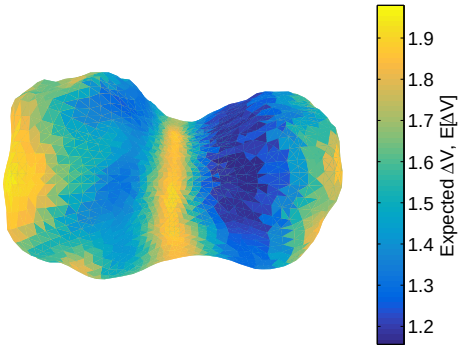


(e) Mithra (prograde)

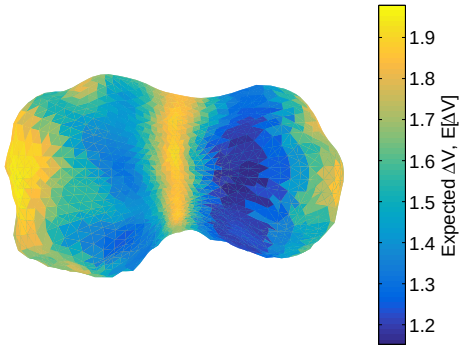


(f) Mithra (retrograde)

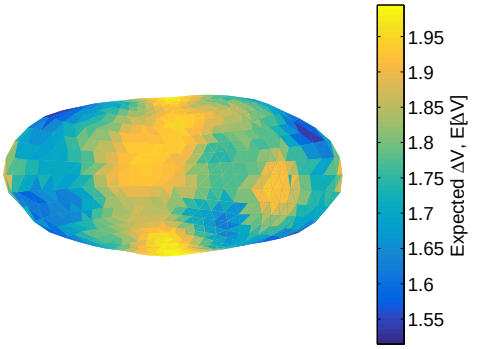


(a) Nereus

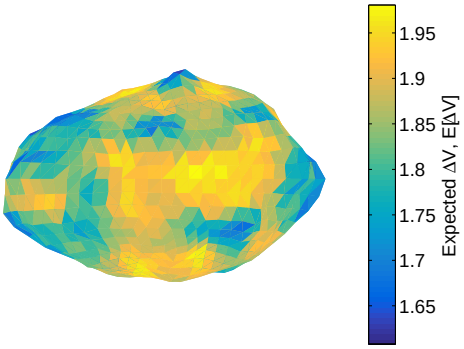


(b) Rashalom

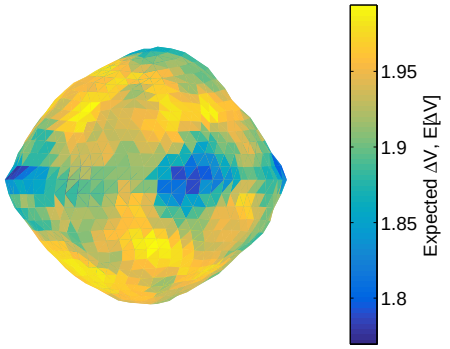


(c) RQ36

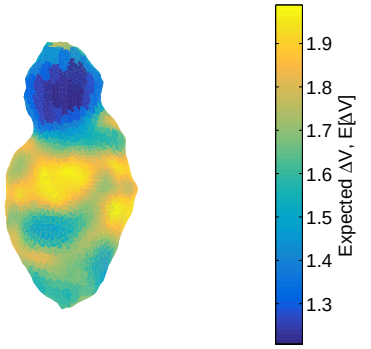


(d) Toutatis (low res)

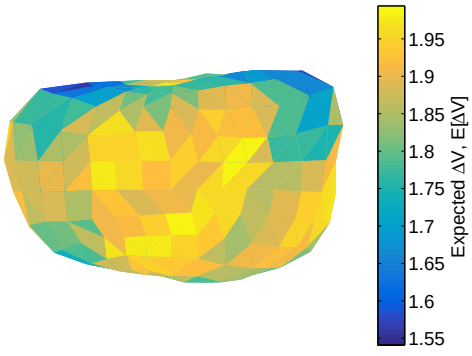


(e) Yorp

# Appendix C

## Sensitivity to Impact Location $S^1_{uw}$ for a Survey of Asteroid Shape Models

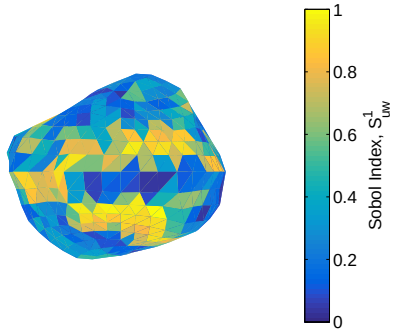


(a) 1950DA (retrograde)

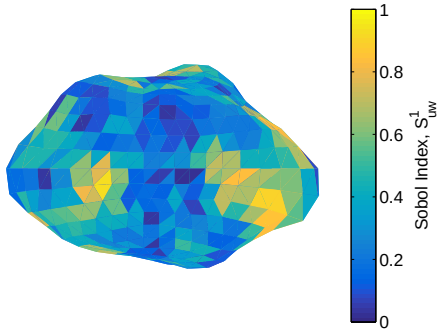


(b) 1992SK

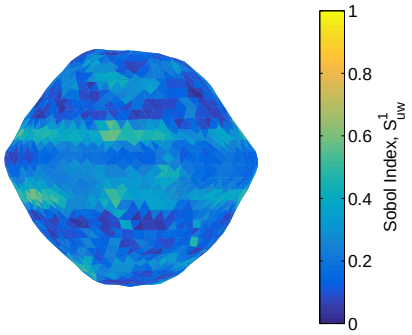


(c) 1994CC

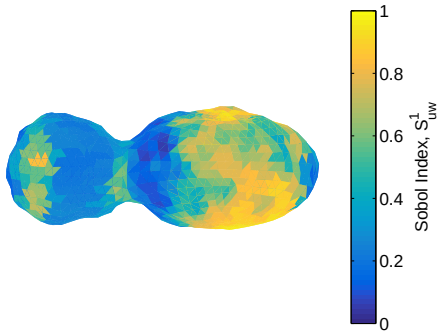


(d) 1996HW1 (low res)

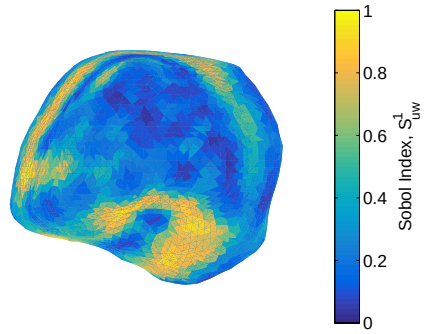


(a) 1998WT24

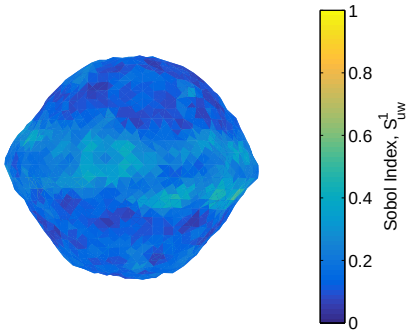


(b) 2008EV5

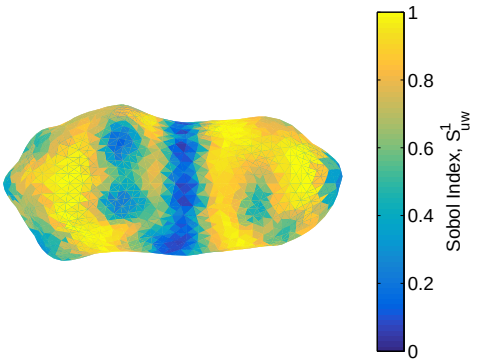


(c) Bacchus

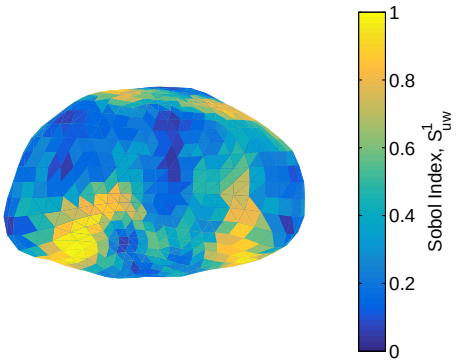


(d) Betulia

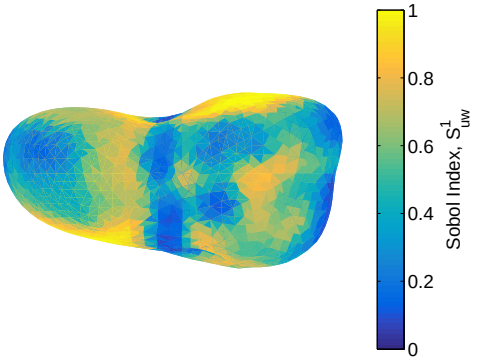


(e) Castalia

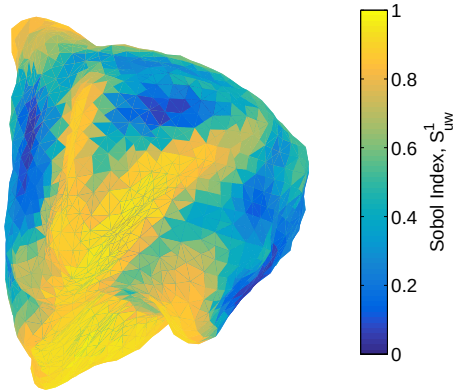


(f) Golevka

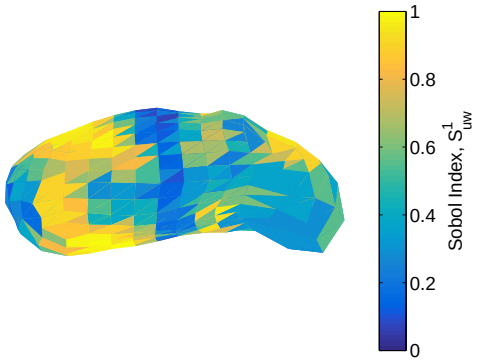


(a) Itokawa (low res)

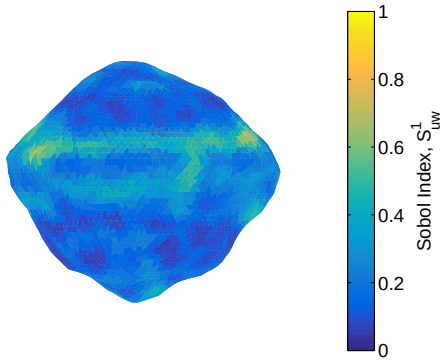


(b) KW4 (alpha)

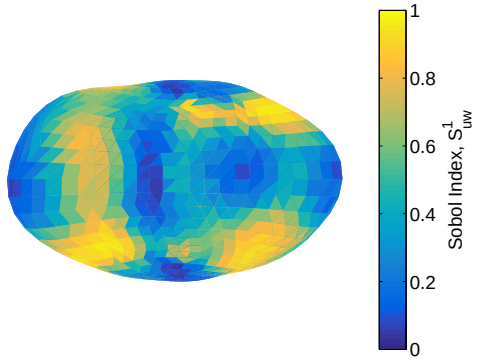


(c) KW4 (beta)

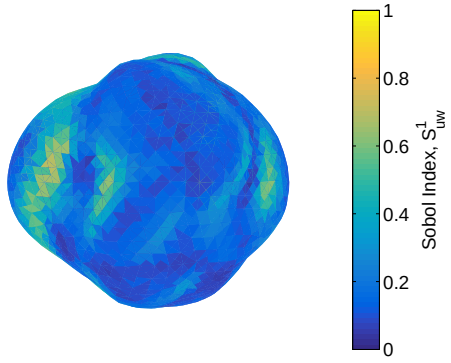


(d) KY26

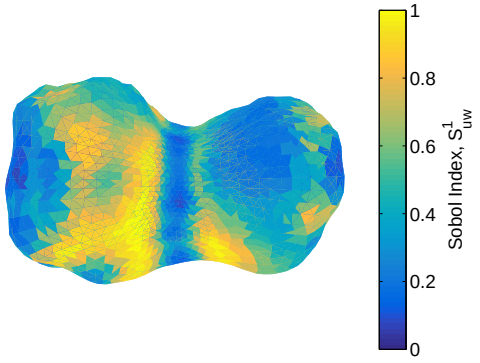


(e) Mithra (prograde)

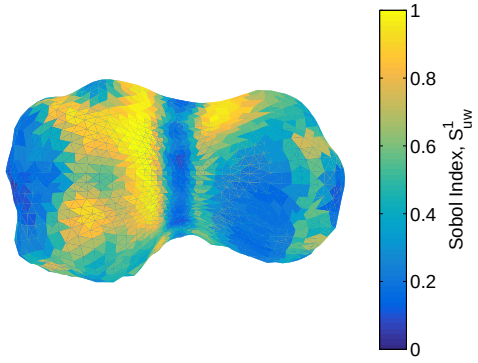


(f) Mithra (retrograde)

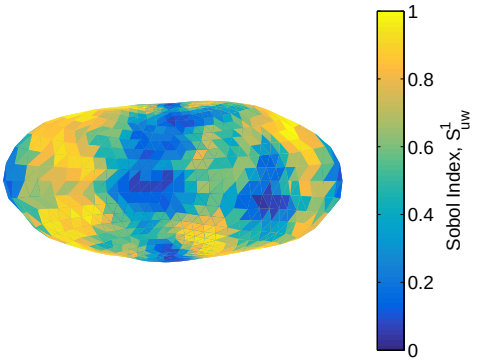


(a) Nereus

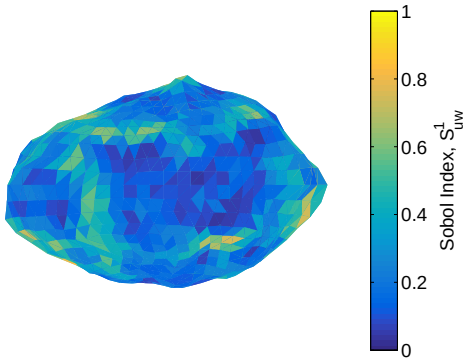


(b) Rashalom

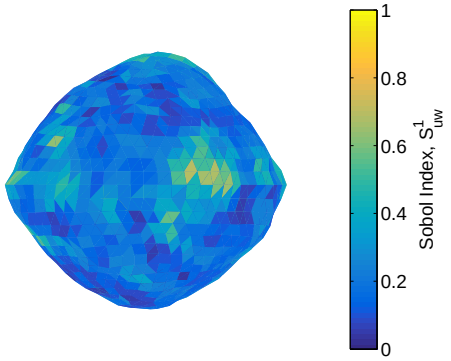


(c) RQ36

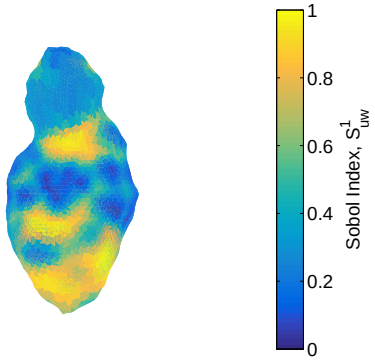


(d) Toutatis (low res)

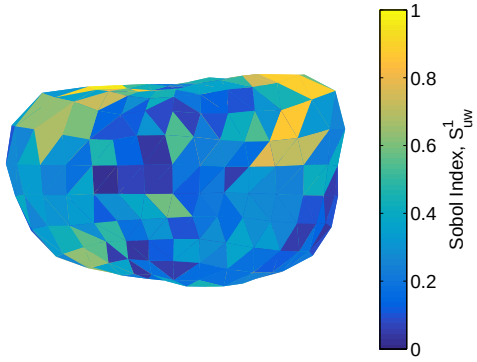


(e) Yorp

# Appendix D

## Sensitivity to $\beta$-Parameter $S^1_\beta$ for a Survey of Asteroid Shape Models

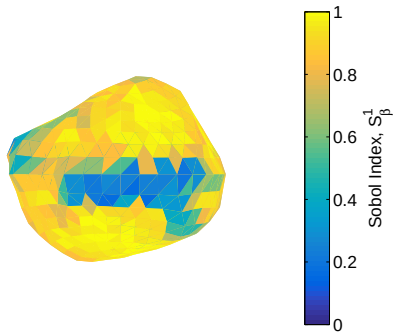


(a) 1950DA (retrograde)

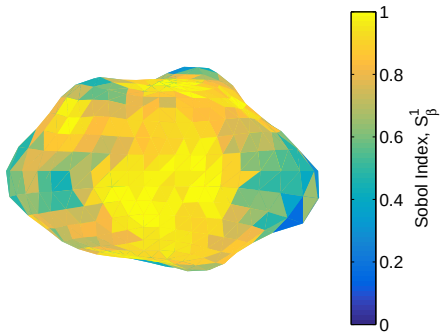


(b) 1992SK

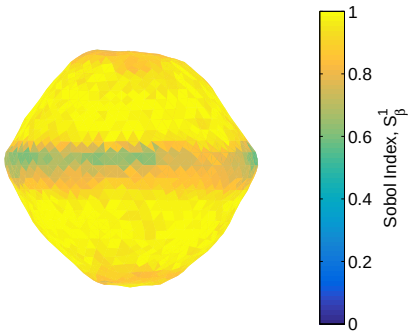


(c) 1994CC

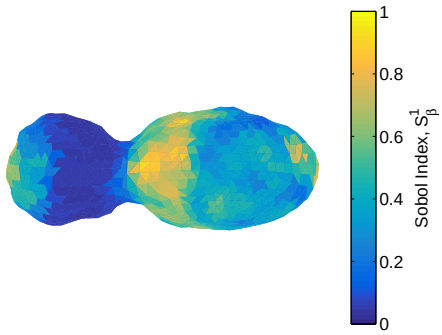


(d) 1996HW1 (low res)

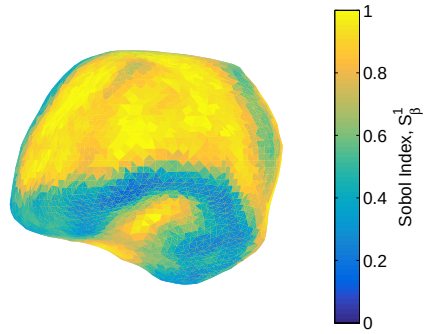


(a) 1998WT24

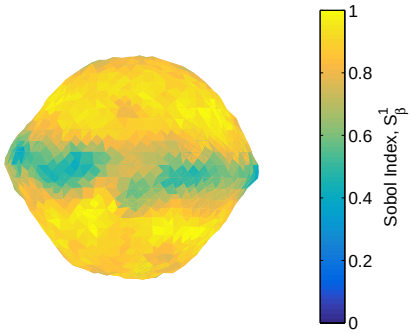


(b) 2008EV5

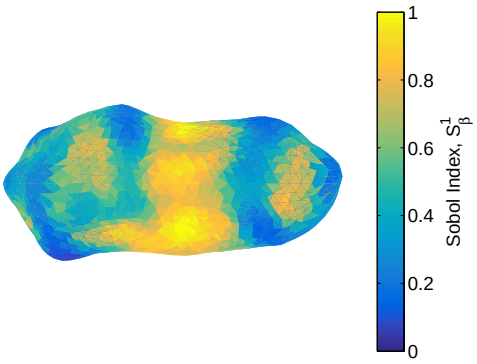


(c) Bacchus

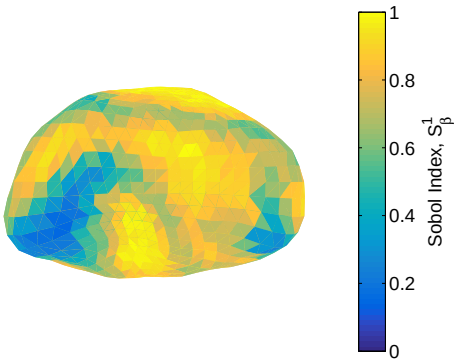


(d) Betulia

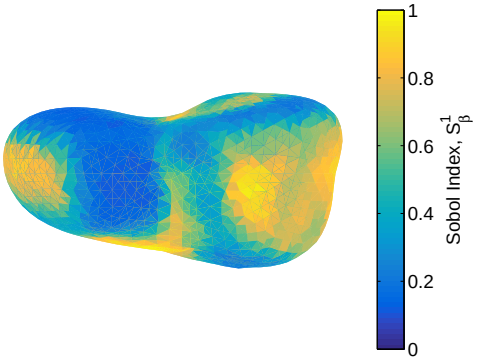


(e) Castalia

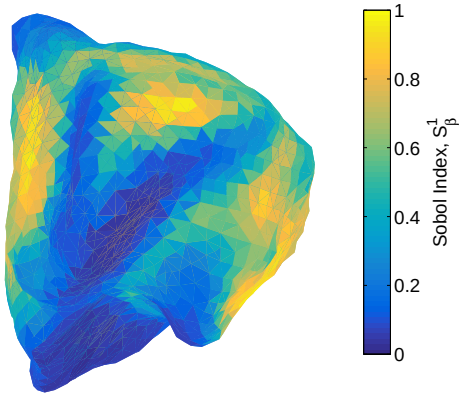


(f) Golevka

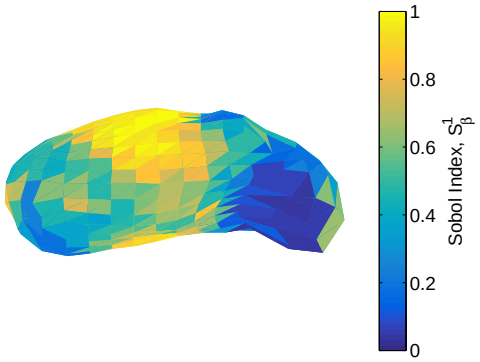


(a) Itokawa (low res)

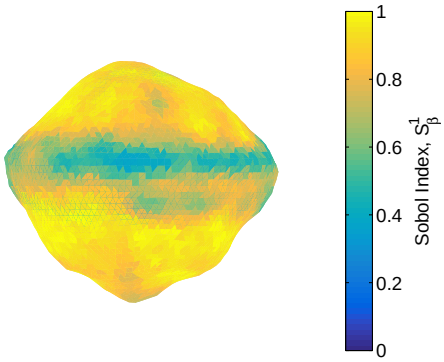


(b) KW4 (alpha)

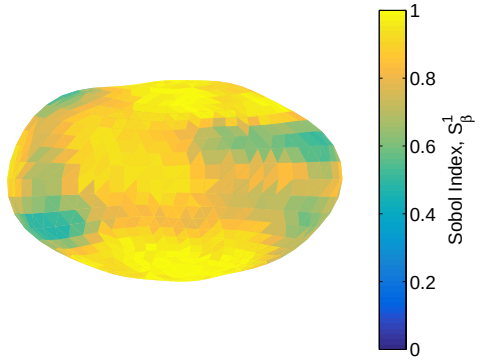


(c) KW4 (beta)

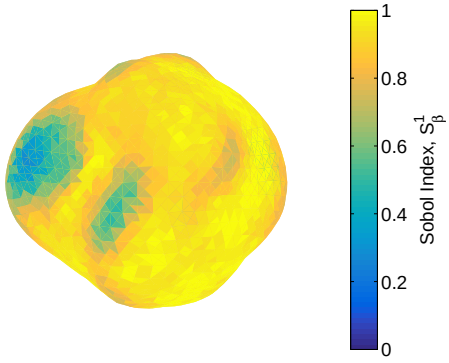


(d) KY26

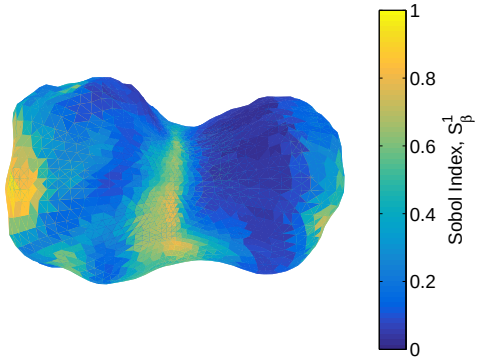


(e) Mithra (prograde)

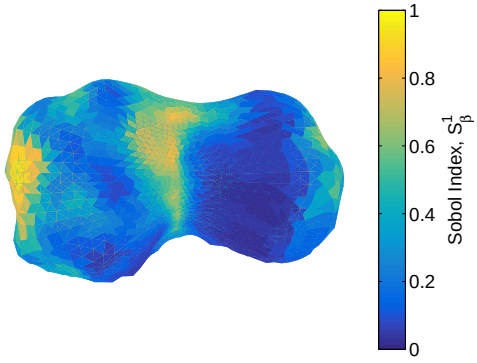


(f) Mithra (retrograde)

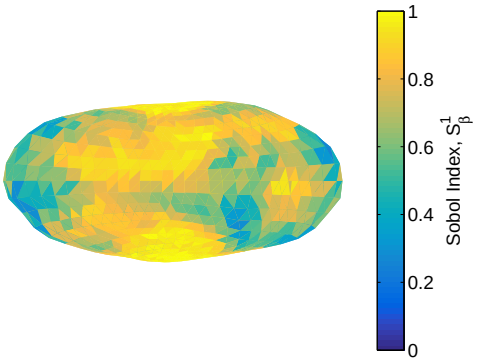


(a) Nereus

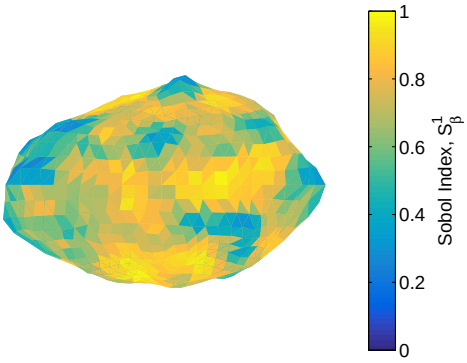


(b) Rashalom

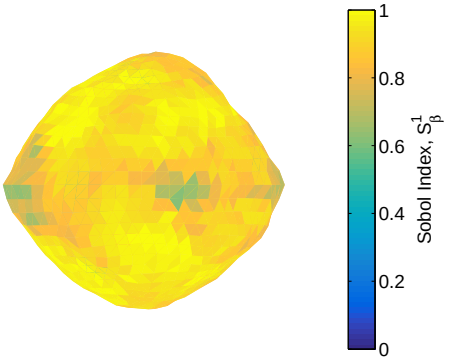


(c) RQ36

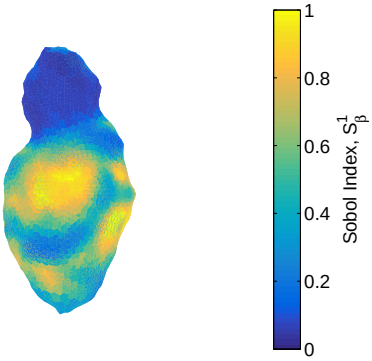


(d) Toutatis (low res)

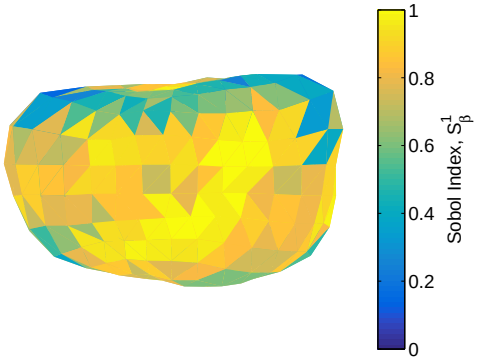


(e) Yorp